ALIGARH MUSLIM UNIVERSITY

DOCTORAL THESIS

Study of production of Low Mass Vector Mesons (LMVM) using Muon Chamber (MuCh) of CBM experiment at FAIR

Author:
OMVEER SINGH

Supervisor:
Dr. NAZEER AHMAD

A thesis submitted in fulfillment of the requirements
for the degree of Doctor of Philosophy

in the

Department of Physics

December 29, 2022

Abstract

Study of production of Low Mass Vector Mesons (LMVM) using Muon Chamber (MuCh) of CBM experiment at FAIR

To explore the QCD phase diagram at low temperatures and moderate to high baryon densities, the CBM experiment at the Facility for Antiproton and Ion Research (FAIR) in Darmstadt, Germany, will collide protons and heavy ions at relativistic energies to a fixed target. Recently, it was predicted that the Critical End Point (CEP) of a possible first-order phase transition could be found at temperatures and baryon densities that can be achieved with beam energies from the SIS100 accelerator. The CBM scientific programme to search for the location of the first-order phase transition and to identify the CEP is currently unique worldwide. To exploit this unique opportunity, CBM prepares its readiness for the first SIS100 beams to be extracted from the machine.

The CBM setup includes detector systems for identifying charged hadrons, electrons, and muons, as well as systems for determining the centrality of collisions and the orientation of the reaction plane. One particular challenge of CBM is its ability to perform heavy-ion collisions at extremely high interaction rates, which are orders of magnitude higher than the rates achieved in other high-energy heavy-ion experiments to date. The CBM setup includes a free-streaming data read-out and acquisition system that enables online reconstruction and event selection up to reaction rates of 10 MHz. With the help of high-intensity beams of FAIR and the high rate capability of CBM, it will be possible to overcome the statistical problems of the rare probes suffered in other recent and former experiments. These features will offer exceptional opportunities for performing highly precise measurements of multi-differential observables. They also help to obtain the signatures of extremely rare diagnostic probes by their decay channels, such as Low Mass Vector Mesons (LMVM) (η, ϕ and ω) and charmonium (J/ψ), which will provide an indication of in-medium modification of hadrons, chiral symmetry restoration.

The idea behind the muon detection system is to track the particles through a

hadron absorber and therefore accomplish momentum-dependent muon identification. This idea is achieved by segmenting the hadron absorber and placing triplets of tracking detector planes between the absorber layers. The MuCh detector will be built up of a different segment of carbon, concrete, and iron hadron absorbers, with the detector stations positioned between the segments. The work presented in this thesis is mainly based on the study of the production and detection of Low Mass Vector Mesons (LMVMs) in the FAIR energy domain. The thesis is broadly divided into two parts.

The first part deals with the optimization of the MuCh chamber geometry, the development of the simulation framework, and the feasibility of detection of muons produced by the decay of LMVM in Au+Au collision at 8 A GeV/c beam momentum using the MuCh detector sub-system.

In the second part of the thesis, we discuss comprehensive results on intermittency using the Scaled Factorial Moment (SFM) technique in Au+Au collisions in the FAIR energy range of 2-12 A GeV in pseudorapidity $\chi(\eta)$, azimuthal $\chi(\phi)$, and pseudorapidity-azimuthal $\chi(\eta$ - $\phi)$ spaces. The simulations are performed with a hybrid version of the Ultra-relativistic Quantum Molecular Dynamics (UrQMD) event generator. Three alternative equations of state (EoS) are employed to investigate the intermittency within the hydrodynamic scenario, namely pure Hadron Gas(HG), Chiral + HG, and Bag Model EoS. Additionally, a multifractal analysis to study the multiparticle dynamics in 60 A and 200 A GeV, ^{16}O-AgBr collisions at SPS, CERN and 14.5 A GeV/c, ^{28}Si-nucleus interaction at AGS, BNL have been performed in the pseudorapidity phase space.

A brief discussion on each of these topics and the main results are given below.

- **Implementation of MuCh geometries in CBMROOT software**
  CbmRoot is a simulation, reconstruction and analysis framework for the CBM experiment based on the ROOT system. Initially, the geometry parameters of the Muon Chamber (MuCh) detector was provided at the time of transport in ASCII format, and the CbmMuchGeoScheme class handled the construction. We had to modify CBM geometries in ROOT format and implement them as nodes to make the system transparent, usable, and user-friendly interfaces. Additionally, each detector geometry can be visualized stand-alone using the GL viewer of ROOT TBrowser, and a geometry database can handle the geometry files. The task of "rootification" includes the development of a macro to create the MuCh geometry and developing GeoHandler classes to include the rootified geometry in transport simulations.

- **First absorber optimization**
  The MuCh detector subsystem comprises multiple hadron absorbers and a triplet of tracking detectors positioned between the absorbers. In previous simulations with the MuCh setup, the first absorber was composed of high-density (ρ=2.26 g/cm^3) pure carbon having a thickness of 60 cm. Subsequent R&D for the mechanical design of the absorber blocks and a detailed market survey reveals the unavailability of high-density pure carbon in bulk, required to build the first absorber of surface area 260×250 cm^2. Therefore to keep the absorption profile and the physical thickness of the 1^{st} absorber block similar to as it was before, the possibility of having a composite absorber block made of two different materials instead of only carbon is explored. Concrete is chosen as an alternate option compared to other materials because it has the advantage of the mechanical and activation point of view. After investigating the influence of different absorber configurations on the reconstruction performance of $\omega(\rightarrow \mu^+\mu^-)$, the composite absorber of carbon with ρ = 1.78 g/cm^3 (28 cm) and concrete with ρ = 2.3 g/cm^3 (30 cm) has been adopted as the feasible configuration for MuCh first absorber. This configuration would provide an additional 2 cm gap between the absorber and detector stations, which could benefit MuCh service work on the detector chambers.

- **Investigation & implementation of realistic GEM chamber design**
  It has been decided from the detector R&D that triple GEM chambers to be used as the tracking detectors in the first two stations of MuCh will be operated with Ar/CO_2 gas mixture in a 70:30 volume ratio. Still, the triple GEM configuration required two 2 mm thick transfer gaps and one 2 mm thick induction gap to make a more realistic simulation. So, We have implemented passive volumes (of 6 mm thickness), and the gas mixture is also changed from Ar to Ar/CO_2 in a 70:30 volume ratio. There is no significant change in the ω reconstruction efficiency and signal-to-background ratio observed after implementing the realistic MuCh chamber geometry. The modified geometry is committed to the git repository and is being used as a default geometry in the physics simulation of dimuon measurement.

- **Low Mass Vector Meson measurements at FAIR**
  The reconstruction of the LMVM (η, ϕ and ω) in the dimuon channel is performed for the Au+Au collision system at 8 A GeV energy. Signal (ω decaying to dimuon) and background particles are generated by event

generators PLUTO and UrQMD, respectively. The GEANT3 simulation package is utilized for muon identification to transport the primary particles through the CBM detector setup. The generated primary and secondary tracks are reconstructed using realistic reconstruction methods. The selection cuts for dimuon candidates, based on the separation powers of these cuts to distinguish between signal and background, are optimised. then final results of the feasibility study on LMVM (ω, ϕ, and η) detection through the dimuon channel in 8 A GeV Au+Au collisions are presented. Due to the absorption of low-energy muons, the phase-space acceptance for LMVM (ω, ϕ, and η) shifts toward forward rapidities. The reconstructed dimuon invariant mass spectra reveal a clearly identifiable peak over the continuum: the combinatorial background from pion and kaon weak decay. The Super Event (SE) technique calculates the dimuon combinatorial background. The efficiency and acceptance correction matrices are constructed to compare the reconstructed spectra with results from other generators, simulations, models, or detectors.

- **Fluctuations from intermittency analysis in relativistic heavy-ion collisions**

  The non-statistical fluctuation in particle number densities throughout the pseudorapidity (or azimuthal) space is a characteristic feature of understanding the particle production in high-energy nucleus-nucleus and p-p collisions. This fluctuation is significantly more prominent than the statistical fluctuations caused by the finiteness of particle yield in a collision. To investigate dynamical fluctuations in terms of the Scaled Factorial Moment (SFM), Bialas and Peschanski introduced a new phenomenon termed intermittency. Assuming that the fluctuations are invariant over a wide range of scales, they anticipated a power-law dependence of the moments on the pseudorapidity bin size. In this section, comprehensive results on intermittency using the Scaled Factorial Moment (SFM) technique are discussed in Au+Au collisions in the FAIR energy range of 2-12 A GeV in pseudorapidity $\chi(\eta)$, azimuthal $\chi(\phi)$, and pseudorapidity-azimuthal $\chi(\eta - \phi)$. The simulations are performed with a hybrid version of the Ultra-relativistic Quantum Molecular Dynamics (UrQMD) event generator. Three alternative equations of state (EoS) were employed to investigate the intermittency within the hydrodynamic scenario, namely pure Hadron Gas (HG), Chiral + HG, and Bag Model EoS. In both one and two-dimensional spaces and at all beam energies, a weak intermittent type

of emission has been seen for Chiral+HG EoS. In contrast, a strong intermittent kind of emission is observed for Bag Model EoS. The incident beam energy dependency of intermittency has also been investigated. The strength of the intermittency is seen to diminish with increasing beam energy.

A multifractal analysis to study the multiparticle dynamics in ^{16}O-AgBr collision at 60 A and 200 A GeV and ^{28} Si-nucleus interaction at 14.5 A GeV/c are also performed separately in the pseudorapidity phase space. Multifractal moments, G_q, as the function of pseudorapidity bin size for the different orders of the moments, q, is calculated. The power-law behaviour is observed in the considered data sets. The variations of multifractal dimension, D_q, and the multifractal spectral function, $f(\alpha_q)$, with the order of the moments, q, are studied thoroughly. D_q is found to decrease with increasing order of the moments, q, indicating thereby a self-similar behaviour in the multiparticle production in the considered collisions.

Acknowledgements

This thesis is an outcome of my work at the Physics department, Aligarh Muslim University, Aligarh. Many individuals had tremendous contributions in helping me to reach this milestone. I take this opportunity to thank all of them.

First and foremost, I express my sincere gratitude to my thesis supervisor, Dr. Nazeer Ahmad, an associate professor in the physics department, for his guidance, unquestioning support, and encouragement throughout my work. I must acknowledge him for his significant involvement, moral support, helpful criticism, and patient attitude, all of which made it possible for me to complete this work.

I am grateful to Prof. Afzal Ansari and Prof. B.P. Singh, Ex-Chairman, and Prof. M. Sajjad Athar, Chairman Department of Physics, Aligarh Muslim University, Aligarh, for providing all research facilities throughout this study.

I am grateful to Prof. Subhasis Chattopadhyay, Variable Energy Cyclotron Center (VECC), for permitting me to work on the Compressed Baryonic Matter (CBM) experiment at VECC. During my PhD, he supported me in several ways, including physics discussions, simulation, software, etc. He had always been there for help, either personal or official.

I am particularly indebted to Prof. Shakeel Ahmad, Dr. M. Danish Azmi, Dr. M. Mohshin Khan, Dr. Ms. Hushnud Jahan, Dr. Anuj Chandra, Ms. Shaista Khan, Ms. Bushra Ali for their valuable suggestions, keen interest and encouragement.

My special gratitude to Dr. Partha Pratim Bhaduri, one of the first people I began working with within the collaboration. He provided me with moral support, encouragement, and a positive mindset at the beginning of the analysis work, all of which helped me finish this task.

I would like to thank all of my CBM collaborators at VECC, including Dr. Partha Pratim Bhaduri, Dr. Anand Kumar Dubey, Dr. Zubayer Ahammed, Dr. Vikas Singhal, Dr. Ajit Kumar, Mr. Joginder Saini, Mr. Chandra Sekhar Ghosh, Mr. Apar Aggrawal, Mr. Vinod Negi, Mitali Mondal and Mrs. Ekata Nandy.

I feel very fortunate to work with Dr. Florian Uhlig in GSI as a project student. I want to thank him for his numerous suggestions and advice and for showing a lot of patience in guiding me, which really helped me to grow my

knowledge of the software. I shall always be grateful to him for taking the time to check the manuscripts and all the corrections of the thesis.

I would like to give special thanks to Dr. David Emschermann (GSI) for his selfless help and support throughout my GSI stay. I have learnt a lot of things from him in my academic as well as personal life.

I would like to thank Dr. Rafi Alam, Dr. Raktim Abir and Dr. Haider Hasan Jafri for their valuable suggestions, keen interest and encouragement.

I am grateful to my software team in GSI, Germany, especially Dr. Volker Friese, Dr. Florian Uhlig, Dr. Pierre-Alain Loizeau, Dr. Sergei Zarko and Ms. Shreya Roy for their support in the CBM software part.

I would like to thank Prof. Tetyana Galatyuk, Dr. Anna Senger, Dr. Ilya Selyuzhenkov and all the other members of the CBM dilepton physics working group for their valuable discussions and suggestions on my simulation studies of dimuon reconstruction at CBM energies with MuCh detector sub-system

I would like to express my sincere gratitude to Dr. Vladimir Nikulin for giving ideas to optimise the first absorber configuration for the MuCh detector sub-system.

I also thank Mrs. Ekata Nandy (VECC) and Dr. Ajit Kumar (VECC) for their support and motivation at various stages of my PhD life.

I would like to thank Mr. Sayak Chatterjee (Bose Institute) for helping me with the simulation and analysis.

I also want to thank all my friends in the VECC guest house; Ajit, Mitali, Apar, Shabbir, Vivek, Deekshit, Vinay and Samrangy for their help and moral support. I always felt happy and motivated in their company. I am thankful to them for many stimulating discussions and for giving me many good memories of birthday parties, movies, outings, and all the fun.

In addition, I would like to thank everyone I met at the GSI Steinhaus: Mr. Utkarsh Verma, Ms. Jelena Bardak, Ms. Bella, Mr. Vishnu Chauhan, Mr. Md. Shahjahan, and Ms. Arzoo Sharma. In their company, I felt encouraged and energized at all times. I appreciate all our wonderful times together at dinner, on trips, and elsewhere.

I would like to thank Mr. Abhishek Seal and Mr. Prasun Singh Roy of VECC for their invaluable technical support.

I especially want to thank my friend and colleague Ms. Shreya Roy (Bose Institute), for her advice, support, and motivation throughout my Ph.D. life.

I would like to thank my colleague and friends in GSI; Ms. Shaifali Mehta and Mr. Mehul Siroya, for throughout support and care during my GSI stay.

I would like to thank Ms. Anjali Sharma (Punjab University) for throughout support and for giving me moral support.

I would also like to express my gratitude to my departmental non-teaching staff members; Mr. Naseem Ahmad Khan, Mr. Siddique Akbar, Mr. Jagdish Prasad, Mr. Musharraf Ali, Mr. Mohan Lal, Mr. Adil Ishrat, Mr. Zulfkar Ahmad, Ms. Amna Afridi, Ms. Shabana Qadeer, Mr. Mohd. Nafisul Hasan, Mr. Qaisar Jameel, Mr. Mohd. Zafar, Mr. Mohd. Zafar Idris Khan, Mr. Mohd. Mutahirul Mulk Mr. Zeeshan, Mr. Maaz Moonis, and Mr. Ashish Jacob, for all their technical and administrative support and motivation during my Ph.D. life.

I also like to thank my AMU lab mates; Mr. Abhishek Kumar Sharma, Ms. Anju Sharma, for always helping me and giving me moral support.

I am also thankful to my friends Akbar, Saqib, Rizwan, Azam and Mohd. Saud for all their help and moral support. I always felt motivated and cheerful in their company.

I am grateful to my best friends; Ms. Faiza Akbar and Ms. Anisa Khatoon, for all their help and moral support. I always felt motivated and cheerful in their company.

I feel so lucky to have Dr. Meeran Zuberi as a best friend and brother. I have never met anyone this loving and supportive. I know that I don't say this often, but I'm really grateful to him for everything he did for me.

I will never be able to repay my mother and late father for all their love and encouragement.

I would want to express my gratitude to my wife, Kalpana Chaudhary, who has stuck with me through all of my struggles, absences, bouts of anger, and impatience. She offered support and encouragement, discusses ideas, and prevents several foolish decisions.

Last but not least, I would like to thank my family members. Without their unconditional love and encouragement, this would not have been possible.

Omveer Singh

Dedicated To My Late Father…

List of Abbreviations

SM	**S**tandard **M**odel
QCD	**Q**uantum **C**hromo **D**ynamics
LHC	**L**arge **H**adron **C**ollider
RHIC	**R**elativistic **H**eavy **I**on **C**ollision
QGP	**Q**uark **G**luon **P**lasma
LQCD	**L**attice **Q**uantum **C**hromo **D**ynamics
CP	**C**ritical **P**oint
RHIC-BES	**R**elativistic **H**eavy **I**on **C**ollider-**B**eam **E**nergy **S**can
SPS	**S**uper **P**roton **S**ynchrotron
AGS	**A**lternating **G**radient **S**ynchrotron
EOS	**E**quation **O**f **S**tate
NICA	**N**uclotron based **I**on **C**ollider **F**acility
BM@N	**B**aryonic **M**atter @ **N**uclotron
CERN	**E**uropean **C**ouncil for **N**uclear **R**easearch
FAIR	**F**acility for **A**ntiproton **I**on **R**easearch
CBM	**C**ompressed **B**aryonic **M**atter
RPC	**R**esistive **P**late **C**hamber
LMVM	**L**ow **M**ass **V**ector **M**eson
SIS	**S**chwer **I**onen **S**ynchrotron
APPA	**A**tomic, **P**lasma **P**hysics and **A**pplication
PANDA	**A**ntiproton **A**Nnhilation at **DA**rmstadt
NUSTAR	**NU**clear **ST**ructure **A**strophysics and **R**eactions
MVD	**M**icro **V**ertex **D**etector
STS	**S**ilicon **T**racking **S**ystem
RICH	**R**ing **I**mage **CH**erenkov
MuCh	**Mu**on **Ch**amber
TRD	**T**ransition **R**adiation **D**etector
TOF	**T**ime **O**f **F**light
ECAL	**E**lectromagnetic **CAL**orimeter
PSD	**P**rojectile **S**pectator **D**etector
HEP	**H**igh **E**nergy **P**hysics
MC	**M**onte **C**arlo

$\mathbf{P}_{beam}$	Beam momentum
$\mathbf{E}_{beam}$	Beam Total Energy
$\mathbf{E}_{kinetic}$	Beam Kinetic Energy
$\sqrt{s_{NN}}$	Center of mass energy
UrQMD	**U**ltra **r**elativistic **Q**uantum **M**olecular **D**ynamics
GEANT	**GE**ometry **AN**d **T**racking
HADES	**H**igh **A**cceptance **D**i-**E**lectron **S**pectrometer
MWPC	**M**ulti **W**ire **P**roportional **C**ounter
MIP	**M**inimum **I**oninizing **P**article
HERA	**H**adron **E**leactron **R**ing **A**ccelerator
LHCb	**L**arge **H**adron **C**ollider **b**eauty
CMS	**C**ompact **M**oun **S**olenoid
TPC	**T**ime **P**rojection **C**hamber
FLUKA	**FLU**ktuierende **KA**skade
GSI	**GSI** Helmholtzzentrum für Schwerionenforschung
BNL	**B**rookhaven **N**ational **L**aboratory
Thermal-FIST	**T**hermal **F**ast and **I**nteractive **S**tatistical **T**oolkit
CEP	**C**ritical **E**nd **P**oint
SFM	**S**caled **F**actorial **M**oment
HG	**H**adron **G**as
BM	**B**ag **M**odel
CMOS	**C**omplementary **M**etal-**O**xide-**S**emiconductor
MAPMT	**M**ulti **A**node **P**hoto-**M**ultiplier **T**ube
BFTC	**B**eam **F**ragmentation **T**0 **C**ounter
MRPC	**M**ultigap **R**esistive **P**late **C**hamber
BMON	**B**eam **MON**itor
CPU	**C**entral **P**rocessing **U**nit
CERES	**C**loud and **E**arth's **R**adiant **E**nergy **S**ystem
S/B	**S**ignl-to-**B**ackground ratio
R&D	**R**esearch and **D**evelopment
DAQ	**D**ata **A**c**Q**uisition
HEED	**H**igh **E**nergy **E**lectro **D**ynamics
ADC	**A**nalog-to-**D**igital **C**onverter
ASIC	**A**pplication-**S**pecific **I**ntegrated **C**ircuit
CA	**C**ellular **A**utomation
KF	**K**alman **F**ilter
ASCII	**A**merican **S**tandard **C**ode for **I**nformation **I**nterchange
QED	**Q**uantum **E**lectro **D**ynamics

NA49/NA61	**N**orth **A**rea 49/61
ATLAS	**A** **T**ropical **L**HC Appratu**s**
ALICE	**A** **L**arge **I**on **C**ollider **E**xperiment
PHENIX	**P**ioneering **H**igh **E**nergy **N**uclear **I**nteraction E**X**periment
STAR	**S**olenoid **T**racker **A**t **R**HIC
DCUTE	**D**elta-ray **CUT** by **E**lectron

Contents

List of Figures

List of Tables

Chapter 1

Introduction

All the matter that we see around us is made up of atoms and can be characterized by its properties. The matter can be categorized into three states: solid, liquid, and gas. For example, ice is solid, the vapour is gas, and water is liquid at the Standard Temperature and Pressure (STP). Some macroscopic observables, such as temperature, pressure, etc., are control parameters. These parameters can be used to describe the properties of matter in thermal equilibrium. The state of matter depends on these control parameters. These different phases of matter in thermodynamics are represented by a graphical representation which is known as “Phase Diagram". The phase diagram of water is the most popular and well-known example. Water exists as ice or snow when it is in a solid state. It exists as water vapour or steam in the gaseous state. In addition, water is referred to as "water" when it is in its liquid state. Similarly, the properties of nuclear matter, which are controlled by a strong nuclear force, can undergo various phases. The various phases of nuclear matter can be obtained by either heating the nucleons to extremely high temperatures or compressing them to extremely high densities. A relativistic quantum field theory known as Quantum Chromodynamics (QCD) describes the strong nuclear force [1]. The quarks and gluons are the fundamental degrees of freedom in QCD, and quarks exist in six flavours: up, down, charm, strange, top, and bottom. The conjectured phases of strongly interacting matter can be described in the thermodynamic variable (Temperature (T) vs baryon chemical potential (μ_B)) known as the QCD phase diagram.

1.1 Quantum Chromodynamics (QCD)

The quantum field theory of strong interaction within the Standard Model of particle physics is known as Quantum Chromodynamics (QCD). In QCD, the fundamental degrees of freedom are point-like quarks and gluons. Quarks come in six different “flavours" in addition to the relativistic quantum numbers

mandated by Lorentz invariance (up, down, strange, charm, bottom and top). It turns out that quarks and gluons must additionally carry 'colour' as an extra quantum number in order to produce the right quantum statistics for hadronic wave functions [2, 3]. In contrast to QED, where photons have no electric charge, gluons in QCD have a colour charge. As a result, gluon self-interactions develop, which in turn cause the QCD coupling constant $\alpha_s = g_s^2/4\pi$ to run with (space-time) distance or momentum transfer Q, with the result that α_s drops logarithmically as Q rises (or separation "r" falls) [4]. The success of perturbative QCD is due to a phenomenon known as asymptotic freedom, which makes the description of some high-energy processes simpler (pQCD). On the other hand, the interaction between two quarks is strong at small Q. Infrared slavery refers to the amplification of strong force with increasing distance.

1.2 Exploring the phase diagram of nuclear matter

The primary subject of discussion in heavy-ion physics is the phase diagram of strongly interacting matter. The possible nuclear phases and their limits are shown in a temperature vs baryon chemical potential diagram in Fig. 1.1. Normal nuclei with a net-baryon density of one contain only protons and neutrons (i.e., nucleons). At moderate temperatures and densities, nucleons are excited to transient states (baryonic resonances) that decay by the emission of mesons. At higher temperatures, baryon-antibaryon pairs are also formed. This mixture of baryons, anti-baryons, and mesons, all of which are strongly interacting particles, is known as hadronic matter or baryonic matter if baryons dominate. When the nuclear matter is heated to extremely high temperatures and compacted to extremely high densities, the hadrons melt and the constituent quarks and gluons form the new phase, the quark-gluon plasma (QGP). The quantum chromodynamics on the lattice predicts that hadrons disintegrate into quarks and gluons above a temperature of around 155 MeV at extremely low net-baryon densities when the number of particles and anti-particles are roughly equal [5–7]. During the first few microseconds after the big bang, the universe suffered the inverse process: quarks and gluons were confined into hadrons. The transition from partonic to hadronic matter is expected to occur smooth crossover in this region of the phase diagram [7]. At relatively high baryon chemical potential, calculations suggest a critical endpoint [8]. One expects a first-order phase transition from hadronic to partonic matter with a phase coexistence region in between beyond this critical endpoint at higher values of net-baryon densities (and for lower temperatures). Beyond the first-order phase transition, a new

phase of so-called quarkyonic matter has been suggested to exist at high baryon chemical potentials and moderate temperatures [9]. The core of neutron stars is believed to consist of cold, high-density nuclear matter. The formation of a colour superconductor from correlated quark-quark pairs is expected to happen at very high densities.

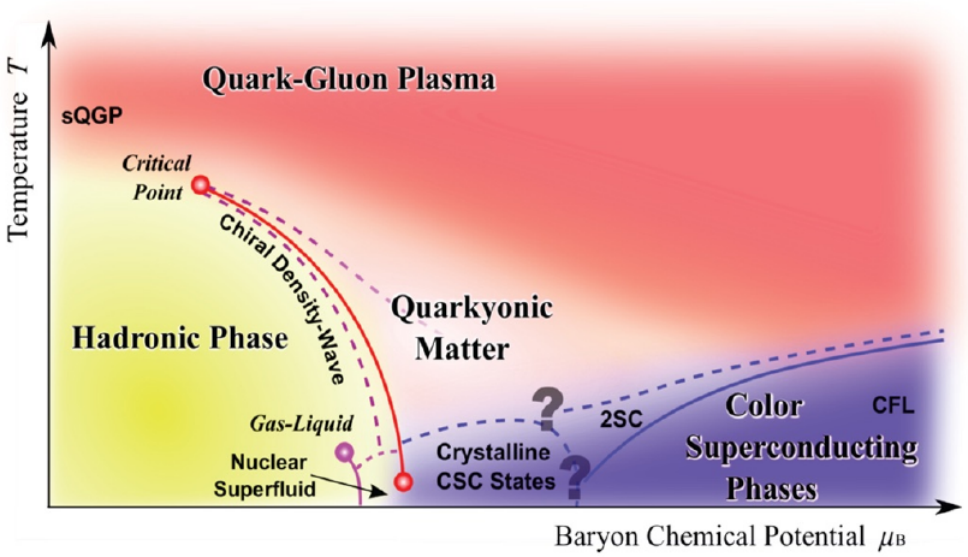

Figure 1.1: Sketch of the phase diagram of strongly-interacting matter (taken from [10]).

In the laboratory, hot and dense nuclear matter is generated in a wide range of temperatures and densities by colliding atomic nuclei at high energies. The experiments at RHIC and LHC are intended to investigate the characteristics of deconfined QCD matter at high temperatures and net baryon densities close to zero. Several experimental activities focus on investigating the QCD phase diagram at high net-baryon densities. The STAR collaboration at RHIC scanned the beam energies to locate the QCD critical endpoint and even performed a fixed target programme with the collider detector [11, 12]. The upgraded NA49 detector (NA61) is used in measurements at the CERN-SPS using light and medium size ion beams for the same purpose [13, 14]. To investigate the phase transition of nuclear matter at the high baryon density, a new heavy-ion collider (NICA) is being designed at the Joint Institute for Nuclear Research (JINR) in Dubna [15]. However, due to luminosity or detector limitations, these experiments are restricted to investigating particles that are abundantly produced. While using the high-intensity heavy-ion beams provided by the SIS100 accelerator, the Compressed Baryonic Matter (CBM) experiment at the Facility for

Antiproton and Ion Research (FAIR) in Darmstadt, is intended for high precision of multidimensional observables, including particles with pretty low production cross sections.

1.3 Diagnostic probes of the high-density fireball

Fig. 1.2 depicts the time of generation and final emission of several particle species throughout the development of a heavy-ion collision at FAIR energies as estimated by the UrQMD transport code [16, 17]. In the very first stage of the process, it is anticipated that the particles carrying charm quarks will be formed. D and J/ψ mesons may explore the dense fireball and its degrees of freedom. During the reaction, vector mesons like ω, ρ, η, and ϕ mesons are continually created by $\pi\pi$ annihilation. These mesons then decay either back into mesons or a pair of leptons. However, because final-state interactions do not affect leptons, the dileptonic decay offers a possibility to look into the fireball. In particular, the short-lived ρ meson has the potential to serve as an effective diagnostic probe for hot and dense nuclear matter. Due to their small hadronic cross sections, particularly by their collective flow, multi-strange hyperons and ϕ mesons also carry information about the dense collision phase. Finally, at densities below saturation density, most of the particles freeze out. In heavy-ion collisions (at fixed target) at beam kinetic energies between 2 and 15 A GeV, essentially, only these particles have been measured yet. The CBM experiment, therefore, provides an exceptional opportunity for unique findings.

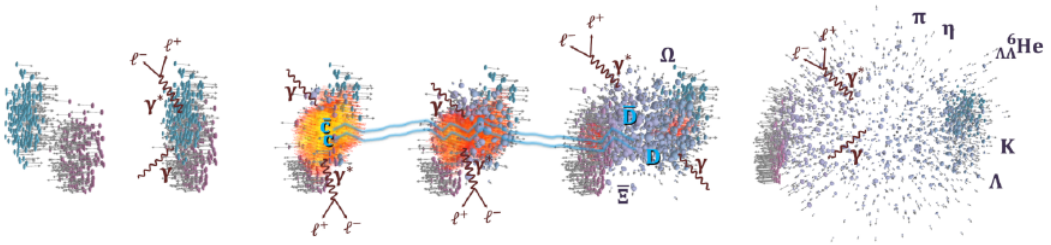

Figure 1.2: The UrQMD study estimates an Au+Au collision at a laboratory beam energy of 10 A GeV (Figure credit: T. Galatyuk and F. Seck).

The CBM experiment is designed to operate at high average reaction rates at the technological edge in order to provide high-statistical data even for the particles with the lowest production cross sections. As seen in Fig. 1.3, the rate capability of the CBM is orders of magnitude more than the rate capabilities of other heavy-ion experiments that are ongoing or that are planned. The detailed discussion about the CBM experiment is in chapter 2.

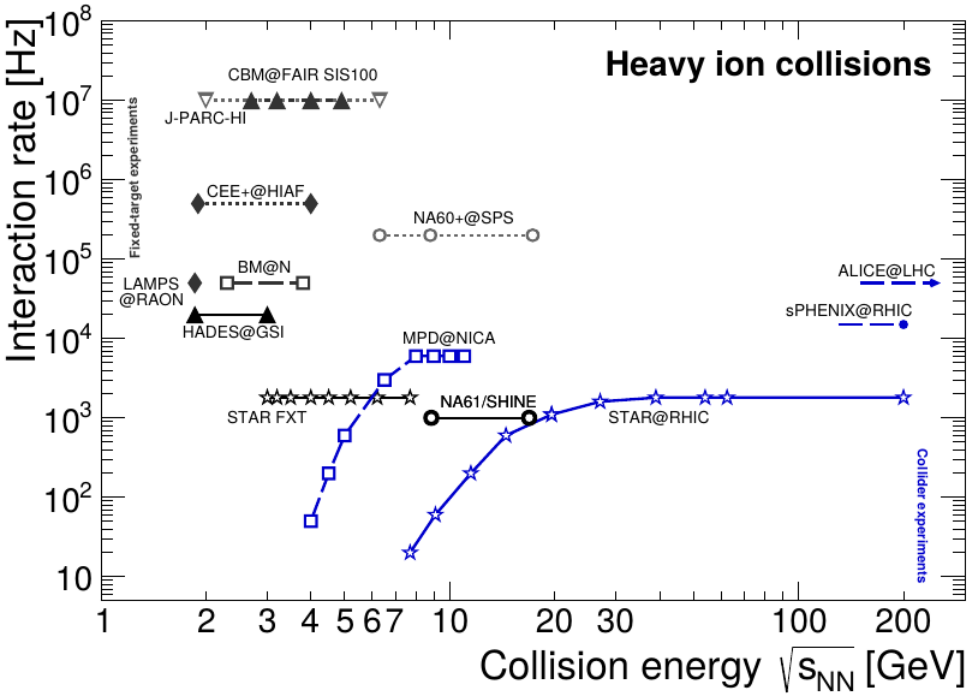

Figure 1.3: Existing and planned heavy-ion interaction rates as a function of center-of-mass energy [18]. The term "STAR FXT" refers to STAR's fixed-target operation.

1.4 Relativistic Heavy-Ion collisions

Relativistic heavy-ion collisions provide a way to study the properties of strongly interacting matter at energy densities substantially greater than that of normal nuclear matter. The concept is that by accelerating heavy nuclei to high velocities and colliding them, a large amount of their kinetic energy is deposited in a limited spatial region and transferred to thermal energy, resulting in extremely high temperatures. In the laboratory, by colliding heavy ions at various energies one can produce nuclear matter over a range of temperatures and densities. In principle, the phase diagram of strongly interacting matter can thus be experimentally accessible in nucleus-nucleus collisions at relativistically high energy.

1.4.1 Glauber Model

The geometrical arrangement of colliding nuclei is the basis of the Glauber model's [19] description of nucleus-nucleus collisions. A key element of this model (see Fig. 1.4) is the impact parameter "b", which determines the centrality of the collision by measuring the distance between the centres of colliding nuclei in the transverse plane. Collisions are central if $b \approx 0$, whereas peripheral collisions are those with a big impact parameter. Participant nucleons are those that engage at least once with a nucleon from the opposing nucleus, whereas

spectator nucleons are those that do not interact during a collision. Participants are left stranded in an interactive almond-shaped zone while spectators remain on their original path with little disturbance.

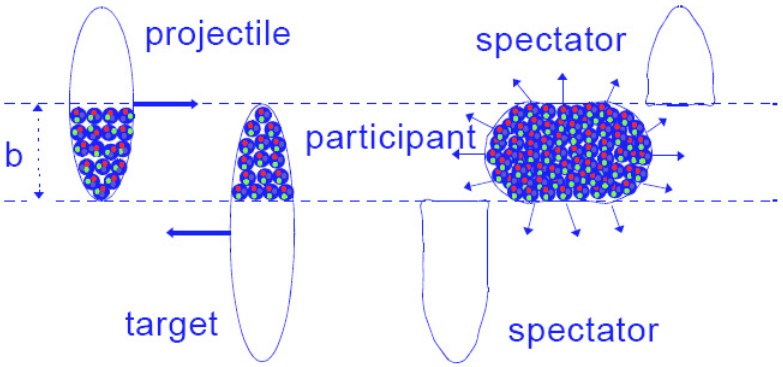

Figure 1.4: On the left, the state before the relativistic heavy-ion collision, and on the right, the subsequent production of dense matter following the impact [20].

1.4.2 Evolution of heavy-ion collisions

The collision of two ultra-relativistic atomic nuclei results in a short-lived and intensely interacting system. One of the topics under examination in heavy-ion experiments is the development of such a system as well as the characterization of its features. The current understanding of how heavy-ion collisions change over time is seen in fig. 1.5. The various phases of the collision with respect to the collision time “t" are as follows:

1. **t $<$ 0 fm/c**: The two atomic nuclei move along the beamline, nearly approaching the speed of light. The nuclei are strongly Lorentz contracted in the laboratory reference frame at the relativistic energy attained by contemporary accelerators and acquire a disc-like shape.

2. **At t = 0 fm/c**: The collisions happen and often describe by the Glauber model, as described in the previous section.

3. **for 0 fm/c $<$ t $<$ $\tau_0 \sim$ 1fm/c**: Due to the nature of hard processes and the basic uncertainty involved between the time and the energy in quantum mechanics, hard processes between colliding partons-processes with large transferred momentum occur at the very first stage of the collisions. All the high-energy particles (those with either high momentum or/and high mass) are formed during this stage, which is referred to as pre-equilibrium.

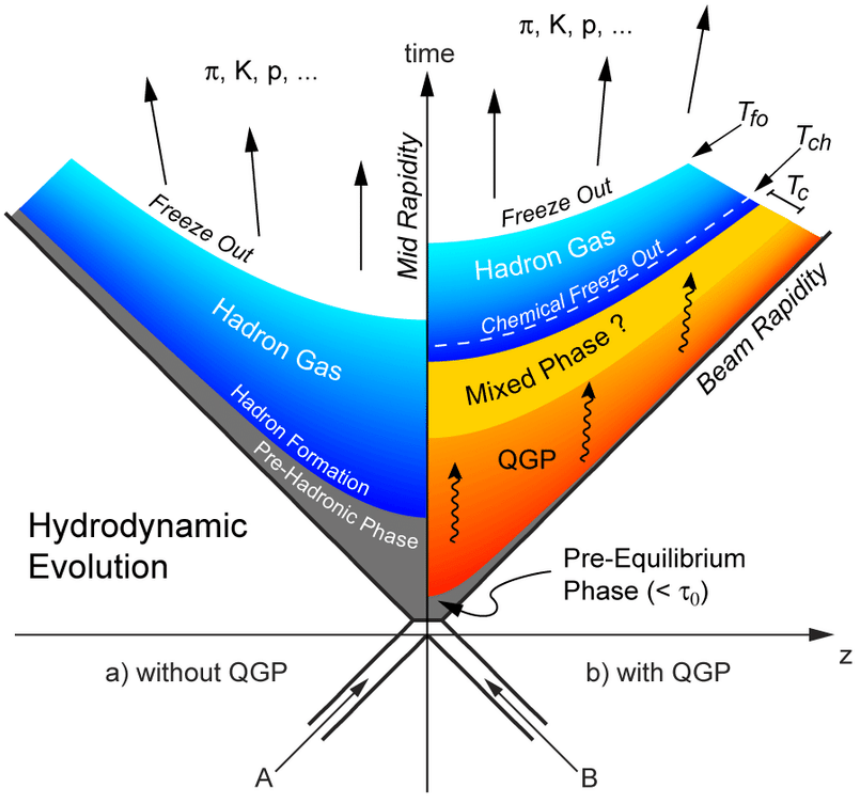

Figure 1.5: The space-time evolution of heavy-ion collision.

Such processes typically take place within 0.1 fm/c of time. The momentum of the nuclei in collisions with large collision energies is such that, at the first collision stage, their constituent partons conduct many contacts, losing energy in the mid-rapidity region ($y \sim 0$) and subsequently escaping at forward rapidities ($|y| \gg 0$). The system that results possesses the diminishing baryonic chemical potential and a heated, interacting medium at mid-rapidity. The fleeing valence quarks and the nucleons that were not involved in the collision quickly accelerate the baryonic potential carried by the colliding nuclei (the spectators). The energy density in HICs at RHIC and the LHC is sufficient that a shift to the QGP state is anticipated. The obtained droplet of QGP matter reaches equilibrium at the appropriate time τ_0 after a brief strong Parton rescattering phase.

4. **for 1 fm/c $<$ t $<$ 10 fm/c**: Under the pressure of the thermal pressure gradients created at the system boundaries, the equilibrated QGP droplet grows quickly. Relativistic hydrodynamics is frequently used to simulate this phase of the QGP droplet's fast growth, and the results may be used to understand experimental data. The system cools down as it expands,

finally bridging the phase transition between QGP and regular hadronic matter.

5. **for 10 fm/c $<$ t $<$ 15 fm/c**: The system progressively transforms into an interacting hadron resonance gas once the threshold temperature between the two phases is attained. During this phase, elastic and inelastic interactions between the hadrons in the system continue to take place while the system continues to expand and contextually cool down. The point at which momentum transfer between hadrons is insufficient for inelastic interactions is referred to as chemical freeze-out. After the chemical freeze-out, the relative abundances of various particle types are frozen since no additional inelastic reactions will occur. The kinetic freeze-out, when hadrons cease interacting with one another and the particle momenta are fixed, is the second significant event in the development of the hadron gas.

6. **for t $>$ 15 fm/c:** With no further interactions, hadrons produced in the collision leave the interaction zone. "Free hadron stream" is another name for this system.

Of course, the final stage is to use the experimental equipment to find any particles created by collisions. Although the development for high multiplicity p-p collisions is similar to that of a Pb-Pb collision, the end state of p-p collisions is fundamentally different because of the decreased creation of quarks and gluons in the early stages.

1.5 Signatures of QGP

This section will provide a brief description of some of the different signatures that indicate the formation of QGP in relativistic heavy-ion collisions. The main problem with the detection of QGP in relativistic heavy-ion collisions is that the fireball has a short lifetime, making it impossible to measure it directly. Therefore, one needs to look for signals to find indirect evidence of QGP formation. As a result, it is particularly crucial to find experimental observables that carry information (preferentially) from a particular stage, specifically the QGP phase. Over the years, several QGP probes have been proposed that are believed to carry unambiguous and experimental signatures for deconfinement transition in nuclear collisions [21–24]. The experimental signals proposed over the years to probe the matter created in heavy-ion collisions will now be briefly discussed.

1.5.1 Global observables

Global observables such as the transverse energy E_T, particle multiplicities (N_γ, N_{ch}, etc.), p_T-spectra of the generated particles, and their pseudo-rapidity distributions with the mass number and beam energy, offer insight into the dynamics of the system and the generation of QGP [25, 26]. It is also suggested that the correlation between the number of generated particles and transverse momentum p_T may act as a test for the EoS of hot hadronic matter [27]. The rapidity density (dN/dy), which reflects both the entropy and the mean transverse momentum, ($\langle p_T \rangle$) linearly scales with $\langle p_T \rangle$, with the exception at the locations of phase transition as predicted by Landau's hydrodynamic model. If the phase transition is of the first order, the temperature stays constant at the coexistence of the hadron gas and the QGP phase, resulting in an increase in entropy density. Consequently, when entropy rises, $\langle p_T \rangle$ will reach a plateau. Therefore, the global observables such as dN/dy and p_T will indicate the QGP phase as well as the order of phase transition.

1.5.2 Jet Quenching

At the initial stages, high-momentum partons are created and they propagate across the medium. As a result, they are regarded as the primary QGP medium probes. The generation of heavy quarks and gluon scattering occurs in the initial phases of collisions. As the collision progresses, these quarks and gluons are fragmented, hadronized, and distributed into the collimated spray of hadrons known as "Jets". Therefore, the measurement of jets can provide insight into the propagation across the media, such as the process of energy loss in the medium. The fragmentation function refers to the distribution of the parton momentum carried by the fragments. Due to the existence of the medium in the A-A collision, the fragmentation function differs from that in a p-p collision. The di-jets, which have identical amounts of energy and are created back-to-back on the transverse plane at a 180° azimuthal angle separation. One parton travels through the medium and loses energy by interacting with the QGP medium before fragmenting if the scattering occurs close to the fireball's surface. This process, called jet quenching, is schematically depicted in Fig. 1.6.

The nuclear modification factor (R_{AA}) is defined as :

$$R_{AA}(p_T) = \frac{1}{\langle N_{coll} \rangle} \frac{\sigma_{inel}^{AA}}{\sigma_{inel}^{pp}} \frac{\frac{d^2 N_{AA}}{dp_T dy}}{\frac{d^2 N_{pp}}{dp_T dy}} \tag{1.1}$$

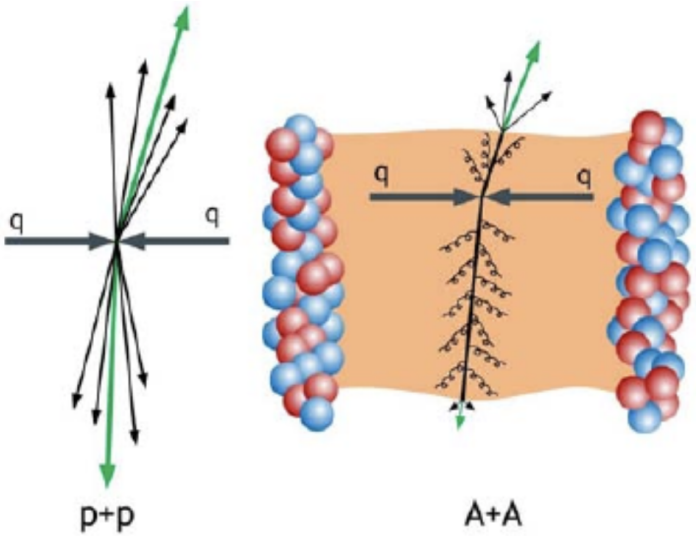

Figure 1.6: The pictorial depiction of jet quenching in heavy-ion collisions in comparison to p+p collisions.

where, $\langle N_{coll} \rangle$ stands for the average number of nucleon-nucleon collisions; σ_{inel}

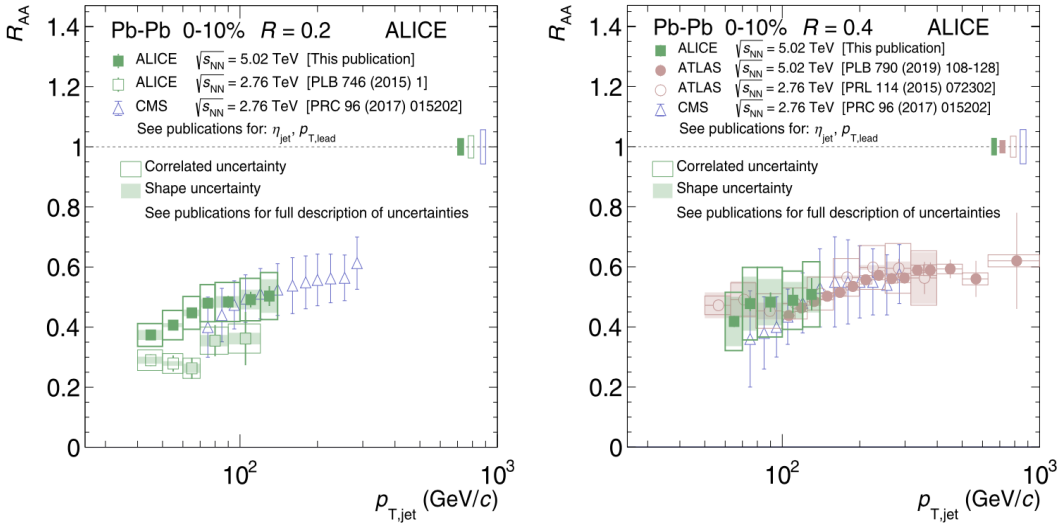

Figure 1.7: Left : Jet R_{AA} for R = 0.2 in 0–10% central Pb-Pb collisions. Right: R = 0.4 in comparison with published results [28].

is the term for inelastic cross section and A+A (p+p) stands for the heavy-ion (p-p) collisions. The formula makes it obvious that R_{AA} should be equal to 1 if there are only p-p collisions, and any deviation from this value denotes the presence of medium effects. Fig. 1.7 depicts the observed jet nuclear modification factor (R_{AA}) for central collisions (0–10%) from the ALICE [28–31], STAR [32], ATLAS [33, 34], and CMS [35] collaborations at 2.76 and 5.02 TeV. In comparison to p-p collisions, the observed jet spectrum in Pb-Pb collisions exhibits a significant suppression with a little p_T dependency.

1.5.3 Quarkonia suppression

For analysing QGP properties, the bound states of a heavy quark and its anti-quark, known as quarkonia, is quite useful. Quarkonia are created during the earliest phases of collisions by scattering of partons because of the enormous masses [36]. Due to their large lifetime, quarkonia can encounter all phases of the medium evolution of collisions [37]. On the other hand, the presence of QGP medium may have an impact on how the quark-antiquark pairs were hadronized. Debye colour screening, a phenomenon of colour charge screening brought on by quarks, antiquarks, and gluons, decreases the bonding between quarks and antiquarks in the presence of a dense and deconfined medium. Due to the dissociation of quarkonium inside QGP, the yield of nucleus-nucleus collisions is decreased. In order to discriminate between p-p and A-A collisions, the quarkonium suppression is a useful probe [38]. Ritcher and Ting independently discovered J/Ψ ($c\bar{c}$), the most prevalent type of quarkonium, in 1974.

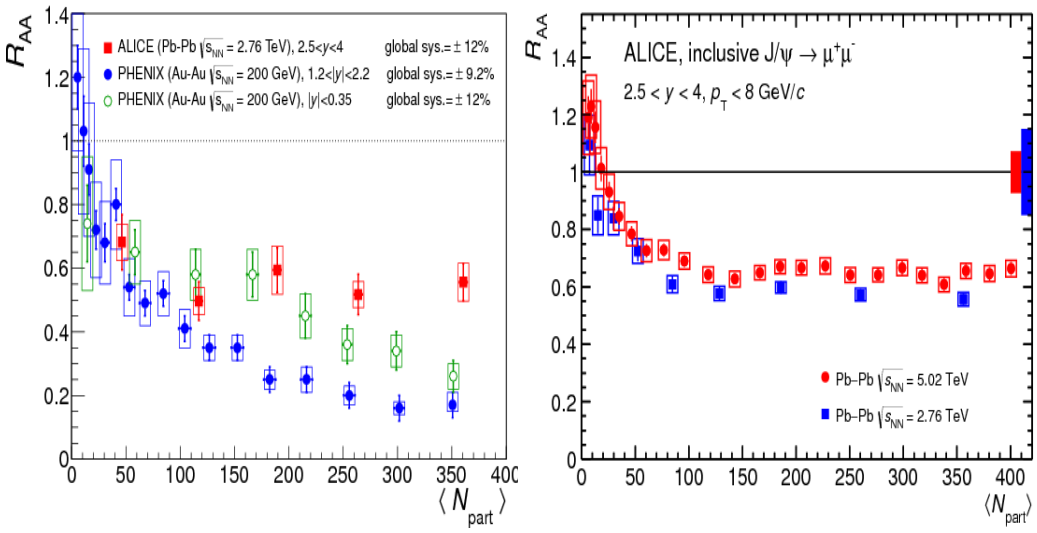

Figure 1.8: Left: The nuclear modification factor of inclusive J/Ψ as a function of N_{part} [39]. Right: R_{AA} as a function of N_{part} for 2.76 TeV and 5.02 TeV [40].

Through the nuclear modification factor, the J/Ψ ($c\bar{c}$) suppression is investigated in Pb-Pb collisions at ALICE at $\sqrt{s_{NN}}$ = 2.76 TeV and 5.02 TeV [39, 40], as well as at CMS [41]. Fig. 1.8 (Left) depicts the visible suppression of J/Ψ in Au+Au collisions at $\sqrt{s_{NN}}$ = 200 GeV in comparison to the PHENIX experiment findings [42–44]. Furthermore, it is evident from Fig. 1.8 (Right) that the suppression is nearly the same for the energies both (2.76 TeV and 5.02 TeV).

1.5.4 Direct Photons

We can directly observe the actions of quarks due to electromagnetic radiation produced by photons that they release. In QGP, quarks interact through real or virtual photons, the former of which has a long mean free path because of their interaction, allowing them to cleanly leave and convey the information about the state's temperature. On the other hand, the message carried by the direct photon is retained when the virtual photon decays through the dileptonic channel. Experimentally, the inclusive photon can only be measured and is essentially divided into two groups decay photons (γ_{dec}), which are all photons originating from hadron decays, and direct photons (γ_{dir}), which are not coming from particle decays. The primary sources of direct photons in A+A collisions are (1) direct photons resulting from initial hard scattering, (2) thermal photons emitted by the medium, (3) thermal photons coming from the hadron gas created after hadronization, and (4) photons produced in interactions [45–47].

First measurements of direct photon generation in S+Au (200 GeV) and Pb+Pb (158A GeV) at SPS were made by the WA98 collaboration [48, 49]. Along with p+p results, the PHENIX experiment detected the direct photon spectrum in Au+Au collisions [50, 51]. Subsequent results were validated by ALICE [52, 53], CMS [54], and ATLAS [55]. The ALICE reported direct photon excess ratio for Pb + Pb collision at $\sqrt{S_{NN}}$=2.76 TeV with different centrality shown in Fig. 1.9.

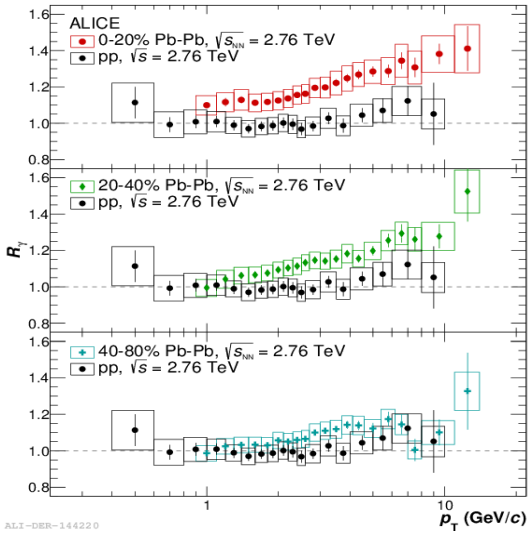

Figure 1.9: Direct photon excess ratio for Pb-Pb collisions [53].

1.5.5 Dilepton production

The dileptons, which do not interact strongly and provide information from the very early stage of the fireball, are of particular interest for the understanding

of matter. These electromagnetic observables can predict the fireball's lifetime, temperature, chiral symmetry, and other properties [56]. Especially dielectrons have a vast phase space available due to their low mass. On the other hand, dimuon signals have the advantage that they are relatively easy to identify. Dileptons can be emitted at any time during the collision. A differential investigation as a function of the invariant mass and transverse momentum allows one to differentiate between the various sources. The primary dilepton sources at low invariant masses (below 1 GeV/c^2) are the direct decays of vector mesons (ρ, ω, ϕ ...) and Dalitz decays of pseudoscalar mesons (π^0, η, $\eta^{'}$ ..). An important observable for the QGP is the strangeness production, which can be studied by measuring ϕ mesons because of their s$\bar{s}$ quark composition. The ρ meson is very sensitive to the restoration of chiral symmetry, which is expected to close the phase transition to the QGP in heavy-ion collisions [57]. This meson's lifetime is shorter than that of the medium. As a consequence, the dense medium and the anticipated restoration of chiral symmetry influence its spectral function, which may be estimated by studying its dielectron decay channel. The ϕ meson may also be sensitive to the restoration of chiral symmetry, which may be observed by measuring a broadening of its spectral function; however, no evidence of such an effect has been reported. The dileptons are also produced by thermal QGP radiation from the medium in heavy-ion collisions. The thermal radiation from the QGP and the hadronic phase covers a broad mass range. The entire dilepton spectrum can be divided into three categories based on the lepton pair invariant mass: low mass region (M $\leq$ 1.02 GeV), intermediate mass region (1.02 < M < 3.1 GeV) and high mass region (M $\geq$ 3.1 GeV). One of the most valuable probes for studying the in-medium modification of the hadrons is the decay of LMVM (ρ, ω, ϕ) in the dilepton channel [58]. Because the radiation from the QGP medium dominates the dilepton spectra in the intermediate mass region, this region is crucial for obtaining any possible QGP signature [59]. Heavy quarkonia, such as J/ψ,$\psi^{'}$ decay into dileptons and their suppression can indicate the formation of QGP in the high mass region [60].

In the mass range between 0.3 GeV/c^2 and 0.7 GeV/c^2, CBM will look into the enhancements of dimuons. It was demonstrated by [56] that these low-mass dimuons could also be used to measure the fireball's lifetime. The area where the CBM experiment will measure dileptons has many unexplored territories. The ability of CBM to measure dimuon and dielectron signals may significantly contribute to global data. The MuCh detector sub-system at CBM is dedicated to detecting the dimuons generated by the decay of LMVM and J/ψ. In contrast,

the RICH detector sub-system will be utilised to detect the dielectrons, providing the entire di-lepton spectrum to be measured at CBM SIS100 energies. The simulation study of the feasibility of dimuon decaying from low mass vector mesons (ω, η and ϕ) in the CBM experiment using muon chamber detector system is discussed in chapter 5.

1.5.6 Fluctuations

The behaviour of the phase transformation from hadronic to quark-gluon plasma produced in heavy-ion collisions is studied using fluctuations of thermodynamic observables [61]. Large energy density variations are anticipated for first-order phase transitions, whereas specific heat diverges for second-order phase transitions. Furthermore, it is anticipated that variations would significantly increase close to the critical point [62]. The fluctuations of conserved variables like electric charge, baryon number, or strangeness are commonly investigated in experiments [63]. These fluctuations are formed during the initial plasma stage of the system created in heavy-ion collisions with quark and gluon degrees of freedom. As the system develops over time, it is anticipated that the fluctuation produced during the partonic phase would rise [64, 65]. Net charge fluctuations are widely studied along with all the fluctuations.

PHENIX studied net charge fluctuations shown in Fig. 1.10 for Au+Au collisions at center-of-mass energy 130 GeV; STAR measured it for Au+Au at 200, 130, 62.4 and 19.6 GeV [66, 67] and ALICE reported for Pb-Pb collisions at 2.76 TeV [68].

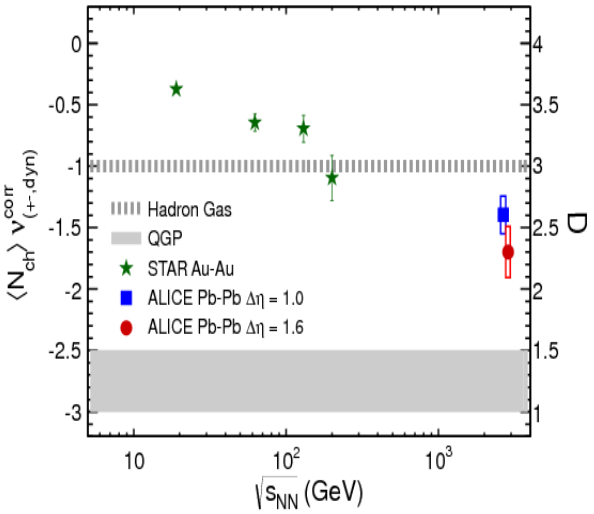

Figure 1.10: The beam energy dependence of $\langle N_{ch} \rangle v^{corr}_{+-,dyn}$ on the left axis and D on the right axis for most central collisions along with STAR and theoretical predictions [68].

1.5.7 Strangness enhancement

According to Johann Rafelski and Berndt Muller's predictions, the QGP state will emit strange particles more frequently than other hadrons [69–73], which might be utilised as a QGP signature. According to predictions [70], the increase in strangeness production will increase by a factor of 10-50. The following are the causes of the strangeness enhancement:

- Through the gluon-gluon fusion g + g $\rightarrow$s +$\bar{s}$, more gluons are produced in the QGP, which increases the creation of strange quarks [74]. Due to the constrained volume preventing such reactions, the gluon density and energy density are lower inside hadrons.

- The strange quark mass is significantly reduced as a result of the restoration of chiral symmetry in QGP, making it considerably simpler to form s + $\bar{s}$ pairs in q-q or g-g collisions. A quark's mass is only its present mass in the chirally symmetric state of QGP; however, in a chiral condensate, the mass is bigger and is known as the component quark mass.

The strange particles chemically freeze out early in a system's existence and interact with quarks of all flavours before finally manifesting as a strange hadron. Strange quarks have an extremely quick chemical equilibration period in dense nuclear matter (order of 5-6 fm/c), which is equivalent to the QGP lifetime. Since interactions with incoming beam particles need anti-nucleons, the production of anti-hyperons is implausible. Multi-strange anti-baryons behave differently in QGP, which makes them an effective probe.

The strangeness enhancement are studied by NA57 [75, 76], STAR [77–79] and ALICE [80] for various systems and different energies. Along with the STAR and NA57 data, Fig. 1.11 displays the yields of strange particles for Pb-Pb collisions as a function of N_{part}. The increase in the generation of strange particles is evident in the results.

1.5.8 Azimuthal Anisotropy

As a result of the system's thermalization, azimuthal anisotropies in particle formation are another important property of the particles produced in heavy-ion collisions. It is typical for two nuclei to collide in non-head-on collisions. In these cases, the partial overlap of the colliding nuclei creates an asymmetric interaction volume [81], which is typically shown as having the shape of an almond (Fig. 1.12). The pressure gradient produced by this asymmetric overlap (spatial anisotropy) is more pronounced in the direction of the reaction

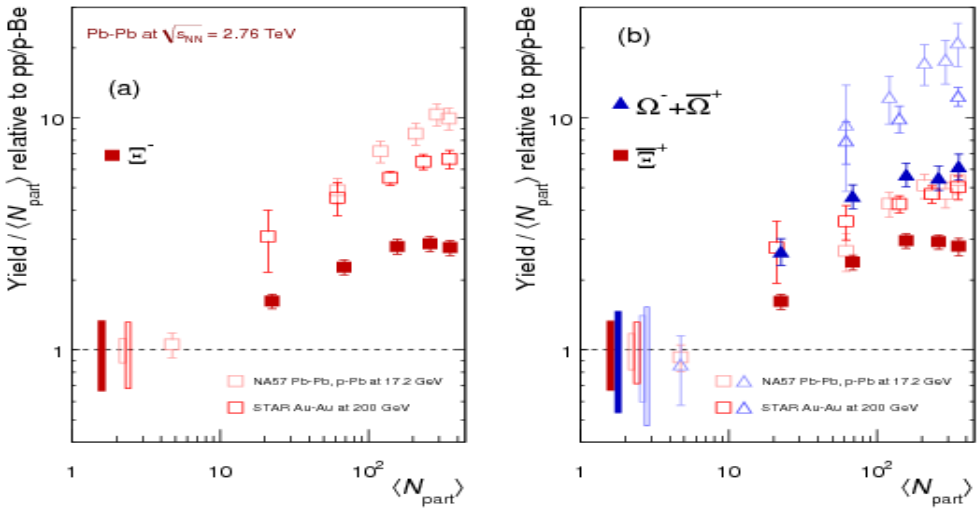

Figure 1.11: Strangeness enhancements as a function of N_{part} [80].

plane than orthogonally to it [81, 82]. The plane that is covered by the collision axis and the impact parameter vector ('b') is known as the reaction plane. The medium continues to expand in a non-uniform way due to the pre-existing pressure gradients and the asymmetry, which causes more particles to come from the short axis of an almond-like shape than that of its long axis because of the higher pressure. Early-stage spatial deformations of the overlapping zone are converted to an anisotropic momentum distribution in the final state. The anisotropic flow, another name for this transfer, shows that partons are strongly interacting in the presence of a QGP.

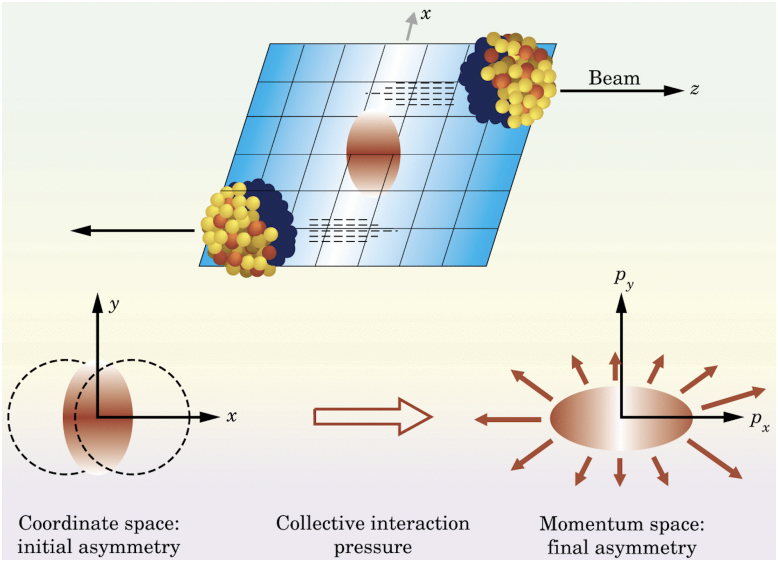

Figure 1.12: A visual representation of a heavy-nuclear non-centred collision at very high energy [83].

It is usual practice to use a Fourier series to measure the azimuthal distribution of produced particles [84]:

$$E\frac{d^3N}{dp^3} = \frac{1}{2\pi}\frac{d^2N}{p_T dp_t dy}(1 + \sum_{n=1}^{\infty} 2v_n \cos(n(\phi - \psi_R)) + \sum_{n=1}^{\infty} 2a_n \sin(n(\phi - \Psi_R))) \tag{1.2}$$

where “E" stands for the particle’s energy, “p" stands for momentum, “p_T" stands for transverse momentum, “ϕ" stands for azimuthal angle, “Ψ_R" stands for reaction plane (RP) angle, and “y" [85] stands for rapidity. The Fourier coefficients v_n stand for the “FLOW" coefficients, which define the strength of the asymmetry, and n = 1, 2, 3, and so on.

We have many situations for v_n depending on the changing “n":

- v_1 is referred to as “Directed Flow." Particles are emitted in a single preferred direction if the initial Fourier expansion coefficient has a non-zero value.

- Elliptic Flow, or v_2, has achieved the rank of “STAR" in the azimuthal anisotropic domain. In contrast to directed flow, a non-zero v_2 means that there are differing numbers of particles produced parallel to and orthogonally to the impact parameter. The emission is largely out-of-plane if v_2 is less than zero; the emission is mostly in-plane if v_2 is greater than zero.

  The v_2 can be obtained by:

  $$v_2 = \langle cos(2(\phi - \Psi_{RP}))\rangle \tag{1.3}$$

  In this case, “$\langle\rangle$" stands for the average across the particles in an event, followed by the total of all the events in a sample.

- According to the initial inhomogeneities, v_3 and v_4 are referred to as “Triangular Flow" and “Quadilateral Flow," respectively.

Among these flows, the elliptic flow has received the most investigation and is the subject of several approaches, including the probability $p(v_2)$ [87], Q-cumulant method [88], and the event-plane method [89, 90]. The v_2 has been measured by the STAR [91, 92], PHENIX [93], [94] and ALICE [86, 95] experimets using various techniques and for various systems.

The initial findings from ALICE’s study of elliptic flow in Pb-Pb collisions at the center of mass energies of 2.76 TeV are shown in Fig. 1.13. Along with the $v_2\{4\}$ for Au+Au collisions at 200 GeV for the same centrality, the p_T differential

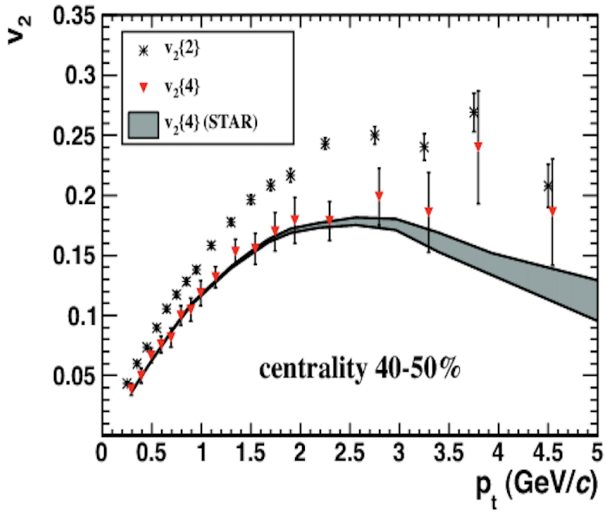

Figure 1.13: Results from the STAR experiment show the dependency of v_2 (2-particle and 4-particle) on transverse momentum for 40–50% centrality for Pb–Pb collisions at 2.76 TeV [86].

elliptic flow is computed for 40–50% centrality. Within uncertainties, the transverse momentum dependency for the two systems at various energies is substantially identical. Fig. 1.14 depicts the centrality dependence of elliptic flow,

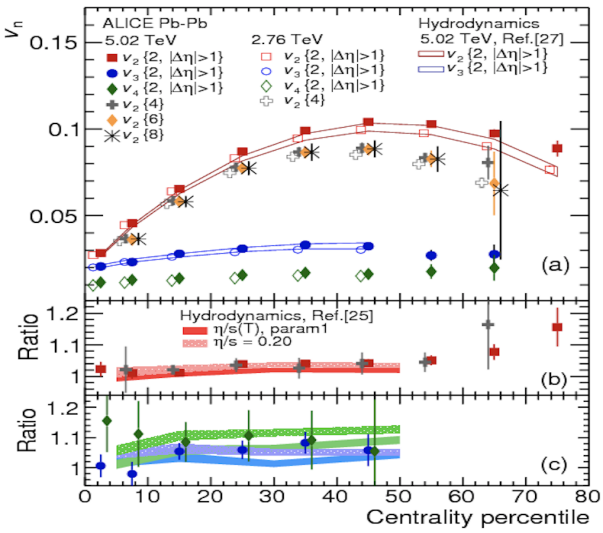

Figure 1.14: (a) For energies of 2.76 and 5.02 TeV, anisotropic flow as a function of centrality and hydrodynamic model predictions. The ratios of v_2, v_3, and v_4 in (b) and (c) range from 5.02 TeV to 2.76 TeV [95].

triangular flow, and quadrilateral flow from two- and multi-particle cumulants summed throughout the $0.2 < p_T < 5.0$ GeV/c along with the hydrodynamic model [95] for 2.76 and 5.02 TeV Pb-Pb collisions. For the v_2, v_3, and v_4, an average rise of $3.0 \pm 0.6\%$, $4.3 \pm 1.4\%$, and $10.2 \pm 3.8\%$ is shown across the centrality range of 0-50%, from 2.76 TeV to 5.02 TeV.

Energy Dependence of v_2: In Fig. 1.15 [95], the p_T integrated v_2 is compared from lower energies to the LHC energies for 20-30% collision centrality in Pb-Pb collisions. Anisotropic flow for 20-30% centrality has steadily increased from SPS/RHIC to LHC energies. From 200 GeV to 2.76 TeV, there is an about 30% increase in elliptic flow, and from 2.76 TeV to 5.02 TeV, there is an approximately 5% increase. The increase in integrated flow coefficients is mostly attributable to a rise in average transverse momentum.

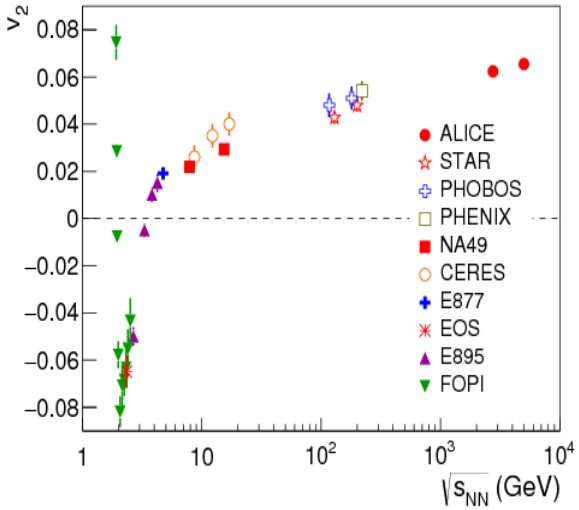

Figure 1.15: The p_T dependent elliptic flow ($v_2\{4\}$) for the Pb-Pb collisions at 20-30% centrality at $\sqrt{s_{NN}}$ = 5.02 TeV along with similar measurements at lower energies [95].

1.6 Motivation and Organization of the thesis

The basic goals of relativistic heavy-ion collision experiments are to explore the QCD phase diagram and understand how quark-gluon plasma is formed in the laboratory. The objective of the CBM experiment at FAIR is to determine the phase structure of nuclear matter at moderate temperatures and extremely high net baryon densities. The SIS100 accelerator's high-intensity heavy-ion beams also enable precise measurements of multidimensional observables, including particles with exceptionally low production cross sections. In-medium modifications of LMVM and J/ψ suppressions offer possibilities as diagnostic probes for identifying the presence of a deconfinement phase transition in extremely dense nuclear matter. Consequently, the CBM experimental physics programme

provides measurements of LMVM and charmonia via their dileptonic channel decays.

The Muon Chamber (MuCh) detector system in the CBM experiment is designed to reconstruct the entire dimuon spectrum in high-energy heavy-ion (A+A) and proton-nucleus (p+A) collisions. The primary goal of this work is to optimise the MuCh chamber geometry, develop a simulation framework, and investigate the feasibility of detecting muons produced by the decay of LMVM in Au+Au collision at 8 A GeV beam momentum using the MuCh detector subsystem. The work done for the thesis can be broadly divided into the following parts:

- The first part covers a detailed description of the MuCh detector geometry as implemented in the CbmRoot simulation and the optimization of the muon detection system by performing simulations and investigating the feasibility of the detection of LMVM using the CBM muon detector setup. The optimized setup is then used for LMVM detection in Au+Au collisions at 8 A GeV/c beam momentum.

- Second part of this thesis will discuss comprehensive results on intermittency using the Scaled Factorial Moment (SFM) technique in Au+Au collisions in the FAIR energy range of 2-12 A GeV in pseudorapidity $\chi(\eta)$, azimuthal $\chi(\phi)$, and pseudorapidity-azimuthal $\chi(\eta$ - $\phi)$ spaces. The simulations are performed with a hybrid version of the Ultra-relativistic Quantum Molecular Dynamics (UrQMD) event generator. Three alternative equations of state (EoS) are employed to investigate the intermittency within the hydrodynamic scenario, namely pure Hadron Gas(HG), Chiral + HG, and Bag Model EoS. Additionally, a multifractal analysis to study the multiparticle dynamics in 60 A and 200 A GeV, ^{16}O-AgBr collisions at SPS, CERN and 14.5 A GeV/c, ^{28}Si-nucleus interaction at AGS, BNL have also been performed in the pseudorapidity phase space.

This thesis is divided into seven chapters, including an introduction and summary. First is the Introduction which has been discussed already above. Chapter 2 provides an overview of the CBM experiment at FAIR, including a brief description of the FAIR accelerator facility, the primary physics goals and the associated potential observables, as well as the different detector subsystems. Chapter 3 describes the muon chamber detector set-up used for muon identification. The measurement of muons produced by the decays of LMVM (ω, η, etc.) or charmonia (J/ψ) is one of the most essential segments of the

CBM experiment. Consequently, MuCh is required for their detection. In addition, the simulation process for optimising the MuCh detector parameters is discussed in this chapter.

Chapter 4 discusses the implementation of MuCh geometries in CBMROOT software and the optimisation of the MuCh sub-system geometry configuration. Chapter 5 covers the physics performance studies for LMVM (η, ϕ and ω) in Au+Au collisions at 8 A GeV/c beam momentum using CBM-Muon setup. In chapter 6, fluctuations from Intermittency analysis in relativistic hydrodynamic simulations of heavy-ion collision at FAIR energies have been discussed. It also covers a multifractal analysis to study the multiparticle dynamics in 60 A and 200 A GeV, ^{16}O-AgBr collisions at SPS, CERN and 14.5 A GeV/c ^{28}Si-nucleus interaction at AGS, BNL. Finally, Chapter 7 provides a summary and outlook of the works based on the various investigations discussed in previous chapters.

Chapter 2

The Compressed Baryonic Matter Experiment

The QCD, a theory that describes strongly interacting matter, predicts that at high temperatures and/or high densities, a phase transition into a new state of matter, where strongly interacting matter exhibits partonic behaviour. The relativistic heavy-ion collision experiments allow us to create and investigate such a novel state of matter in the laboratory. FAIR's forthcoming Compressed Baryonic Matter (CBM) experiment [96] seeks to create and characterize extremely dense nuclear matter in the laboratory. The principal objective of the CBM experiment is to explore the phase diagram of nuclear matter at moderate temperatures and extremely high densities. On the other hand, the experiments at the RHIC and the LHC are looking at the characteristics of deconfined QCD matter at extremely high temperatures and near-zero net-baryon densities. Exploration of the QCD phase diagram at high net-baryon densities is the focus of several experimental initiatives. To find the QCD critical endpoint [97], the STAR collaboration at RHIC scanned the beam energies. In the low and intermediate energy regimes, Table 2.1 highlights existing and planned experiments. For the same purpose, measurements are carried out in the NA61 experiment at the CERN-SPS utilizing light, and medium-sized ion beams [98]. NICA (Nuclotron-based Ion Collider fAcility) is a new accelerator complex being built at the JINR (Joint Institute for Nuclear Research) in Dubna, Russia, to explore the characteristics of dense baryonic matter [99]. However, these experiments are limited to investigating abundantly generated particles due to luminosity or detector constraints. In contrast, the CBM detector is intended to assess the collective behaviour of hadrons and rare diagnostic probes (i.e. multi-strange hyperons, charmed particles, and lepton pairs) with exceptional accuracy and statistics. In order to achieve the required accuracy, the measurements will be performed at reaction rates of up to 10 MHz.

S. No.	Experiment	Energy Range	Reaction Rate (Hz)	Limitation
1	STAR-BES @RHIC, BNL	$\sqrt{s}$ = 7-200 GeV	1-800	luminosity
2	NA61 @SPS, CERN	E_k = 20-160 A GeV	80	detector
3	MPD @NICA, Dubna	$\sqrt{s}$ = 4-11 GeV	1000	luminosity
4	CBM @FAIR, Darmstadt	E_k = 2-35 A GeV	10^5-10^7	detector

Table 2.1: The existing and planned experiments in the low and intermediate energy regimes with their energy range and reaction rates which trigger the limitation. Compared to the other experiments, CBM has a higher reaction rate of orders of magnitude.

The international accelerator facility FAIR, one of the world's most significant research projects, is now under construction in Darmstadt, Germany, and its layout is shown in Fig. 2.1. It will offer incredible research opportunities in nuclear, hadron, atomic, and plasma physics. The four experiment pillars are separated into the FAIR research: Nuclear Structure Astrophysics and Reactions (NUSTAR), Compressed Baryonic Matter (CBM), Proton ANtiproton Detector Array (PANDA), Atomic Physics, Plasma physics and Applied sciences (APPA). The available kinetic beam energy per nucleon is mostly limited by the bending power, $B \cdot r$, of the dipole magnets;

$$E/A = \sqrt{(0.3 \times B \cdot r \times Z/A)^2 + m^2} - m \tag{2.1}$$

Where, Z and A are the atomic and mass numbers, respectively, and m is the mass of the nucleon.

So, the SIS100 synchrotron will provide beams with energy ranging from 2 to 11 A GeV for heavy nuclei, up to 14 A GeV for light nuclei, and 29 GeV for protons (if this even comes), kicking off the CBM physics program.

2.1 Physics at CBM Experiment

The following physics scenarios are the focus of the CBM research program:

The equation-of-state of baryon-rich matter at neutron star densities

The following are the important measurements:

- The excitation function of the collective flow of hadrons which is driven by the the pressure created in the early fireball.

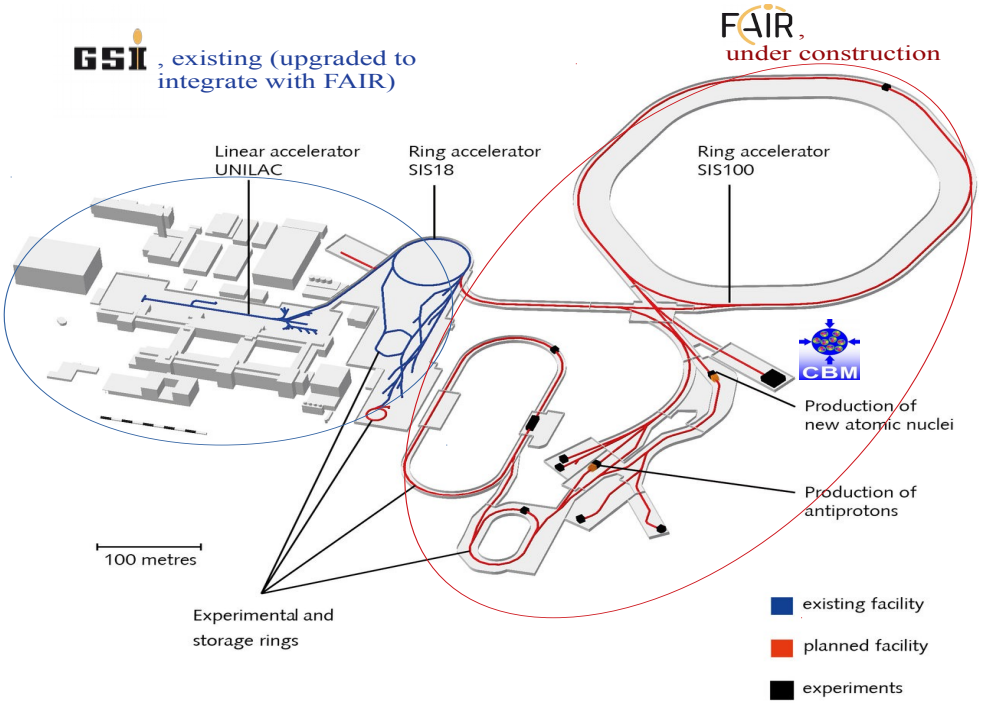

Figure 2.1: Layout: On the left (blue), the existing GSI facility, and on the right (red), the planned FAIR facility [100].

- The excitation functions of multi-strange hyperon yields in Au+Au and C+C collisions at energies from 2 to 11 A GeV. At sub-threshold energies, Ξ and Ω hyperons are produced in sequential collisions involving Λ and kaons; as a result, their production is sensitive to the density of the fireball.

In-medium properties of hadrons

- The in-medium mass distribution of vector mesons decaying into lepton pairs in heavy-ion collisions at different energies (2 to 15 A GeV) and for different collision systems. Leptons are penetrating probes carrying the information out of the dense fireball.

- Reference measurements of vector meson production in pN and pA collisions to separate in-medium effects from elementary production processes.

- Flow measurements of charged kaons in heavy-ion collisions.

- Yields and transverse mass distributions of charmed mesons in heavy-ion collisions as a function of collision energy.

Phase transitions from hadronic matter to the quarkyonic or partonic matter at high net-baryon densities

- The excitation function of yields, spectra and collective flow of strange particles in heavy-ion collisions.
- The excitation function of yields and spectra of lepton pairs in the intermediate mass region in heavy-ion collisions.
- Event-by-event fluctuations of conserved quantities like baryon number, strangeness and net-charge number or proxy thereof in heavy-ion collisions measured with high precision as a function of beam energy.

Hypernuclei, strange dibaryons and heavy multi-strange objects
According to theoretical models, heavy-ion collisions create single and double hypernuclei, strange dibaryons, heavy multi-strange short-lived objects, and strange dibaryons with the highest yield occurring in the range of SIS100 energies. Planned measures include:

- The decay chains of single and double hypernuclei in heavy-ion collisions.
- Investigate the possibility of identifying the strange matter in the form of heavy multi-strange short-lived objects and strange dibaryons. If these multi-strange particles undergo a decay process that results in charged hadrons, including hyperons, then the decay product may be used to identify the particles.

Charm production mechanisms, charm propagation and in-medium properties of charmed particles in (dense) nuclear matter

- Cross sections and momentum spectra of open charm (D-mesons) in proton-nucleus collisions at SIS100 energies. The in-medium characteristics of D-mesons may be deduced from the transparency ratio $T_A = (\sigma_{pA} \rightarrow \mathrm{DX})/(\mathrm{A} \times \sigma_{pN} \rightarrow \mathrm{DX})$, which is measured for various sized target nuclei.
- Cross sections, momentum spectra and collective flow of charmonium (J/ψ) in proton-nucleus and nucleus-nucleus collisions at SIS100 energies.

2.2 The Setup of the Compressed Baryonic Matter Experiment

The CBM experiment is designed to measure the collective behaviour of hadrons and rare diagnostic probes like multi-strange hyperons, charmed particles, and vector mesons decaying into lepton pairs with unprecedented precision and

statistics. Most of these particles will be investigated in the FAIR energy range for the first time. In order to obtain the required statistics, the measurements will be carried out at reaction rates of up to 10 MHz. It demands high-speed and radiation hard detectors, a novel data readout and analysis architecture with free streaming front-end electronics, and a high-performance computer cluster for event selection online.

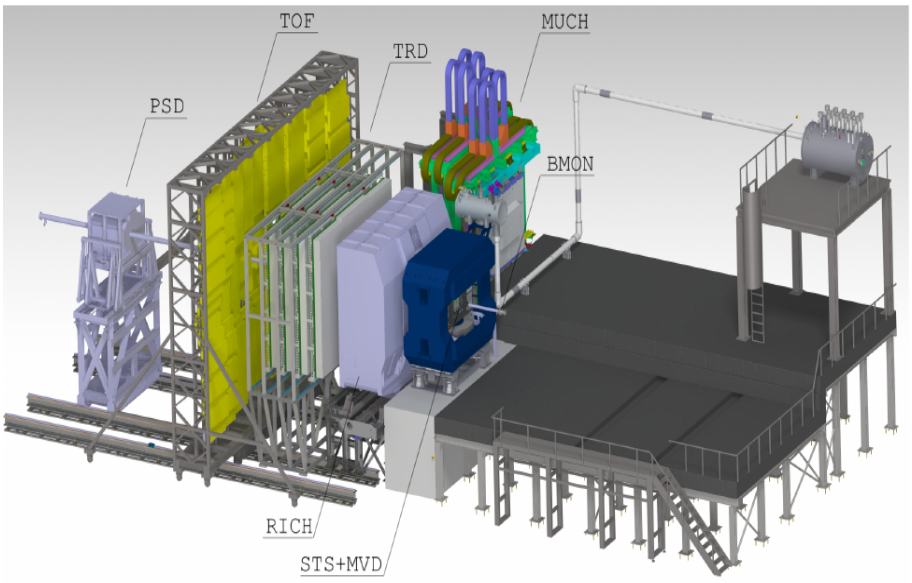

Figure 2.2: CBM experimental setup layout.

The full CBM experiment setup is shown in Fig. 2.2 with both electron detection layout and muon detection system. The Muon Chamber is shown in its parking position. The MuCh detector will take the position of the RICH for muon measurements. The following systems and detectors comprise the CBM experimental setup:

2.2.1 Superconducting Dipole Magnet

The target and the Silicon Tracking System (STS) are housed in a large-aperture ($\approx \pm 25^\circ$ polar angle) superconducting dipole magnet. It provides the magnetic field required for determining the momentum of the charged particles created in the collisions. The magnet weighs approximately 150 tons and has a vertical and horizontal aperture of 144 cm and 300 cm. With a maximum field value of 1 T, the field integral is 1 Tm over a distance of ± 0.5 m around the centre. Fig. 2.3 illustrates the magnet. See [101] for further information.

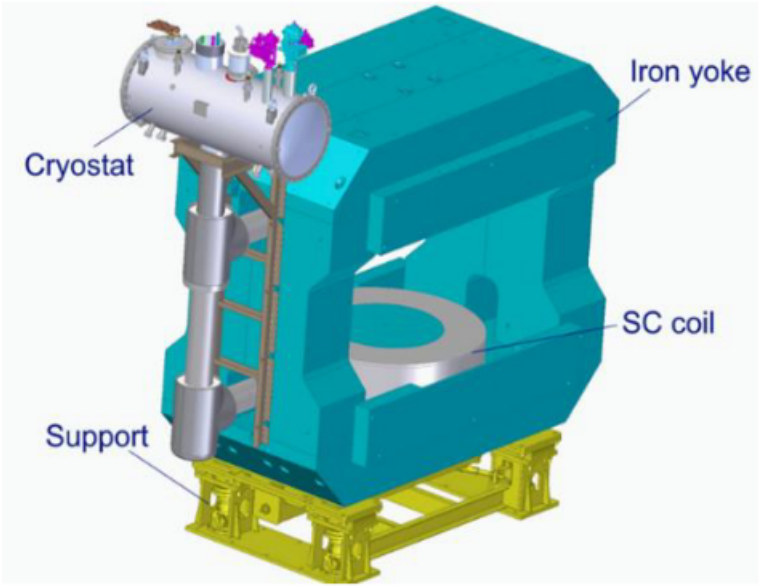

Figure 2.3: The superconducting CBM magnet [102].

2.2.2 Micro-Vertex Detector (MVD)

The Micro-Vertex Detector (MVD) [103] is the first detector system after the target. The MVD performs several tasks, such as:

1. It measures the decay vertices of short-lived particles such as mesons containing charm quarks.

2. It is used to reconstruct tracks of unstable particles with one neutral daughter, such as hyperons, which can then be identified using the missing mass method.

3. It measures charged particles with minimal relative emission angles, such as electron-positron pairs from gamma conversion in the target.

These “close pairs" must be excluded to decrease the background for lepton measurements. Furthermore, the MVD detector supports the STS detector in primary vertex reconstruction. As a result, it helps to suppress fake tracks. The detectors with the good spatial resolution are required to determine the decay vertices of open charm particles (c_τ = 123 μm for D^0 mesons and c_τ = 314 μm for $D^\pm$ mesons). To prevent multiple scattering, it also requires an extremely low material budget. The CMOS Monolithic Active Pixel Sensor (MIMOSIS) will have to fulfil 5 μm spatial resolution requirements in combination with a material budget of $0.3\% - 0.5\%$ X_0 for a full detector station. The MVD will be built from four planar detector stations positioned at 5, 10, 15, and 20 cm

downstream of the target in the magnet. Fig. 2.4 depicts the MVD's engineering design, including its cooling system. The secondary decay vertex of a D-meson can be determined with a precision of roughly 50-100 μm along the beam axis with this detection setup. More information on the MVD may be found in [103]. For further details, see the CBM Progress Reports [102, 104–107].

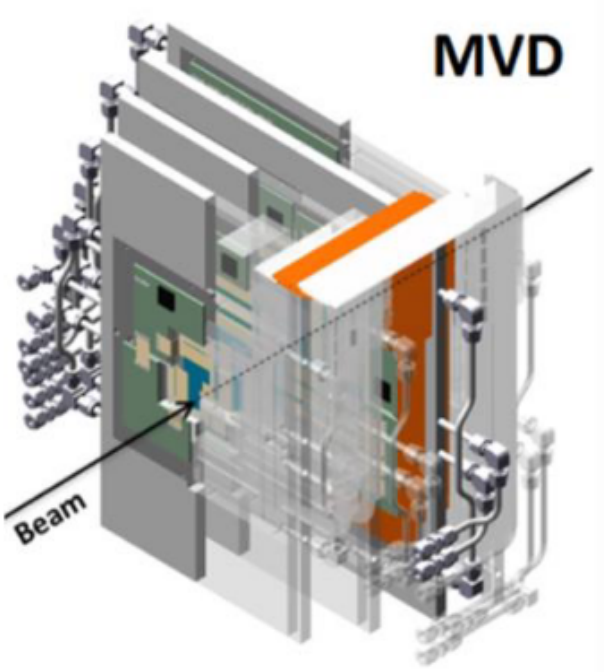

Figure 2.4: An engineering design of the Micro-Vertex Detector [102]

2.2.3 Silicon Tracking System (STS)

The Silicon Tracking System (STS) is also housed in the superconducting dipole magnet and aims to provide high track reconstruction efficiency and momentum determination of charged particles from beam-target interaction. This system allows pile-up free track point determination in a high-rate collision environment (10^5 - 10^7/s for A+A, up to 10^9/s for p+A). The STS comprises eight detector stations staggered 30 to 100 cm downstream of the target. They cover the physics aperture between the polar angles $2.5^\circ \leq \theta \leq 25^\circ$. The double-sided silicon sensors comprise of 1024 strips on each side, a stereo angle of 7.5° at the p-side, and a strip pitch of 58 μm. The strip length varies from 2 cm for sensors close to the beam axis to 12 cm for sensors where the flux of reaction products reduces significantly. Fig. 2.5 shows a schematic side view of the STS detector. In total, the STS consist of 896 double-sided microstrip sensors mounted on 106 detector ladders with eight modules. It provides a momentum resolution of $\Delta p/p \approx 1.5\%$ over a wide range of 0.1 GeV/c to 12 GeV/c. The track

reconstruction efficiency is about 95% for tracks at momentum greater than 1 GeV/c. Only a meagre material budget of 0.3% - 1%X_0 per tracking station can accomplish this level of performance. [102, 108] provide even more information on the STS.

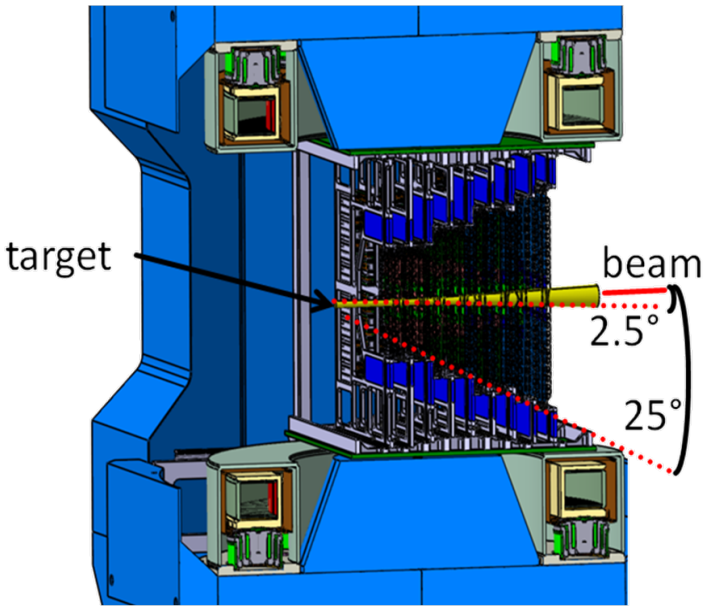

Figure 2.5: The CBM Silicon Tracking System [108]

2.2.4 Ring Imaging Cherenkov Detector (RICH)

The RICH detector will be used to investigate the dielectronic decay channel of vector mesons by detecting electrons from the lowest momenta up to 8 GeV/c. The RICH detector will be installed outside the dipole magnet, behind the STS, and roughly 1.6 m downstream of the target. In conjunction with the Transition Radiation Detector (TRD), the RICH detector should provide a pion suppression by a factor of around 5000. The RICH detector is a large 2 m $\times$ 4 m $\times$ 5 m, focusing gaseous detector made up of 80 trapezoidal glass mirror tiles evenly placed in two half-spheres to concentrate the emitted Cherenkov light onto photon detectors with spectral reflectivity down to the UV region. Photon detection will be accomplished using Hamamatsu (H12700) Multi-Anode Photo-Multipliers (MAPMTs), placed on a cylindrical surface, and CO_2 will serve as a radiator. The RICH detector must be replaced with the muon detection system (MuCh) annually or bi-annually. Fig. 2.6 depicts a schematic of the RICH detector. Detailed information on the current status of RICH development provides in [102]

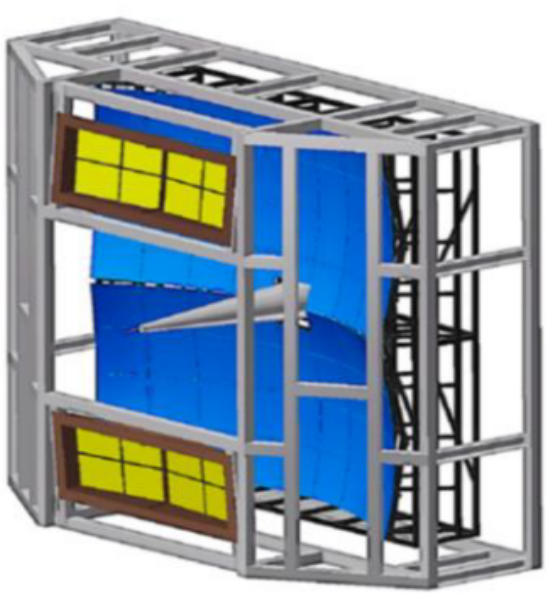

Figure 2.6: Sketch of the RICH detector. The two mirror arrays are illustrated in blue, whereas yellow boxes represent the photomultipliers. The aluminium support structure [109] is depicted in grey.

2.2.5 Transition Radiation Detector (TRD)

The Transition Radiation Detector will allow electron identification in dielectron measurements for electron momenta greater than 1 GeV/c and charged fragment identification, which is especially important for hypernuclei studies. The Transition Radiation Detector (TRD) in CBM utilizes irregular PE-foam radiators and MWPCs in its development. The MWPCs of the detector will be operated with a mixing ratio of 85:15 Xe/CO_2 for efficient absorption of transition radiation photons. The MWPC's entrance area will be polyimide foils coated with a thin aluminium layer that will act as a negative electrode for the drift field. The chambers are to be operated at a maximum differential over-pressure of 1 mbar. The TRD's baseline design includes one station comprised of four detector layers, as seen in Fig. 2.7. It will be placed between the RICH and the Time-Of-Flight (TOF) detector, allowing it to eliminate the background in the TOF produced by track mismatches by providing additional position information for high-precision tracking between the Silicon Tracking System (STS) and TOF. The TRD will also be utilized as a tracking station behind the last absorber of the MuCh detector. More information about the TRD can be found in [102] as well as the newly finalized Technical Design Report [110].

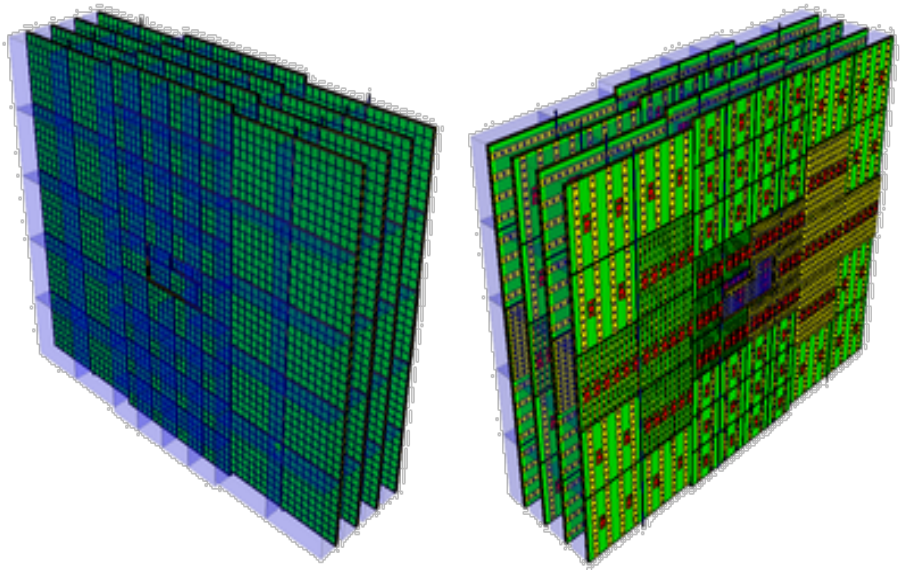

Figure 2.7: A TRD station geometry with four detector layers [110]. Left: Front-side and Right: Back-side

2.2.6 Time-of-Flight Detector (TOF)

The Time-of-Flight (TOF) system will detect charged hadrons (protons, kaons, and pions) in the aperture range of 2.5° - 25° (polar angle) with a particle momentum of around 4 GeV/c. The system must have a time resolution of less than 80 ps and an overall efficiency of more than 95%. The capacity to deal with rates of up to 30 kHz/cm^2 is the most challenging requirement for the detector. Below 2.5°, no momentum information is available; however, it is planned to install a “Beam Fragmentation T0 Counter" (BFTC), which will provide start time information and deal with particle fluxes of up to 100 kHz/cm^2. The existing conceptual design proposes a 120 m^2 TOF wall (including BFTC) made of Multi-gap Resistive Plate Chambers (MRPC) that can be adjusted between 6 m and 10 m from the interaction point. Fig. 2.8 depicts a TOF detector configuration with five distinct MRPC module types that differ in size, granularity, and rate capability based on the projected particle flux rate for central Au+Au collisions at high FAIR energies. An update of the development activities can be found in [102, 111].

2.2.7 Muon Chamber System (MuCh)

The idea behind the muon detection system is to track the particles through a hadron absorber and therefore accomplish momentum-dependent muon identification. This idea is achieved by segmenting the hadron absorber and placing

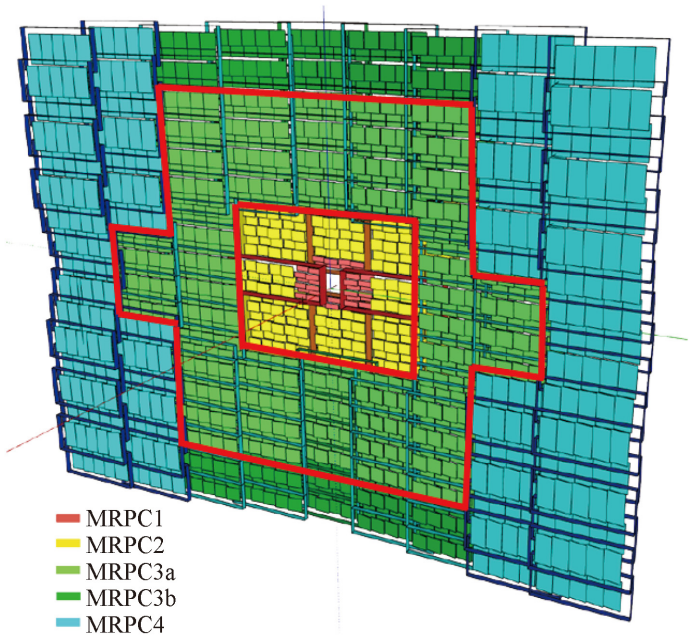

Figure 2.8: The MRPC module arrangement for the CBM TOF wall with different MRPC module types [102].

triplets of tracking detector planes between the absorber layers. The MuCh system is being installed just after STS. In the muon setup of CBM, it is designed to be as compact as feasible to minimize meson decays into muons. The muon system is being proposed with three different configurations at SIS100 energies [112], based on the beam energy and hardness of the muon tracks. The initial version of MuCh will include two stations and three absorbers with thicknesses of 58 cm, 20 cm, and 20 cm, respectively, for measuring Low Mass Vector Mesons (LMVM) in nucleus-nucleus collisions at 2-4 A GeV. The second version of MuCh will be utilized to measure LMVMs in the 4-11 A GeV beam energy range. It comprises 4 stations and 4 hadron absorbers, with a thickness of 58 cm, 20 cm, 20 cm, and 30 cm. The third version of the MuCh system will include an extra absorber with a thickness of one metre at the end to identify charmonium at the highest SIS100 energies. The TRD detector acts as the last station of this setup. This version is depicted in Fig. 2.9. The detector technology adopted for each detector station is somewhat influenced by the particle density at each location. The first two stations for all three MuCh configurations at SIS100 will be built of GEM detectors that really can tolerate high particle rates. A single-gap low-resistivity high-rate Resistive Plate Chamber (RPC) is being considered as a possibility for MuCh's third and fourth stations. It can be built with a large surface area for a relatively low material cost than the GEM detector. You will find further details about the MuCh's design in chapter 3..

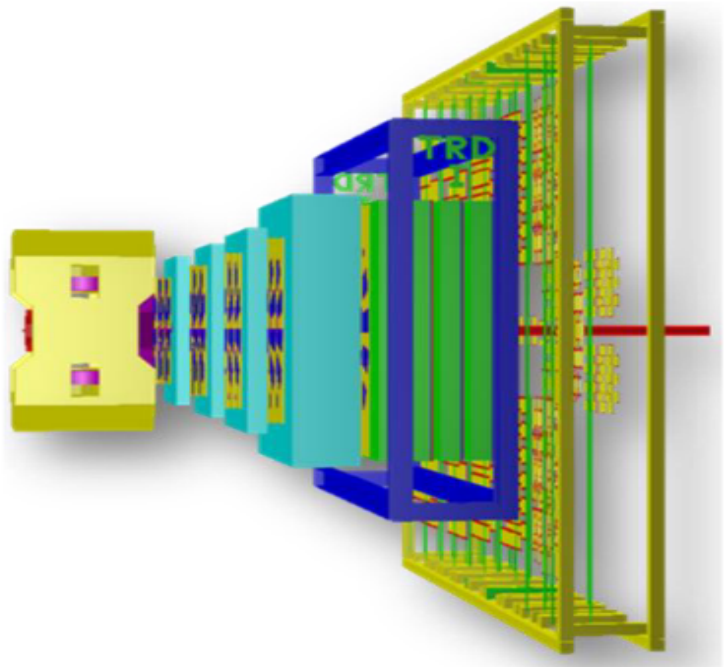

Figure 2.9: The CBM detector setup for dimuon measurement. From left to right: the STS magnet (yellow), the MuCh (5 absorbers are sandwiching 2 triplets of GEM detectors and 2 triplets of RPC detectors), the TRD (green radiators and multi-wire chambers with blue support structure) behind MuCh, and the TOF wall (yellow).

2.2.8 Projectile Spectator Detector (PSD)

The Projectile Spectator Detector (PSD) is a forward hadron calorimeter that will be utilised in CBM to quantify the centrality of events and the orientation of the reaction plane. The modular hadron calorimeter will be able to detect the energy of the projectile spectators and the transverse spectator coordinate during each collision. This will allow it to estimate the reaction plane. The PSD supermodule comprises 9 separate modules with 20×20 cm^2 transverse sizes arranged in a 3×3 array [113]. The module comprises 60 lead/scintillator layers with a sampling ratio of 4:1 (the lead plates and scintillator tiles have thicknesses of 16 mm and 4 mm, respectively), which satisfies the compensation condition. Fig. 2.10 shows a picture of the future CBM-PSD, complete with its support structure. The PSD system is described in detail in [102].

2.2.9 Beam monitor (BMON)

The BMON subsystem consists of two diamond-based beam detector stations in front (upstream) of the target chamber. The T0 station is planned to measure the reaction's start time at moderate rates with a precision of around 50 ps. The HALO station will be designed for beam monitoring.

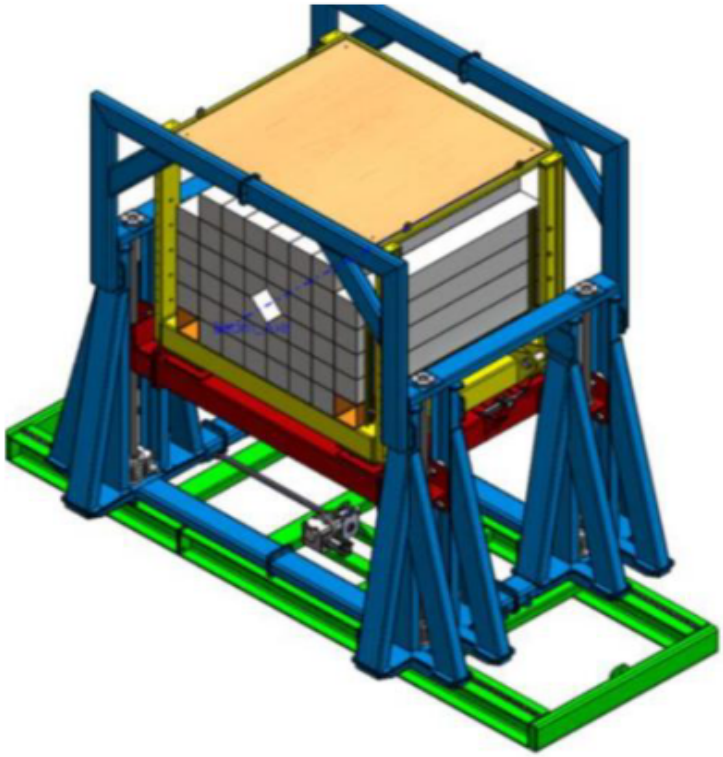

Figure 2.10: The Projectile-Spectator Detector (PSD) for the CBM experiment.

2.2.10 Online event selection and data acquisition

High reaction rates are required for high-statistical measurements of particles with very small production cross-sections. The CBM detectors, data acquisition, and online event selection systems will be designed to handle peak event rates of 10 MHz, which correspond to a beam intensity of 10^9 ions/s and a target with a 1% interaction rate. The rate and amount of archived data, however, are limited by the archiving bandwidth and storage media costs to about 10^5 events per second. As a result, highly selective algorithms are required for measurements with peak event rates of up to 10 MHz, effectively suppressing background events (events with no signal) by a factor of 100 or more. The event selection algorithm will be based on fast online data reconstruction, which will take place on a high-performance computer farm equipped with many-core CPUs and GPUs (located in the GSI Green IT Cube).

Chapter 3

The Muon Chamber Detection System of CBM Experiment

The dimuon measurements at FAIR aim to search for the chiral symmetry restoration and the predicted first-order phase transition from hadronic to the quark-gluon matter at high net baryon densities. The chiral symmetry restoration [114] can be attributed to observing in-medium modifications of hadrons. For low-mass vector mesons, various theoretical models anticipate a broadening of the width and/or a shift of the spectral peak (ρ, ω etc.). The NA38/NA50 experiment at SPS, the CERES experiment, and the Helios collaborations started measuring vector mesons in heavy-ion collisions. The NA60 collaboration's latest results of In-In collisions at 158 A GeV beam energy reveal the broadening of the in-medium ρ-meson spectral function [115]. Vector mesons are expected to melt inside the fireball as baryon density increases at FAIR energy, making them a critical observable for probing the dense medium.

The measurement of hidden charm, or charmonium ($c\bar{c}$), is another crucial observable in the CBM experiment. The anomalous suppression of charmonium formation in the QGP due to Debye colour screening was expected to be an experimental probe of the onset of colour de-confinement. At the FAIR, the production of open and hidden charms will be investigated at beam energies near the kinematic threshold. Additionally, it is predicted that the production processes of D and J/ψ mesons will be sensitive to the circumstances inside the early fireball. The NA50/NA60 collaborations investigated charmonium suppression in Pb+Pb, and In+In collisions [116]. They reported an anomalous suppression of 20-30% for central Pb+Pb collisions. At beam energies below 158 A GeV, no data on J/ψ production in nucleus-nucleus collisions are available. The detailed discussion and results on dimuon measurements are presented in chapter 4. This chapter discusses the conceptual design of the muon chambers detector and the simulation analysis in depth.

3.1 Muon Chamber (MuCh) detector

Measurement of dimuons is an essential aspect of the CBM research programme. A sophisticated muon chamber detector system, positioned after the Silicon Tracking System, is required for these measurements. At CBM, the MuCh system is designed to reconstruct the entire dimuon spectrum in high-energy heavy-ion (A+A) and proton-nucleus (p+A) collisions. In heavy-ion collisions at FAIR energies, the experimental challenge is to detect low-momentum muons in a high-particle-density environment. The CBM approach uses a hadron absorber system that identifies muons based on their momentum. An instrumented hadron absorber comprising staggered absorber plates and tracking stations allows this concept to be implemented. The material and thickness of the hadron absorbers vary, and the tracking stations are made up of detector triplets of various technologies, which will be discussed later.

3.1.1 Absorber Optimization

The basic concept behind implementing absorbers in the Muon chamber is that all other particles produced in high-energy nuclear collisions are absorbed inside the absorber, while muons, highly non-interacting, penetrate through the absorber and reach the detector. The absorber performance in the first (very crude) approximation is defined by two parameters, i.e. nuclear/hadron interaction length λ_I and radiation length of the absorber material. The radiation length of a material is the average length (in cm) required to reduce the energy of an electron by the factor 1/e. Whereas nuclear interaction length is defined as the average distance travelled by a high-energy hadron within the medium before it undergoes a nuclear interaction for a particular medium, and it can be expressed as:

$$\lambda_I = \frac{A}{N_A \sigma_{inel} \rho} \tag{3.1}$$

Where A represents the atomic mass number of material, ρ defines its density, N_A denotes the Avogadro's number, and σ_{inel} refers to the total inelastic cross-section for hadron nucleus interaction. In the context of a nucleus-nucleus interaction, σ_{inel} is define as:

$$\sigma_{inel} = \sigma_0 (A_{projectile}^{1/3} + A_{target}^{1/3} - \delta)^2 \tag{3.2}$$

The hadronic interaction length may be calculated empirically as: $\lambda_I \sim 35\ A^{1/3}$ gm cm^{-2} (where, σ_0 = 68.8 mb and δ = 1.32 [117]).

The CBM muon setup is designed in such a way that it can deal with the high luminosity and huge background produced in heavy-ion collisions. Major design factors have been considered to confront such a harsh environment to fulfil the specific experimental constraints related to dimuon and J/ψ measurements.

- The total space occupied by the muon detector system should be kept as minimal as feasible to minimize the combinatorial background. As a result, materials with a high mass number (A) should be adopted so that λ_I is as small as feasible.

- Because the cross-section for dimuons with masses more than 2 GeV/c^2 is extremely small, high luminosity is required; this demands detectors with high rate capabilities, especially close to the interaction point where particle density is extremely high.

The CBM muon detection system is unique from conventional high energy physics (HEP) muon detectors in that the whole absorber is sliced, and detectors are mounted between absorbers to allow for momentum-dependent track identification. This enhances the efficiency of capturing low-momentum muons that the thick absorber would otherwise block. Substantial detection efficiency is required to reconstruct low-mass vector mesons in the muon chamber. In order to improve the design of the MuCh system, several simulations have been carried out. Such simulations have focused on aspects such as the number of stations and absorbers, the thickness and material of absorber slices, and the granularity of the tracking detector. The main component of the hadron absorber is iron, intending to stop as many hadrons as possible before they decay into muons. The weak decays of pions and kaons contribute the most to the background muons.

To absorb the hadrons in an acceptable absorber length, hadronic interaction length (λ_I) should be as small as feasible, whereas radiation length (X_0) should be as high as possible to reduce multiple scattering. With these requirements in mind, iron has been found to be the optimum absorber material. Fig. 3.1 depicts the absorption of various particles as a function of the iron absorber thickness. This figure may be used to estimate the thickness of the hadron absorbers required for LMVM and charmonia measurements. Muons with low momentum originating from ω mesons are absorbed by a factor of 10 in such a thick absorber. But muons originating from J/ψ mesons may travel up to 2.5 metres through iron without having severe suppression. Furthermore, the slope of absorption for muons from ω mesons, pions, and protons is comparable beyond an iron thickness of 1.5 m, implying that the signal-to-background ratio (S/B)

will not increase any further. In conclusion, in order to effectively detect low-mass vector mesons, the thickness of the iron absorber should not be greater than 1.5 metres. On the other hand, for precise measurement of muons resulting from J/ψ decays, one must incorporate an iron absorber with a thickness of approximately one metre with some detector layers.

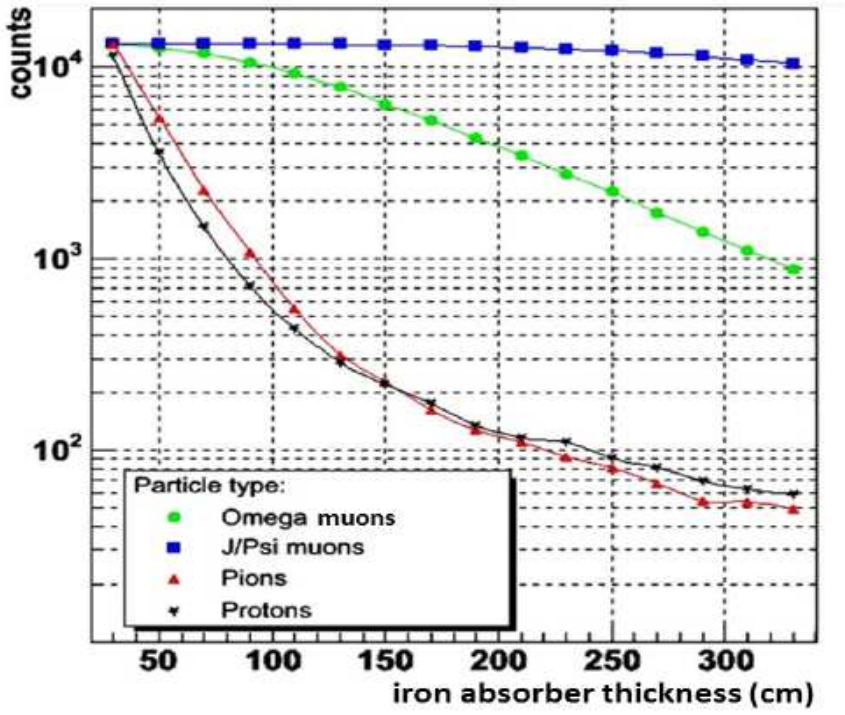

Figure 3.1: The absorption of different particles as a function of iron block thickness. The particle momentum distribution is based on a simulation of central Au+Au collisions at 25 A GeV [118]. ω or J/ψ muons: muons from the decay of an ω or J/ψ meson.

Apart from the total thickness of the absorber, it is also necessary to optimize the thickness of the individual absorbers layers. Because the first tracking station is immediately after the first absorber, the first absorber should be thick enough to reduce the hadron multiplicity and hit density, which decides the rate for the tracking chambers that must tolerate. Due to a thick absorber, multiple scattering increases; as a result, the number of mismatched tracks (fake tracks) increases, which increases the combinatorial background and results in a poor S/B ratio. Based on the initial simulation, it was estimated that a 20 cm thick iron absorber would be suitable for the MuCh system's first absorber. But iron is magnetic metal which results in problems when placed near the magnet. Later, it was reported that a carbon absorber with a thickness of 60 cm, which is comparable to 20 cm of iron in terms of interaction length, is preferred as the first

absorber slice. The variation in particle multiplicity as a function of the thickness of the first iron and carbon absorbers for central Au+Au collisions at 25 A GeV is depicted in Fig. 3.2. It can be seen in Fig. 3.2 that the multiplicity of particles traversing 60 cm carbon or 20 cm iron is reasonably comparable. In the recent configuration of the CBM muon setup, the first absorber will be housed inside the high magnetic field of the CBM dipole magnet. As a result, carbon (graphite) was preferred over iron in mechanical integration. An extra benefit to employing carbon as an absorber material is that the amount of multiple scattering suffered by tracks through carbon is substantially smaller due to the larger radiation length. Apart from the first, the remaining absorber slices are composed of iron to keep the overall detection system compact.

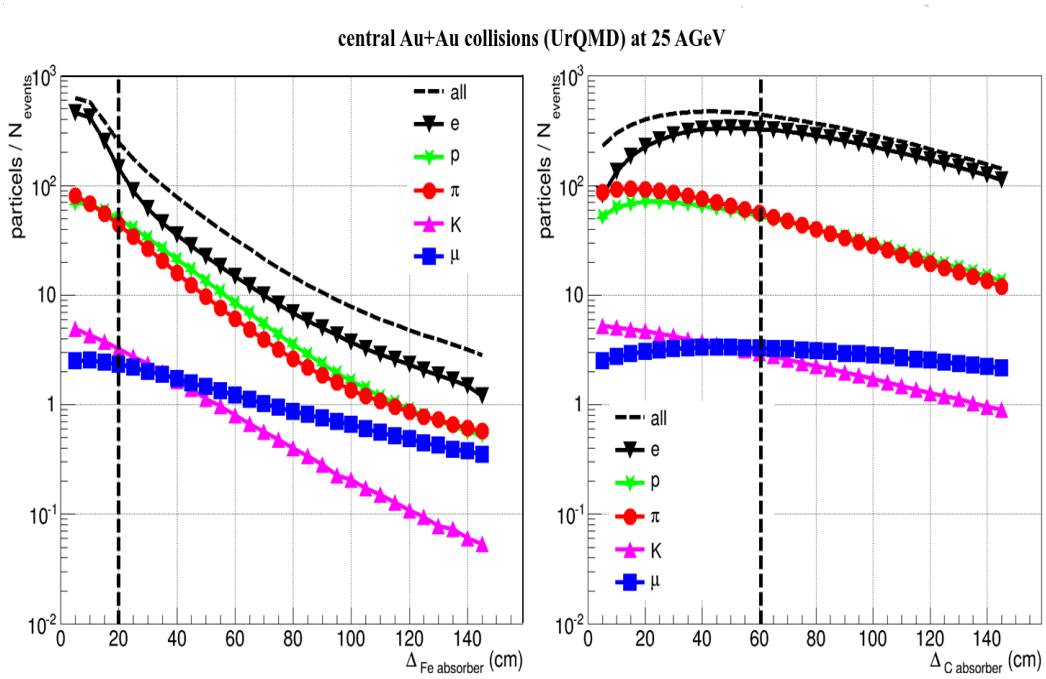

Figure 3.2: Variations in primary and secondary particle yields produced in central Au+Au collisions at 25 A GeV with iron absorber thickness [left] and carbon absorber thickness [right] [119]

The first absorber is divided into two pieces in terms of practical design. The first piece is housed inside the dipole magnet, while the rest is put outside the magnet. After R&D for the mechanical design of the absorber blocks and a thorough market survey, high pure carbon in bulk was inaccessible, which was required to build the first absorber with such a surface area of 260 $\times$ 250 cm^2. The accessible density of bulk carbon has been found to be 1.78 g/cm^3. To maintain the same hadronic interaction length, such a reduction in absorber density would demand a proportionate increase in the physical thickness of the carbon block. However, this would need a downstream shift of the subsequent

absorber blocks and detector chambers, which is not feasible. The composite absorber block that comprises two different materials instead of carbon is finalized to retain the absorption profile and the physical thickness of the first absorber block. Because of its mechanical and activation properties, concrete is chosen over other materials. Following that, several iterations with different thicknesses of a composite block (carbon + concrete) are carried out [105]. As compared to the 2.26 g/cm^3 density carbon, the composite block of 28 cm carbon with a density of 1.78 g/cm^3 and 30 cm concrete with a density of 2.3 g/cm^3 provides the optimum performance in terms of hadron absorption and muon identification (discussed in chapter 4). This would provide a 2 cm gap between the absorber and detector stations, which might be beneficial for MuCh detector chamber servicing tasks. Even though all iron absorbers are placed outside of the magnet to eliminate the influence of any residual magnetic field, they are all composed of stainless steel rather than soft iron, which is not magnetic. The specifications of different MuCh absorbers are summarized in Table 3.1.

Absorber No.	Composition	Density (g/cm^3)	Thickness (cm)	Shape	Start Z (cm)
	Carbon	1.78	16	Trapezium	
I	Carbon	1.78	12	Parallelopiped	125
	Concrete	2.3	30	Parallelopiped	
II	Iron	7.8	20	Parallelopiped	215
III	Iron	7.8	20	Parallelopiped	265
IV	Iron	7.8	30	Parallelopiped	315
V	Iron	7.8	100	Parallelopiped	375

Table 3.1: A specification of different MuCh absorbers [120].

3.1.2 Tracking Chambers

The muon detection system consists of triplets of tracking chambers and sliced absorbers to facilitate tracking and momentum-dependent muon identification. The air gap between the two successive absorbers has been optimised to 30 cm in order to accommodate the whole detector, including cooling arrangements and other mechanical structures. It is important to note that in order to minimize the combinatorial background due to the weak decay, the setup should be as compact as feasible. The reconstructed invariant mass distribution of the combinatorial background for four gap values of 15, 30, 45 and 60 cm between the absorbers are shown in Fig. 3.3. For a 30 cm air gap between the two successive absorbers, the background is found to be minimal. The background rises at larger gap widths due to an increase in the proportion of meson decays.

Due to the short-range secondary electrons emitted by the absorber, the background rises for smaller gaps since they may easily reach the following detector stations. The MuCh has an angular acceptance range of ± 5.7 to ± 25 degrees which corresponds to a pseudo-rapidity coverage $1.51 < \eta < 3.0$.

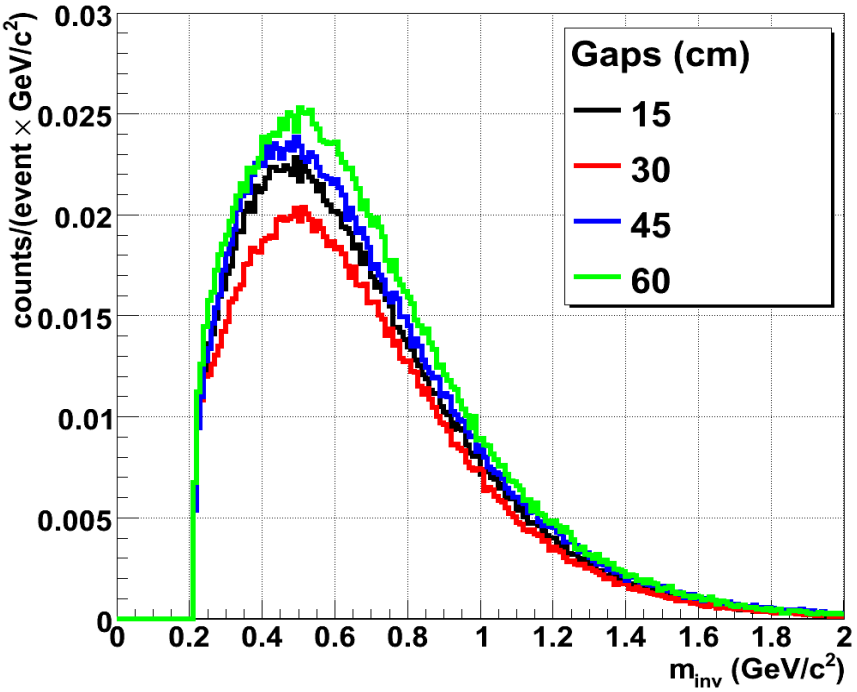

Figure 3.3: Reconstructed invariant mass distribution for combinatorial background with different gaps between the consecutive absorbers. The overall absorber thickness and the thickness of the individually segmented absorbers remain unchanged. The only absorber material employed has been iron.

The particle rates hitting the detector stations have been estimated using FLUKA [121, 122] for Au+Au collisions with a beam energy of 10 A GeV. Fig. 3.4 shows the particle rate as a function of the radial distance of different detector stations. For a total reaction rate of 10 MHz, the particle rate reaches 0.3 MHz/cm^2 at the first station. Because of the relatively high particle rates at the first two stations than the last two, the Gas Electron Multiplier (GEM) detector technology will be included in the existing MuCh design for the first two stations. Whereas at the third and fourth stations, a detector based on a technology known as a Resistive Plate Chamber (RPC) detector would be used.

A thorough description of GEM and RPC can be found in MuCh's technical design report (TDR) and CBM Progress Reports [102, 104–106, 118]. The specification of different MuCh stations has been given in Table 3.2.

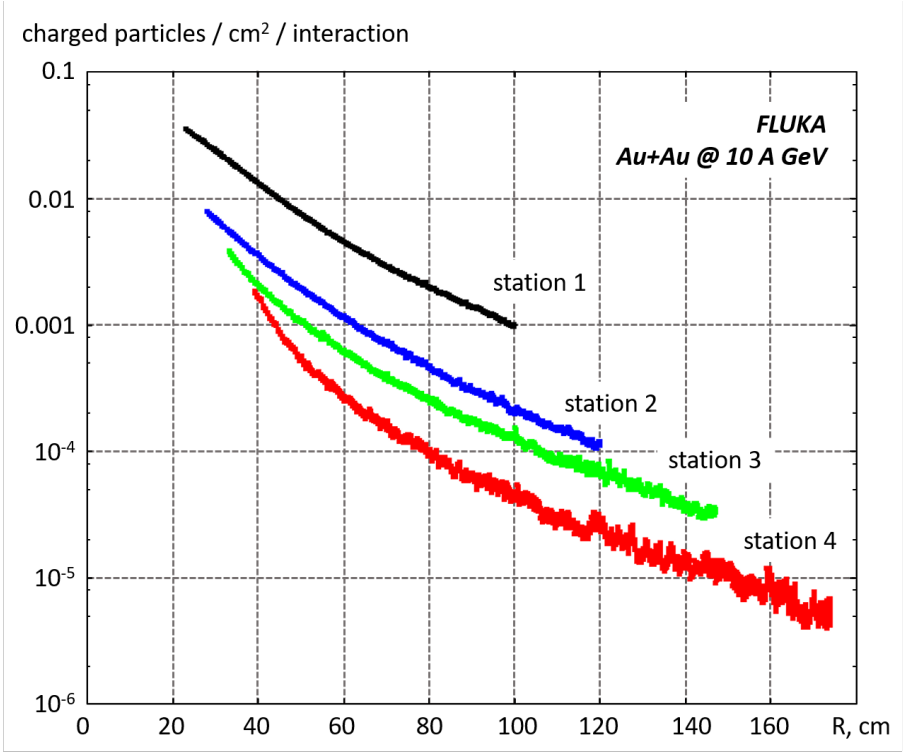

Figure 3.4: Particle rate on each tracking station for central Au+Au collision at 10 A GeV using FLUKA simulation package.

Station No.	No. of modules	Position Z (cm)	Dimension(Active Region) dx1(cm) x dx2(cm) x dy(cm)	Rmin (cm)	Rmax (cm)
I	16	200	6.20 x 21.57 x 38.65	18.92	98.23
II	20	250	6.13 x 21.27 x 47.80	23.92	121.53
III	18	300	7.49 x 27.52 x 57.81	18.97	144.60
IV	20	360	7.88 x 29.35 x 67.79	34.97	172.56

Table 3.2: A specification of different MuCh stations.

The covered active area of each layer has been subdivided into trapezoidal sector-shaped modules. Each GEM module is filled with an $ArCO_2$ gas mixture as the active medium of 3 mm thickness. A trapezoidal-shaped aluminium plate with a thickness of 1.2 cm is installed on one side of each GEM module to support it. The aluminium plate also helps to keep the MuCh electronics cool. The RPC module is filled with 2 mm gas between 2 mm thick glass plates. Likewise, in the GEM module, on one side of each RPC module, a trapezoidal-shaped aluminium plate with a thickness of 2 mm is used to provide support and cooling for DAQ systems. A realistic detector geometry, such as the PCBs (drift and readout), has been incorporated. A detailed discussion can be found in chapter 4.

3.1.3 Muon Chamber Setups

The considerations that influence the design of the various MuCh geometry configurations are as follows:

1. The absorber slices will only be built once and will be inserted in the appropriate order to accomplish the required absorber thickness in a specific configuration.

2. Physics requirements will play a significant role in the decision-making process about the number of tracking stations.

Fig. 3.5 depicts the three different CBM much setups. As shown in the centre panel, the Low Mass Vector Meson (LMVM) setup comprises four detector stations and four hadron absorbers, which are suitable for measuring LMVM at 4-10 A GeV A+A collisions. A 100 cm thick iron absorber is added at the end of the LMVM setup for charmonium measurements. The right panel of Fig. 3.5 demonstrates this setup. For low mass vector mesons at 2-4 A GeV A+A collisions, a minimum version is depicted in the left panel of Fig. 3.5. It consists of only two detector stations and three hadron absorbers. The other specifications of different MuCh setups have been listed in Table 3.3.

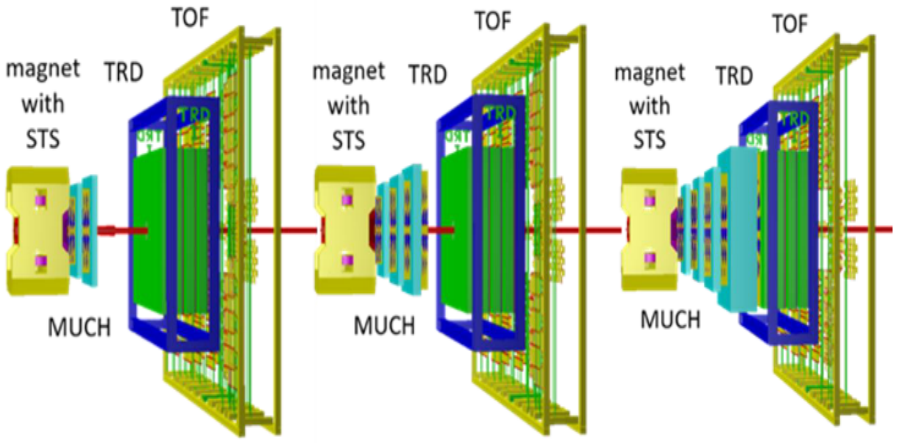

Figure 3.5: The CBM-muon setups incorporate the dipole magnet with the STS inside, the MuCh system, the TRD as an additional tracking system, and the TOF detector. Left Panel: Low energy LMVM Setup, Center Panel: Intermediate energy LMVM setup and Right Panel: J/ψ setup [123]

Setup	No. of Absorbers	No. of Stations	Stations Type	Physics case
LMVM	4	4	2 GEM 2 RPC	low mass vector mesons at 4 - 10 A GeV A+A collisions.
J/ψ	5	4	2 GEM 2RPC	charmonia @ SIS-100 p+A and A+A colliisons
LMVM (Start)	3	2	2 GEM	low mass vector mesons at 2 - 4 A GeV A+A collisions

Table 3.3: The specification of different MuCh setups.

3.2 Methodology for MuCh Simulation and Analysis

The basic steps in performance simulation and analysis are depicted in Fig. 3.6 as a block diagram. Simulations in CbmRoot are done in two stages, each with its intermediate file output. The primary particles generated by the various event generators are tracked through the detector in the first stage, known as "transport simulation." This stage considers the trajectory of the particles through the magnetic field, their interactions with the materials, and the decay of unstable particles. This stage requires the usage of external engines; the framework offers advantages to the ROOT TVirtualMC features [124, 125], which offer the user with the choice to choose between GEANT3 or GEANT4 [126] according to their interests. A realistic description of the detector geometries, adequate material properties, and a magnetic field map are required at the transport level. As outputs of the transport simulation, the geometric intersections of particle trajectories with active detector components (referred to as “MCPoints"), the time-of-flight from the event’s start, and the energy deposit in the active material are all recorded.

The read-out planes of the modules are segmented in pads to account for realistic detector geometry and achieve a final detectable response. The second step of the process is called the detector response simulation, and it mimics the physics processes that take place in the active detector material, in addition to the readout and digitization processes that take place in the front-end electronics. Primary ionization, multiplication, and signal production within the active gas volume are accomplished using MCPoints in the digitization scheme. One MCPoint can create more than one digi. The “Digi" output objects of detector response simulation reflect the simulated measurements of a single read-out channel - equivalent to one read-out pad in the case of the MuCh. These digis are equivalent to real data. This Digi object contains the corresponding channel

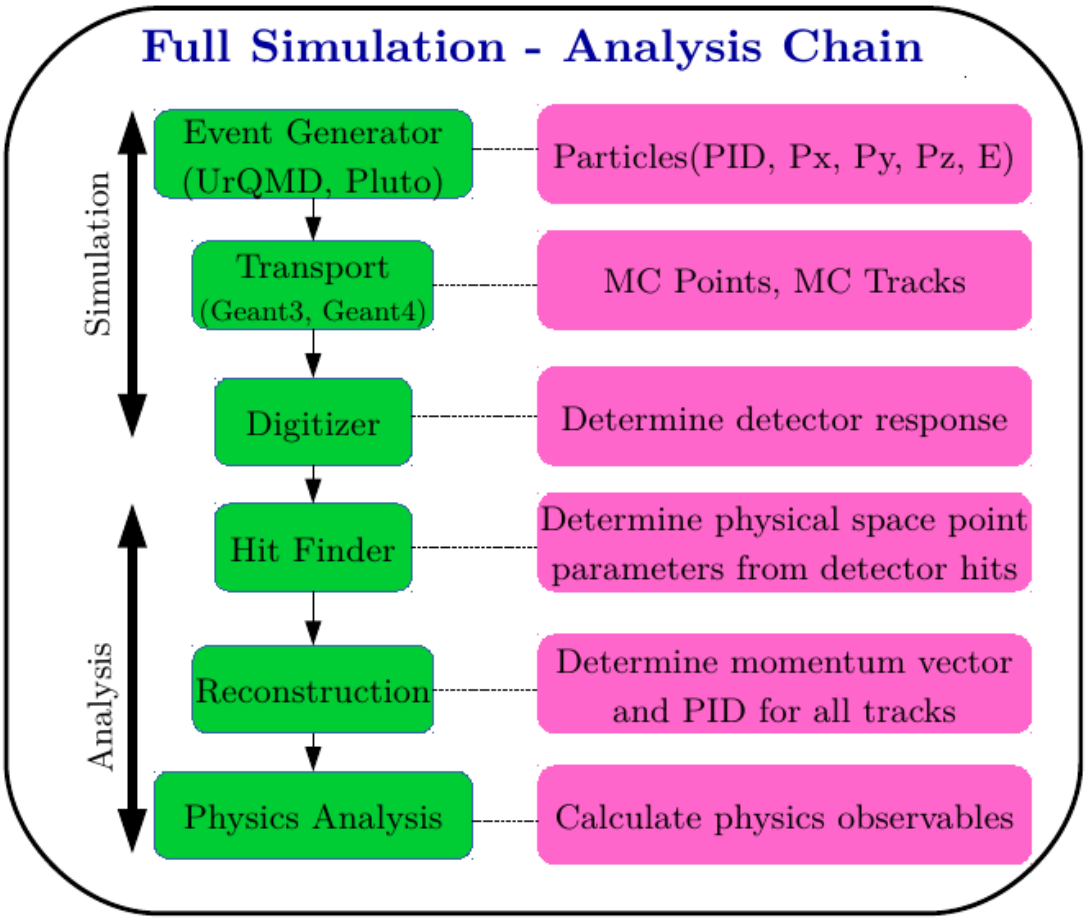

Figure 3.6: A schematic layout of the simulation and analysis chain in MuCh.

address, time stamp, and digitized charge information. After that, the Digi objects are sent to the CBM DAQ software emulation. The link between digis and events is dissolved at this point, resulting in a data stream that closely resembles that of the actual experiment.

A clustering algorithm is used to group digits into clusters. The same algorithm will be used for real data. Based on particle multiplicity and related cluster overlap, the clusters are either split into several sub-clusters that are converted to hits (advanced hit finder) or converted to single hits (simple hit finder). The position of a MuCh hit is attributed to the sub-cluster centroids in an advanced hit finder or the main cluster in a basic hit finder. These hits are considered a candidate for track propagation.

The Kalman Filter technique is used to pass through the MuCh detection layers and propagate the STS reconstructed tracks. Track candidates are selected from the MuCh detector hits closest to the extrapolated track points. The number of STS and MuCh layers associated with the propagating tracks and the χ^2 of track fitting are used as track validation parameters in MuCh analysis.

3.2.1 Event Genrators

The production of particles projected on the detector is the initial stage of simulation.

- **UrQMD [16, 17]** is a microscopic many-body model that can simulate ultra-relativistic p+p, p+A, and A+A collisions in the SIS to RHIC energy range. Colour strings, constituent quarks, and diquarks, as well as mesonic and baryonic degrees of freedom, are all covariantly propagated in this model. The production of particles is depicted as the fragmentation of colour strings from colliding nuclei. Sub-hadronic degrees of freedom become relevant at higher energies, which may be integrated into UrQMD by including formation time for hadrons produced in string fragmentation and hard scattering using the PYTHIA model. There is no incorporation of the phase transition from hadronic to quark-gluon state. In the MuCh simulation, this model is used to generate a background.

- **PLUTO [127]:** PLUTO is a generator that may be used to simulate the phase space decay of LMVM into dimuons ($\mu^+ + \mu^-$). The signal particles created during this process are mixed with the background. Following thermal sources in the center-of-mass frame with thermal m_T and Gaussian rapidity, distribution allows PLUTO to generate signal mesons.

  The m_T distributions are generated by the following:

$$\frac{dN}{m_T dm_T} \propto e^{-m_T/T} \tag{3.3}$$

3.2.2 Transport

The transport process explains how the produced particles propagate through the detector setup with Monte Carlo (MC) methods. “GEANT" [126], which refers to “GEometry ANd Tracking", is the most commonly adopted framework for this task. GEANT estimates the trajectory of each particle and propagates it through space while accounting for any interaction with the material in the path, such as multiple scattering, energy deposition in the detectors, and secondary particle production. The particle’s trajectory and all significant interactions with the detector systems are preserved in a binary “root" file that can be accessed and analyzed. An illustration of the transport procedure is shown in Fig. 3.7. Each particle has an initial set of kinematic properties that allow propagation, such as position, momentum, mass, and particle identity. Each red dot

represents a physical interaction between a propagating particle and a detector material.

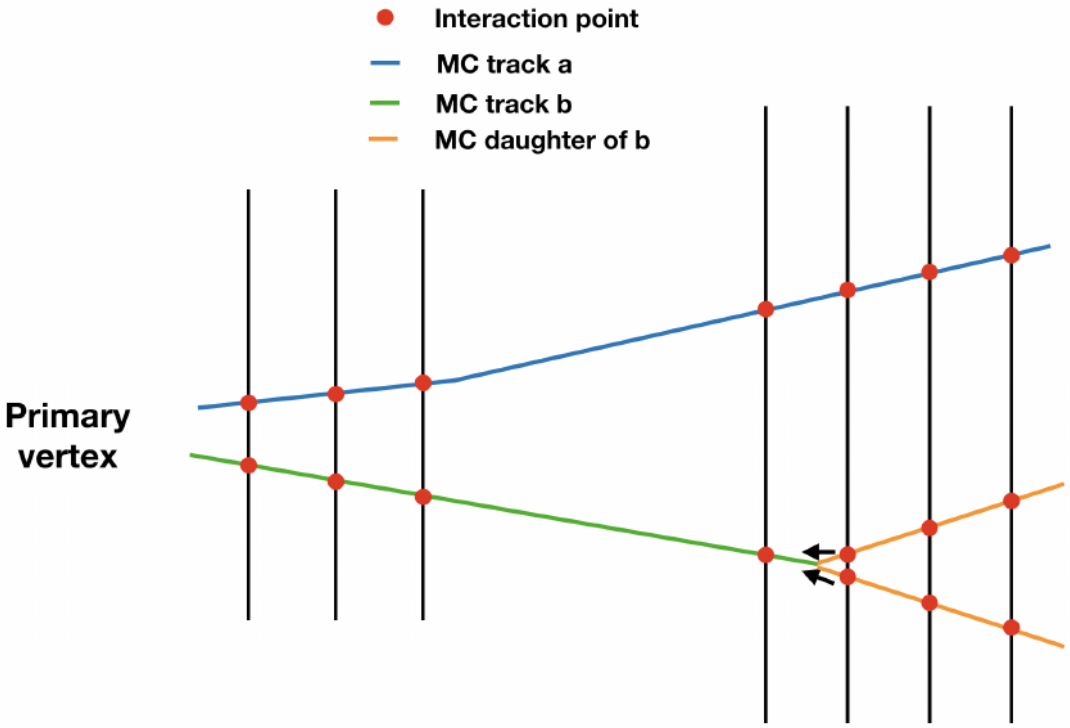

Figure 3.7: Illustration of the transport process.

3.2.3 Detector segmentation

The muon detecting system will be used in environments with a high hit density of up to 4 MHz/cm^2. High hit density is a result of a high event rate of up to 10 MHz. The segmentation study's goal is to develop a realistic and optimized detector layout concerning the physics measurements. The variation of hit density decreases with radial distance from the beam pipe ($\propto 1/r$). So, the muon detector readout planes are segmented into distinct annular regions with pads of appropriate shapes and sizes to acquire the desired pad occupancy ($\lesssim 5\%$) [118]. Another constraint, apart from hit occupancy, is the spatial resolution, which restricts the maximum pad size. As illustrated in Fig. 3.8, projective pads of radially increasing size are used in the segmentation scheme in the case of sector-shaped geometry. The proposed segmentation strategy uses to calculate the angular dimensions and positions of the pads automatically based on the radius. This ensures that the radial dimension of each pad is maintained to be nearly equal to the azimuthal dimension ($\Delta r \sim r\Delta\phi$) at a given radius. As seen in Fig. 3.8, the whole area may be divided into pads with uniform or variable

angular regions. The pads are implemented in our existing system to provide a 1-degree and 2-degree azimuthal angle separation for the first two stations and the remaining two stations, respectively.

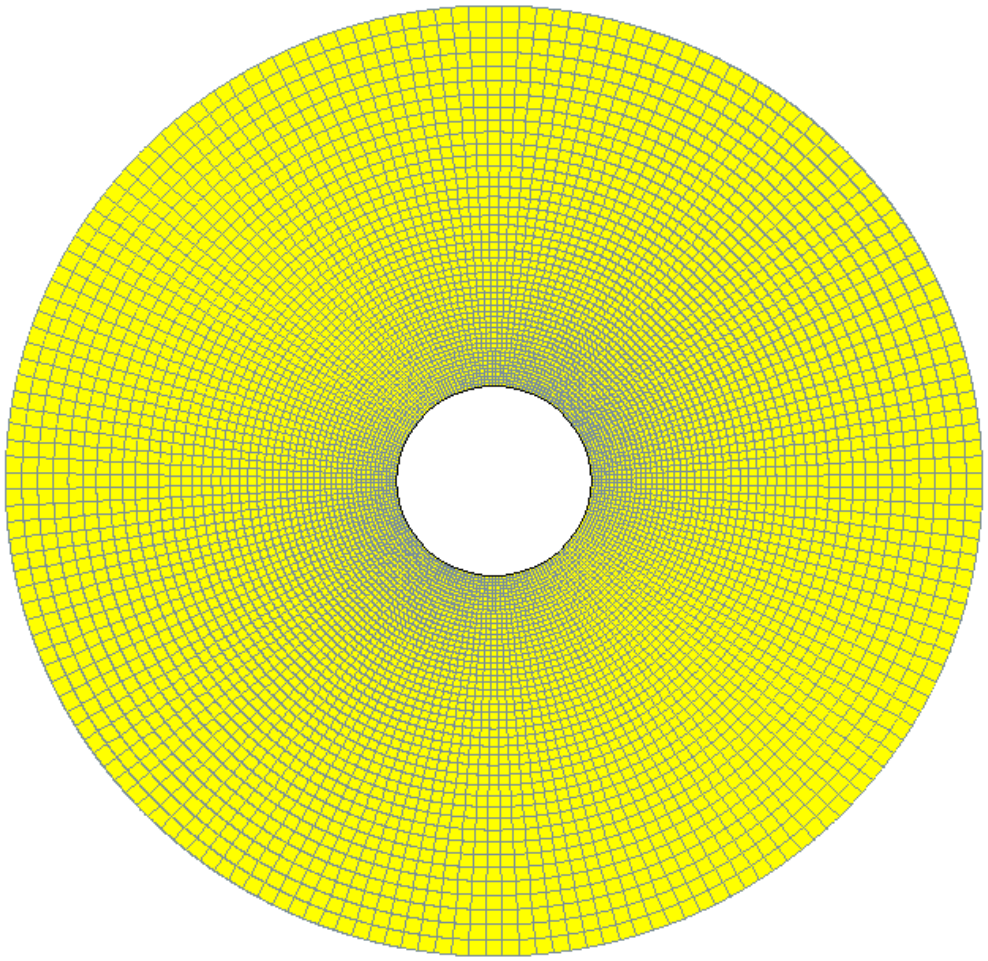

Figure 3.8: A schematic view of a segmented detection layer comprising RPC modules. The whole area has been segmented into projective pads of 2° angular regions in azimuth. For GEM modules, 1° segmentation is implemented.

3.2.4 Digitization

The GEM detector response (digitization) simulation is based on the fundamental concept that a GEM active gas volume may be separated into drift and avalanche zones. This idea is represented in Fig. 3.9 in a schematic form. As a result, the simulation ignores the triple-GEM structure for the time being.

The digitization process can be divided into various steps:

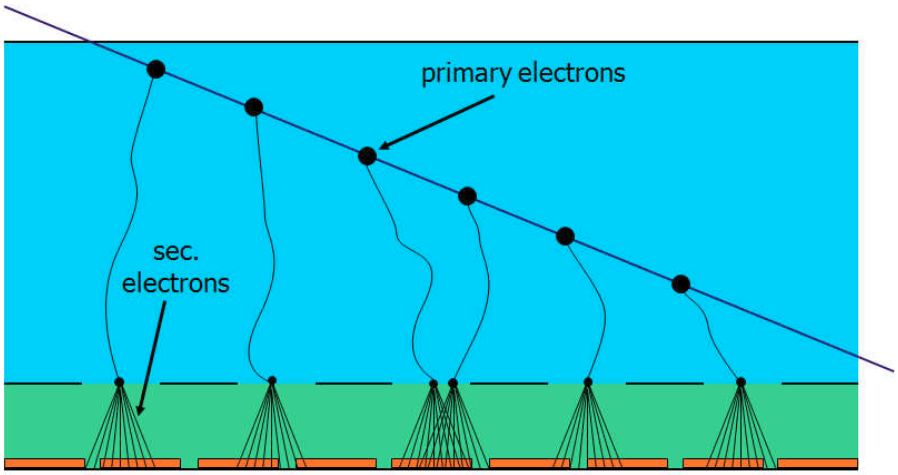

Figure 3.9: The signal generation mechanism in GEM [118].

- The Landau distribution for an argon-based gas mixture calculates the number of primary electrons emitted in the drift volume for each Monte-Carlo point. Additionally, the track length in the drift volume, particle type, and energy are all variables in the calculation. The HEED [128, 129] package is used to determine the Landau distribution's parameters, such as the expected value and variance. According to Poisson's law, the produced primary electrons are subsequently spread at random along the direction of the incidence track.

- An exponential gas gain distribution with a mean gain of 5k is used to determine the number of secondary electrons released in the avalanche region per primary electron [130]. The avalanche's transverse diffusion, which provides the spot size measurement, is considered constant.

- Secondary electron spots hit with a module's pad structure, providing the estimation of the charge collected at each pad. In the existing simulation, the default spot radius for the triple-GEM detectors is set at 500 μm [130]. The primary electron drift time is added to the Monte-Carlo point time to get the charge arrival time. The primary electron drift time can be calculated as follows:

  $$t = d/v$$

  where d is the primary electron's travel distance to the avalanche region and v represents the drift velocity of primary electrons (v = 100 μm/ns) [130].

- The charge information is converted into ADC channels using the following expression;

$$ADC = \frac{Q_{signal} - Q_{th}}{Q_{max} - Q_{th}} \times nADC \tag{3.4}$$

where Q_{signal} represents signal charge, Q_{max} is the maximum charge a pad can accumulate, Q_{th} represents charge threshold, and nADC represents the number of ADC channels for the pads.

- The timestamp and ADC information are decoded into 32-bit words and stored in an array of CbmMuchDigi objects [130].

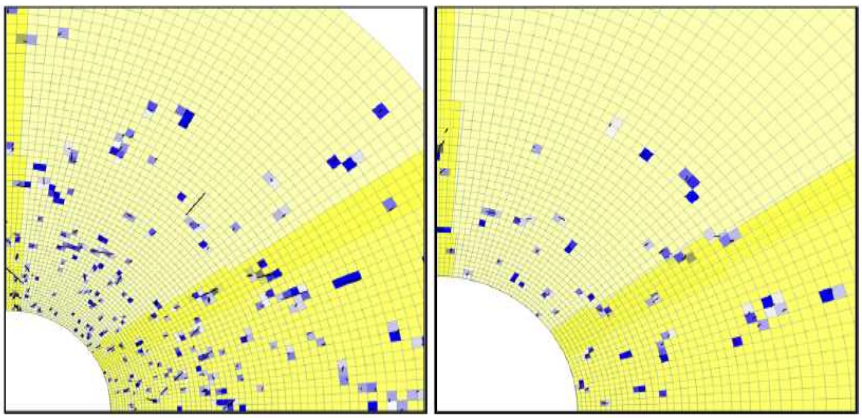

Figure 3.10: Illustration of digitization scheme. Left Panel: First Station and Right Panel: Second Station [118]

Fig. 3.10 depicts the results of the digitization algorithm, exhibiting the reconstructed charge on pads corresponding to Monte-Carlo track projections. A quality assurance algorithm has been implemented in addition to the visual control of the fired pad to MC track correspondence. Fig. 3.12 demonstrates one of the quality criteria, such as the distribution of the total charge from the track as a function of energy for different particles. The obtained distributions are consistent with the Bethe-Bloch dependence of the most-likely value of the input Landau shape corrected for the mean gas gain (see black line). The distribution of deposited charges by the Minimum Ionising Particles (MIP) is depicted in Fig. 3.11. As expected, the Landau distribution is followed by the charge deposition spectrum.

The detector parameters are tunable, and their values are adjusted with measurements. The spot radius is set to match the experimental data as closely as possible. The avalanche spot for each primary electron is projected onto the pad plane to determine the total charge at each pad. In addition to the spot radius, the total number of ADC channels, the maximum charge a pad can receive, and the threshold charge may be tuned. The readout ASIC's dynamic range is

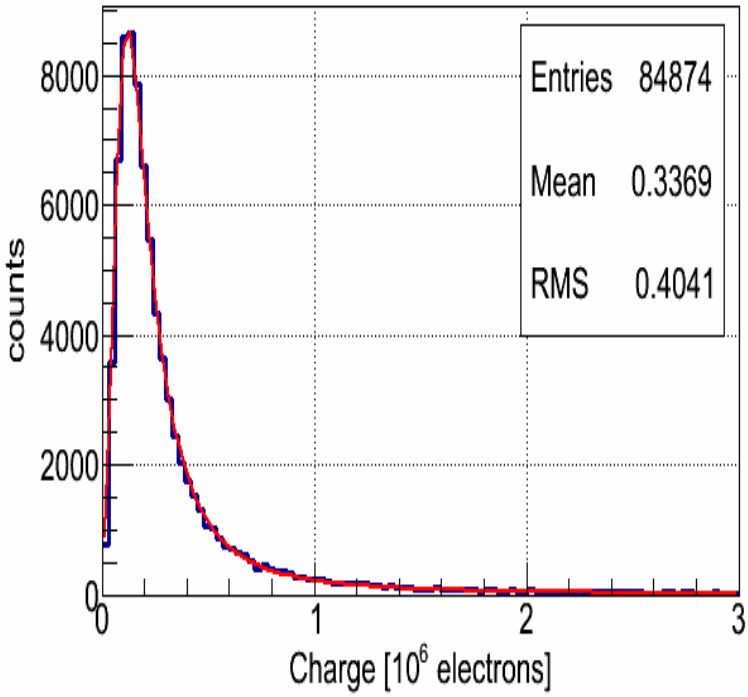

Figure 3.11: Charge deposition in the gas volume by a minimum ionization particle (MIP) [118].

defined by its maximum charge. The channel becomes saturated when the associated energy deposition exceeds the specified dynamic range for that channel. The threshold charge is set to a higher value than the expected amount of noise. However, because no additional noise was added to the simulation, the applied cutoff reduces the signal, reducing efficiency. As a result, the noise threshold has been kept relatively low. A MIP produces 100-120 primary electrons per cm within an $ArCO_2$-filled drift volume; therefore, the number of primary electrons for a drift gap of 3 mm would be around 30-40. The total number of electrons created by an incident muon track with a gain of 5k is 15×10^4, which corresponds to a deposited charge of 25 fC (1 fC corresponds to 6,250 electrons). As a result, choosing a noise threshold of Q_{th} = 2 fC is unlikely to affect the signal substantially. The digitization scheme for RPC is the same as GEM in the current framework, but the parameters have been modified accordingly. For both detection systems, the parameters are presented in a table 3.4.

3.2.5 Clustering and hit formation

The digits formed by the above technique are grouped to form clusters, which are later deconvoluted to create hits. Search for local maxima algorithms has

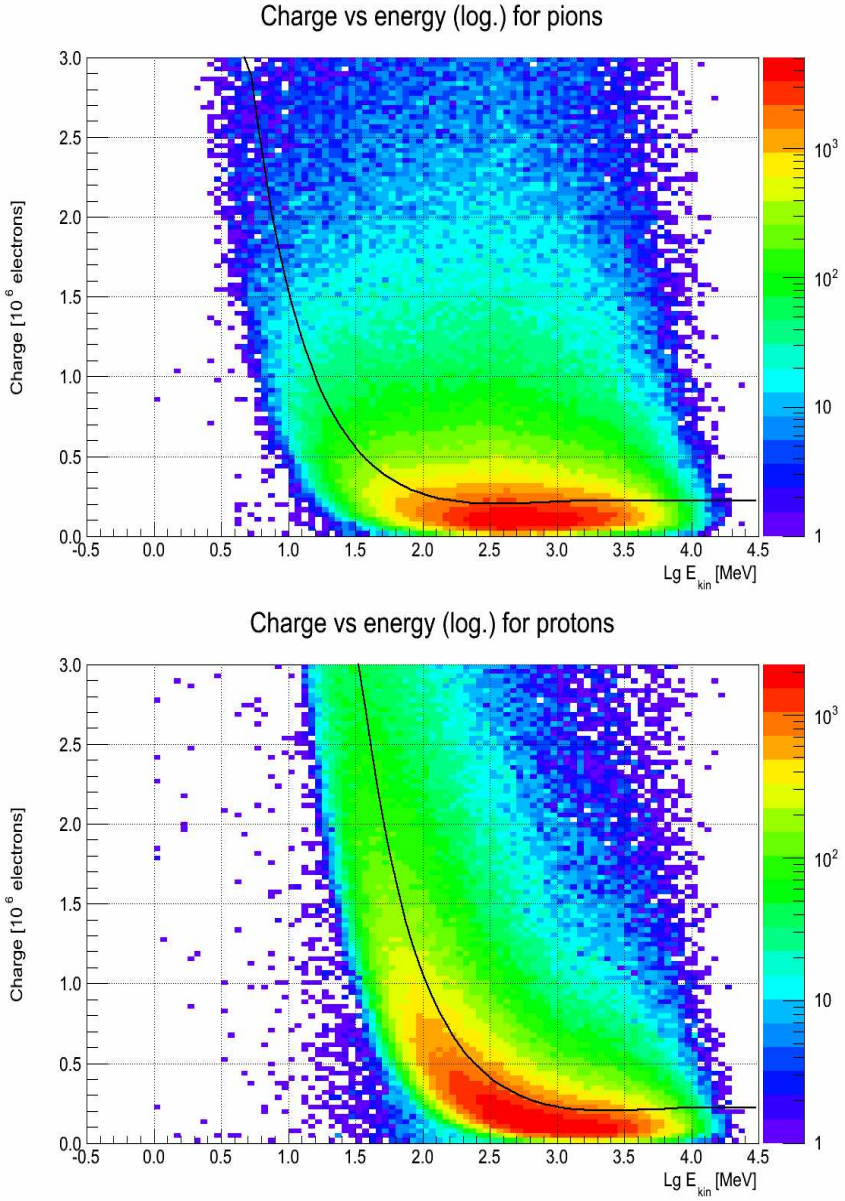

Figure 3.12: The total charge created by incident tracks within the detector's active volume of 3mm gas versus particle kinetic energy for pions [Top] and protons [Bottom] [118]. The black lines represent the results of a Bethe-Bloch [131–133] fit the mean values.

Detector Parameter	GEM	RPC
ADC Channels	32	32
Max charge (Q_{max})	80 fC	130 fC
Minimum charge threshold (Q_{th})	2 fC	30 fC
Spot radius	500 μm	2 mm
Mean gas gain	5k	30k
Drift velocity	100 μm/ns	120 μm/ns

Table 3.4: Digitization parameters for GEM and RPC detectors [130].

been used for cluster deconvolution and finding hits. The centres of the pads are allocated hit coordinates, which correspond to local maxima. One hit is created if cluster dimensions are 2x1 pads (2 Digi per cluster). The method's main benefit is that it works for large clusters and allows you to locate several single track hits that contributed to a single cluster; for illustration, see Fig. 3.13 on the left. However, local maxima may originate from random charge fluctuations on pads in the case of long clusters (which are typically formed by single but extremely inclined low-energy electrons). As a result, searching for local maxima might lead to creating fake hits that don't correlate to real tracks. Nevertheless, consider that this algorithm may still leave some tracks unresolved. The developed cluster and hit-finding algorithms can be employed for simulation and real data reconstruction. The right panel of the Fig. 3.13 shows the results for the central region of the first MuCh layer in a central Au+Au collision at 25 A GeV, which is expected to have the maximum occupancy. This demonstrates that the track positions can be appropriately reconstructed most of the time.

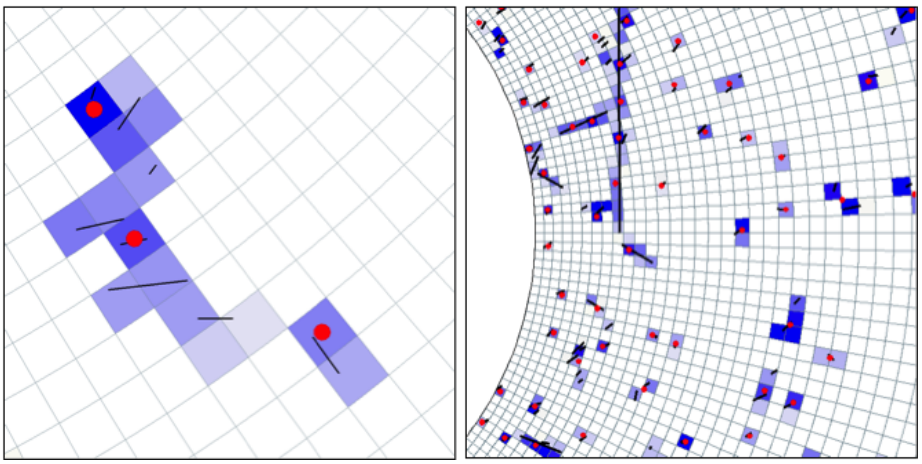

Figure 3.13: Illustration of "the search for local maxima scheme" for hits finding [Left]. Hit-finding in a central Au+Au collision at 25 A GeV for the central region of the first MuCh layer [Right] [118].

3.2.6 MuCh Track Reconstruction

The large multiplicity in heavy-ion collisions presents the major challenge in track reconstruction in the MuCh detector. At CBM energies, central Au+Au collisions produce around one thousand charged particles. Due to the high charged-particle multiplicity, the MuCh detector has high track and hit density, particularly on the first detector planes (see Fig. 3.4). The track reconstruction algorithm for MuCh is based on track following, with reconstructed STS tracks serving as seeds. The STS track reconstruction is based on the Cellular

Automaton (CA) approach [134, 135], with STS track parameters serving as a starting point for further track extension. This approach creates small track segments (tracklets) on adjacent detector planes and combines them into tracks. A Kalman Filter technique [136–139] is used for the track and vertex fitting. Track propagation, track finding, track fitting, and, ultimately, a selection of good tracks are indeed the main logical components. Each of the stages will be detailed in further context below.

Track Propagation : The track propagation method estimates the trajectory and associated errors in a covariance matrix while accounting for three physical phenomena influencing the trajectory: energy loss, multiple scattering, and magnetic field influence. While calculating the estimated average energy loss due to ionization (Bethe-Bloch formula) and bremsstrahlung, the material's effect on track momentum is taken into consideration (Bethe-Heitler formula) [140]. The average scattering angle is estimated using a Gaussian approximation based on the Highland formula [140]. According to the equation of motion, the trajectory is then propagated. When a charged particle travels through a magnetic field, the fourth-order Runge-Kutta method [141] is used to solve the equation of motion. A straight line is adopted for propagation and the calculation of the transport matrix while travelling through a field-free environment. Integrating the derivatives along the so-called zero trajectories [142] provides the transport matrix. A comprehensive description of the developed track propagation can be found in [16].

Track Finding : The hits are connected to the propagated track at each detector station using two different techniques. The nearest hit is associated with the track in the first technique, known as the nearest-neighbour technique [143]. On the other hand, all hits within a specific environment are included in the second technique, i.e., the branching technique. Only one track is propagated further in the nearest-neighbour technique, but the branching technique allows multiple track branches to be followed, one for each associated hit. At each detector station, new hits are assigned one by one. The Kalman Filter updates track parameters once the track propagates to the next station and attaches possible hits.

MuCh Reconstruction : The correctly identified tracks with high efficiency have been preserved after track finding. In contrast, clone tracks (consisting of

an almost identical set of hits) and ghost tracks (consisting of a random collection of hits) have been thrown out. There are two steps to the selection algorithm. First, tracks are sorted according to their quality, which is determined by the length of the track and quality of the track (χ^2). After that, all hits connected to a track are verified, starting with the highest-quality tracks. A specific calculation is carried out to determine the number of hits shared with other tracks. If more than 15% of the hits are shared, the track in consideration is rejected. If a track acquires more than 70% of its hits from a single Monte-Carlo track, it is declared correctly identified; otherwise, it is called a ghost track. The efficiency of track reconstruction is defined as;

$$\varepsilon_{track} = N_{reconstructed} / N_{accepted}$$

$N_{accepted}$ is the number of reconstructable tracks in the MuCh acceptance, whereas $N_{reconstructed}$ is the number of correctly recognized tracks after reconstruction.

3.2.7 Identification of Signal Muons and Analysis

We use a set of cuts at the analytical level to select muon tracks that are likely to have originated from signals (LMVM, J/ψ, etc.) from the global reconstructed tracks. The objective is to suppress the background generated by non-muonic tracks and muons emitted by weak pion and kaon decays. On reconstructed tracks, the following cuts have been used to identify muon candidates:

- χ^2 of vertex.
- **STS:** The number of hits in STS and χ^2 of the STS segment of the track.
- **MuCh:** The number of much detection layers and χ^2 of the MuCh segment of the track.
- **TRD:** The number of hits in TRD.
- **TOF:** By applying a $2\sigma/3\sigma$ cut to the reconstructed track mass on the TOF wall, the contribution of non-muonic tracks is further reduced.

Each reconstructed muon track that satisfies the above set of cuts is considered for dimuon invariant mass analysis. A four-momentum vector represents each selected track:

$$P_\mu = (E_\mu, p_\mu) \tag{3.5}$$

The dimuon four-momentum vector can be constructed from the single muon four-momentum vector and written as:

$$P_{\mu_1\mu_2} = P_{\mu_1} + P_{\mu_2} = (E_{\mu_1} + E_{\mu_2}, \vec{p_{\mu_1}} + \vec{p_{\mu_2}}) \tag{3.6}$$

From this, one can calculate the dimuon pair's invariant mass (m_{inv}), which should equal the signal's mass (LMVM, J/ψ, etc.) due to energy-momentum conservation as;

$$m_{inv}^2 = P_{\mu_1\mu_2}^2 = 2m_\mu^2 + 2(E_{\mu_1}E_{\mu_2} - \vec{p_{\mu_1}} \cdot \vec{p_{\mu_2}}) \tag{3.7}$$

Where m_μ represents the muon's rest mass. The pair p_T, pair rapidity (Y), and the opening/decay angle ($\theta_{\mu_1\mu_2}$) are the additional dimuon kinematic variables. The invariant mass (neglecting the muon mass as compared to energy or momentum) can be written as now;

$$m_{inv} \simeq \sqrt{2p_1p_2[1 - cos\theta_1 cos\theta_2 - sin\theta_1 sin\theta_2 cos(\phi_1 - \phi_2)]} \tag{3.8}$$

Where p_i is the three-momentum magnitude, and θ_i and ϕ_i are the polar and azimuthal angles of the single muon tracks, respectively.

From the four-momentum conservation, the pair p_T can be expressed as;

$$p_{T,\mu_1\mu_2} = \sqrt{p_{x,\mu_1\mu_2}^2 + p_{y,\mu_1\mu_2}^2} \tag{3.9}$$

Where $p_{i,\mu_1\mu_2} = p_{i,\mu_1} + p_{i,\mu_2}$; i, represents the coordinate x,y and z.

The pair rapidities of a particle in the Laboratory System (LS) and Centre of Mass System (CMS) of the collision are respectively,

$$y = \frac{1}{2}ln(\frac{E + p_z}{E - p_z}), \quad y^* = \frac{1}{2}ln(\frac{E^* + p_z^*}{E^* - p*_z}) \tag{3.10}$$

The Lorentz transformation of its energy and momentum components is defined for a particle moving in a longitudinal direction;

$$\begin{bmatrix} E^* \\ P_L^* \end{bmatrix} = \begin{bmatrix} \gamma & -\gamma\beta \\ -\gamma\beta & \gamma \end{bmatrix} \cdot \begin{bmatrix} E \\ P_L \end{bmatrix}, P_T^* = P_T \tag{3.11}$$

where P_L and P_T are the longitudinal and transverse components of $\vec{P}$, respectively. As a result of the inverse Lorentz transformations on E and p_z;

$$\begin{aligned} y &= \frac{1}{2} ln \left[\frac{\gamma(E^* + \beta p_z^*) + \gamma(\beta E^* + p_z^*)}{\gamma(E^* + \beta p_z^*) - \gamma(\beta E^* + p_z^*)} \right] \\ &= \frac{1}{2} ln \left[\frac{E^* + p_z^*}{E^* - p_z^*} \right] + \frac{1}{2} ln \left[\frac{1+\beta}{1-\beta} \right] \\ &= y^* + y_{cm} \end{aligned} \tag{3.12}$$

Consider a particle travelling in the z-direction with a longitudinal velocity β. The particle's energy E and longitudinal momentum p_z are

$$E = \gamma m, \quad p_z = \gamma \beta m, \quad p_z = \beta E \tag{3.13}$$

where m is the rest mass of the particle. Therefore the rapidity of the particle travelling in the z-direction with velocity β is

$$\begin{aligned} y_\beta &= \frac{1}{2} ln \left[\frac{E + p_z}{E - p_z} \right] = \frac{1}{2} \left[\frac{\gamma m + \gamma \beta m}{\gamma m - \gamma \beta m} \right] \\ &= \frac{1}{2} ln \left[\frac{1+\beta}{1-\beta} \right] \end{aligned} \tag{3.14}$$

It is important to note that y_β is independent of particle mass. β can be calculated as;

$$\beta = \frac{|\vec{P_{lab}}|}{E_{lab}} = \frac{|\vec{P_{beam}}|}{E_{lab} + m_{tgt}} \tag{3.15}$$

Where P_{beam} and E_{beam} represent projectile momentum and energy, respectively, and m_{tgt} represents target mass. For 25 A GeV Au+Au collisions, y_{beam} = 3.99 and y_β = 1.99.

3.2.8 Kinematics Resolution:

In general, three factors govern the kinematic resolutions of dimuon experiments:

- Muon multiple scattering in the target and hadron absorber.
- Muon energy loss in the hadron absorber.
- The proper error of the measurement in the tracking chambers.

The last one is insignificant in comparison to the first two. In contrast to past and existing experiments, the CBM experiment will perform full tracking in the STS detection system upstream of the absorber. As a result, the multiple scattering and energy loss effects inside the absorber will not influence the

momentum measurements. In addition, compared to existing measurements, the target thickness of CBM is significantly less, which helps to reduce multiple scattering improving momentum resolution. Only the magnetic field will significantly impact the momentum resolution in such circumstances. It is worth noticing that, with a dipole magnetic field of strength B and length L, the momentum resolution of a track with momentum p can be expressed as;

$$\frac{\Delta p}{p} \propto \frac{p}{BL^2} \tag{3.16}$$

The momentum resolution of muon tracks is $\Delta p/p \sim 1\%$ with the existing dipole magnet designed for tracking. In terms of dimuon mass resolution, recall that we may write by ignoring the muon mass in Eq. 3.8.

$$m_{inv}^2 = 2p_{\mu_1}p_{\mu_2}(1 - cos(\theta_{\mu_1\mu_2})) \tag{3.17}$$

Because the average single momentum rises with mass, multiple scattering, which contributes to angular resolution ($\Delta\theta_{\mu_1\mu_2}$), is more relevant at low masses and does not influence high masses (e.g., J/ψ, ψ'). On the other hand, as earlier mentioned, the energy loss of single muons has a larger impact, which in our scenario is also not extremely significant. We can estimate the expected mass resolution by ignoring the angular resolution:

$$\frac{\Delta m_{inv}}{m_{inv}} = \frac{\Delta p_\mu}{\sqrt{2p_\mu}} \tag{3.18}$$

Chapter 4

Simulation Framework and MuCh detector Optimization

In the present chapter, we will present a detailed description of the MuCh detector geometry as implemented in the CbmRoot simulation framework based on the ROOT system. The first section contains the description of rootified MuCh detector geometry and the development of GeoHandler class to include the rootified geometry in the transport simulation. The optimization of the first absorber, implementation of realistic GEM chamber design and the simulated performance of muon measurement in the MuCh detector are discussed further in detail.

4.1 Implementation of the MuCh detector geometries in the CbmRoot framework

Initially, the geometry parameters of MuCh were provided at the time of transport in ASCII format, and the `CbmMuchGeoScheme` class handled the construction of the geometry. We need to create CBM geometries in ROOT format and implement them as nodes to make the system transparent, usable, and user-friendly. Additionally, each detector geometry can be visualized stand-alone using the GL viewer of ROOT `TBrowser` as Fig. 4.1, and a geometry database [144] can handle the geometry files.

Within the CbmRoot software framework [145], the detector geometries are conventionally provided in the ROOT `TGeoManager` format [146]. The task of "rootification" includes the development of a macro to create the MuCh detector geometry and the development of GeoHandler classes to include the rootified geometry in transport simulations. The macros used to create MuCh detector geometry are located in cbmroot/macro/much/geometry directory. The

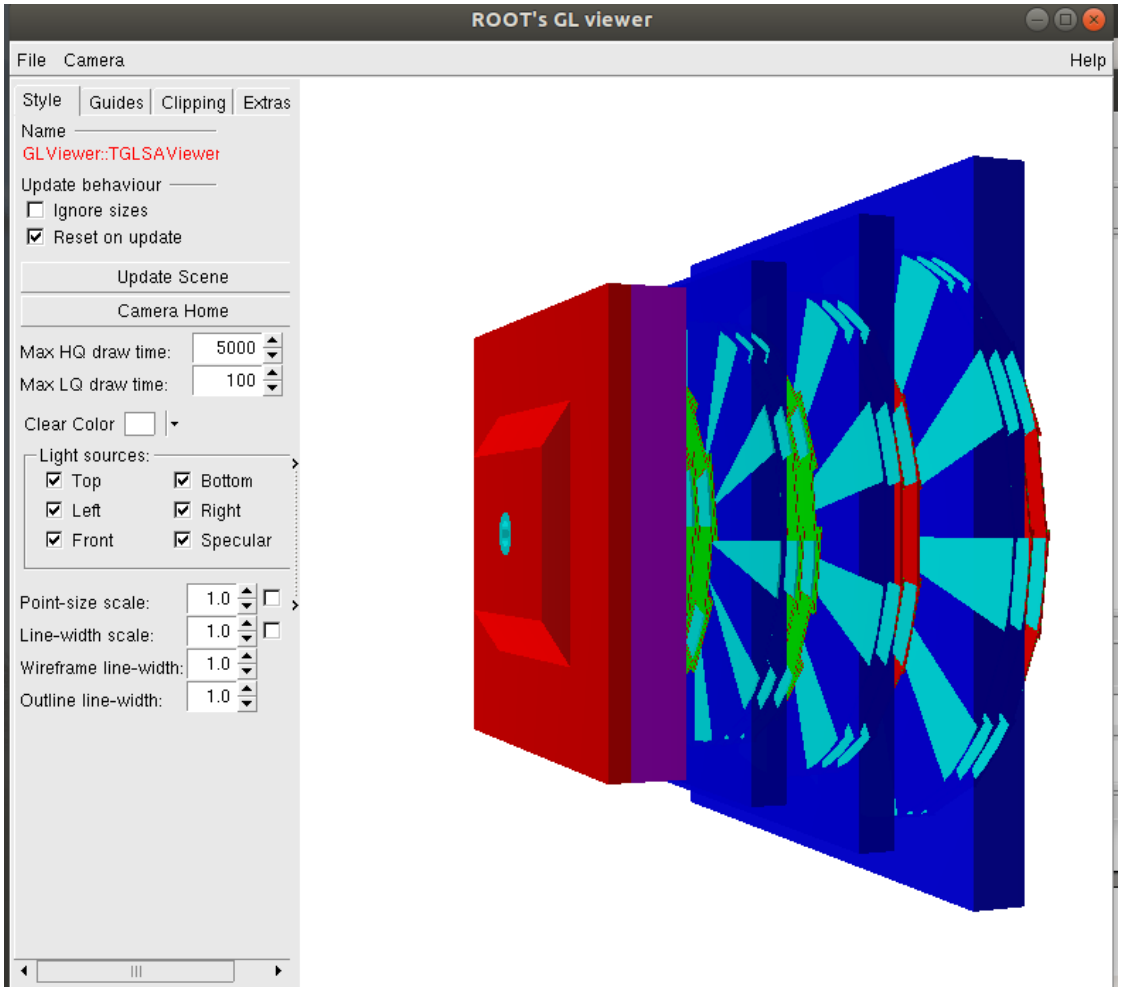

Figure 4.1: The "much_v21a_sis100_1m_lmvm" geometry view in GL viewer.

macros are named create_MUCH_geometry_version_lmvm(jpsi).C. These geometry macros can be found on the git repository [147]. It is important to note that these macros create the basic detector geometry for transport simulation. Details of the detector response, including readout specification and signal extraction, are implemented at the digitizer level (discussed in chapter 3). The macro consists of different functions to generate different parts of MuCh geometry. To develop the geometry using a macro, the following procedure has been adopted. First, we have created a top volume filled with air using the `TGeoVolume` class. A `TGeoVolume` named "much" is created and added as a node to the top volume. Inside "much", different volumes are created for stations, absorbers, and beam pipe shields. Each station node contains three "layer" nodes which in turn contain trapezoidal gas detector "modules" of realistic size (40 cm $\times$ 80 cm). A schematic layout of the entire procedure is shown in Fig. 4.2. The interface of the MuCh geometry in ROOT format is shown in Fig. 4.3. Materials for building different geometry parts are defined in the global "media.geo" file

[148].

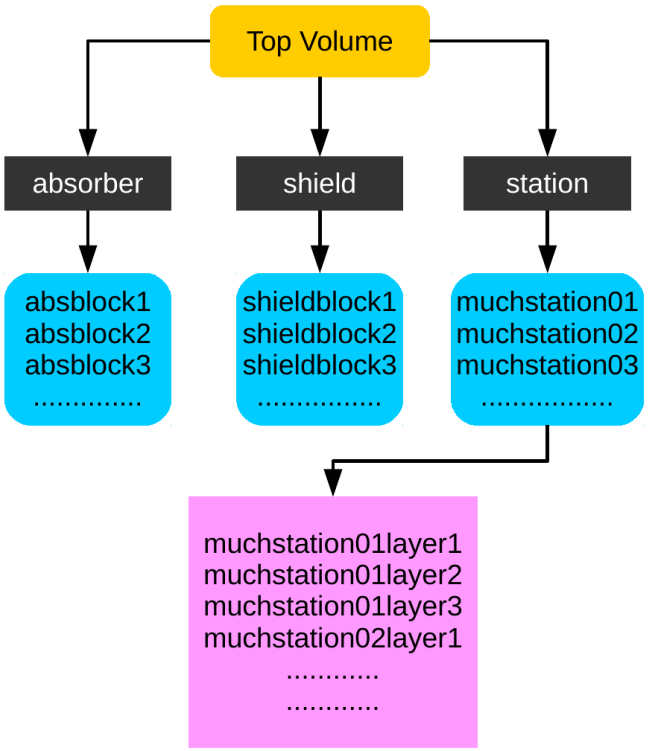

Figure 4.2: A schematic layout of the implementation of MuCh geometry within CBMROOT software.

To implement the rootified geometry in the transport process, modifications to the `CbmMuch` and `CbmMuchGeoScheme` classes, which contain all processes of earlier geometry creation, were necessary. In the older version of the `CbmMuch` class, the function `ConstructGeometry` was used to call the instance of `CbmMuchGeoScheme` for reading the ASCII file. This was replaced by the function `ConstructRootGeometry`, which takes the MuCh geometry prepared in ROOT format as input.

The modified classes and the macro were committed to the repository. The entire simulation chain was tested in the CbmRoot framework with ROOT6.

The following is a comprehensive description of the current simulation:

1. The geometry of the CBM modules is stored in ROOT files, which contain the module's top-level volume. For example, much_v21c_lmvm is a running version tag.

2. Each module's geometry file must be provided in the run macro for the transport run.

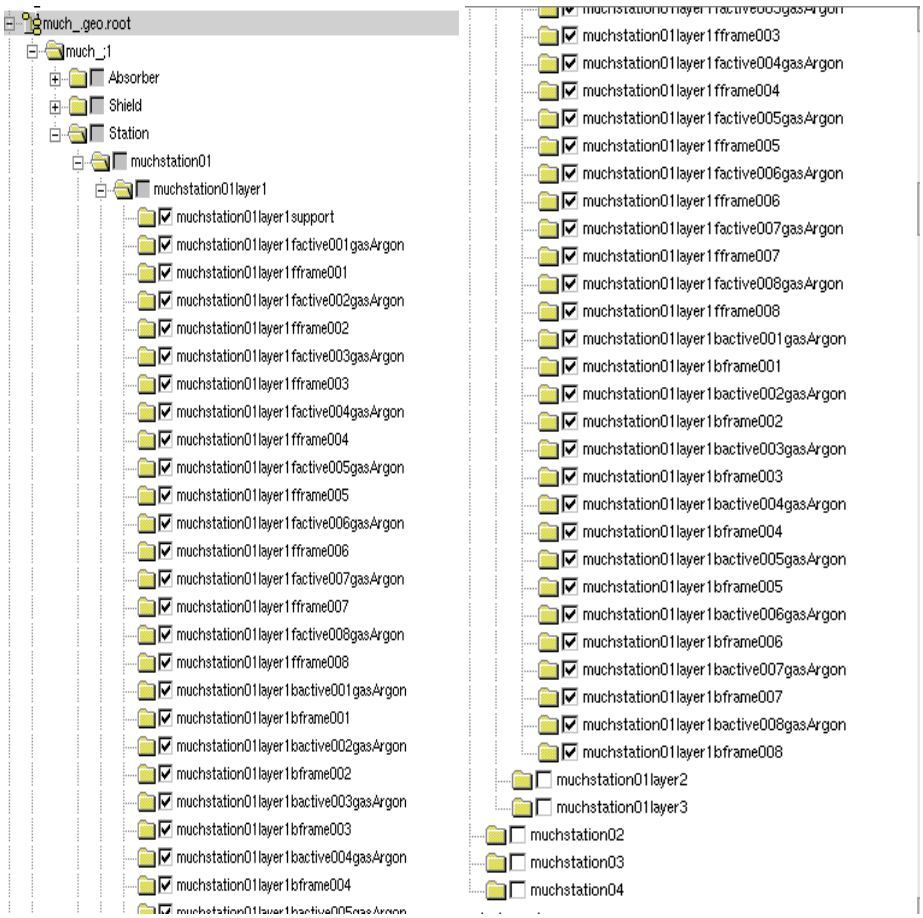

Figure 4.3: Interface of rootified MuCh geometry

3. The geometry files are available for download from the software repository. They aren't supposed to change with repository revisions; instead, versioning is implemented via an explicit version tag in the file name.

4. The user can select a predefined setup (e.g., "sis100_muon_lmvm"). This is done via ROOT macros that are included in the run macro. They are subject to change when the repository is updated, or new software is released.

5. The run manager class FairRun constructs the complete geometry (`TGeoManager`) from the provided geometry files during run initialization by calling the method `ConstructGeometry()` of the registered module objects (`class FairModule`). The parameter container is subsequently stored in a parameter file.

The simulation is performed to see how the MuCh geometry in ROOT format responds to the transport for central Au+Au collisions at a beam momentum of 10 A GeV/c. The UrQMD event generator [16, 17], which explains

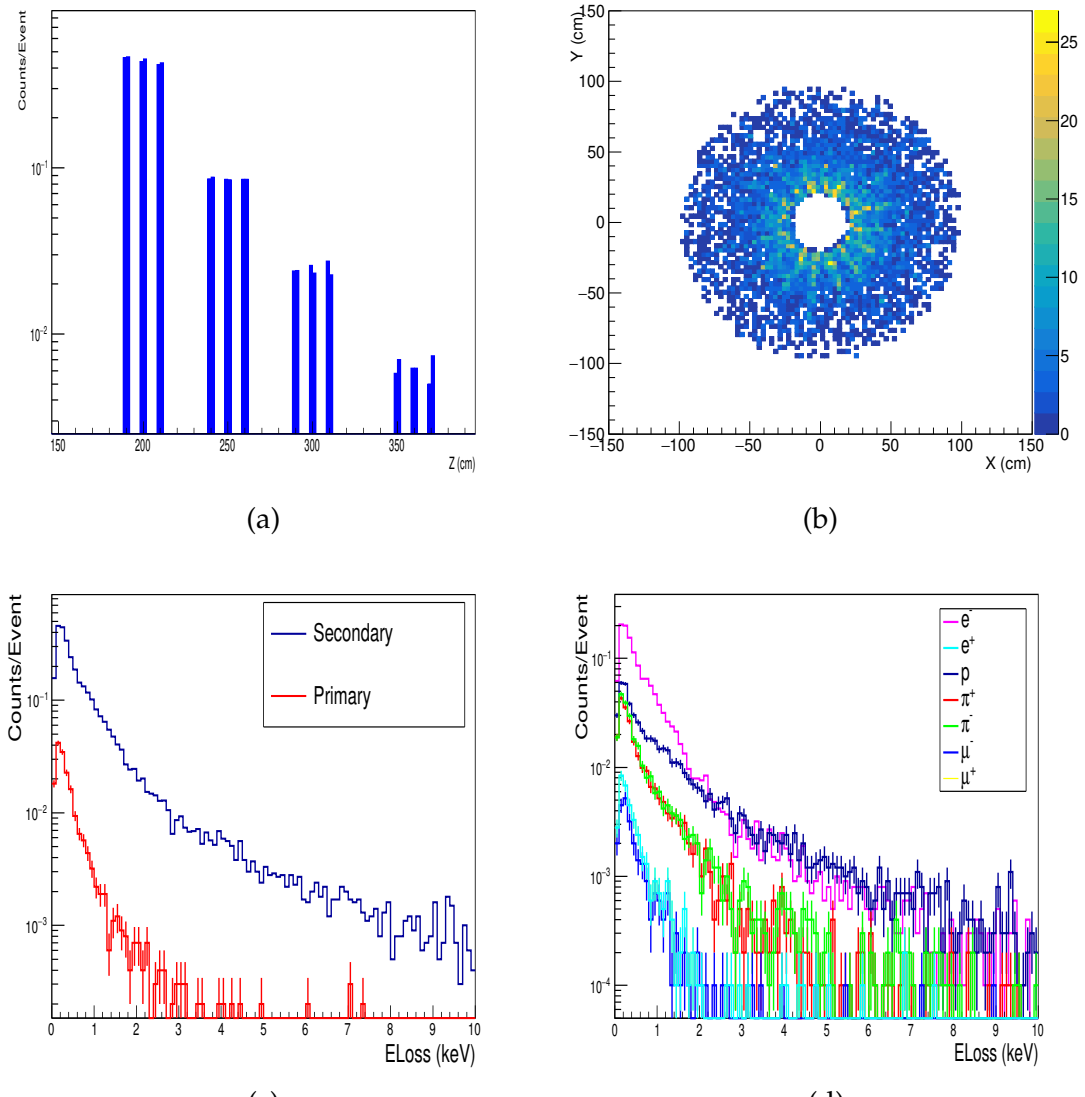

(a) (b)

(c) (d)

Figure 4.4: Some typical plots characterize the MuCh geometry response for central Au+Au collisions at 10 A GeV: (a) Z-position distribution of points on each layer, (b) XY-distribution of MuCh point at the first layer of the first station, (c) Energy loss of primary and secondary particles and (d) Energy loss distribution for different particle compositions

hadronic interactions between known hadrons and their resonances, was used to produce the events. Fig. 4.4a depicts the Z-position distribution of MuCh points on each detection layer. The XY distribution of MuCh points at the first layer of the first station is depicted in Fig. 4.4b. Particle density is higher near the beam pipe and progressively drops towards the periphery, a trend that is consistent throughout all layers. Fig. 4.4c illustrates the energy loss of primary and secondary particles, whereas Fig. 4.4d depicts the energy loss distribution for different particle compositions. A muon is seen to deposit typical energy of 0.6 keV.

4.2 First absorber optimization

In previous simulations with the MuCh detector setup, the first absorber was composed of high density (ρ=2.26 g/cm^3) pure carbon having a thickness of 60 cm [118]. Subsequent R&D for the mechanical design of the absorber blocks and a detailed market survey reveals the unavailability of high-density pure carbon in bulk, required to build the first absorber of surface area 260$\times$250 cm^2. The available density of bulk carbon is 1.7 g/cm^3. Such a reduction in absorber density would demand a proportionate increase in the physical thickness of the carbon block to keep the hadronic interaction length the same. However, this would imply a downstream shift of the following absorber blocks and detector chambers, which is not feasible. Therefore to keep the absorption profile and the physical thickness of the 1^{st} absorber block similar as it was with the carbon of density 2.26 g/cm^3, the possibility of having a composite absorber block made of two different materials instead of only carbon is explored. Concrete is chosen compared to other materials because of the mechanical and activation point of view. Afterwards, different iterations are done with varying thicknesses of the composite block (carbon+concrete). It has been found that the composite block of 30 cm carbon with a density of 1.7 g/cm^3 and 30 cm concrete with a density of 2.3 g/cm^3 gives us the optimum performance in terms of hadron absorption and muon identification as compared to the 2.26 g/cm^3 density carbon. Meanwhile, a broad market survey on existing carbon samples demonstrated that the carbon blocks with a somewhat higher density (1.78 g/cm^3) are available. To keep the hadronic interaction length equivalent to 30 cm of low-density carbon, the physical thickness of the carbon block is reduced to 28 cm. This would allow an extra 2 cm gap between the absorber and detector stations, which could be helpful for MuCh service works for the detector chambers. In Fig. 4.5, four different configurations of MuCh 1^{st} absorber are shown.

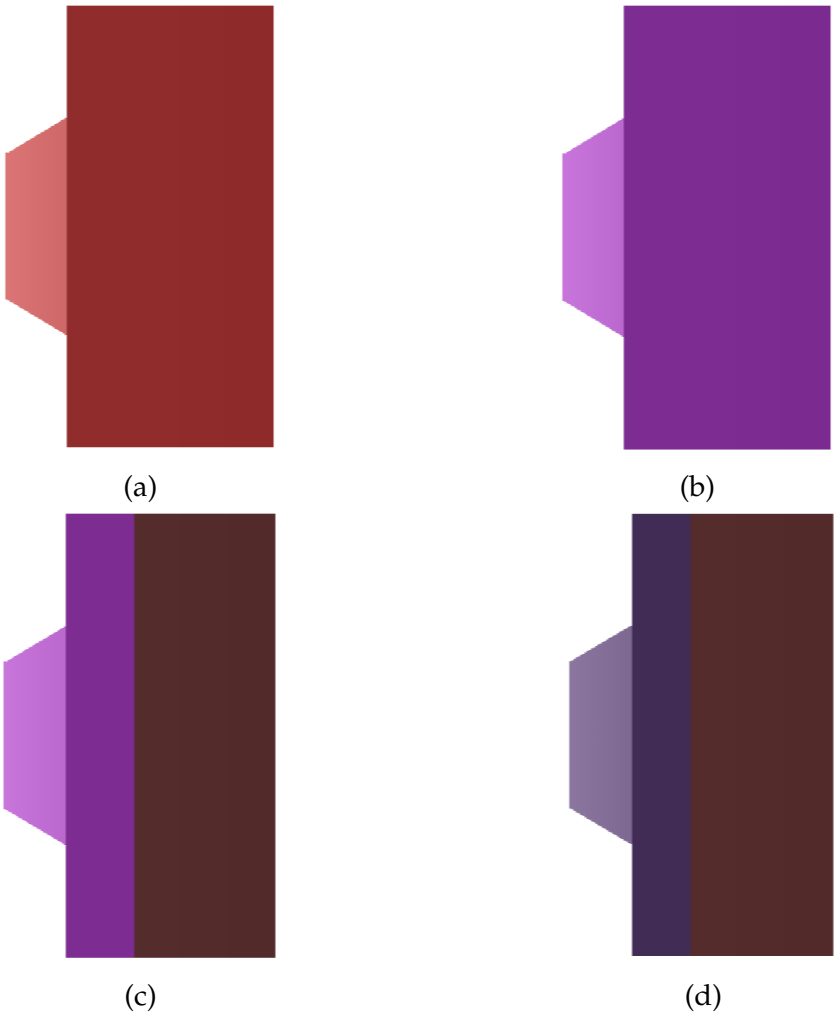

Figure 4.5: First absorber configurations: (a) Configuration I: 60 cm pure carbon of density 2.26 g/cm^3 (b) Configuration II: 60 cm pure carbon of density 1.7 g/cm^3, (c) Configuration III: a composite form of 30 cm carbon (1.7 g/cm^3) and 30 cm concrete (2.3 g/cm^3) and (d) Configuration IV: a composite form of 28 cm carbon (1.78 g/cm^3) and 30 cm concrete (2.3 g/cm^3).

To study the effect on the dimuon detection with these new 1^{st} absorber configurations, the simulation is performed for central Au+Au collisions at beam momentum of 8 A GeV/c. The phase space decay of $\omega \rightarrow \mu^+ + \mu^-$ is simulated using the PLUTO event generator [127] and embedded into background events generated with UrQMD [16, 17] event generator. One $\omega \rightarrow \mu^+ + \mu^-$ from PLUTO is embedded per event into the background. All the particles are transported through the entire CBM setup using the GEANT3 transport engine [126]. To examine the immediate impact on the performance of the muon detector chambers, the radial distribution of MuCh point density (number of Monte Carlo points per unit area per event registered on MuCh planes) from the first station placed after the 1^{st} absorber is investigated and shown in Fig. 4.6.

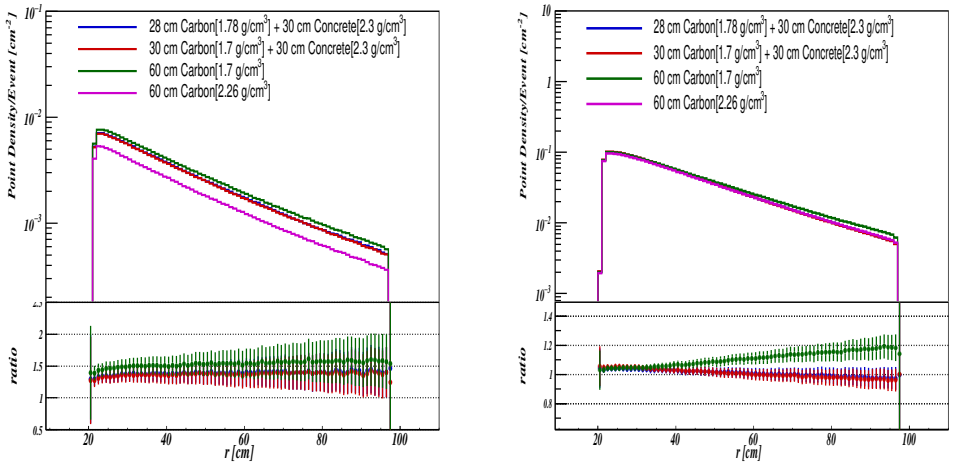

(a) (b)

Figure 4.6: Radial distribution of point density for primary (left) and secondary (right) particles in central Au+Au collisions at 8 A GeV/c momentum for the first station of the MuCh detector starts at a horizontal distance of 190 cm from the target.

An enhancement in point densities of primary particles is observed as compared to the configuration with 60 cm pure carbon of density 2.26 g/cm^3, which could be attributed to the reduced absorption of the incident particles inside the first absorber. The standard dimuon analysis software within CbmRoot (APR20 release [149]) framework is utilized to calculate the invariant mass spectra of the reconstructed muon tracks. To identify the muon track candidates, a set of track quality cuts are applied to the reconstructed global tracks. Reconstructed global tracks having more than six hits in the STS detector (STS hits ≥ 7), more than ten hits in the MuCh detector (MuCh hits ≥ 11), at least one hit in the TRD detector (TRD hits ≥ 1), for quality of a fitted vertex ($\chi^2_{VERTEX} \leq 3$), STS track segments

($\chi^2_{STS} \leq 2$) and MuCh track segments ($\chi^2_{MuCh} \leq 3$) are considered as the muon track candidates. The contribution of non-muonic tracks is reduced further by applying a 2σ cut on the reconstructed track mass on the Time of Flight (TOF) wall [150]. The signal is extracted from the embedded set of events by selecting oppositely charged muon candidate tracks on an event-by-event basis. The combinatorial background is calculated using the super event (SE) technique, where one negatively charged muon candidate track is combined with all the other oppositely charged muon candidate tracks. To ensure that the acceptance is not changing with the MuCh 1^{st} absorber configuration change, the Y-p_T distributions of the reconstructed ω mesons for the different configurations are studied and shown in Fig. 4.7. No significant change in the acceptance is observed in the four different MuCh 1^{st} absorber configurations.

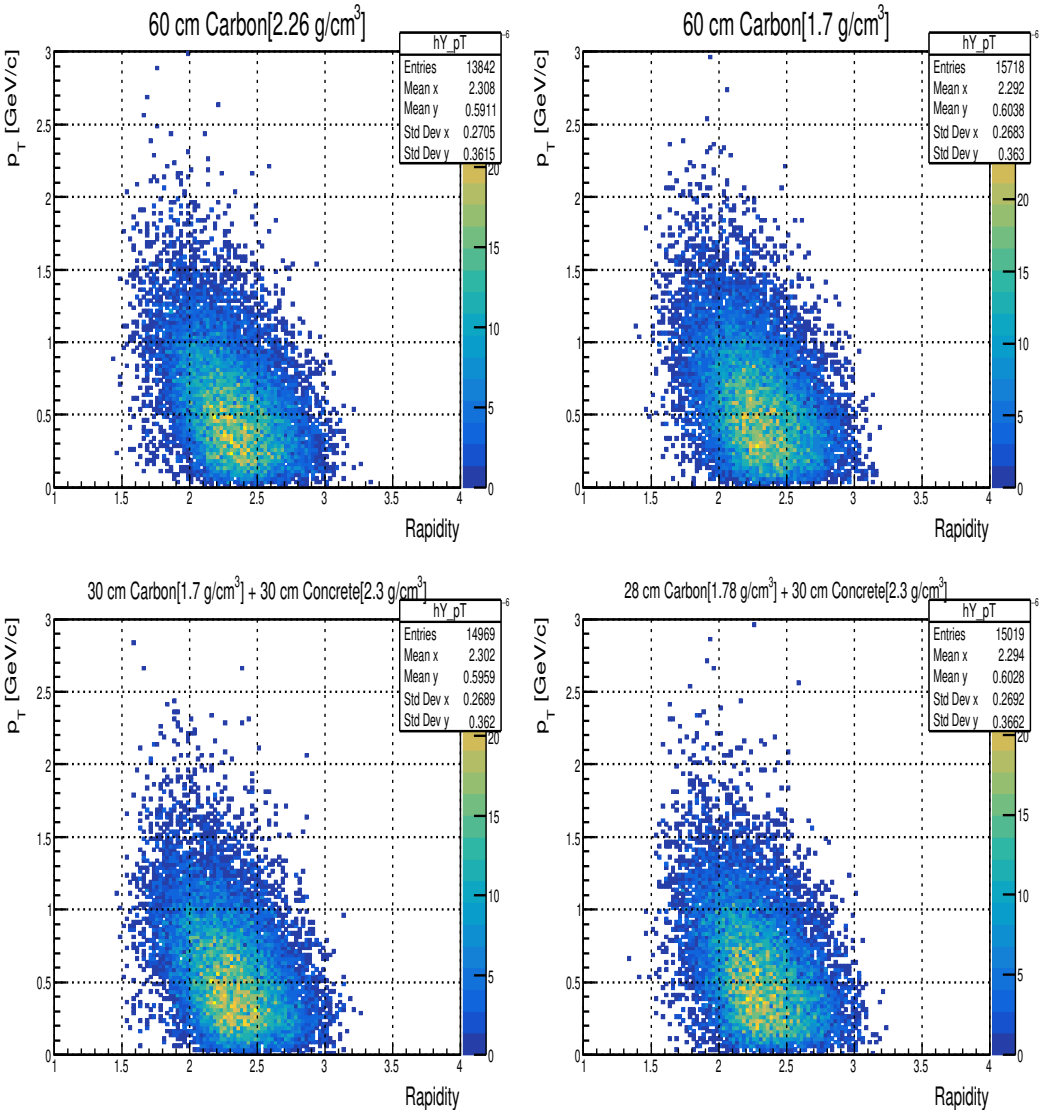

Figure 4.7: Y-p_T coverage for different first absorber configurations.

The invariant mass spectra for the combinatorial background for the different configurations are shown in Fig. 4.8. As expected, the combinatorial background increases in the new absorber configurations due to the lesser absorption of the incident particles. Since the performance with configuration IV (28 cm carbon of density 1.78 g/cm^3 and 30 cm concrete of density 2.3 g/cm^3) is close to the performance with the configuration I (60 cm carbon of density 2.26 g/cm^3), therefore configuration IV is considered as the feasible configuration for MuCh 1st absorber. The reconstruction efficiencies, signal-to-background ratios, and Significance for ω mesons are estimated within a $\pm 2\sigma$ mass window around the signal peak and tabulated in Table 4.1. Fig 4.9 shows the invariant mass distribution of ω mesons for all MuCh 1st absorber configurations.

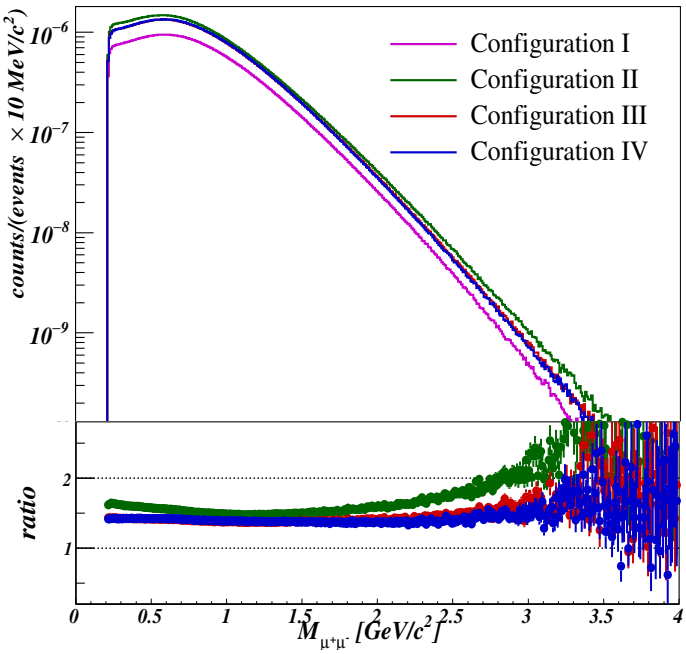

Figure 4.8: Invariant Mass Spectra for the Combinatorial Background for various configurations. The ratios with respect to the initial configuration (60 cm pure carbon of density 2.26 g/cm^3) are plotted in the bottom panel.

Absorber I Configuration	**Efficiency** ω, %	**S/B**
(I) 60 cm carbon ($\rho = 2.26\ g/cm^3$)	0.73	0.31
(II) 60 cm carbon ($\rho = 1.70\ g/cm^3$)	0.76	0.22
(III) 30 cm carbon ($\rho = 1.70\ g/cm^3$) + 30 cm concrete ($\rho = 2.3\ g/cm^3$)	0.73	0.23
(IV) 28 cm carbon ($\rho = 1.78\ g/cm^3$) + 30 cm concrete ($\rho = 2.3\ g/cm^3$)	0.72	0.22

Table 4.1: Reconstruction efficiency and signal-to-background ratio for ω in central Au+Au collision at 8 A GeV for various first absorber configurations.

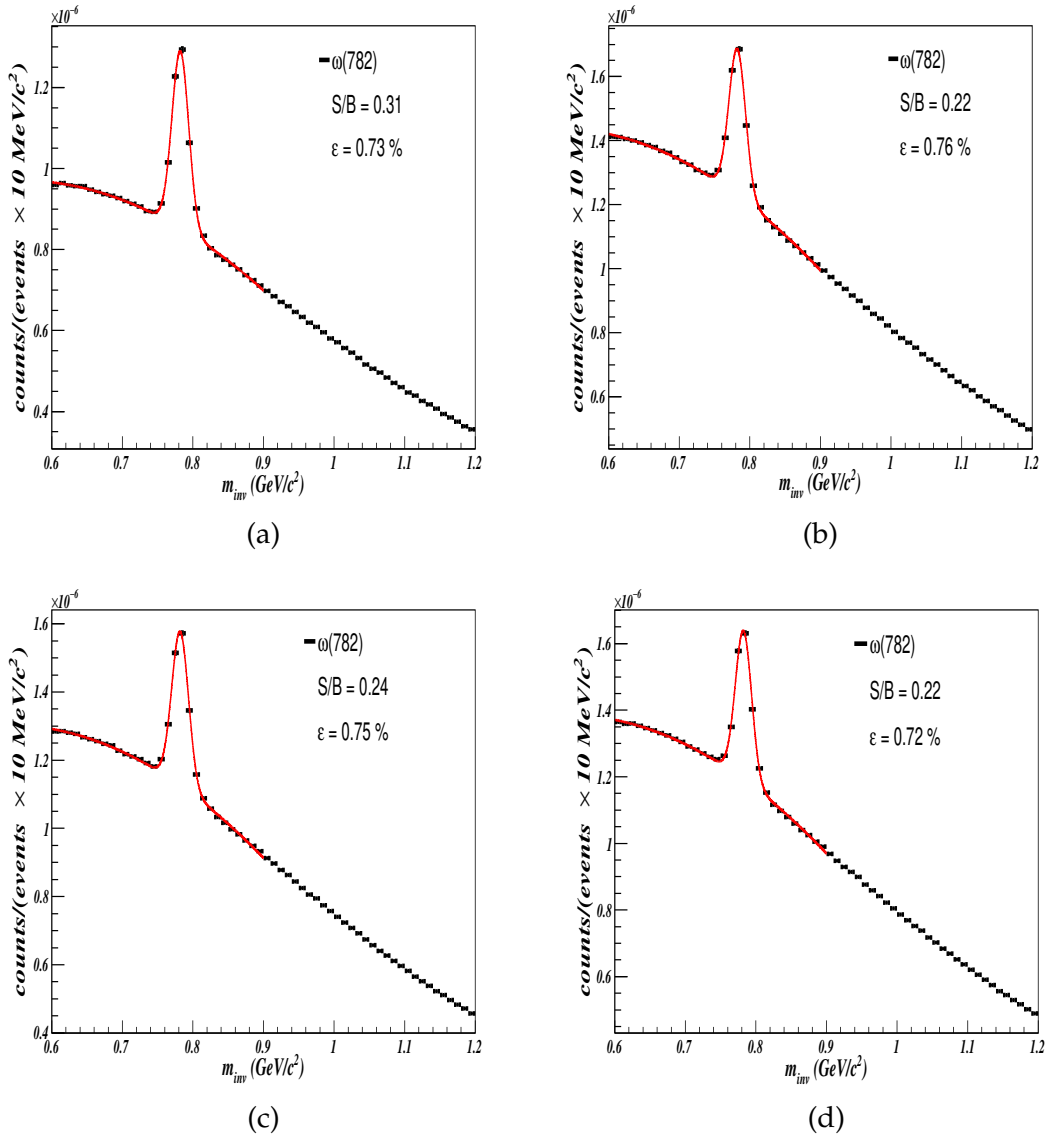

Figure 4.9: Invariant mass spectra for reconstructed ω meson in central Au+Au collision at 8 A GeV for different first absorber geometry configurations. (a) Configuration I: 60 cm carbon of density 2.26 g/cm^3, (b) Configuration II: 60 cm carbon of density 1.7 g/cm^3, (c) Configuration III: 30 cm carbon of density 1.7 g/cm^3 and 30 cm concrete of density 2.3 g/cm^3, (d) Configuration IV: 28 cm carbon of density 1.78 g/cm^3 and 30 cm concrete of density 2.3 g/cm^3.

4.3 Investigation & implementation of realistic GEM chamber design

The detector R&D results in the choice of triple GEM chambers [151–153] as a tracking detector in the first two stations of the MuCh detector will be operated with Ar/CO_2 gas mixture in 70:30 volume ratio [154]. The drift gap of the chambers will be 3 mm, and the transfer and induction gaps will be 2 mm each. In MuCh simulations, only the 3 mm drift gap is implemented as an active volume filled with pure Ar gas as the active medium for primary ionization. The subsequent amplification is implemented in the digitization of the MuCh points registered in the active volume. To make the simulation more realistic, passive volumes (of 6 mm thickness) and the realistic GEM gas mixture Ar/CO_2 in a 70:30 volume ratio are implemented. Also, recent investigations on the chamber mechanics suggest that the foreseen thickness of the aluminium cooling plates might be 12 mm instead of 10 mm for cooling detector electronics and providing mechanical support to the GEM chambers. We implement these finer aspects of chamber design in our simulations and investigate the effects of each modification independently on dimuon detection, as discussed below.

4.3.1 Investigation of the realistic GEM gas mixture

In all the previous simulations [155], only Ar gas was used as the active element in the geometry, but in the actual setup, chambers will be used with an Ar/CO_2 gas mixture in a 70:30 volume ratio where the CO_2 will act as a quencher. In order to implement the realistic gas mixture, the media definition needs to be changed. Since Ar has a lower density than CO_2 hence 70% volume of Ar will only account for about 67.8% of the mass. For the remaining 32.2%, though the ratio of the number of atoms is (O:C) 2:1 but as oxygen atoms are heavier, they account for 72.8% of the mass of the CO_2 and the carbon for the remaining 27.2%. The gas mixture can be implemented by considering the proportion of the weight of each material in the mixture or by considering the number of atoms of each kind. In Table 4.2, the respective media definition for the mixture is summarised.

The MC point density with the different gas mixture configurations for the first two stations are shown in Fig. 4.10. As evident, there is no significant change in point density compared to pure Ar gas. After studying the effect of different gas mixture configurations in terms of MC points, different energy loss methods are also studied to understand the effect of the gas mixture in

Configuration	ncomp	Mass number A	At. number Z	Density (g/cm^3)	Proportions
Mixing by the weightage (ncomp $>$ 0)	3	Ar (39.948), C (12.01), O (15.9994)	Ar (18), C (6), O (8)	0.001843	Ar (0.678), C (0.088), O (0.234)
Mixing by the number of atoms (ncomp $<$ 0)	-3	Ar (39.948), C (12.01), O (15.9994)	Ar (18), C (6), O (8)	0.001843	Ar (7), C (3), O (6)

Table 4.2: Media definition for realistic GEM gas mixture (Ar/CO_2) with two different configurations. ncomp; stands for a number of components.

more detail. In the CbmRoot framework, the GEANT settings [156, 157] can be changed to choose different energy loss models that can also switch the energy straggling in the medium. The different available configurations are tabulated in Table 4.3.

Energy loss models	Description
Model 0	No continuous energy loss
Model 1 (Default)	Continuous energy loss with the generation of delta-rays above the value defined for the DCUTE cut and restricted Landau fluctuations below DCUTE
Model 2	Continuous energy loss without generation of delta-rays and full Landau-Vavilov-Gauss fluctuations
Model 3	Same as Model 1, kept for backward compatibility
Model 4	Energy loss without fluctuations

Table 4.3: A description of different models available within the CbmRoot framework to simulate the energy loss in the medium [156]. Model 1, with no energy straggling, is the default model used in the framework.

The energy loss distribution for μ^+ and μ^- in the first station of MuCh is shown in Fig. 4.11 with different models and energy straggling conditions. The peak in the energy loss distribution with models 1 and 2 with energy straggling off is for the double-counting due to the delta-ray productions. But the peak vanished with Model 2 and straggling on. These particular cuts (Model 2, Straggling 1) are applied as a special physics cut for the GEM detector.

Even though the energy loss distribution shows some peak with Model 1 and 2 (without energy straggling), the MC point density, as shown in Fig. 4.12 for the first station, does not significantly change for both the primary and secondary particles.

4.3.2 Implementation of passive volume in GEM

In all the former simulations, only the drift volume of the GEM was implemented as an active medium of a thickness 3 mm. Still, the actual triple GEM

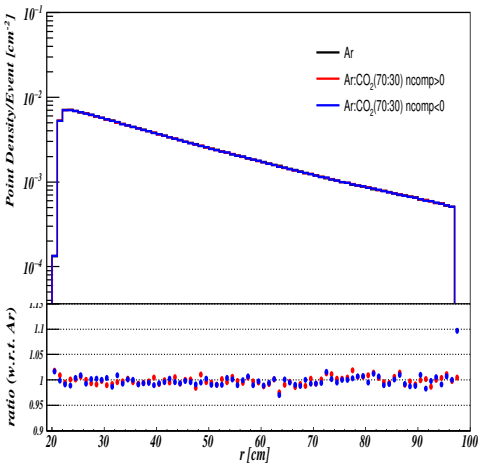

(a)

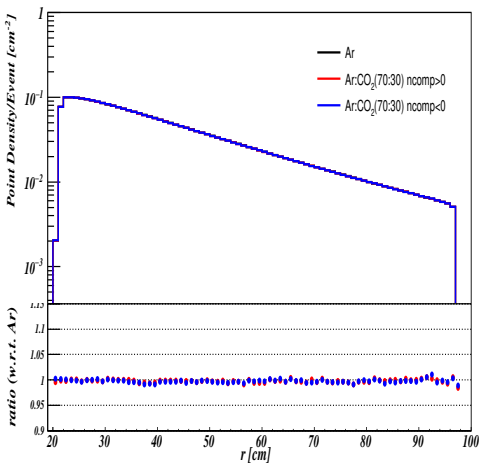

(b)

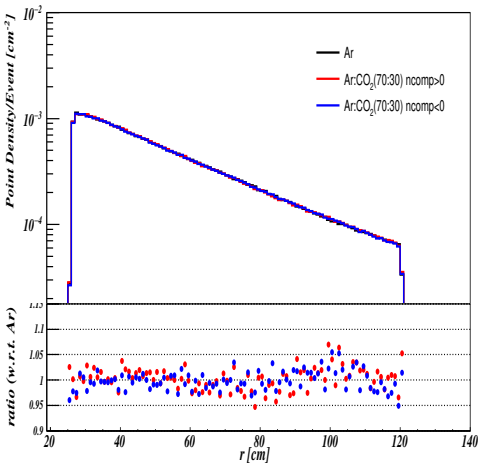

(c)

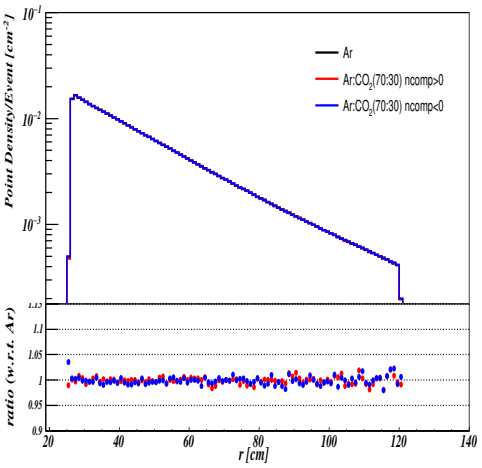

(d)

Figure 4.10: Radial distribution of point density for primary (left) and secondary (right) particles at the first station (top panel) and the second station (bottom panel) with different gas mixtures and gas mixture configurations. The ratios for Ar filled GEM module are plotted in the same figure in the bottom panel.

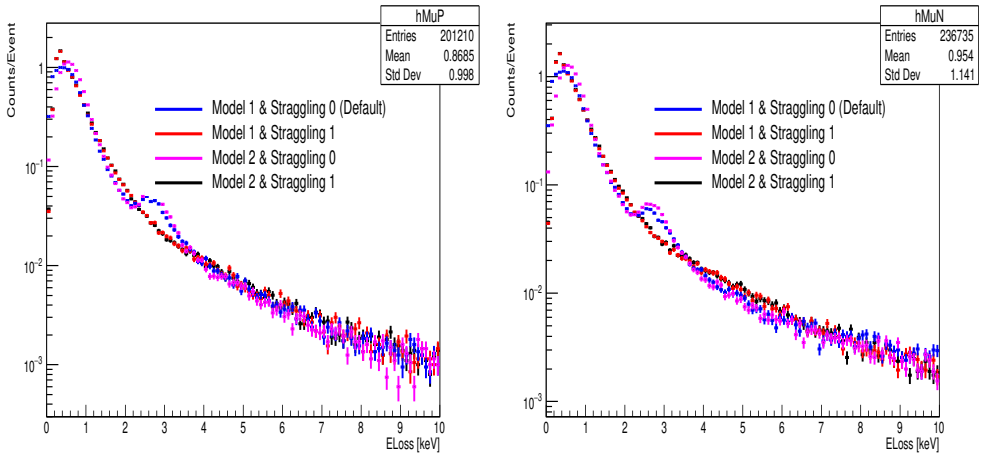

Figure 4.11: Energy deposition of μ^+ (left panel) and μ^- (right panel) at the first station of MuCh with different models as listed in table 4.3.

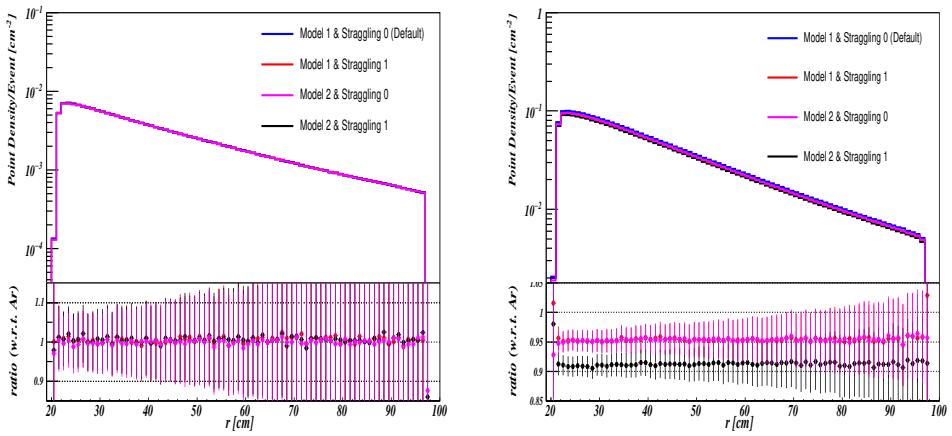

Figure 4.12: Radial distribution of point density for primary (left) and secondary (right) particles at the first station and their ratios with respect to default settings in the bottom panel of the same figure.

configuration will consist of two 2 mm thick transfer gaps and one 2 mm thick induction gap [153]. The GEM foil has a 50 μm Kapton film with 5 μm copper foil on either side. It also has a drift and readout, which consists of 3 mm G10 material. Therefore to make the GEM configuration more realistic, three 2 mm passive gas volumes and additional materials like GEM foil, drift and readout are implemented in the chamber design.

In Fig. 4.13, the detailed and most realistic configuration of the GEM chambers is shown. The configuration without passive volume is labelled as *Configuration I*, and with the passive volumes, it is labelled as *Configuration II*. After implementing three 2 mm passive gas volumes, the MC point density is calculated and compared with the previous version (without the passive volume).

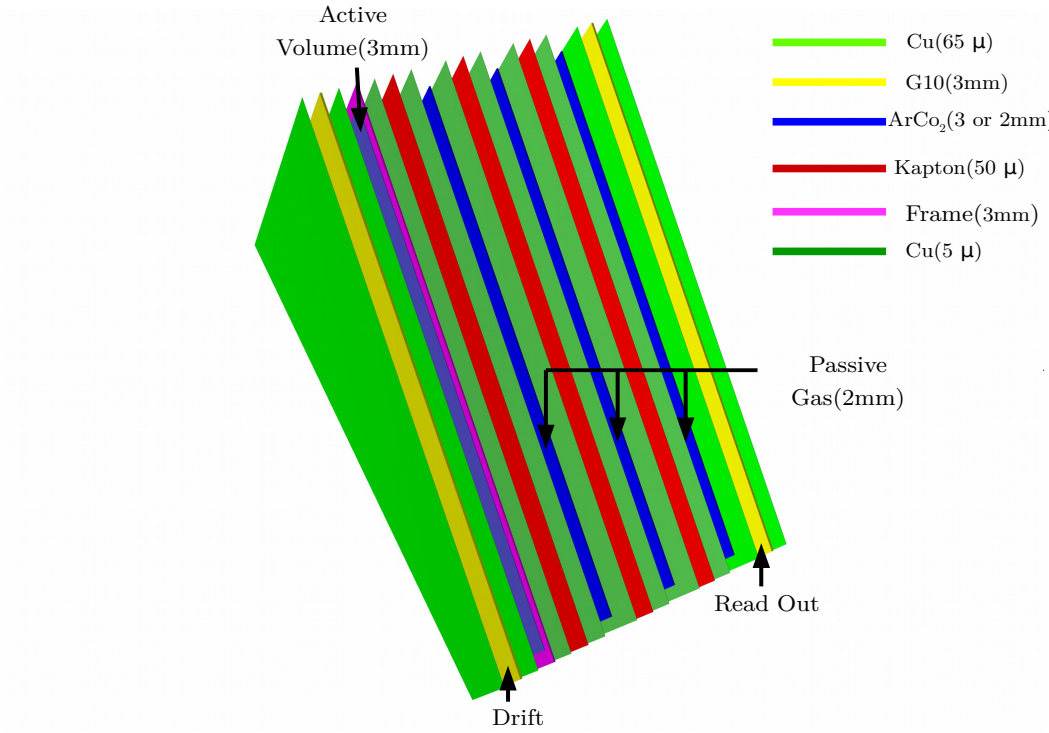

Figure 4.13: A schematic view of GEM module. The materials used in the geometry are listed in the legend.

The comparison of point densities at the first two stations of MuCh is shown in Fig. 4.14.

No significant change in the MC points is observed. To check the effect of passive volume on the physics performance, the invariant mass distribution is calculated for the combinatorial background and for the ω meson by using the techniques and cuts discussed in Section 4.2. The invariant mass distribution for the combinatorial background is shown in Fig. 4.15, and in Fig. 4.16, the invariant mass distribution of ω meson is shown. As expected, no significant change in the ω meson reconstruction efficiency and the signal-to-background ratio is observed after implementing the three 2 mm passive volumes.

4.4 Summary

This chapter described in detail the CBM simulation framework and the optimization of the muon chamber detector geometry of the CBM experiment. Initially, the "CbmMuchGeoScheme" class handled the construction and the geometry parameters of MuCh were provided at the time of transport in ASCII format. To design the system's transparent, efficient, and user-friendly interfaces, we had to convert CBM geometries into ROOT format and implement them as

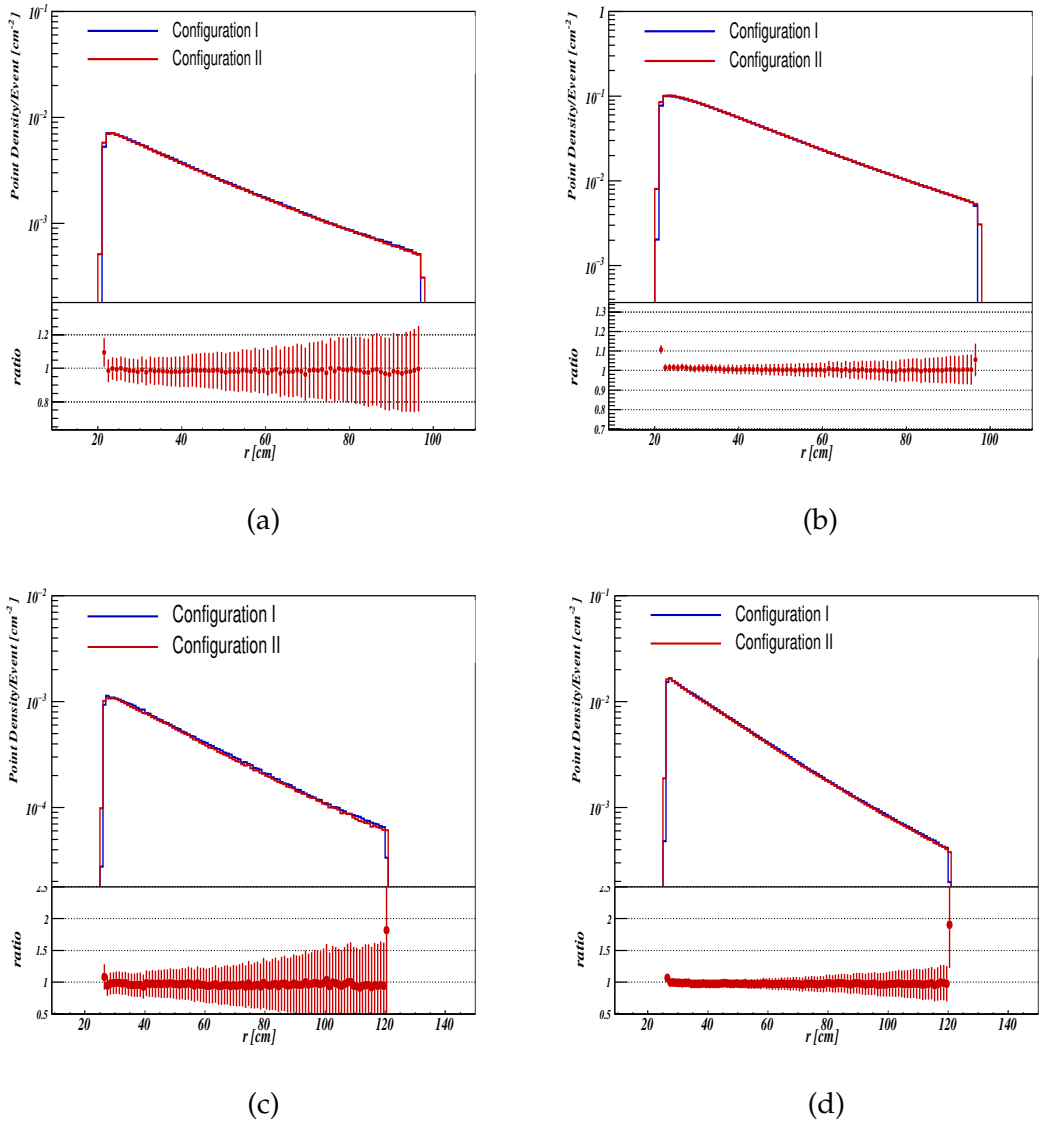

Figure 4.14: Radial distribution of point density for primary (left) and secondary (right) particles at the first station (top panel) and the second station (bottom panel) for two different GEM geometry configurations.

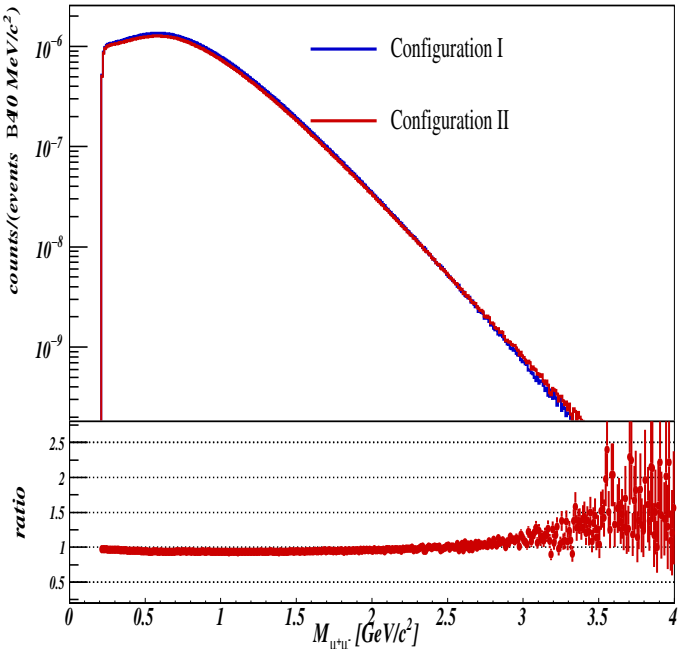

Figure 4.15: Invariant mass spectra for the combinatorial background for the two different GEM configurations.

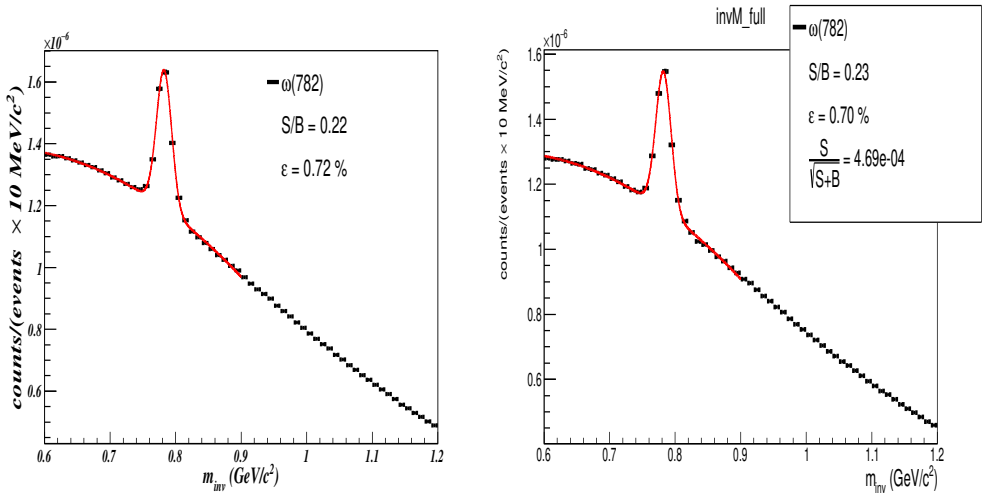

Figure 4.16: Invariant mass spectra for reconstructed ω meson in central Au+Au collision at 8 A GeV for *Configuration I* (left panel) and *Configuration II* (right panel)

nodes. Additionally, a geometry database can handle the geometry files and the GL viewer of ROOT TBrowser allows for standalone visualisation of each detector geometry. The design of a macro to generate the MuCh geometry as well as the development of GeoHandler classes to incorporate the rootified geometry in transport simulations is discussed in detail. In addition, the optimisation of the

first absorber of MuCh is also discussed in detail. It is finalised that the configuration with 28 cm of carbon with a density of 1.78 g/cm^3 and 30 cm of concrete with a density of 2.3 g/cm^3 is the most feasible configuration for MuCh first absorber in terms of the availability of the material and the physics performance of the subsystem. Aside from that, more realistic geometry combinations are implemented and investigated to understand their effect on the performance of the muon chamber. The thickness of the aluminium cooling plates is extended from 10 mm to 12 mm, the GEM gas composition is changed from pure Argon gas to an Ar/CO_2 gas mixture in a 70/30 volume ratio, and three 2 mm-thick passive volumes are implemented. Each of these modifications is done individually in order to determine the effects of each change. From the results presented in this chapter, it can be concluded that the implementation of a more realistic geometry configuration does not have a significant effect on the overall performance of the MuCh subsystem.

Chapter 5

LMVM measurements at FAIR

This chapter focuses on the measurements of muon pairs in Au+Au collisions at FAIR energies, which are used to estimate the temperature of the fireball and, hence, to explore a caloric curve of QCD matter. Strong absorption and rescattering effects do not influence electrons and muons produced in the hot and dense fireball of a heavy-ion collision; therefore, they bring undisturbed information about to the detection system. The lepton pairs are either decay products of vector mesons or are thermally radiated away from the hot matter in the same manner as photons. The decay of η, ϕ, ω, and ρ mesons dominates the spectrum at invariant masses up to around 1 GeV/c^2. The information on their in-medium mass modifications related to chiral symmetry restoration [114] can be obtained by measuring their decay leptons, especially from short-lived ρ mesons. The dilepton invariant mass spectrum provides the average temperature of the emitting source, integrated over the entire collision history, above 1 GeV/c^2, where the contributions from vector meson decay are significantly reduced. Because the source temperature is unaffected by radial flow, it can be calculated directly from the slope of the dilepton invariant mass spectrum. At the CERN-SPS, the NA60 collaboration performed such a measurement. The average source temperature of 205 $\pm$ 12 MeV was estimated from the $\mu^+\mu^-$ invariant mass spectrum measured in In-In collisions at 158 A GeV [158]. Recently, the HADES collaboration has extracted a source temperature of 72 $\pm$ 2 MeV from the low-mass region of the dielectron invariant mass spectrum. It was reported in Au+Au collisions at a beam kinetic energy of 1.25 A GeV by eliminating the known contribution coming from vector meson decays [159].

Fig. 5.1 illustrates the temperature of a fireball as a function of collision energy [160]. The NA60 and HADES data points are also included in the same figure. The dashed magenta line indicates the average fireball temperature, which corresponds to the slope of the dielectron invariant mass spectrum between 1 and 2 GeV/c^2 calculated using a coarse-graining approach applied to a transport model calculation. The solid blue line shows the parameterization of the

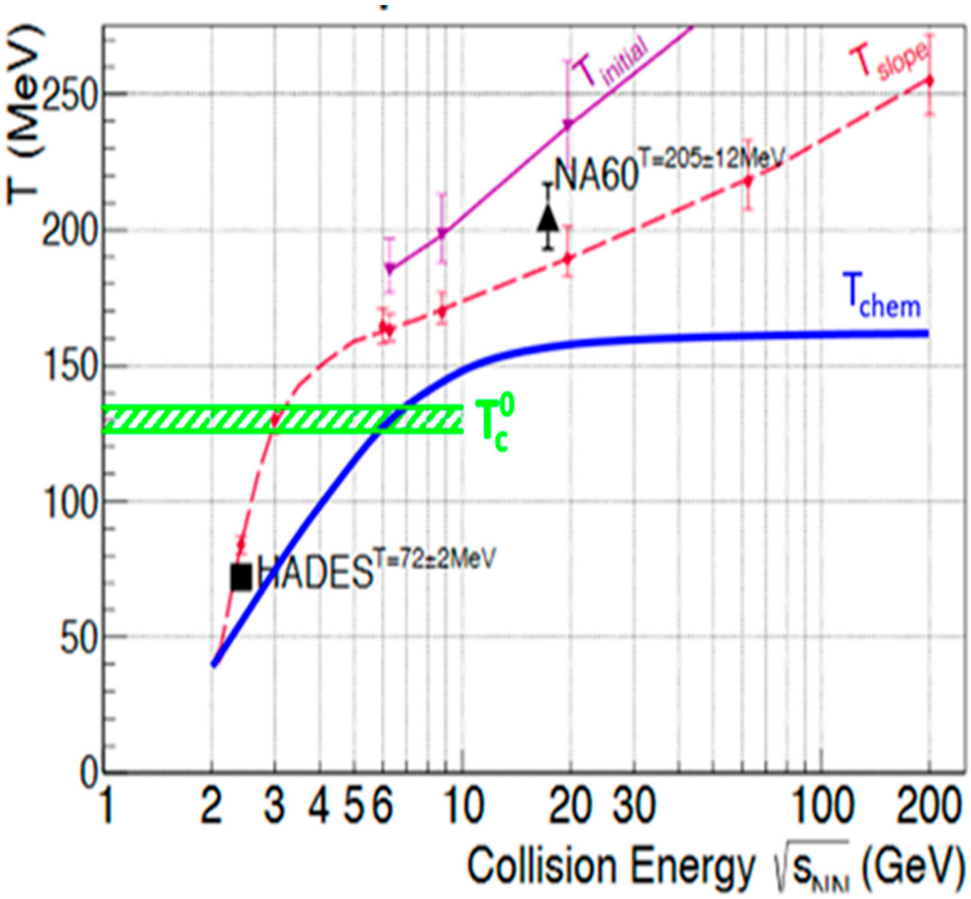

Figure 5.1: The fireball temperatures as a function of collision energy in heavy-ion collisions [160]. The purple and magenta lines are calculated using a coarse-graining method applied to a transport model [161], with $T_{initial}$ expressing the initial temperature and T_{slope} obtained from the dilepton invariant mass distribution in the region above 1 GeV/c^2. The data points for NA60 [158] and HADES [159] are extracted from the measured dilepton invariant mass spectra. The chemical freeze-out curve can be seen in blue as a solid line [162], while the upper bound for the temperature of the critical endpoint calculated using lattice QCD [163] can be seen in the green dashed region.

freeze-out temperature, i.e. when the particles seize to interact inelastically at a late stage of the collision. Recent lattice QCD estimations report a relatively low chiral phase transition temperature of $T_c^0 = 132^{+3}_{-6}$ MeV at zero baryon chemical potential ($\mu_B = 0$) in the chiral limit [163]. Based on this calculation, the critical endpoint of a first-order phase transition for physical quark masses and finite B will be found at an even lower temperature if it even exists. The temperature of the critical endpoint is bounded by the green dashed band [163].

The measurement of fireball temperature using lepton pairs in heavy-ion collisions at various beam energies is a unique way to identify a probable first-order phase transition and reveal or rule out the existence of a critical endpoint. The phase coexistence and its endpoint are identified if a caloric curve emerges

from the temperature scan. Furthermore, according to the lattice QCD calculation, the critical endpoint and the beginning of deconfinement should be in the FAIR energy range. As a result, a vital component of the CBM research program will be the detailed investigation of both dielectron and dimuon emissions in heavy-ion collisions ranging from $\sqrt{s_{NN}}$ = 2.5 to 5 GeV collision energies, where a first order phase transition should occur if one exists.

Due to the enormous combinatorial background coming from the different sources for electrons and muons, dilepton measurements in heavy-ion collisions are challenging. To reduce the systematic uncertainties, the CBM experiment involves detector systems for the independent identification of e^+e^- and $\mu^+\mu^-$ pairs because electron and muon background sources are fundamentally different. In order to emphasize the capabilities of the MuCh detector system, the focus of this chapter will be on the track reconstruction methods, the particle identification, and, finally, the physics performance studies for LMVM.

5.1 Background and Signal Inputs

In chapter 3, we already covered event generation and their transportation through the medium. The background is generated using the UrQMD model [16, 17], which describes hadronic interactions between known hadrons and their resonances. It measures particle production based on a microscopic transport technique. As a result, it is most beneficial to gather a realistic picture of the general bulk of particles produced in heavy-ion collisions. Most of the particles produced by UrQMD are charged and light particles, as well as neutral pions and photons. The heavier particles are also included, although their production probability is substantially reduced than the others. As a result, to obtain a valuable estimate of the reconstruction efficiency in the experiment, the number of rarer probes in the events must be intentionally increased.

The PLUTO event generator [127] produces transport simulation input for rare probes. It is quick and employs a physics database to extract the essential information about specific particles and allow for the user definition of specific decay channels. The parameters of the PLUTO signal generator have been modified to correspond to the FAIR energy regime. There are two different kinds of inputs to simulate the performance in CBM: dimuon decays from the low-mass vector mesons and charmonium. The kinematic properties of an ω particle decaying via dimuonic channel ($\omega \rightarrow \mu^+\mu^-$) are shown in Fig. 5.2.

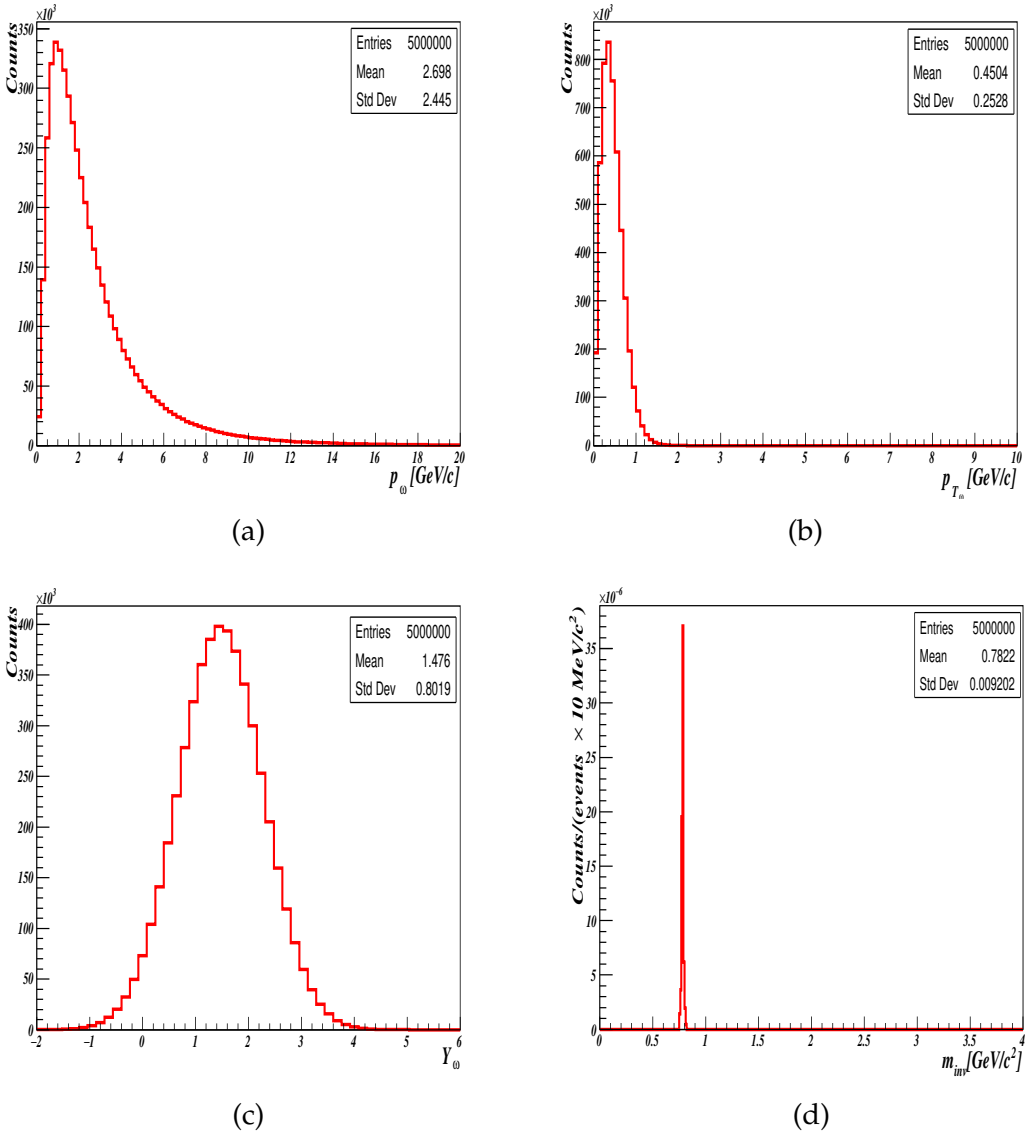

Figure 5.2: Input distributions of different kinematic variables for ω meson in central Au+Au collisions at 8 A GeV/c beam momentum, as calculated with the PLUTO events. (a) Momentum distribution, (b) transverse momentum distribution, (c) rapidity distribution and (d) invariant mass distribution from the decays of ω meson.

Fig. 5.3 depicts the reconstructed invariant mass distributions of the entire spectrum for the LMVM case generated by using the PLUTO model. The mixture of all contributions of various LMVM is referred to as the “cocktail". The Dalitz decay is most dominant in the extremely low mass regime. The expected multiplicities of the ω and ϕ mesons are significantly higher than the rest of the contributions in their mass range.

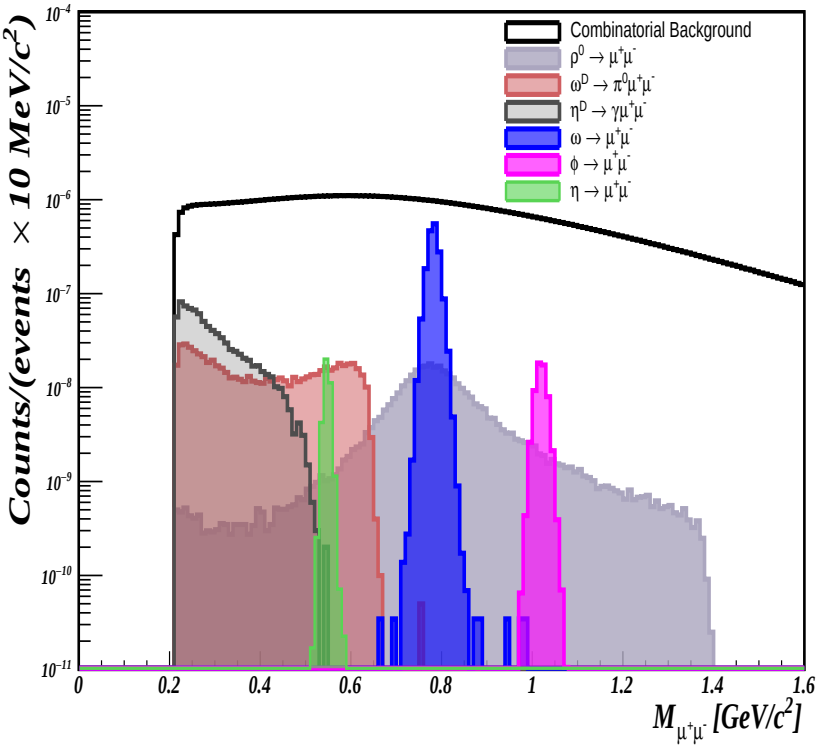

Figure 5.3: A cocktail of the invariant mass spectra for several dimuon sources in central Au+Au collisions at 8 A GeV/c beam momentum in the low mass region. Different shades represent dimuon decays of various low-mass vector mesons, including their Dalitz decays, as identified using Monte Carlo particle information.

Estimation of LMVM multiplicity: Aside from the kinematic properties, the multiplicity of LMVM production is another variable necessary for estimating the S/B ratio of LMVM detection. As the PLUTO does not provide any information about multiplicity; therefore, the multiplicity values for distinct signal particles are often obtained from the Hadron String Dynamics (HSD) transport code [164] in CBM simulations. The values of the branching ratios (BR) are collected from the Particle Data Group (PDG) database [165]. The required signal weighting factor is then calculated by multiplying the particle multiplicity by the branching ratio of the respective decay channel.

5.2 Identification of Muon candidates (Cuts and Selections)

To reject as much background as possible, we apply various cuts at the single muon level. For the identification of the muon candidates, various cuts have been applied to the reconstructed tracks; STS: Number of hits in STS and χ^2 of the STS segment of the track, MuCh: Number of MuCh layers and χ^2 of the

MuCh segment of the track, TRD: Number of hits in TRD. In addition, a cut on χ^2_{vertex} vertices and a cut on the particle mass-squared versus provided by time-of-flight as Fig. 5.4 are being used.

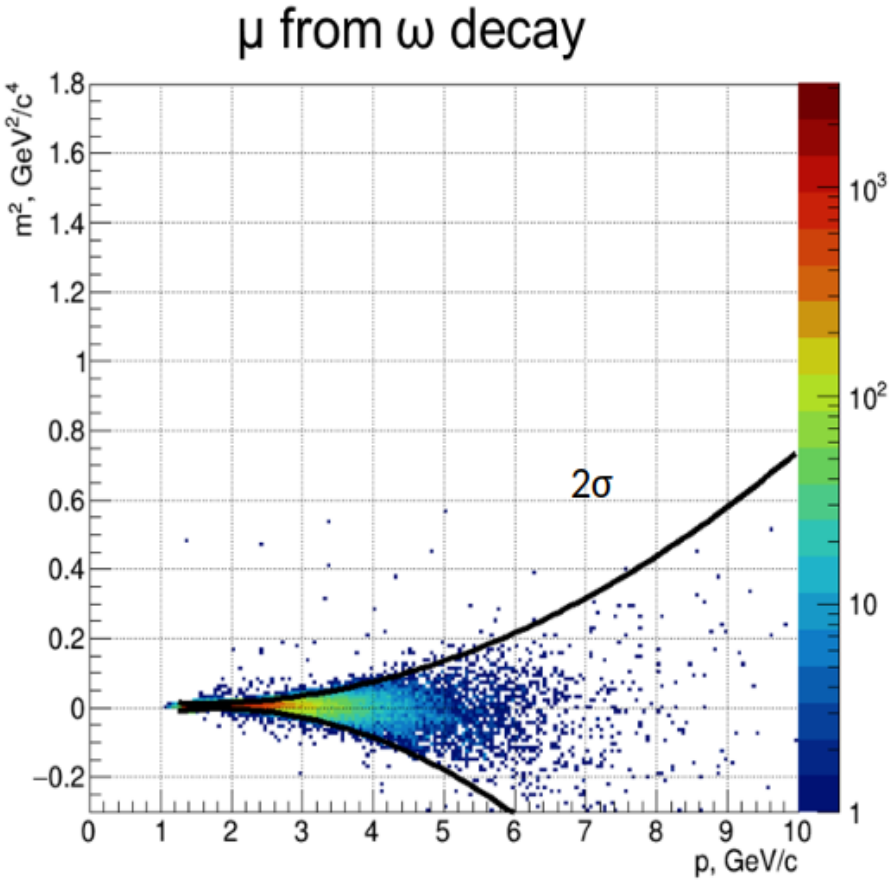

Figure 5.4: The reconstructed muon tracks from ω meson decay as a function of mass squared and momentum based on TOF information for central Au+Au collisions at 8 A GeV/c beam momentum. Signal muons have been identified using Monte Carlo particle information. The black lines represent a second-order polynomial fit using the $\pm 2\sigma$ of Gaussian distribution. The mass square of signal muons has been fitted with the Gaussian distribution in each momentum bin.

We obtain a set of final cuts based on the separation power of these cuts between signal and background, which have been utilized in our analysis for muon candidate selection. It's worth noting that the numbers of MuCh hits in a track are assumed to be different while picking muons from LMVM and charmonia. For example, while the number of MuCh layers for low-mass vector mesons might be up to 12, charmonium demands more than 12 MuCh hits to ensure that the associated track has penetrated the thick absorber.

5.2.1 Optimization of cuts

The signal-to-background (S/B) ratio and the reconstruction efficiency are the two quantities essential to quantify the performance of the CBM muon setup. The number of reconstructed and input MC LMVMs are used to estimate the reconstruction efficiency of the LMVMs. The dimuon efficiency is related to the reconstruction efficiency of single muon tracks that satisfy all the necessary reconstruction and selection criteria for LMVM analysis. The chamber detection efficiency is directly related to the reconstruction of single muons. If ϵ_{μ} is the efficiency for single muon tracks originating from LMVM, then the detection efficiency for LMVM can be stated as follows:

$$\epsilon_{LMVM} = \epsilon_{\mu^+} \times \epsilon_{\mu^-} \tag{5.1}$$

Figs. 5.5, 5.6 and 5.7 illustrate the distributions of track quality parameters (χ^2) of primary vertex, STS and MuCh tracks for reconstructed muon tracks from LMVM (ω, η and ϕ meson) decay and reconstructed background tracks for central Au+Au collisions at 8 A GeV/c beam momentum. The identification of signal muons is done via Monte Carlo information. We obtained a set of final cuts based on the separation powers of these cuts to distinguish between signal and background, and we used these cuts in this analysis to pick probable muon candidates.

The application of strict track selection cuts decreases the reconstruction efficiency but helps to enhance the S/B ratio by reducing background. Higher reconstruction efficiency ensures a larger data sample over a given time period, whereas S/B reflects any measurement's actual figure-of-merit. As a result, an optimal selection between these two quantities must be adopted. In order to accomplish this, we estimated the reconstruction efficiency for LMVMs (ω, η and ϕ) and the S/B ratio for a set of track quality selection cut values, as listed in Table 5.1. In order to optimisation of the track quality parameters (χ^2), the selection criteria for accepting tracks have been applied as the number of hits in STS ($\geq$7), number of hits in MuCh ($\geq$ 5), number of hits in TRD ($\geq$ 1) and number of hits in TOF ($\geq$ 1). The best possible results are achieved for tracks with $\chi^2_{vertex} < 3.0$, $\chi^2_{STS} < 3.0$ and $\chi^2_{MuCh} < 3.0$. The tracks are picked by using the optimal values of analysis cuts and are now projected to the TOF plane, where the TOF mass cut is used as the final selection cut.

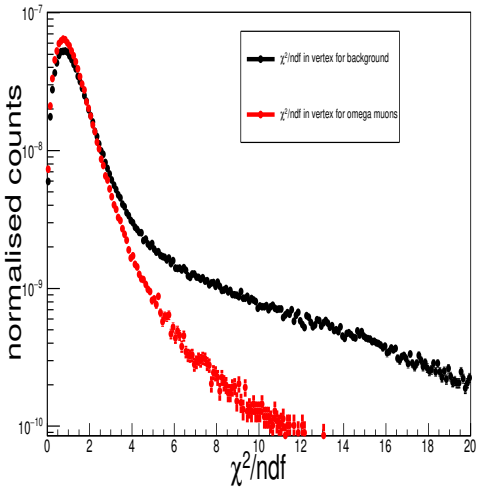

(a)

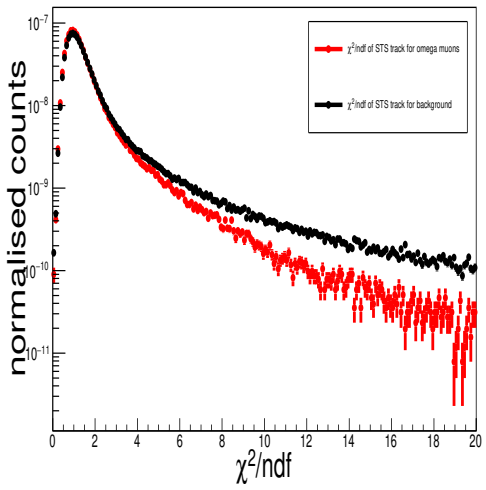

(b)

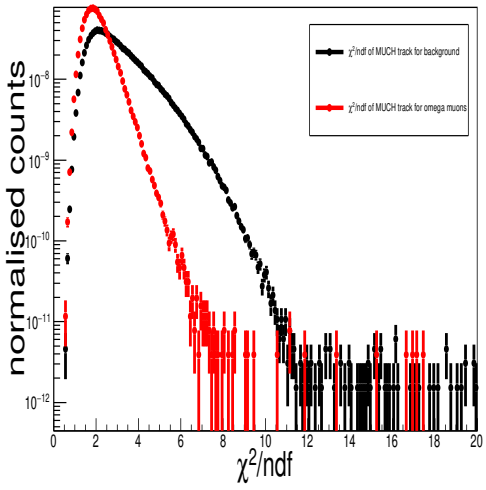

(c)

Figure 5.5: Various track quality parameter distributions obtained for the reconstructed muon tracks from ω meson decays (red) and reconstructed background tracks (black) for central Au+Au collisions at 8 A GeV/c beam momentum. Signal muons are identified by Monte Carlo information. (a) χ^2 of primary vertex (b) χ^2 of STS tracks and (c) χ^2 of MuCh tracks.

5.3 Feasibility study on LMVM detection at SIS100

This section presents the final results of our feasibility study on LMVM (ω, ϕ, and η) detection through the dimuon channel in Au+Au collisions at 8 A GeV/c beam momentum. The STS reconstructs charged particle tracks using a cellular automaton method [134, 135], the first step towards particle identification. The reconstructed tracks are then extrapolated via detectors downstream of the STS, such as the MuCh, TRD, and TOF. The selection criteria for muon candidate has already been discussed in section 5.2.1.

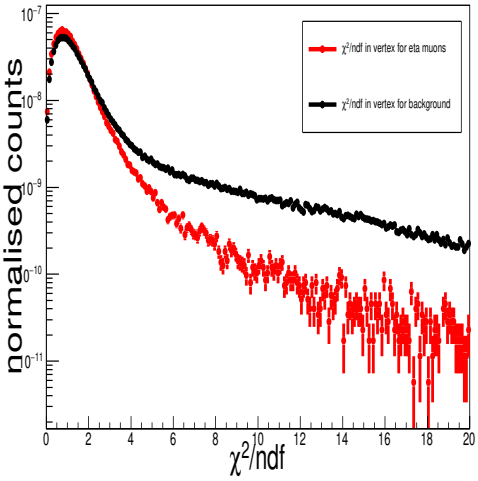

(a)

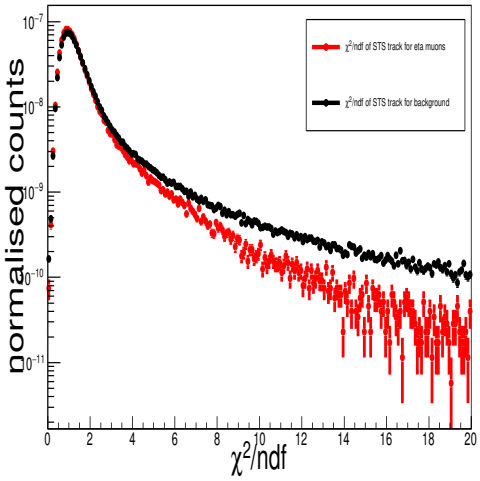

(b)

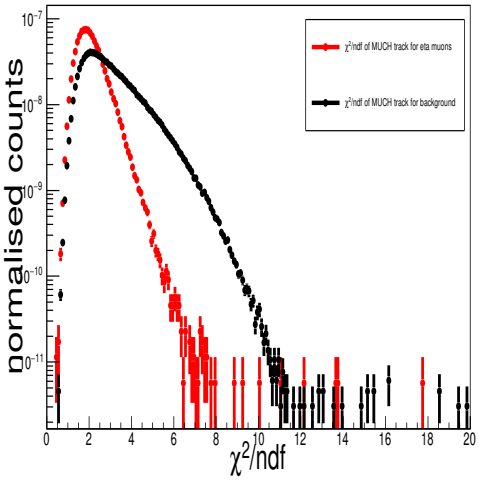

(c)

Figure 5.6: Various track quality parameter distributions obtained for reconstructed muon tracks from η meson decays (red) and reconstructed background tracks (black) for central Au+Au collisions at 8 A GeV/c beam momentum. Signal muons are identified by Monte Carlo information. (a) χ^2 of primary vertex (b) χ^2 of STS tracks and (c) χ^2 of MuCh tracks.

Due to the absorption of low-energy muons, the phase-space acceptance for LMVM (ω, ϕ, and η) is shifted toward forward rapidities. This can be illustrated in Fig. 5.8, 5.9 and 5.10, which displays the simulated input generated by the PLUTO as a function of transverse momentum against rapidity in the left panel to the reconstructed dimuon yield for LMVM's in the right panel. Let's now examine the results in more detail. To understand the effect of finite geometrical acceptance of the CBM Muon setup and the effect of hadron absorbers on signal muons, the rapidity distributions have been plotted for accepted tracks

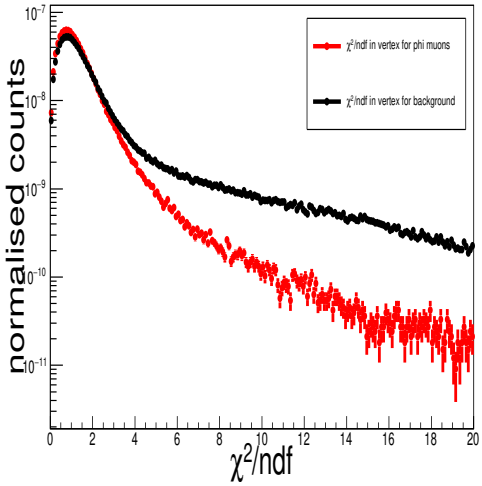

(a)

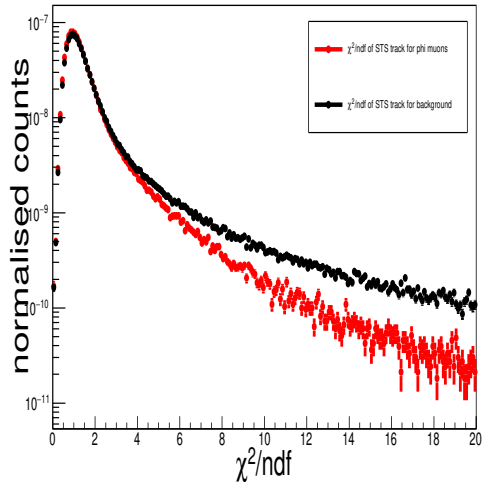

(b)

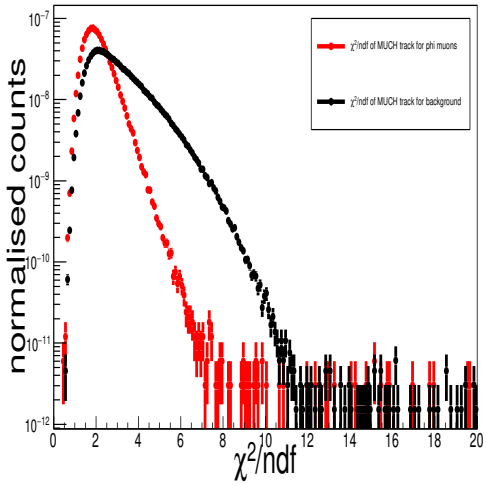

(c)

Figure 5.7: Various track quality parameter distributions obtained for reconstructed muon tracks from ϕ meson decays (red) and reconstructed background tracks (black) for central Au+Au collisions at 8 A GeV/c beam momentum. Signal muons are identified by Monte Carlo information. (a) χ^2 of primary vertex (b) χ^2 of STS tracks and (c) χ^2 of MuCh tracks.

in different sub-systems and reconstructed ω meson in Fig. 5.11. The blue line shows the rapidity distribution of ω generated with PLUTO generator in 4π phase space. This can be clearly visualised in Fig. 5.11, how the peak of the rapidity distribution of ω meson is shifted toward the higher value due to the combined effects of finite geometrical acceptance as well as the absorption of soft muons by the hadron absorbers in muon chamber.

On an event-by-event basis, the signal is extracted from the embedded set of events by selecting oppositely charged muon candidate tracks. The method

χ^2_{Vertex}	χ^2_{STS}	χ^2_{MUCH}	$\omega \to \mu^+\mu^-$			$\eta \to \mu^+\mu^-$			$\phi \to \mu^+\mu^-$		
			ϵ(%)	S/B	σ	ϵ (%)	S/B	σ	ϵ (%)	S/B	σ
2	2	2	0.19	0.47	3.23	0.08	0.02	1.09	0.31	0.03	1.64
2	2	2.5	0.22	0.43	3.37	0.09	0.02	1.11	0.36	0.02	1.69
2	2	3	0.23	0.4	3.37	0.09	0.01	1.14	0.38	0.02	1.73
2	2.5	2	0.22	0.46	3.42	0.09	0.02	1.17	0.36	0.02	1.74
2	2.5	2.5	0.25	0.42	3.56	0.11	0.02	1.25	0.41	0.02	1.79
2	2.5	3	0.26	0.39	3.56	0.12	0.02	1.28	0.44	0.02	1.82
2	3	2	0.23	0.46	3.53	0.1	0.02	1.23	0.39	0.02	1.78
2	3	2.5	0.27	0.42	3.67	0.11	0.02	1.28	0.44	0.02	1.83
2	3	3	0.28	0.39	3.68	0.12	0.02	1.31	0.47	0.02	1.83
2.5	2	2	0.44	0.33	4.3	0.17	0.01	1.37	0.66	0.02	2.02
2.5	2	2.5	0.5	0.31	4.51	0.18	0.01	1.38	0.75	0.02	2.06
2.5	2	3	0.53	0.3	4.56	0.21	0.01	1.4	0.83	0.02	2.17
2.5	2.5	2	0.5	0.32	4.57	0.2	0.01	1.44	0.77	0.02	2.11
2.5	2.5	2.5	0.58	0.3	4.79	0.23	0.01	1.54	0.91	0.02	2.23
2.5	2.5	3	0.61	0.29	4.86	0.27	0.01	1.62	0.98	0.02	2.29
2.5	3	2	0.54	0.32	4.69	0.21	0.01	1.52	0.8	0.02	2.15
2.5	3	2.5	0.62	0.3	4.92	0.25	0.01	1.63	0.94	0.02	2.24
2.5	3	3	0.66	0.28	4.99	0.27	0.01	1.62	1	0.02	2.26
3	2	2	0.58	0.25	4.46	0.25	0.01	1.36	0.97	0.01	2.18
3	2	2.5	0.66	0.24	4.67	0.24	0.01	1.35	1.11	0.01	2.23
3	2	3	0.71	0.23	4.72	0.29	0.01	1.39	1.19	0.01	2.25
3	2.5	2	0.66	0.25	4.7	0.29	0.01	1.42	1.1	0.01	2.28
3	2.5	2.5	0.7	0.23	4.69	0.36	0.01	1.54	1.29	0.01	2.32
3	2.5	3	0.81	0.22	5.01	0.44	0.01	1.65	1.37	0.01	2.34
3	3	2	0.71	0.24	4.83	0.29	0.01	1.46	1.1	0.01	2.25
3	3	2.5	0.81	0.22	4.69	0.4	0.01	1.61	1.31	0.01	2.29
3	3	3	0.87	0.21	5.11	0.48	0.01	1.75	1.47	0.01	2.39

Table 5.1: The effect of various track parameters (χ^2) on LMVM reconstruction efficiency, S/B ratio and significance. For this optimisation, the only tracks that have been accepted have at least 7 STS hits, 11 MuCh hits, 1 TRD hit and 1 TOF hit.

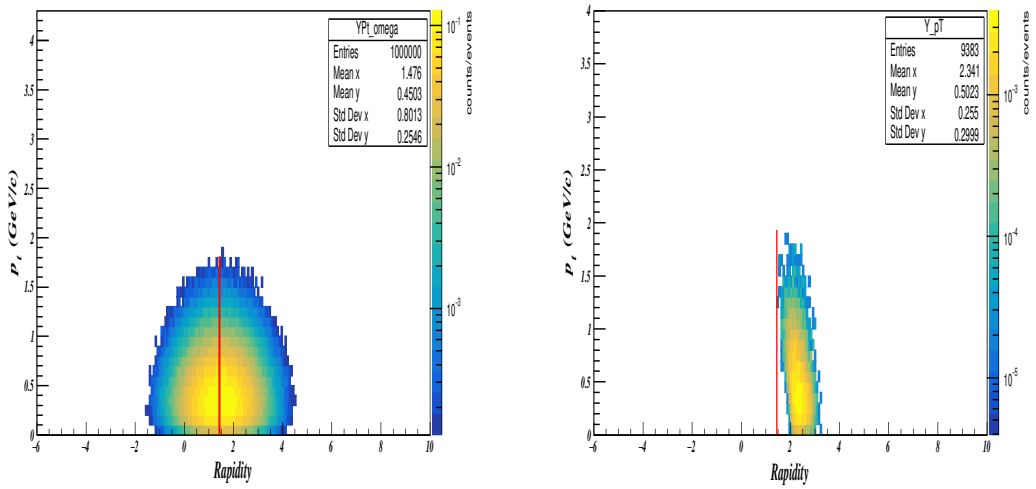

Figure 5.8: Acceptance of ω mesons decaying into muon pairs as a function of transverse momentum and rapidity in central Au+Au collisions at 8 A GeV/c beam momentum. Left Panel: Phase space distribution in 4π generated by the PLUTO code. Right Panel: Reconstructed ω mesons for a muon detection system (using MC information).

used to estimate the combinatorial background is the so-called Super Event (SE) technique. The SE technique is applied to a set of UrQMD (i.e. pure background) generated tracks. In this technique, one positive track from one event

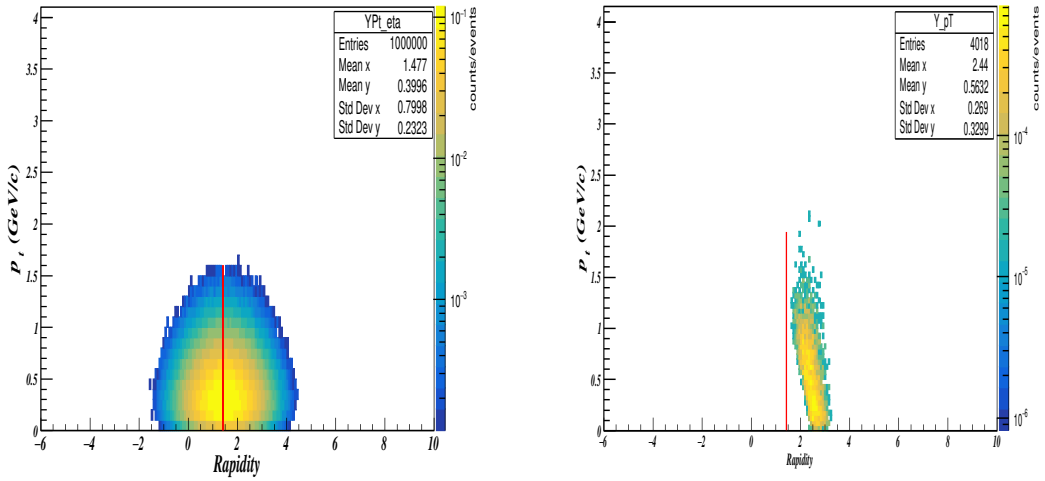

Figure 5.9: Acceptance of η mesons decaying into muon pairs as a function of transverse momentum and rapidity in central Au+Au collisions at 8 A GeV/c beam momentum. Left Panel: Phase space distribution in 4π generated by the PLUTO code. Right Panel: Reconstructed eta mesons for a muon detection system (using MC information).

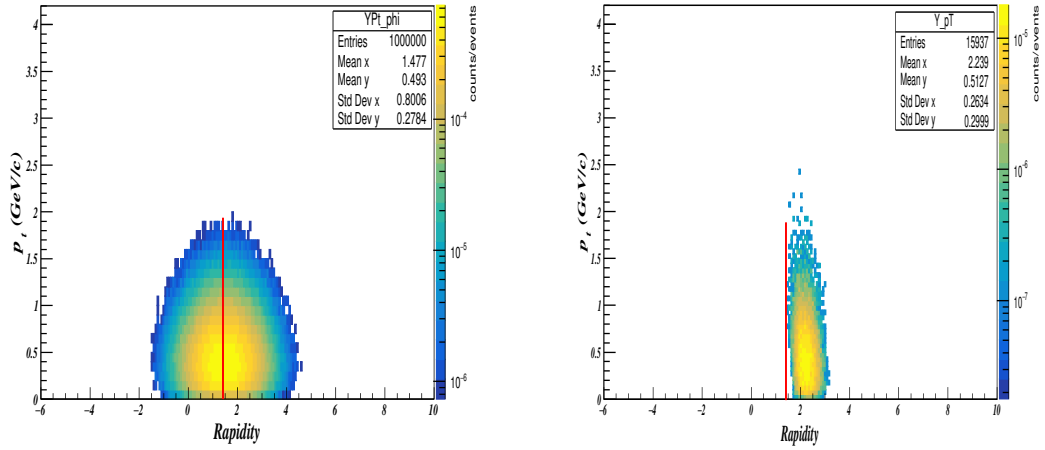

Figure 5.10: Acceptance of ϕ mesons decaying into muon pairs as a function of transverse momentum and rapidity in central Au+Au collisions at 8 A GeV/c beam momentum. Left Panel: Phase space distribution in 4π generated by the PLUTO code. Right Panel: Reconstructed ϕ mesons for a muon detection system (using MC information).

satisfying all selection cuts is combined with all negative tracks from all the events. So the combinatorial background is normalized by the square of the total events, whereas the signal is normalized with the total number of events. The signal is further normalized with Multiplicity × Branching ratio (dimuon channel) for different LMVMs.

The reconstructed invariant mass spectrum of dimuons decaying from LMVM's

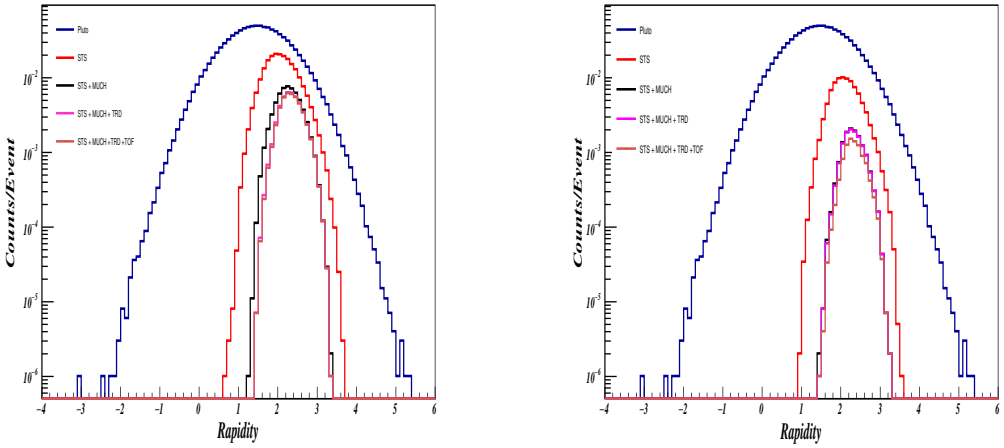

Figure 5.11: Rapidity distribution of accepted Monte-Carlo [Left] and reconstructed [Right] ω meson in different detector sub-systems. The blue line in both figures shows the rapidity distribution of ω generated with the PLUTO generator in 4π phase space. Accepted MC ω meson selection criteria: STS Points ≥ 7; MuCh Points ≥ 11; TRD Points ≥ 1 and TOF Points ≥ 1. Reconstructed ω selection criteria: STS Hits ≥ 7; MuCh Hits ≥ 11; TRD Hits ≥ 1, TOF Hits ≥ 1, $\chi^2_{vertex} < 3.0$, $\chi^2_{STS} < 3.0$ and $\chi^2_{MuCh} < 3.0$.

(ω, ϕ, and η) by applying the optimised selection criteria mentioned in section 5.2.1 can be seen in Figs. 5.12, 5.13 and 5.14.

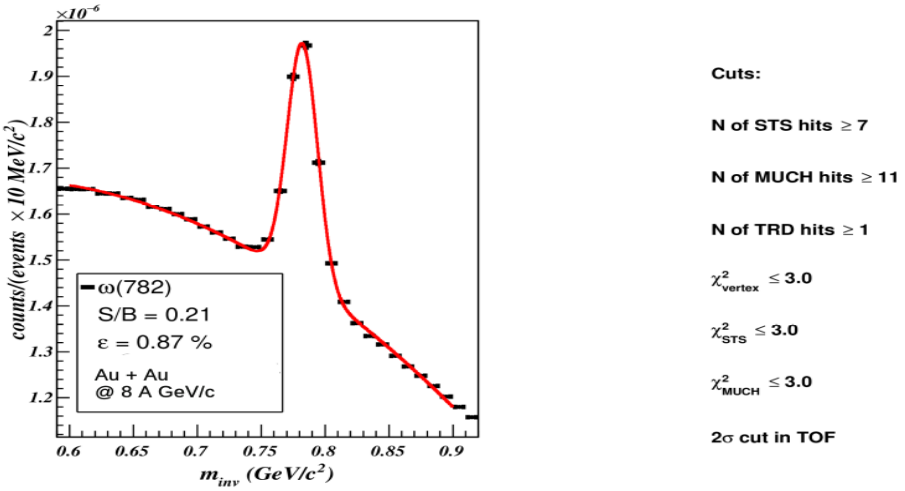

Figure 5.12: Dimuon invariant mass distribution from the decays of ω meson in central Au+Au collisions at 8 A GeV/c. The yields are weighted based on the branching ratio of the decay and the expected multiplicity per event. The Gaussian and second-order polynomial functions are used to fit the signal peak and combinatorial background, respectively. The error bars are smaller than the size of the markers.

The signal peak is fitted by a Gaussian function, and the background can be well described by a second-order polynomial function. The efficiency and

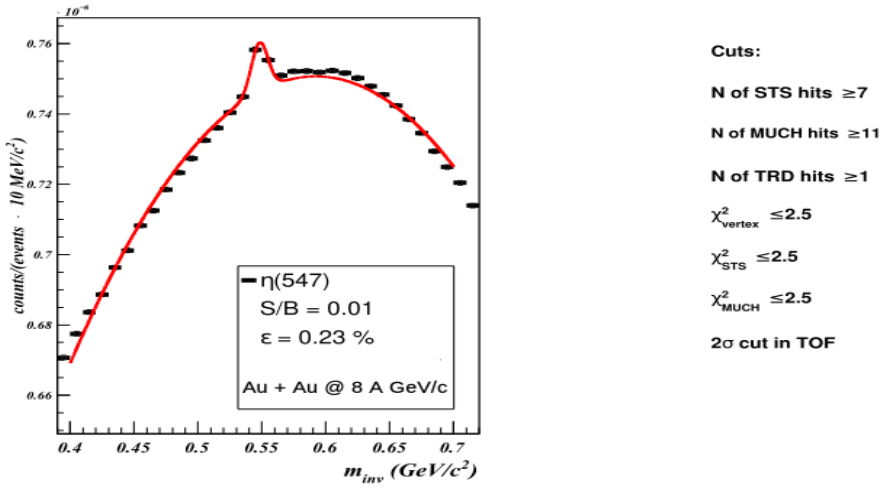

Figure 5.13: Dimuon invariant mass distribution from the decays of η meson in central Au+Au collisions at 8 A GeV/c. The yields are weighted based on the branching ratio of the decay and the expected multiplicity per event. The Gaussian and second-order polynomial functions are used to fit the signal peak and combinatorial background, respectively. The error bars are smaller than the size of the markers.

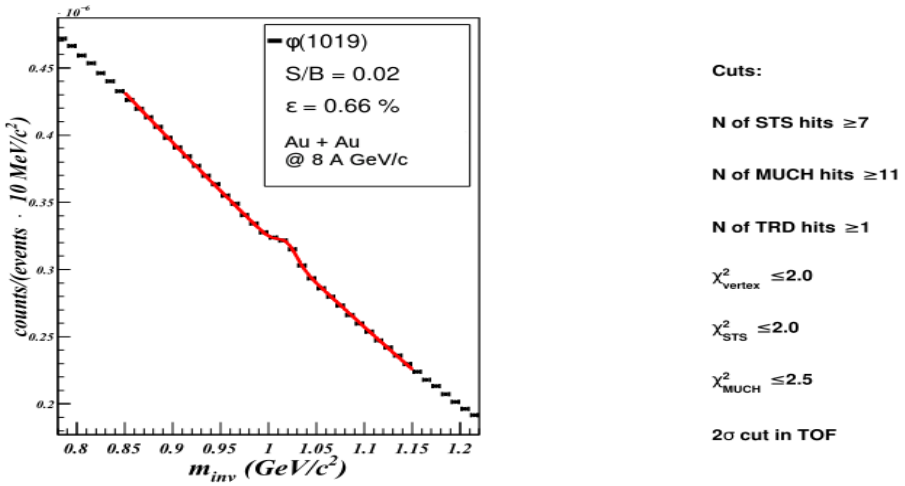

Figure 5.14: Dimuon invariant mass distribution from the decays of ϕ meson in central Au+Au collisions at 8 A GeV/c beam moemntum. The yields are weighted based on the branching ratio of the decay and the expected multiplicity per event. The Gaussian and second-order polynomial functions are used to fit the signal peak and combinatorial background, respectively. The error bars are smaller than the size of the markers.

the signal-to-background ratio are calculated within a $\pm 2\sigma$ mass range around the signal peak and presented in the right panel of each figure. The reconstructed invariant mass spectra for ω mesons in central Au+Au collisions at 8 A

GeV/c beam momentum with different p_T-ranges (y-inclusive) are also investigated and illustrated in Fig. 5.15. The reconstruction efficiencies and signal-to-background ratios are listed in the panel of the same figure. As a function of the mean value of different p_T bins (y-inclusive), the variation of the ω reconstruction efficiency and the signal-to-background ratio is shown in Fig. 5.16. Due to the nature of the input distribution of the muons originating from the decay of ω (see Fig. 5.8) and the effect of detector acceptance, the reconstruction efficiency at the higher p_T region is reduced.

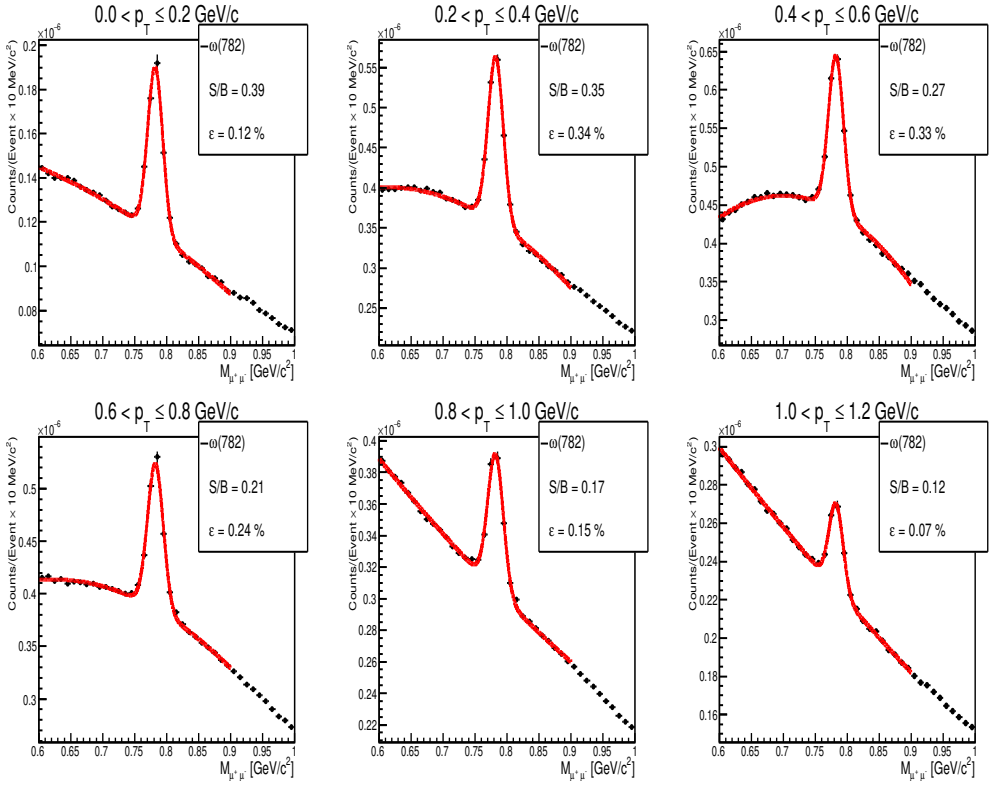

Figure 5.15: Dimuon invariant mass distribution from the decays of ω meson in central Au+Au collisions at 8 A GeV/c beam momentum in different p_T range (y-inclusive). The Gaussian and second-order polynomial functions are used to fit the signal peak and combinatorial background, respectively.

5.4 Efficiency and acceptance correction of the spectra

In particle physics, the motive for efficiency and acceptance correction is straightforward: One aims to exclude the detector's effects to access a quantity that is directly comparable to alternative generators and simulations, various theory predictions, or even results produced by other experiments. Acceptance and

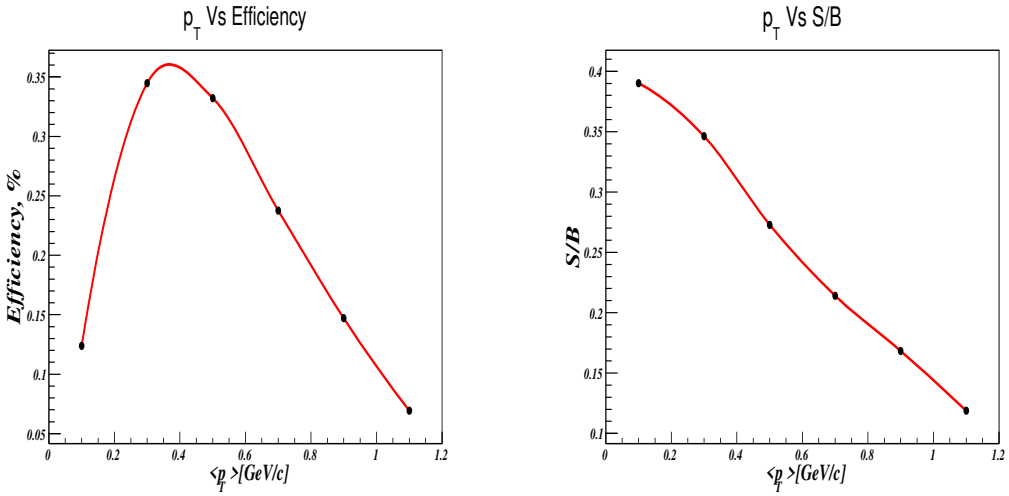

Figure 5.16: Variation of reconstruction efficiency [Left] and signal-to-background ratio [Right] for ω meson in central Au+Au collisions at 8 A GeV/c beam momentum as function of mean value of p_T (y-inclusive)

efficiency corrections would generally be performed using a three-dimensional correction matrix that considers transverse momentum, rapidity, and invariant mass of the muon pairs. This is extremely difficult to do in a simulation due to statistical constraints. As a result, the correction is only performed as a function of transverse momentum (p_T) and beam rapidity (y).

The efficiency and acceptance correction matrices are extracted from a signal MC sample and defined as follows:

$$Acceptance\,Matrix = N^{Acc}/N^{MC(4\pi)}$$
$$Efficiency\,Matrix = N^{Reco}/N^{MC(4\pi)}$$

where N^{Acc} is the bin content of detector acceptance, N^{Reco} that at reconstruction-level and $N^{MC(4\pi)}$ the bin content of the input signal (PLUTO 4π).

To perform this correction, first, a three-dimensional histogram is constructed with the reconstructed invariant mass distributions for different Y-p_T bins. The ω meson yield is then retrieved for each Y-p_T bin using the full fit method after the projection of the ω mass region's histogram is taken for different Y-p_T bins. Using the Monte-Carlo information from the entire phase space input signal distribution and taking into account the acceptance criteria as follows; no of STS point ($\geq$7), MuCh point ($\geq$11), TRD point ($\geq$1), and TOF point ($\geq$1), the information on the number of pairs accepted in different Y-p_T bins is retrieved. The acceptance matrix can be calculated by dividing the accepted yield by the

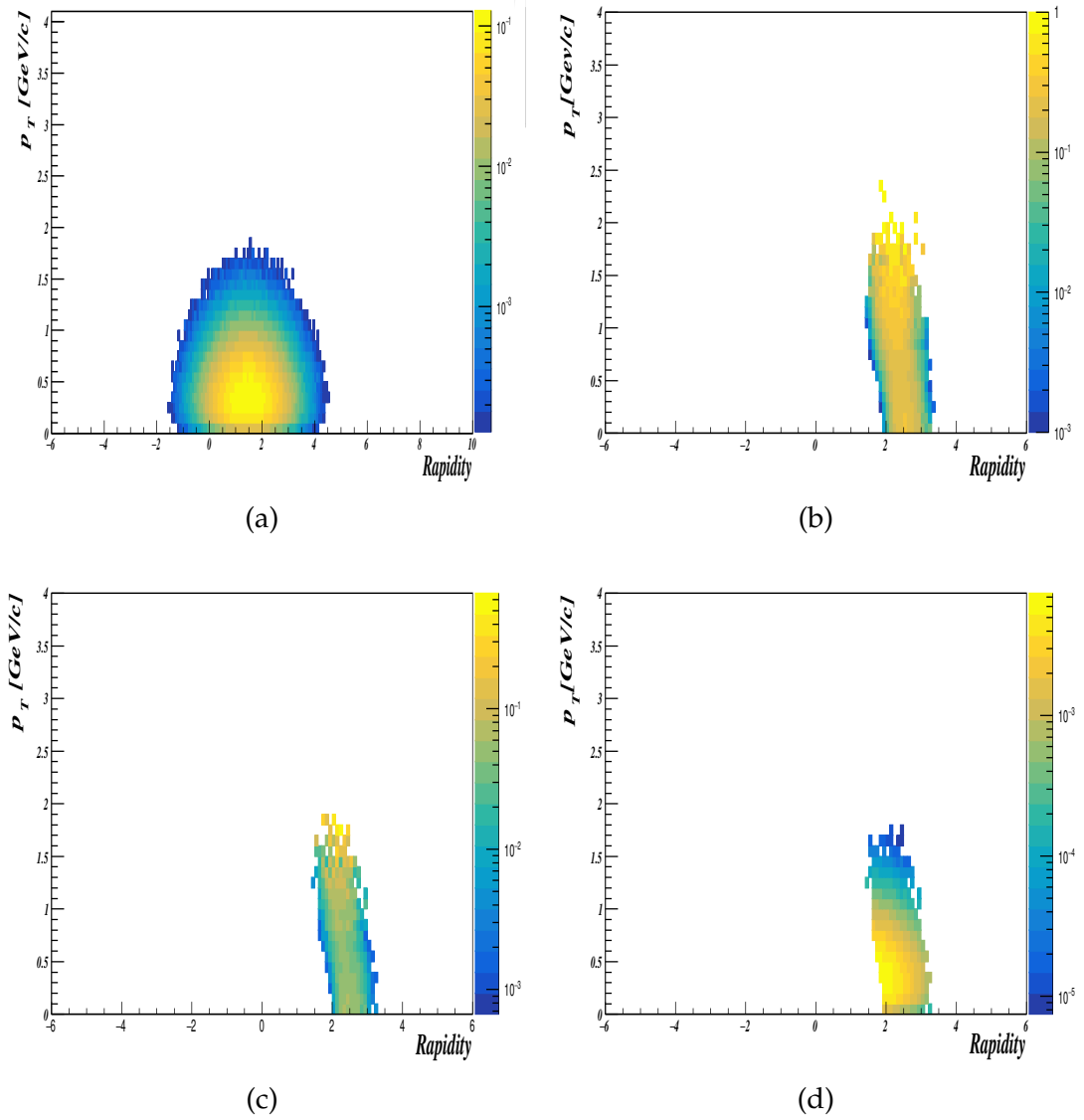

Figure 5.17: Phase space distribution for ω meson in central Au+Au collisions at 8 A GeV/c beam momentum. (a) Phase space distribution in 4π generated by the PLUTO code. (b) Acceptance correction matrix. (c) Efficiency correction matrix. (d) Corrected phase space spectra.

input ω yield in 4π produced by the PLUTO generator. The acceptance matrix can be seen in the middle panel of Fig. 5.17. Then the efficiency matrix demonstrated in the right panel of Fig 5.17 can be calculated by dividing the reconstructed muon pair yield by the accepted matrix. The selection criteria for reconstructed muon pairs follows as same as mentioned in the previous section 5.2.1. Ultimately, the reconstructed spectra can be corrected using the efficiency matrix.

5.5 Summary

The muon detection system of the CBM experiment at FAIR is important to the execution of the proposed research programme, particularly for exploring the QCD phase diagram at high baryon chemical potential. The invariant mass distribution of lepton pairs indicates in-medium modifications of ρ mesons, which might indicate symmetry restoration and the temperature of the fireball, making it possible to search for the caloric curve of QCD matter. According to recent lattice QCD calculations, if it exists, the critical endpoint of a first-order phase transition will be located at temperatures below 130 MeV. The CBM experiment provides a unique opportunity to discover or dispute the existence of the critical endpoint of a first-order phase transition. This chapter examines MC-based feasibility analysis of the dimuon detection resulting from the decay of LMVMs using a muon chamber detector. The reconstruction of dimuon decaying from LMVM's (ω, ϕ, and η) are carried out for central Au+Au collisions at 8 A GeV/c beam momentum. The detailed simulation using a realistic muon chamber detector setup achieves the LMVMs measurements via the dimuon channel in FAIR energy collisions.

In conclusion, the dimuon measurements with the CBM experiment at FAIR provide an extremely promising and unique research programme with a high potential for discovery concerning the fundamental properties of QCD matter under extreme condition.

Chapter 6

Fluctuations from intermittency analysis in relativistic heavy-ion collisions

One of the primary aspects of high-energy Nucleus-Nucleus (NN) and Hadron-Hadron (HH) collisions is to understand the particle production mechanism. The fluctuation in particle number densities over the pseudorapidity space is a feature of primary charged particles produced in any collision. Such fluctuation is substantially more significant than the statistical fluctuations caused by the finite number of particles in a collision. Such fluctuations might be interesting to study for mainly two reasons. First, because enormous fluctuations are expected during the transition from quark-gluon plasma to the hadron phase, [166, 167], a study of such fluctuations is critical for determining the events that resulted in the plasma formation. Second, based on QCD calculations, one would expect many mini-jets to form due to semi-hard Parton-Parton collisions or gluon bremsstrahlung [168–170].

By incorporating well-known results obtained in the studies of cascading phenomena and turbulent behaviour, Bialas and Peschanski [168] introduced a new approach to analyzing distributions in large multiplicity events. In particular, they suggested investigating the factorial moments of the rapidity distribution of particles in an event as a function of resolution, i.e., the size of the rapidity interval employed to construct the distribution. Unlike normal moments, which correspond to averaging the number of particles raised to some power over all rapidity intervals, adopting factorial factors allows one to reduce statistical bias due to the finite particle yield. This measure presents possibly interesting dynamical phenomena such as the emergence of new scales or the occurrence of an “intermittent" background, i.e., cascading fluctuations at various scales. The advantage of this measure over others, such as rapidity correlations, is based on the easy method in which the complicated patterns of fluctuations

are represented in few numbers, despite the number of scales involved in the process.

6.1 Scaled Factorial Moments (SFM)

Scaled factorial moments are classified into two approaches for investigating non-statistical fluctuations. These approaches are based on the normalizing processes and how to average over events and different regions of phase space. Horizontal averaging is one approach that calculates the moments for each event and then average them. A second approach, vertical averaging, calculates the moments for a particular pseudorapidity bin in all events and average them over all bins.

Assume that the single-particle distribution in a variable (i.e. pseudorapidity, azimuthal angle, etc.) x is measured. If the entire interval of variable x, i.e., Δx is divided into M equal bins. Then the size of each interval will be;

$$\delta x = \Delta x / M \tag{6.1}$$

The factorial moment (f_q) of q^{th} order can be calculated for ith bin as [168, 170];

$$f_q = n_i(n_i - 1) \ . \ . \ . \ . \ (n_i - q + 1). \tag{6.2}$$

where n_i, is the total number of charged particles in ith bin of a single event.

The moments are first calculated for each event and then averaged over all events. This is called horizontal averaging [168, 170, 171].

$$\langle F_q \rangle_H = \frac{1}{N_{ev}} \sum_{j=1}^{N_{ev}} M^{q-1} \sum_{i=1}^{M} \frac{n_{i,j}(n_{i,j} - 1)...(n_{i,j} - q + 1)}{\langle N \rangle^q} \tag{6.3}$$

where N_{ev}, is the total number of events in the data sample, $n_{i,j}$ is the number of particles of i^{th} bin in j^{th} event, and $\langle N \rangle$ is the average number of a charged particle in entire phase space limit.

On the other hand, in vertical averaging [168, 171], the moments for the i^{th} bin in all the events is first calculated and then averaged over all bins.

$$\langle F_q \rangle_V = \frac{1}{M} \sum_{i=1}^{M} \frac{1}{N_{ev}} \sum_{j=1}^{N_{ev}} \frac{n_{i,j}(n_{i,j} - 1)...(n_{i,j} - q + 1)}{\langle n_i \rangle^q} \tag{6.4}$$

where,

$$\langle n_i \rangle = \frac{1}{N_{ev}} \sum_{j=1}^{N_{ev}} n_{i,j} \tag{6.5}$$

It is important to note that the horizontal averaging method is limited by its dependence on the shape of single-particle density distribution and the variables employed in the study. To avoid these dependencies, Bialas and Gazdzicki proposed that intermittency can be studied in terms of a new cumulative variable χ(x) defined as a constant single-particle density as [172, 173];

$$\chi(x) = \frac{\int_{x_{min}}^{x} \rho(x)\, dx}{\int_{x_{min}}^{x_{max}} \rho(x)\, dx} \tag{6.6}$$

The single-particle distribution in the variable χ(x) would be uniform from 0 to 1.

Any intermittent pattern can be verified by looking for a power-law relationship between these moments and the bin size (δx) or number of bins (M) i.e.

$$\langle F_q \rangle \propto M^{\alpha_q} \tag{6.7}$$

As a result, we anticipate a linear relationship between $\ln\langle F_q \rangle$ and $\ln M$.

The slope α_q, independent of the form of the single-particle density, is called the intermittency index. It is related to the anomalous fractal dimensions d_q by the relation [174, 175]

$$d_q = \frac{\alpha_q}{(q-1)} \tag{6.8}$$

Anomalous fractal dimensions, d_q, are said to be sensitive to phase transition's nature [176]. It could be an indication of a second-order phase transition [177–179], if the final hadron system exhibits intermittency with d_q, independent of the order of the moments, q. On the other hand, if the final hadron system is created via cascading process, one would anticipate d_q to be roughly linear in q.

6.1.1 UrQMD Model

The UrQMD model (Ultra-relativistic Quantum Molecular Dynamics) is a microscopic many-body model which extensively used to simulate p-p, p-nucleus, and nucleus-nucleus collisions at relativistic energies. The model is based on the covariant propagation of all hadrons with stochastic binary scattering, color string formation, and resonance decay [17], and it offers phase space descriptions of various reaction mechanisms. As independent degrees of freedom, the model comprises 55 baryonic and 40 mesonic states with masses up to 2.25

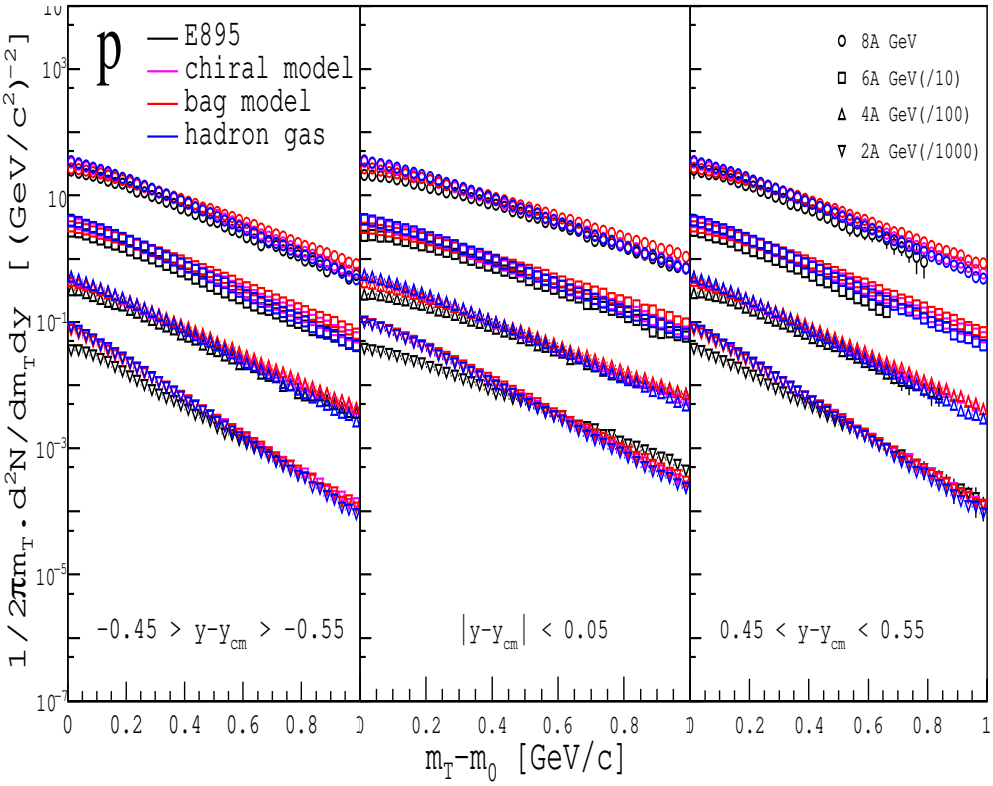

Figure 6.1: Invariant yield of protons at different rapidity regions as a function of m_T-m_0 in Au+Au collision at different energies. 8 A GeV is shown unscaled while other energies 6, 4 and 2 A GeV are scaled down by successive factors of 10. Experimental data for protons are taken from E895 [180, 181] and compared with different UrQMD hydrodynamic models.

GeV/c^2, as well as corresponding antiparticles and explicit isospin, projected states. UrQMD-hybrid is a microscopic plus macroscopic (micro + macro) technique that integrates transport and hydrodynamical descriptions of heavy-ion collisions for a more consistent representation of such events from the initial collision state to the final decoupling of hadrons. Different underlying EoS options are available for the intermediate hydrodynamic phase in UrQMD's hybrid model.

The Equation of State (EoS) has a significant impact on the dynamics of an expanding system since it is used as an input for hydro-dynamical calculations. In the present work, we opt for three different Equations of State (EoS) to investigate the non-statistical fluctuation using Scaled Factorial Moments (SFM) technique. The `Hadron Gas (HG)` [182] is the first EoS, and it depicts a non-interacting gas of free hadrons. It includes all reliably known hadrons with masses up to 2.25 GeV/c^2, which corresponds to the UrQMD model's active

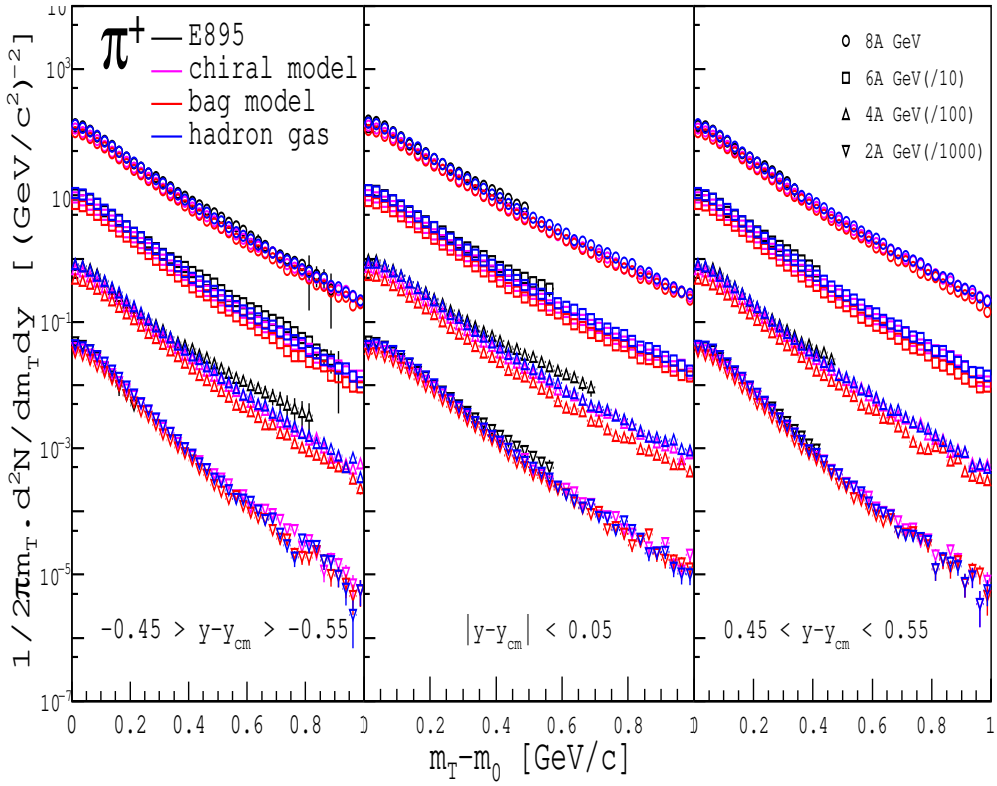

Figure 6.2: Invariant yield of π^+ mesons at different rapidity regions as a function of m_T-m_0 in Au+Au collision at different energies. 8 A GeV is shown unscaled, while other energies 6, 4 and 2 A GeV are scaled down by successive factors of 10. Experimental data for π^+ taken from E895 [180, 181] and compared with different UrQMD hydrodynamic models.

degrees of freedom. It's worth noting that this EoS does not contain any phase transition. It allows us to compare the hydrodynamic scenario to the transport simulation directly. The second EoS, `Chiral+HG (CH)` [183], is derived from a chiral hadronic SU(3) Lagrangian and contains the complete set of baryons from the lowest flavor-SU(3) octet. It also includes multiple scalars, pseudoscalar, vector, and axial-vector mesons. It contains both chiral and deconfinement phase transitions. The third EoS named `Bag Model (BM)` [184] assumes a version of the $(\sigma - \omega)$ model for the hadronic phase and a non-interacting gas of massless u and d quarks and gluons confined by a bag pressure for the QGP phase. The Bag Model EoS exhibits a strong first-order phase transition for all baryonic chemical potentials (μ_B).

The nonstatistical fluctuation using the scaled factorial moments technique in pseudorapidity (η), azimuthal (ϕ), and pseudorapidity-azimuthal ($\eta - \phi$) distribution of primary charged particles for Au+Au collision at 2, 4, 6, 8, 10, and 12

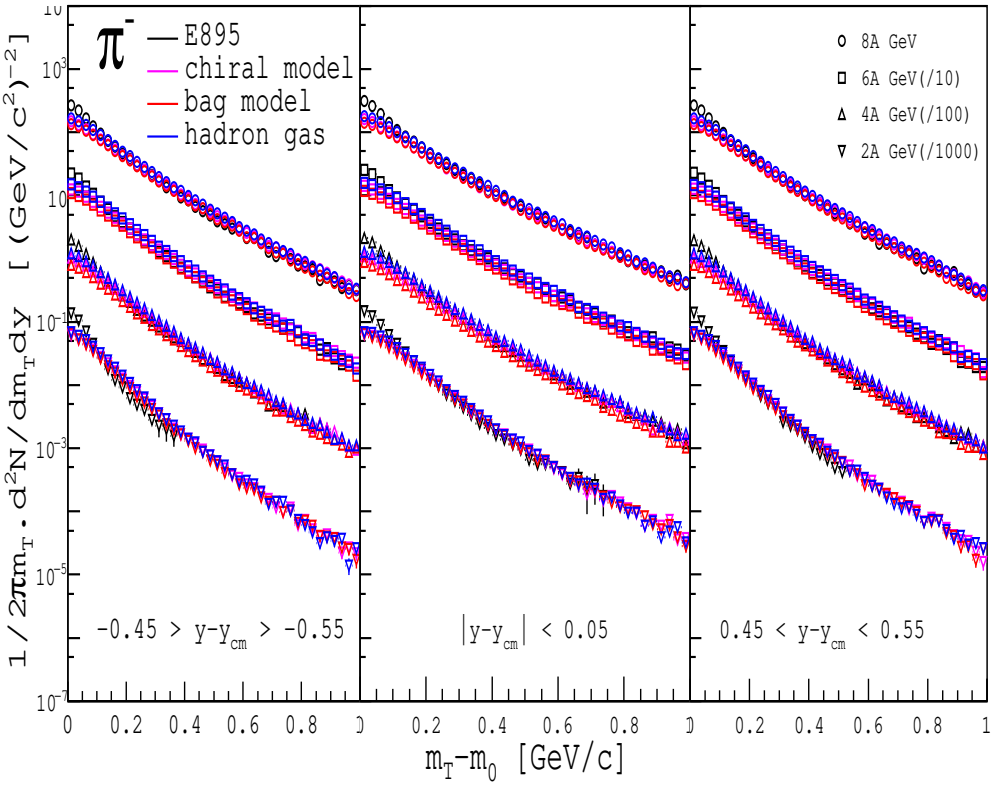

Figure 6.3: Invariant yield of π^- mesons at different rapidity regions as a function of m_T-m_0 in Au+Au collision at different energies. 8 A GeV is shown unscaled while other energies 6, 4 and 2 A GeV are scaled down by successive factors of 10. Experimental data for π^- taken from E895 [180, 181] and compared with different UrQMD hydrodynamic models.

A GeV energies have been discussed in this chapter. The impact parameter, b, is set to 0-3 fm, corresponding to the existing experimental results representing (0-5 %) central events [185]. As mentioned in the previous section, hydrodynamic simulations are performed for three equations of state. Figs. 6.1, 6.2 and 6.3 show invariant yield at different rapidity regions as a function of m_T-m_0 in Au+Au collision at different energies. The comparison with E895 experimental data [180, 181] reveals that almost all the hydrodynamic models do not entirely describe the proton spectrum at 2 A GeV in all rapidity regions. Whereas at 4 A, 6 A, and 8 A GeV, proton spectra are well reproduced by hydrodynamic EoS models. Within errors, the pions ($\pi^+/\pi-$) spectra for the entire pseudorapidity range match well with all the hydrodynamic EoS models for all energies. Based on these results, we hope that adopting the scaled factorial moment techniques to further analyze hydrodynamic model data might be informative. In addition, we look at the beam energy (E_{lab}) dependence by extending the beam energy up

to 12 A GeV.

By transforming the pseudorapidity (η) and phi (ϕ) distributions to new cumulative variables using Eq. 6.6, the intermittency parameters are no longer dependent on the shape of the single-particle distribution. The single-particle distribution in the variable $\chi(\eta)$ and $\chi(\phi)$ would be uniform from 0 to 1. Therefore, its value for a particular particle is determined only by the form of the single-particle spectrum, not by choice of the original variable (η or ϕ). In the present chapter, we have studied the fluctuation in one-dimensional ($\chi(\eta)$ and $\chi(\phi)$) as well as two-dimensional spaces ($\chi(\eta - \phi)$).

6.1.2 Fluctuation in one-dimensional space

Using the horizontal averaging method in one-dimensional space, the averaged scaled factorial moments have been estimated for different orders, q = 2-6 in Au+Au collisions at 2, 4, 6, 8, 10, and 12 A GeV energies. The comparison between different hydrodynamic models is also carried out. Here the entire η window ($\Delta\eta \leq \pm 5$) is selected for the present investigation. We have plotted $\langle F_q \rangle$ against the number of phase space bins M in log-log scale for the Chiral+HG (default mode) hydrodynamic model at 8 A GeV in Fig. 6.4. A uniform random number (RAN) generator with values between 0 and 1 is being used to construct an equal number of events, and the $\ln\langle F_q \rangle$ against $\ln(M)$ is depicted in the same Fig. 6.4. The linear dependence of $\ln\langle F_q \rangle$ on $\ln(M)$ in hydrodynamic models shows that the SFMs follow the power-law scaling behaviour indicated in Eq. 6.7. This confirms Bialas and Peschanski's [168] prediction of an intermittent pattern in nonstatistical multiparticle production. Whereas the random number generated data has no substantial rise, revealing no dynamical fluctuation in the emission spectra of primary particles in $\chi(\eta)$ space. The solid lines reflect the straight-line fit to data points, and the errors depicted in these plots are simply statistical.

Depending on the nature of the emission spectra, the intermittent pattern in the particle's emission source in high-energy nuclear collisions may differ in distinct phase spaces. The same study is carried out in 1-d azimuthal ($\chi(\phi)$) space to understand the (a)symmetric nature of the intermittent pattern in Au+Au collisions at FAIR energies.

The averaged SFM $\ln\langle F_q \rangle$ for Au+Au collision at FAIR energies are plotted against $\ln(M)$ in $\chi(\phi)$ space. A clear rise in $\ln\langle F_q \rangle$ with phase space bins is observed. The intermittency index (α_q) for different energies and hydrodynamical models are extracted using straight line fit of the $\ln\langle F_q \rangle$ vs $\ln(M)$ plots in both

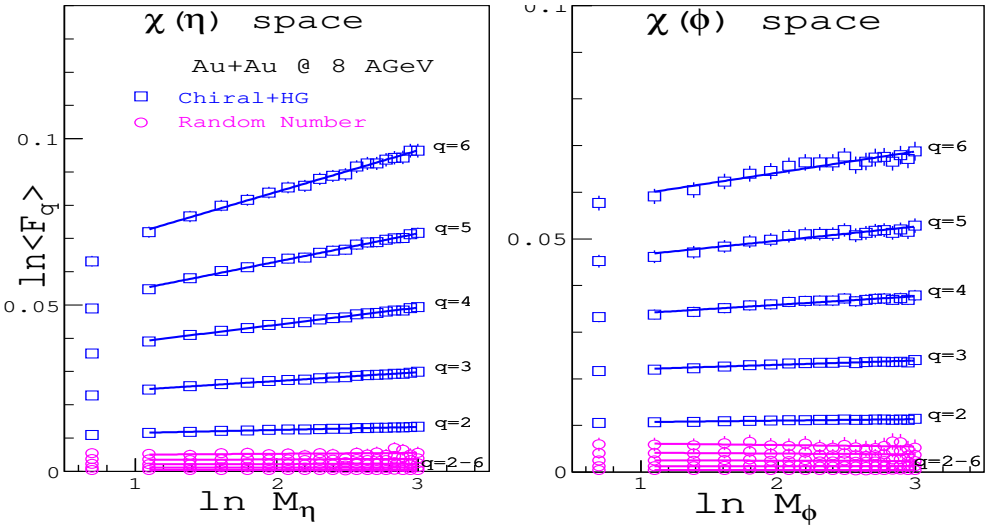

Figure 6.4: $\ln\langle F_q\rangle$ as a function of $\ln M$ for hydrodynamic EoS (Chiral+HG) Au+Au collision at 8 A GeV and randomly generated events in one dimensional $\chi(\eta)$ [left panel] and $\chi(\phi)$ [right panel] spaces. Where q reflects the order of the moment.

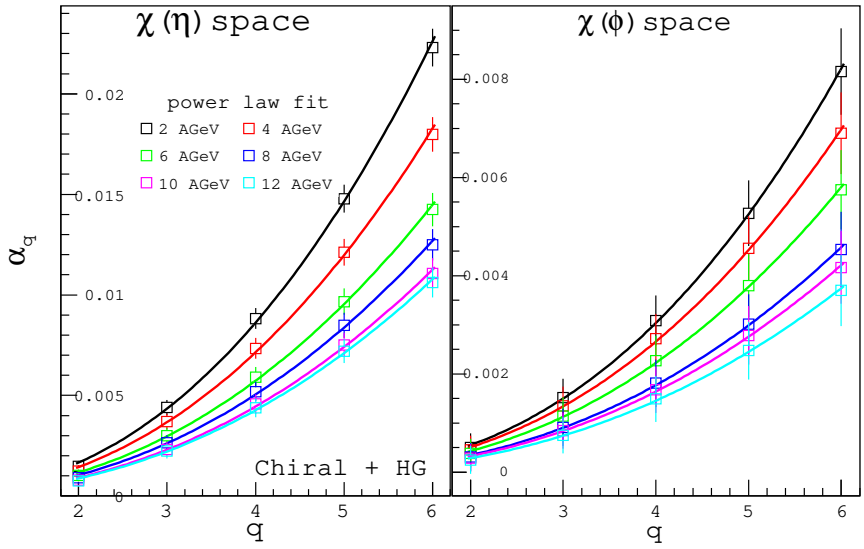

Figure 6.5: The intermittency index, α_q as a function of q (order of moment) for Au+Au collision data generated with Chiral+HG hadronic EoS at different beam energies in one dimensional $\chi(\eta)$ and $\chi(\phi)$ spaces. The solid lines represent the power-law fit function.

$\chi(\eta)$ and $\chi(\phi)$ spaces. The corresponding values are presented in Table 6.1 and displayed in Fig. 6.5.

The intermittency index, α_q, shows an increasing trend with different orders of moments for all energies. It has also been observed from Fig. 6.6, α_q decreases with increasing beam energy for a given q. The entire exercise is performed for each hydrodynamical EoS. The values of the extracted α_q are listed in Table

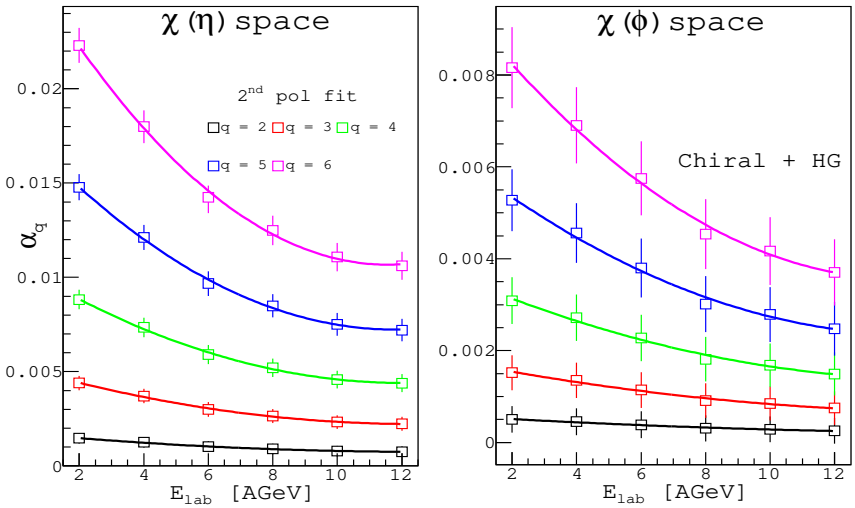

Figure 6.6: The intermittency index, α_q as a function of beam energy, E_{lab} for Au+Au collision data generated with Chiral+HG hadronic EoS with different order of the moment, q in one dimensional $\chi(\eta)$ and $\chi(\phi)$ spaces. The solid lines represent the second-order polynomial fit function.

6.1. It has been observed from Table 6.1 that the emission of particles is more intermittent in $\chi(\eta)$ space than in $\chi(\phi)$ space.

The variations of α_q against the order of the moment, q in $\chi(\eta)$ and $\chi(\phi)$ spaces for UrQMD-hydro events with different EoS are shown in Fig. 6.7. The observed relatively high intermittency in the UrQMD-hydro data set with Hadron Gas EoS than that of Chiral+HG EoS generated data may be connected to cascade particle production in a partonic medium induced by the usage of chiral EoS.

Through the anomalous dimension, d_q computed from Eq. 6.8, the scaling behaviour of factorial moments has been associated with the physics of fractal objects (particle emission sources). Fig. 6.8 shows the variation of d_q with the order of moments, q for Chiral+HG hydrodynamic EoS model in $\chi(\eta)$ and $\chi(\phi)$ spaces at various beam energies. The solid lines in the figures are just there to direct the viewer's gaze. Similar patterns are also observed in Hadron Gas and Bag Model EoSs. A rising pattern of d_q, with q, reflects the self-similar cascade mechanism of particle production in heavy-ion collisions is observed. The rise is observed to be more significant in $\chi(\eta)$ space than in $\chi(\phi)$ space. It is also noticed that with the increase in beam energy, the dimension d_q decreases for each order of the moment. From Fig. 6.9, d_q is observed to be greater in Bag Model EoS than other hydrodynamic EoSs, indicating that particles in UrQMD-hydro data with Bag Model EoS occupy less phase space than others.

Table 6.1: The values of intermittency index, α_q in Au+Au collision data generated with the different hydrodynamic models at different beam energies for the different order of moment in one-dimensional spaces.

Collision Energy	Intermittency index ($\times 10^{-3}$) in $\chi(\eta)$ space					Intermittency index ($\times 10^{-3}$) in $\chi(\phi)$ space				
	α_2	α_3	α_4	α_5	α_6	α_2	α_3	α_4	α_5	α_6
Hadron Gas (HG)										
2 A GeV	1.46 ± 0.2	4.39 ± 0.37	8.74 ± 0.50	14.50 ± 0.67	21.63 ± 0.89	0.28 ± 0.28	0.89 ± 0.38	1.85 ± 0.50	3.24 ± 0.65	5.10 ± 0.85
4 A GeV	1.17 ± 0.27	3.47 ± 0.35	6.83 ± 0.46	11.18 ± 0.60	16.43 ± 0.77	0.16 ± 0.27	0.51 ± 0.36	1.07 ± 0.46	1.85 ± 0.59	2.85 ± 0.75
6 A GeV	0.97 ± 0.28	2.87 ± 0.37	5.64 ± 0.48	9.23 ± 0.61	13.59 ± 0.77	0.16 ± 0.28	0.50 ± 0.37	1.01 ± 0.47	1.70 ± 0.60	2.59 ± 0.75
8 A GeV	0.85 ± 0.28	2.52 ± 0.37	4.95 ± 0.48	8.10 ± 0.61	11.95 ± 0.76	0.22 ± 0.28	0.65 ± 0.37	1.27 ± 0.48	2.09 ± 0.60	3.13 ± 0.74
10 A GeV	0.76 ± 0.28	2.23 ± 0.37	4.39 ± 0.48	7.18 ± 0.60	10.55 ± 0.75	0.20 ± 0.28	0.61 ± 0.37	1.22 ± 0.47	2.03 ± 0.59	3.04 ± 0.73
12 A GeV	0.75 ± 0.28	2.21 ± 0.37	4.32 ± 0.48	7.05 ± 0.60	10.34 ± 0.75	0.19 ± 0.28	0.58 ± 0.37	1.18 ± 0.47	2.00 ± 0.59	3.05 ± 0.73
Chiral + HG (CH)										
2 A GeV	1.465 ± 0.286	4.397 ± 0.385	8.823 ± 0.519	14.781 ± 0.696	22.302 ± 0.931	0.50 ± 0.29	1.52 ± 0.38	3.09 ± 0.51	5.27 ± 0.67	8.16 ± 0.88
4 A GeV	1.247 ± 0.291	3.706 ± 0.388	7.342 ± 0.511	12.118 ± 0.666	17.988 ± 0.862	0.45 ± 0.29	1.35 ± 0.39	2.72 ± 0.51	4.56 ± 0.65	6.91 ± 0.83
6 A GeV	1.015 ± 0.293	2.999 ± 0.39	5.901 ± 0.508	9.668 ± 0.652	14.242 ± 0.828	0.38 ± 0.29	1.14 ± 0.39	2.27 ± 0.51	3.80 ± 0.64	5.75 ± 0.81
8 A GeV	0.897 ± 0.287	2.645 ± 0.377	5.195 ± 0.488	8.493 ± 0.622	12.484 ± 0.782	0.31 ± 0.29	0.91 ± 0.38	1.81 ± 0.49	3.01 ± 0.61	4.54 ± 0.76
10 A GeV	0.784 ± 0.282	2.321 ± 0.369	4.577 ± 0.476	7.51 ± 0.603	11.074 ± 0.754	0.29 ± 0.28	0.85 ± 0.37	1.68 ± 0.47	2.79 ± 0.60	4.17 ± 0.74
12 A GeV	0.753 ± 0.282	2.228 ± 0.368	4.39 ± 0.473	7.2 ± 0.597	10.615 ± 0.744	0.25 ± 0.28	0.75 ± 0.37	1.49 ± 0.47	2.48 ± 0.59	3.70 ± 0.72
Bag Model (BM)										
2 A GeV	2.61 ± 0.30	7.70 ± 0.42	15.35 ± 0.62	25.73 ± 0.90	39.17 ± 1.34	1.03 ± 0.29	3.05 ± 0.39	6.12 ± 0.53	10.30 ± 0.70	15.75 ± 0.94
4 A GeV	1.37 ± 0.29	4.07 ± 0.38	8.05 ± 0.51	13.22 ± 0.67	19.49 ± 0.89	0.81 ± 0.29	2.41 ± 0.38	4.86 ± 0.50	8.21 ± 0.66	12.59 ± 0.85
6 A GeV	1.14 ± 0.29	3.33 ± 0.39	6.49 ± 0.51	10.49 ± 0.67	15.23 ± 0.86	0.72 ± 0.29	2.15 ± 0.39	4.29 ± 0.51	7.15 ± 0.65	10.76 ± 0.83
8 A GeV	1.06 ± 0.30	3.14 ± 0.40	6.19 ± 0.52	10.19 ± 0.68	15.06 ± 0.87	0.58 ± 0.30	1.76 ± 0.40	3.60 ± 0.52	6.12 ± 0.66	9.39 ± 0.83
10 A GeV	1.06 ± 0.30	3.14 ± 0.40	6.19 ± 0.52	10.18 ± 0.68	15.06 ± 0.86	0.50 ± 0.30	1.50 ± 0.40	2.98 ± 0.51	4.94 ± 0.65	7.39 ± 0.81
12 A GeV	1.09 ± 0.30	3.25 ± 0.40	6.46 ± 0.53	10.70 ± 0.68	16.00 ± 0.87	0.50 ± 0.30	1.50 ± 0.40	3.01 ± 0.52	5.03 ± 0.65	7.59 ± 0.81

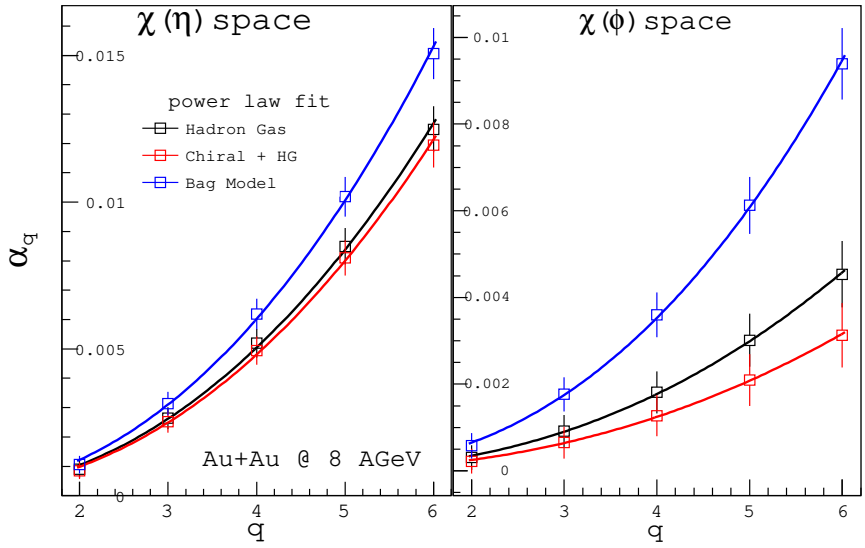

Figure 6.7: The intermittency index, α_q as a function of the order of the moment, q for Au+Au collision data generated with different hydrodynamic equations of state at 8 A GeV in one dimensional $\chi(\eta)$ and $\chi(\phi)$ spaces.

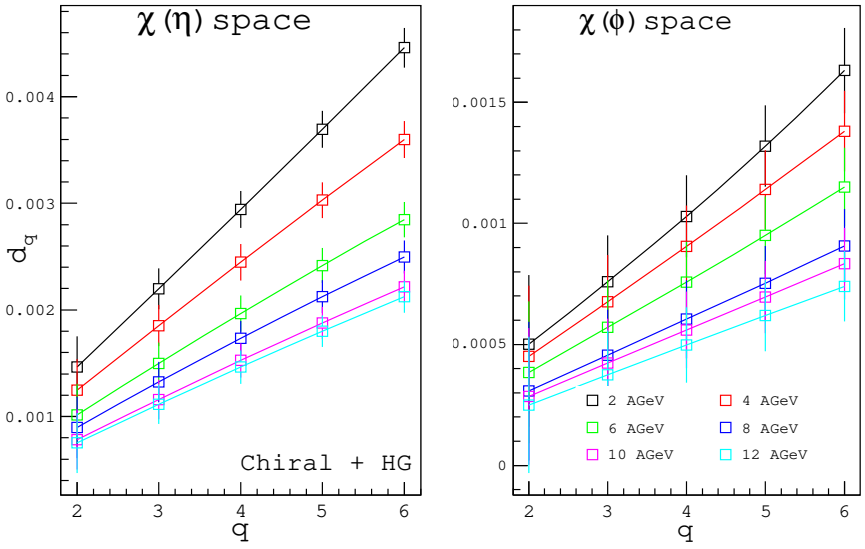

Figure 6.8: The anomalous dimension, d_q as a function of order of moment, q for Au+Au collision data generated with Chiral+HG hydrodynamic EoS at different beam energies in one dimensional $\chi(\eta)$ and $\chi(\phi)$ spaces.

6.1.3 Fluctuation in two-dimensional space

Ochs and Wosiek [169] have already discussed that the increase of factorial moments is driven by clusters of strongly collimated particles, i.e., local fluctuations in rapidity (or pseudorapidity) correspond to local fluctuations in the azimuthal angle (ϕ) around the beam direction. As a result, it is recommended

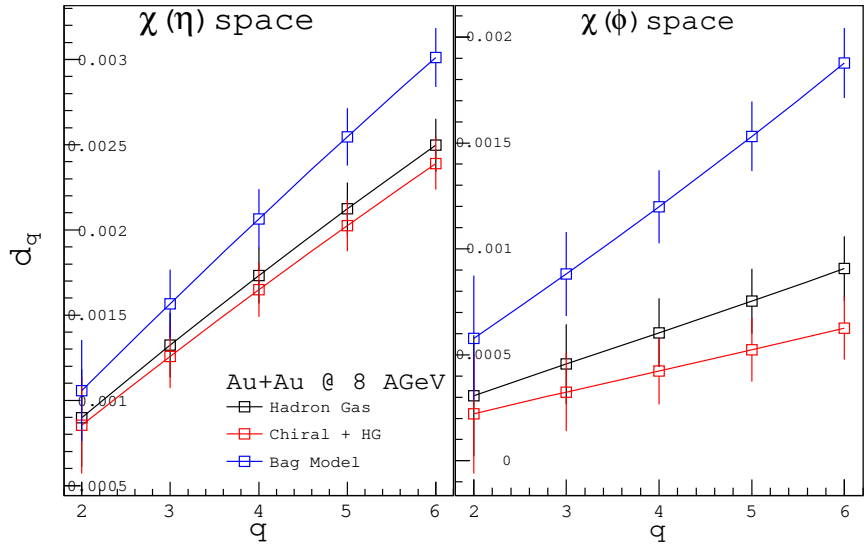

Figure 6.9: The anomalous dimension, d_q as a function of the order of the moment, q for Au+Au collision data generated with different hydrodynamic equations of state at 8 A GeV in one dimensional $\chi(\eta)$ and $\chi(\phi)$ spaces.

that while investigating a two-dimensional $(\eta - \phi)$ space, the rise of moments is much more prominent.

The scaled factorial moments in a two-dimensional space are estimated by only changing the M in Eq. 6.3. M is now number of $\delta\eta\delta\phi$ bins i.e the entire $\chi(\eta - \phi)$ space is successively divided into $M_{\eta_i} \times M_{\phi_i}$ bins.

Fig. 6.10 shows the $\ln\langle F_q \rangle$ as a function of bin size in two-dimensional $\chi(\eta - \phi)$ space for a different order of the moment, q in Au+Au UrQMD-hydro (Chiral + HG) events at 8 A GeV. An equal number of events are generated using Random Event Generator and plotted $\ln\langle F_q \rangle$ against $\ln M_\eta M_\phi$ in the same figure. The random number generated data showed no signs of any dynamical fluctuation in the emission spectra of primary particles; however, the observed intermittency in UrQMD-hydro (Chiral + HG) data might thus be related to the hydrodynamic evolution of the matter formed in collisions or/and the usage of chiral EoS.

The intermittency indices, α_q, are estimated and tabulated in Table 6.2 for all energies as well as various hydrodynamical EoS within the statistical error. Fig. 6.11a depicts the variance of α_q against q for UrQMD-hydro (Chiral+Hg) generated data at different beam energies. The intermittency indices, α_q exhibit a rising trend with distinct order of moment for all energies, as shown in Fig. 6.11a. As one-dimensional space, the strength of intermittency falls as beam energy increases for each value of q in two-dimensional space shown in Fig. 6.12. It is also observed from both Tables 6.1 and 6.2 that the strength of intermittency

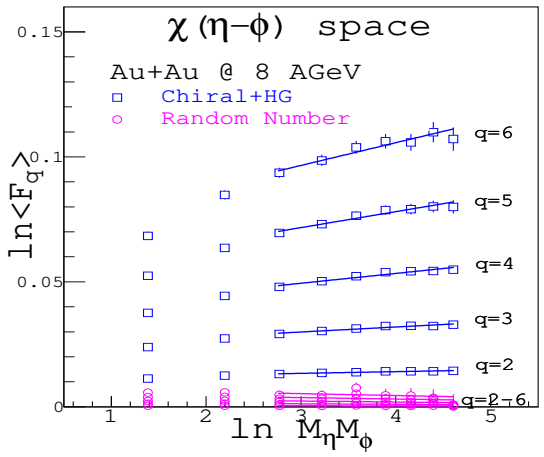

Figure 6.10: $\ln\langle F_q\rangle$ as a function of $\ln M_\eta M_\phi$ for hydrodynamic EoS (Chiral+HG) Au+Au collision at 8 A GeV and randomly generated events in two dimensional $\chi(\eta-\phi)$ space.

Table 6.2: The values of intermittency index, α_q in Au+Au collision using different hydrodynamic models at different beam energies for the different order of moment in two-dimensional ($\chi(\eta-\phi)$ space).

Collision Energy(A GeV)	Intermittency index ($\times 10^{-3}$) α_2	α_3	α_4	α_5	α_6
Hadron Gas (HG)					
2	1.40 ± 0.42	4.03 ± 0.64	8.12 ± 1.04	14.19 ± 1.79	22.87 ± 3.19
4	0.73 ± 0.40	2.34 ± 0.57	4.99 ± 0.86	8.92 ± 1.36	14.85 ± 2.27
6	0.50 ± 0.41	1.41 ± 0.57	2.76 ± 0.81	4.64 ± 1.21	6.96 ± 1.85
8	0.41 ± 0.41	1.23 ± 0.56	2.49 ± 0.79	4.30 ± 1.14	6.77 ± 1.70
10	0.39 ± 0.41	1.21 ± 0.56	2.50 ± 0.77	4.32 ± 1.09	6.78 ± 1.58
12	0.49 ± 0.41	1.40 ± 0.56	2.67 ± 0.76	4.30 ± 1.06	6.31 ± 1.50
Chiral + HG (CH))					
2	1.98 ± 0.43	5.84 ± 0.65	11.53 ± 1.07	19.05 ± 1.85	28.59 ± 3.28
4	1.24 ± 0.43	3.75 ± 0.62	7.54 ± 0.94	12.52 ± 1.50	18.50 ± 2.45
6	1.00 ± 0.43	2.93 ± 0.60	5.77 ± 0.88	9.62 ± 1.33	14.71 ± 2.08
8	0.68 ± 0.42	2.01 ± 0.58	3.94 ± 0.82	6.39 ± 1.19	9.10 ± 1.78
10	0.61 ± 0.41	1.75 ± 0.56	3.31 ± 0.78	5.16 ± 1.12	7.26 ± 1.64
12	0.56 ± 0.41	1.67 ± 0.55	3.32 ± 0.76	5.49 ± 1.07	8.23 ± 1.55
Bag Model (BM)					
2	3.07 ± 0.44	9.36 ± 0.71	19.17 ± 1.25	32.74 ± 2.31	49.67 ± 4.39
4	1.91 ± 0.42	5.73 ± 0.62	11.43 ± 0.98	18.86 ± 1.61	27.57 ± 2.72
6	1.38 ± 0.43	4.23 ± 0.61	8.63 ± 0.92	14.59 ± 1.43	22.28 ± 2.31
8	1.26 ± 0.43	3.70 ± 0.61	7.31 ± 0.88	12.04 ± 1.32	17.75 ± 2.03
10	1.29 ± 0.43	3.85 ± 0.60	7.64 ± 0.86	12.63 ± 1.25	18.77 ± 1.88
12	1.28 ± 0.44	3.90 ± 0.60	7.88 ± 0.85	13.28 ± 1.22	20.22 ± 1.81

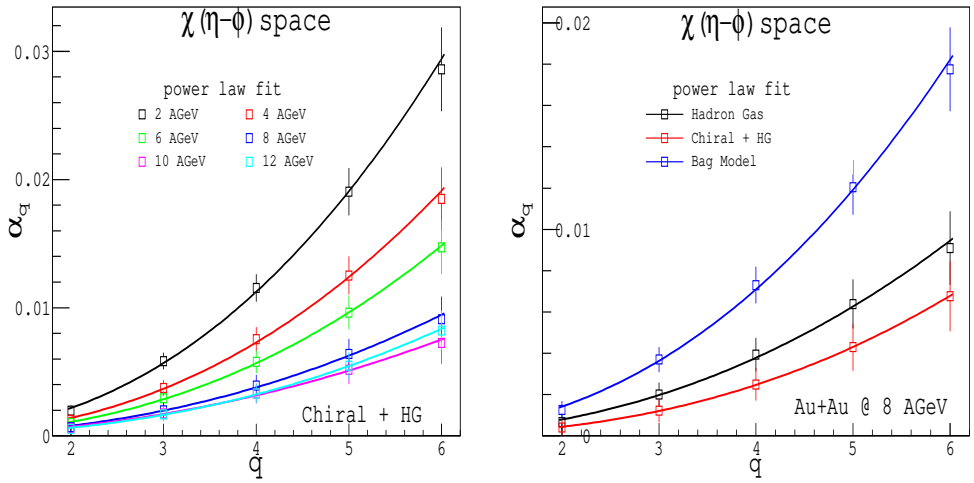

Figure 6.11: The intermittency index, α_q as a function of the order of the moment, q for Au+Au collision data generated in two dimensional $\chi(\eta - \phi)$ space. (a) Chiral+HG hydrodynamic EoS at different beam energies (b) different hydrodynamic equations of state at 8 A GeV.

is found to be strongest in $\chi(\eta - \phi)$ space and weakest in $\chi(\phi)$ space for the various orders of the moment q. The intermittency index, α_q for the different order of the moment, is found to be substantially greater in Bag Model EoS than in other hydrodynamic EoS models shown in Fig. 6.11b.

The variation of d_q with q is illustrated in Fig. 6.13a for UrQMD-hydro produced data with Chiral+HG equation of state at different beam energies is shown and found a gradual rise with the increasing order of the moment, q for all energies. A significant q dependence of d_q suggests particle production via a self-similar cascade process, revealing the particle spectra's multifractal nature. In Fig. 6.13b, d_q is consistently shown to be highest in data with Bag Model EoS than other hadronic EoSs.

6.2 Multifractals

The study of intermittency in scaled factorial moments has already been discussed in the previous section, where only the positive order of the moments are examined. Intermittency is a phenomenon that reveals the self-similar behaviour of multiplicity fluctuations in particle production at high energy. However, in certain circumstances, the dynamical explanation for the origin of intermittency is not unambiguous. The idea of self-similarity is closely linked to

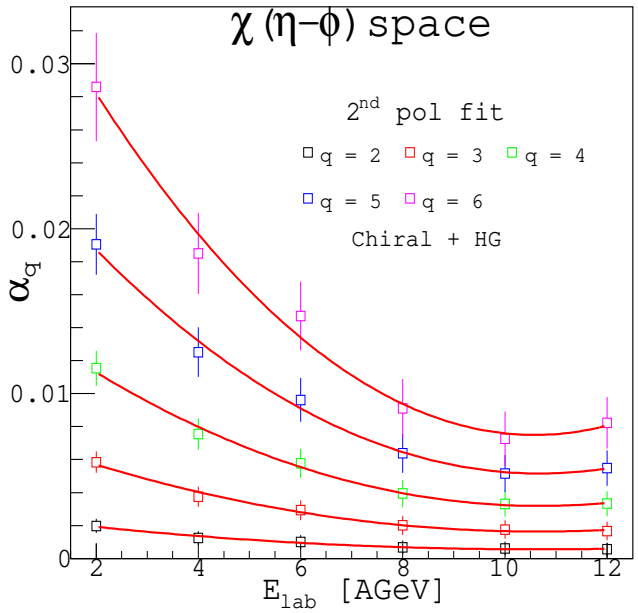

Figure 6.12: The intermittency index, α_q as a function of beam energy, E_{lab} for Au+Au collision data generated with Chiral+HG hydrodynamic EoS with different order of the moment, q in two dimensional $\chi(\eta - \phi)$ space.

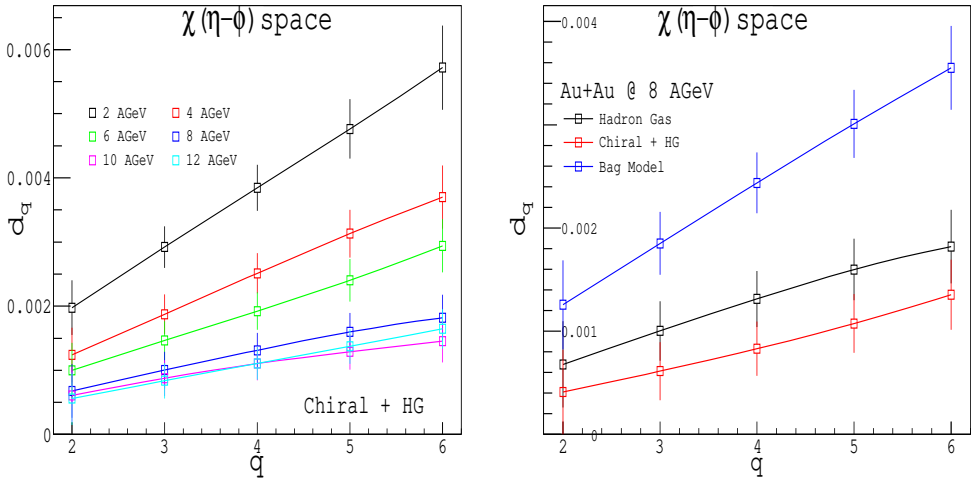

Figure 6.13: The anomalous dimension, d_q as a function of the order of the moment, q for Au+Au collision data generated in two dimensional $\chi(\eta - \phi)$ space. (a) Chiral+HG hydrodynamic EoS at different beam energies (b) different hydrodynamic equations of state at 8 A GeV

fractal theory [186], a natural outcome of the cascading mechanism that prevails in multiparticle production. As a result, the need for multifractal techniques emerged [187]. Inelastic collisions can be considered purely geometrical objects with non-integer dimensions in multifractal analysis. A formalism

for analyzing fractal dimensions was devised [187–191] and effectively used to study intermittent behaviour in turbulent fluids and other chaotic transitions. To examine the cascading process [192] of multiparticle production within the framework of the multifractal technique, R.C. Hwa [175] developed a vertical formalism to explain the chaotic nature of the pseudorapidity distribution of produced particles in nuclear collisions. In this part, the intermittency of ^{16}O-AgBr interactions at 60 A and 200 A GeV, and ^{28}Si-nucleus interactions at 14.5 A GeV/c are investigated independently using multifractal techniques.

To investigate the effect of multifractal moments, G_q, on pseudorapidity, η, a given pseudorapidity range $\Delta\eta$ = η_{max} - η_{min} is segmented into M_0 bins of width $\delta\eta = \Delta\eta/M_0$. Let n_i indicate the number of particles spotted in the i^{th} bin. We define M as the number of non-empty bins, which constitutes a fractal set because some of the bins may be empty. A multifractal moment is described by R.C. Hwa [175] as follows:

$$G_q = \sum_{j=1}^{M} p_j^q \tag{6.9}$$

where, $p_j = n_j/\mathrm{n}$; $n = n_1 + n_2 + \ldots\ldots\ldots + n_M$. q is a real number that can be both positive and negative. Only non-empty bin contents are summed. The vertical average of the horizontal moments may be calculated as follows:

$$\langle G_q \rangle = \frac{1}{N_{ev}} \sum_{1}^{N_{ev}} G_q \tag{6.10}$$

N_{ev} denotes the total number of events in a particular data set. The multifractal moment, G_q can be expressed as a power law if the production of particles is self-similar.

$$\langle G_q \rangle = (\delta\eta)^{\tau_q}; \quad \delta\eta \to 0 \tag{6.11}$$

Where τ_q, denotes mass exponents. For overall windows, the linear dependency of $\langle G_q \rangle$ on $\ln \delta\eta$ is expressed as;

$$\tau_q = \lim_{\delta\eta \to 0} (\Delta \ln \langle G_q \rangle / \Delta \ln \delta\eta) \tag{6.12}$$

After determining τ_q from G_q, the Legendre transform can be used to calculate $f(\alpha_q)$ functions employing multifractal theory [186, 189].

$$\alpha_q = d\tau_q/dq, \tag{6.13}$$

$$f(\alpha_q) = q\alpha_q - \tau_q. \tag{6.14}$$

The properties of $f(\alpha_q)$ for multifractal behaviour are defined [175, 187, 193, 194] by;

$$\frac{df(\alpha_q)}{d\alpha_q} = q\ , \frac{d^2 f(\alpha_q)}{d\alpha_q^2} < 0 \tag{6.15}$$

For multifractals, this downward concave form of $f(\alpha_q)$ has the following characteristics:

1. $f(\alpha_q)$ is downward concave
2. $f(\alpha_q = \alpha_0)$ is maximal
3. $f(\alpha_q) < f(\alpha_0)$, for $q \neq 0$

The behaviour of $f(\alpha_q)$ shows that $f(\alpha_q) = \alpha_q = 1$ for all q as a special case if there are absolutely no fluctuations. The width of $f(\alpha_q)$ is a measure of the size of the fluctuations, and the value $f(\alpha_0) < 1$ is a measure of the number of empty bins.

The formula below relates the mass exponents τ_q to the generalized dimensions D_q [187–189].

$$D_q = \frac{\tau_q}{q-1} \tag{6.16}$$

Different types of dimensions are given below:

1. $D_0 = f(\alpha_0)$; **Capacity dimension:** This shows how the data points of the multifractal pattern fill the phase space domain.
2. $D_1 = f(\alpha_1) = \alpha_1$; **Entropy dimension:** This is a measure of order-disorder of the data points in the phase space domain under study. Larger the value higher the disorder.
3. $D_2 = 2\alpha_2 - f(\alpha_2)$; **Correlation dimension:** This quantifies the degree of clustering. The larger value corresponds to higher-level clustering.

6.2.1 ^{16}O-AgBr interactions at 60 A and 200 A GeV

The data analyzed in the present study were collected using two emulsion stacks exposed to oxygen beams at 60 A and 200 A GeV at CERN, SPS (EMU01 Collaboration) [195–198]. Along-the-track scanning method has been used to record the interactions in emulsion because of inherent high detection efficiency [196,

199–201]. In each event, the polar and azimuthal angles of all the particles emitted in the interactions were measured with a high-magnification microscope. Tracks of the particles in the interactions were classified based on their relative ionization, $g = I/I_0$, where I_0 and I are, respectively, the ionizations of singly charged particles and charged particles to be identified. The tracks having relative ionization $g \geq 10$ are known as black tracks, and their number in interaction is denoted by N_b. This ionization cut corresponds to relative velocity $\beta < 0.3$. The grey tracks have relative ionization in the range $0.3 \leq g \leq 0.7$ and N_g denotes their number in an event. However, relativistic charged particles, called shower tracks (N_s), have relative ionization, $g < 1.4$ and this ionization cut corresponds to the relative velocity, $\beta > 0.7$.

Two data samples of 391 and 212 interactions of ^{16}O with AgBr at 60 A and 200 A GeV, respectively having $N_s \geq 10$ were used for analysis using standard emulsion criteria [202]. The pseudorapidity distribution for 60 A and 200 A GeV, ^{16}O-AgBr interaction are plotted in Fig. 6.14. In the figure, the red regions show the pseudorapidity ranges (1.6-3.6 ($\langle\eta\rangle \pm 1$) for 60 A and 2.1-4.1 ($\langle\eta\rangle \pm 1$) for 200 A GeV) which have been used in the present analysis.

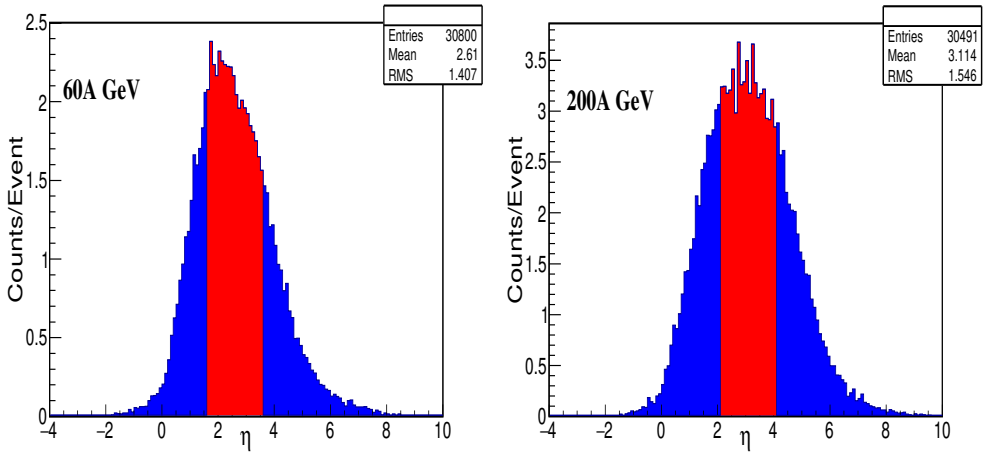

Figure 6.14: η distribution for ^{16}O-AgBr interactions at 60 A and 200 A GeV. The red regions show the pseudorapidity ranges of analysis.

The variation of $\langle G_q \rangle$ as a function of $1/\delta\eta$ for ^{16}O-AgBr at 60A and 200 A GeV are plotted in Figs. 6.15 and 6.16. The errors displayed in these figures represent the standard deviations from the mean values of G_q moments.

last

From the figures, it may be noted that the moments with negative q values saturate as $\delta\eta$ decreases whereas for positive q values, it shows linearity over a wide range of $\delta\eta$. This saturation could be due to a decrease in the number of particles as bin size is reduced. The variation of $\ln\langle G_q \rangle$ as a function of

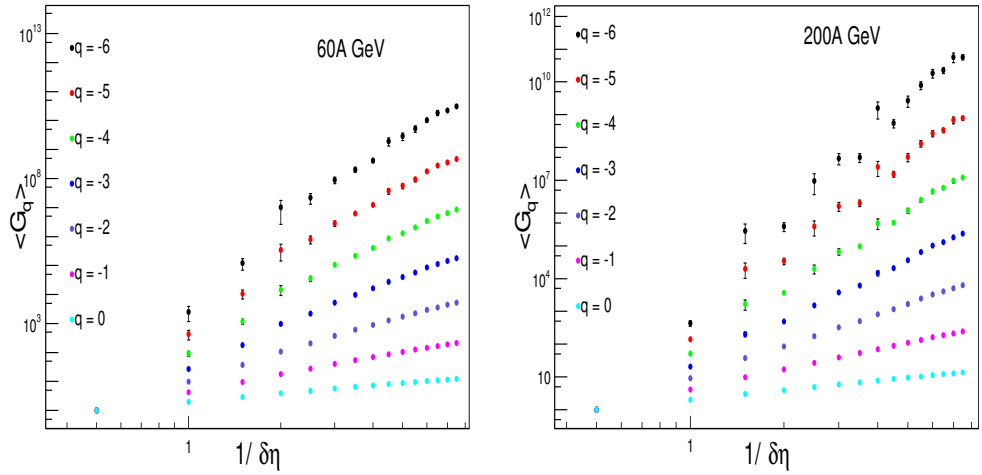

Figure 6.15: $< G_q >$ as a function of $1/\delta\eta$ for $-6 \leq q \leq 0$ in ^{16}O-AgBr interactions at 60 A GeV [Left] and 200 A GeV [Right].

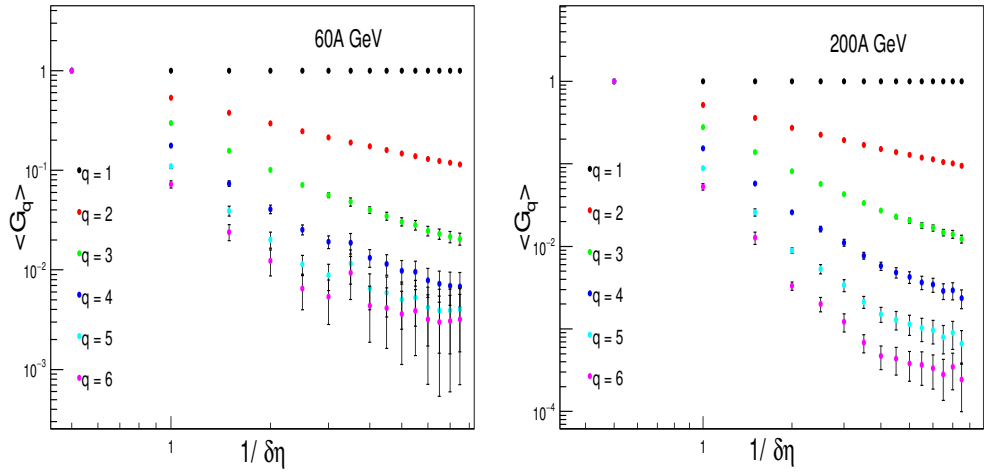

Figure 6.16: $< G_q >$ as a function of $1/\delta\eta$ for $1 \leq q \leq 6$ in ^{16}O-AgBr interactions at 60 A GeV [Left] and 200 A GeV [Right].

$-\ln\delta\eta$ is also plotted in Fig. 6.17. The data have been fitted using the least squares method for $-\ln\delta\eta > 1$. The linear rise of the multifractal moments with decreasing bin size of pseudorapidity shows a power-law behaviour in experimental data, which is the indication of the self-similarity in the production mechanism of investigated reactions.

The mass exponents (τ_q) have been calculated for the linear region of plots $\ln\langle G_q\rangle$ against $-\ln\delta\eta$ and plotted as a function of q in Fig. 6.18. τ_q increases significantly for negative q values while it becomes flattened with increasing positive q values for both data sets.

The generalized dimensions, D_q, have been calculated using Eq. 6.16 and

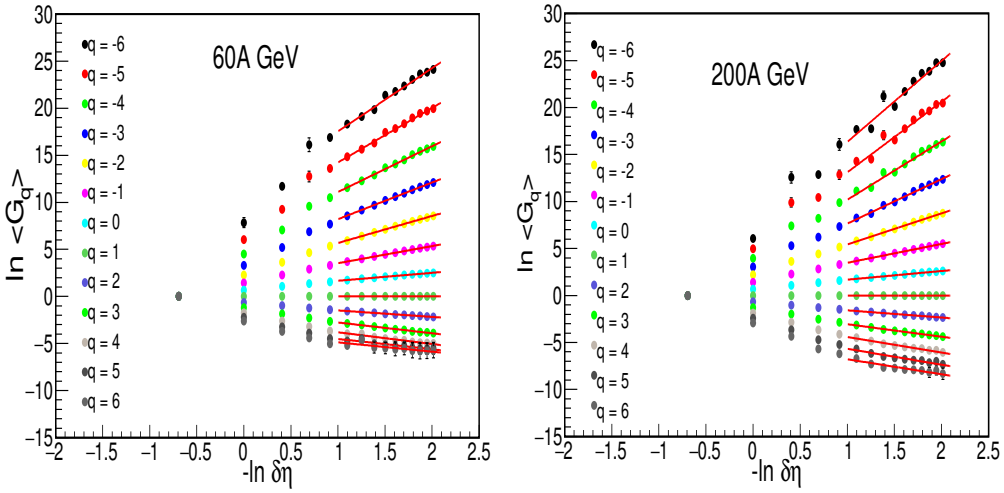

Figure 6.17: $\ln < G_q >$ as a function of $-\ln\delta\eta$ for $-6 \leq q \leq +6$ in ^{16}O-AgBr interactions at 60 A GeV [Left] and 200 A GeV [Right].

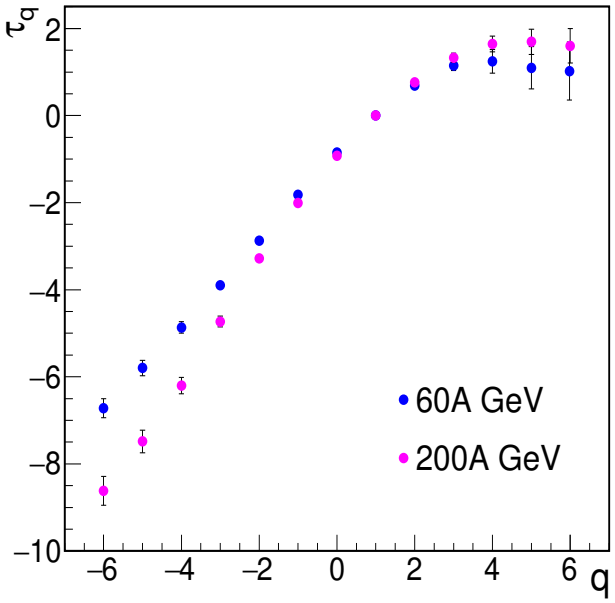

Figure 6.18: Variations of τ_q with q for ^{16}O-AgBr interactions at 60 A GeV and 200 A GeV.

plotted as a function of q in Fig. 6.19 for both data sets. At both, the energies D_q decrease with increasing q, which shows the multifractal behaviour in multiparticle production. It may also be mentioned that for positive q values, D_q increases with increasing beam energy for the same projectile, whereas for negative q values, it seems to be independent of the projectile beam energy.

The multifractal spectrum, $f(\alpha_q)$, can also give an idea about the presence of multifractal behaviour in multiparticle production. We have calculated the

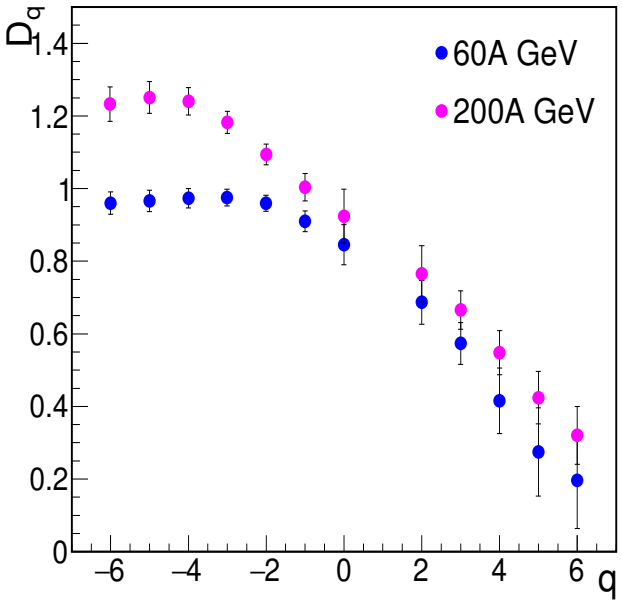

Figure 6.19: D_q versus q plots for ^{16}O-AgBr interactions at 60 A GeV and 200 A GeV.

multifractal spectrum $f(\alpha_q)$ and plotted it in Fig. 6.20. It is represented by a continuous concave downward curve with maximum at q=0, $f(\alpha(0)) = D(0) = 1$ and the dotted line represents a common tangent at an angle of 45^0 at $\alpha_1 = f(\alpha_1)$.

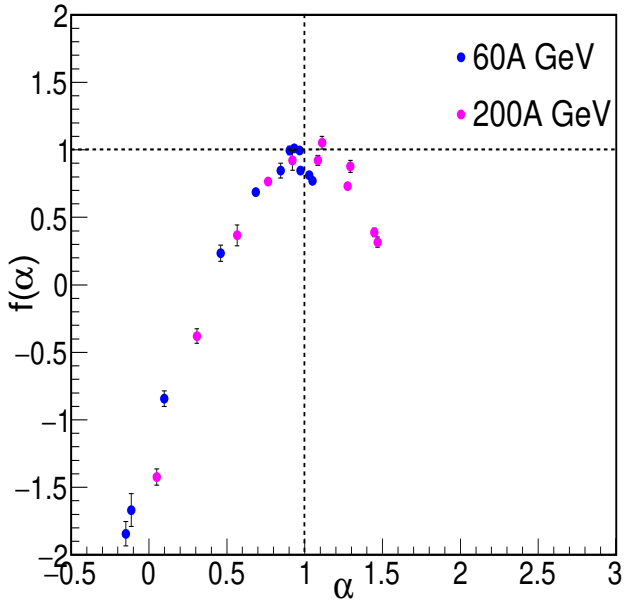

Figure 6.20: $f(\alpha_q)$ versus α_q plots for ^{16}O-AgBr interactions at 60 A GeV and 200 A GeV.

These observations are in accordance with those reported earlier [203–205]. However, all the spectra are wide enough to indicate the occurrence of multifractality in the multiparticle production process in 60A and 200 A GeV ^{16}O-AgBr collisions. It is also observed from Fig. 6.20 that the width of $f(\alpha_q)$ increases with increasing beam energy for the same projectile.

6.2.2 ^{28}Si-nucleus interactions at 14.5 A GeV/c

The emulsion stack used in the present study was exposed to a 14.5 A GeV/c silicon beam at Alternating Gradient Synchrotron (AGS), Brookhaven National Laboratory (BNL). The method of line scanning was adopted to search the interactions by using M4000 Cooke's series microscopes with 15× eyepieces and 20× objectives. The events/interactions were picked up after leaving 3 mm from the leading edges of the pellicles to avoid any distortion effects. The interactions that were produced 35 μm from the top or bottom surfaces of the pellicles was excluded from the data.

To compare the experimental results with the Lund model, FRITIOF [206], on multiparticle production and Monte Carlo random number generator (MC-RAND), 5000 events for each were generated with similar characteristics as that of experimental events observed in 14.5 A GeV/c ^{28}Si-nucleus interactions. FRITIOF events were generated based on the average value of relativistic charged particles and dispersion of its experimental multiplicity distribution so that we get the average value in the case of simulated data as almost the same as that of the experimental events. However, in the generation of the MC-RAND events, we tried to make sure that the multiplicity distribution of the produced particles should be similar to that of experimental events and that there should not be any correlation amongst the produced particles. The pseudorapidity distribution for experimental as well as generated events are shown in Fig. 6.21. The shape of the distribution is of Gaussian type for both the data. One more criterion which we applied is that the mean value and dispersion of the produced particles are comparable to the experimental values. The basic difference between FRITIOF and MC-RAND is that the MC-RAND events are correlation-free, whereas FRITIOF events have the same correlation as that of the experimental events [206].

Before we proceed further for results and discussions, we calculated the mean number of relativistic charged particles ($\langle N_s \rangle$) for experimental as well as FRITIOF events. The mean number of relativistic charged particles is calculated by dividing the total number of charged particles in the data sample by the

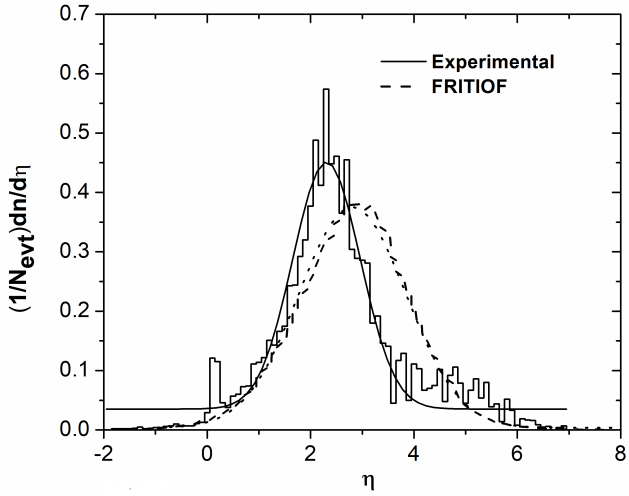

Figure 6.21: Normalized pseudorapidity distributions of relativistic charged particles in ^{28}Si-nucleus interactions. Solid (Experimental) and dotted (FRITIOF) curves are the best fits to the data.

total number of events. Mean pseudorapidity is calculated as the sum of pseudorapidities of all the relativistic charged particles divided by the total number of relativistic charged particles in the entire data sample.

The dispersion of the pseudorapidity distribution, D(η), is calculated as $D(\eta) = \sqrt{\langle\eta^2\rangle \pm \langle\eta\rangle^2}$. We found the mean number of relativistic charged particles, average pseudorapidity, and dispersion of the pseudorapidity distribution as $19.76 \pm 1.91, 2.45 \pm 0.08$, and 0.95 ± 0.08, respectively, for experimental events. The mean multiplicity of the relativistic charged particles, average pseudorapidity, and dispersion of the pseudorapidity distribution for FRITIOF simulated events come out to be 21.32 ± 0.95, 2.83 ± 0.16, and 1.28 ± 0.03, respectively, which are very close to that of the experimental events. As the average values and the dispersion in the two cases, i.e., experimental and FRITIOF, are found to be almost the same, we can say that the experimental data matches with the data of the FRITIOF model.

The values of $ln\langle G_q\rangle$ have been plotted as a function of lnM for experimental and FRITIOF in Fig. 6.22 for q = -6, -4, -2, 0, 2, 4 and 6. A linear increase in the variation of fractal moments with increasing bin size, M, is observed for both data sets. Furthermore, the moments with positive values of q and for negative q values give a linear relationship over a wide range of lnM; thus, the moment shows self-similarity in the mechanism of particle production for the nuclear interactions considered. The plots for the simulated events are in good agreement with that of the experimental events. Similar results have been

reported for h+A [207] and A+A [208] collisions.

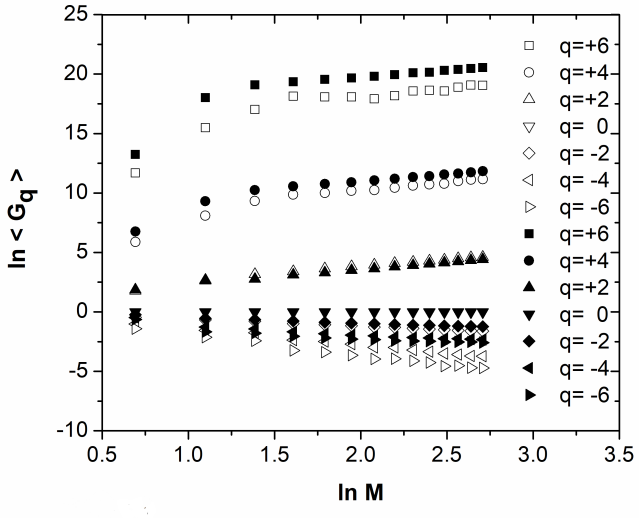

Figure 6.22: The variations of $ln\langle G_q\rangle$ with lnM in ^{28}Si-nucleus interactions. Open symbols (experimental) and solid symbols (FRITIOF).

The variation of $ln\langle G_q\rangle$ with lnM in ^{28}Si-nucleus interactions at 14.5 A GeV/c for two groups of events, i.e. $N_g \leq 1$ and $N_g \geq 2$, is exhibited in Fig. 6.23. The multifractal moments are observed to increase linearly with decreasing bin width, $\delta\eta$ for the two groups of interactions considered in the study. Furthermore, it is observed that G_q moments have slightly higher values for the interactions having $N_g \geq 2$ than those having $N_g \leq 1$.

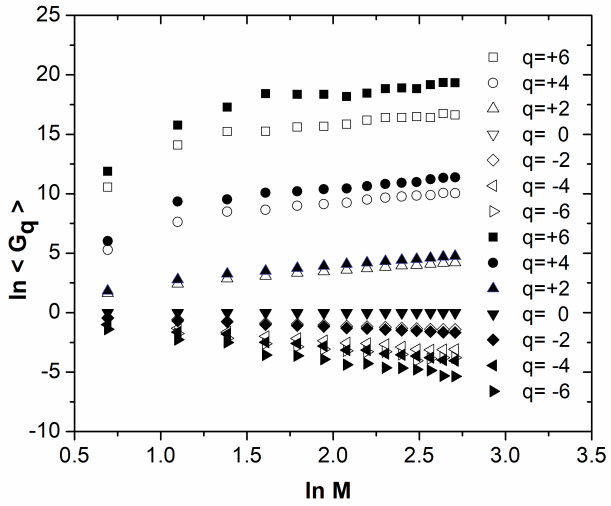

Figure 6.23: The plot of $ln\langle G_q\rangle$ versus lnM for two groups of events in ^{28}Si-nucleus collisions. Open symbols ($N_g \leq 1$) and solid symbols ($N_g \geq 2$).

The mass exponents, T_q (or τ_q) , are obtained by studying the dependence of $ln\langle G_q \rangle$ on lnM. For carrying out approximations, only the portions of the curves that show linearity are taken into account to avoid the saturation effect. The values of T_q, in ^{28}Si-nucleus collisions obtained for experimental and FRITIOF data are displayed in Fig. 6.24. The mass exponents, T_q, are observed to increase with increasing order of the moments, q, for both the data sets.

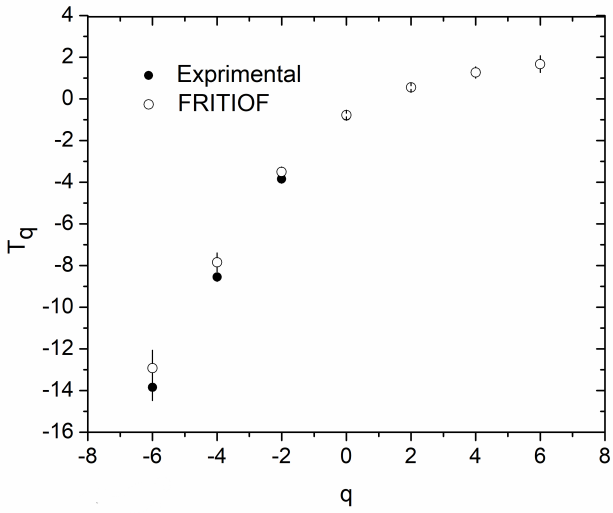

Figure 6.24: The variations of T_q with q in ^{28}Si–nucleus interactions. This is for the entire sample in which all N_g are included.

The dependence of the mass exponents, T_q, on q for two groups of events, i.e. $N_g \leq 1$ and $N_g \geq 2$, is given in Fig. 6.25. From the figure, it may be seen that T_q increases with the increase in the order of the moments, q. However, it seems to saturate at higher values of q. We find that the dependence of T_q on q is almost similar for the two groups of events.

To study the contribution of the dynamical component of the multifractal moments, experimental results were compared with those of the MC-RAND events. For this purpose, the values of G_q as well as T_q moments for the MC-RAND data which is written as ${G_q}^{stat}$ and ${T_q}^{stat}$ respectively, have also been calculated in the same way as that for the experimental data. Further, the statistical component (${T_q}^{stat}$) and dynamical component (${T_q}^{dyn}$) of the mass exponents are related [209] as.

$$ {T_q}^{dyn} = {T_q}^{stat} - T_q + (q-1) $$

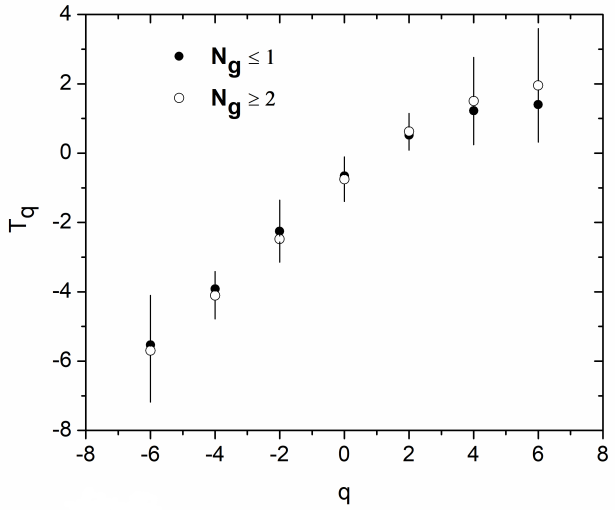

Figure 6.25: T_q versus q plots for ^{28}Si-nucleus interactions having $N_g \leq 1$ and $N_g \geq 2$ groups of experimental events.

The variations of T_q, $T_q{}^{stat}$ and $T_q{}^{dyn}$ with the order of the moment, q, are shown in Fig. 6.26. It may be seen from the figure that T_q increases with increasing q; however, the rate of increase in the regions which correspond to positive and negative values of q are quite different. In the regions corresponding to the negative q values, the increase in T_q is relatively more rapid in comparison with that for the region in which q have positive values. This observation is consistent with the predictions of the gluon model [210].

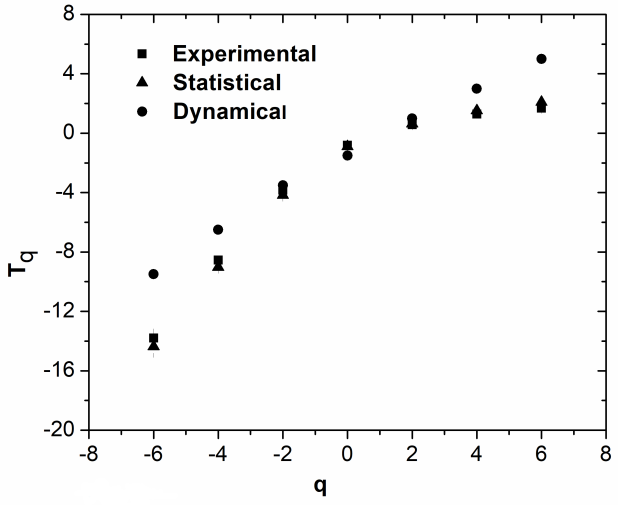

Figure 6.26: The variation of T_q , $T_q{}^{dyn}$ and $T_q{}^{stat}$ with q in ^{28}Si-nucleus collisions.

Furthermore, the deviation in the values of T_q from $T_q{}^{dyn}$ may, therefore, lead

to the deviation in the ${T_q}^{dyn}$ from $(q-1)$. It should be mentioned that any deviation of ${T_q}^{dyn}$ from $(q-1)$ will indicate the presence of dynamical contribution to the fluctuations. Therefore, T_q may be considered as a more sensitive measure of dynamical fluctuation than G_q itself. One more observation that may be made is that ${T_q}^{dyn}$ coincides with ${T_q}^{stat}$ in the mid-region of q values, whereas for the q values in the region $(-2 \leq q \leq 2)$, a significant departure is observed.

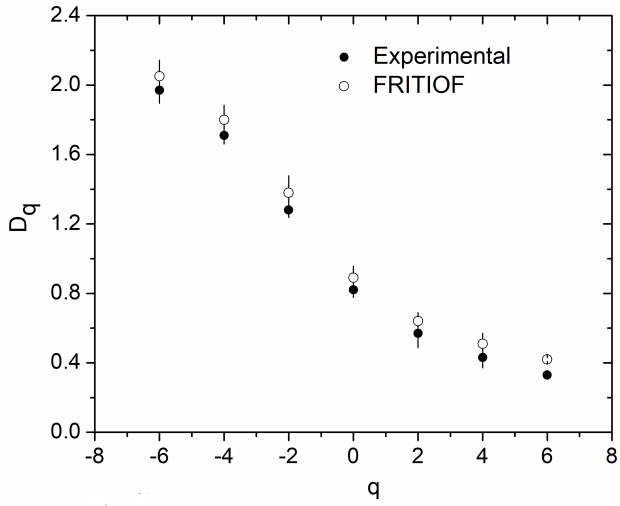

Figure 6.27: Variation of generalized dimension, D_q , with q for experimental and FRITIOF data in ^{28}Si-nucleus collisions.

The variations of the generalized dimensions, D_q, with q, in ^{28}Si-nucleus collisions for experimental and FRITIOF data are exhibited in Fig. 6.27. The generalized dimensions are found to be positive for all orders of the moments, q and demonstrate a decreasing trend with increasing q. This behaviour is in excellent agreement with the predictions of the multifractal cascade model [211]. It may also be observed from the figure that the values of D_q are greater than unity for $q \leq -2$, and this result is in agreement with those reported [212] earlier for different projectiles over a wide energy range.

To examine the variation of the generalized dimensions with a certain order of the moment, we have plotted D_q as a function of q in Fig. 6.28 again for the same two groups of events, i. e. $N_g \leq 1$ and $N_g \geq 2$. From the figure, we note that the generalized dimensions, D_q, are almost the same in the case of negative as well as positive values of q for both groups of events. However, it is also observed that these values are slightly higher for $N_g \geq 2$ group of events for positive q values. One of the reasons for the higher value of D_q in the case of $N_g \geq 2$ may be due to an expected increase in the average multiplicity [213].

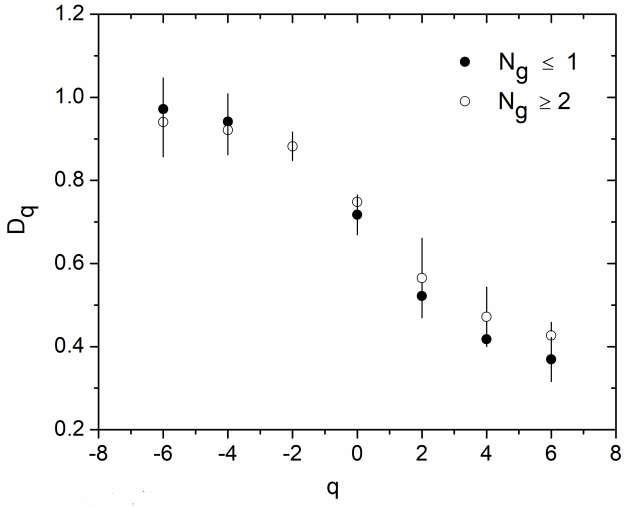

Figure 6.28: The variations of generalized dimension, D_q, with q in ^{28}Si-nucleus interactions.

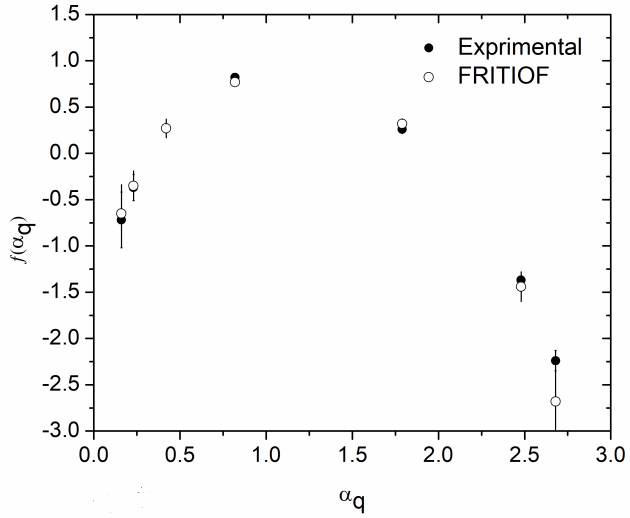

Figure 6.29: The dependence of multifractal spectral function, $f(\alpha_q)$, on α_q in ^{28}Si-nucleus collisions.

Fig. 6.29 shows the dependence of $f(\alpha_q)$ on α_q for the experimental and FRITIOF events. The width of the multifractal spectra for experimental events and for the simulated events is almost the same. This means that the nature of the spectra is the same as concave downwards centred around α_q corresponding to q = 0 and have a common tangent at an angle of 45°. This observation agrees fairly well with the predictions of the gluon model [210]. However, $f(\alpha_q)$ has no peak in any of the cases studied, which is an indication of the non-smooth

nature of the multiplicity distribution of the particles produced in the interactions considered for the present study. To see the dependence of $f(\alpha_q)$ spectra on α_q for two groups of events, $N_g \leq 1$ and $N_g \geq 2$ are plotted in Fig. 6.30. The shape of the spectra is found to be the same for both groups of events.

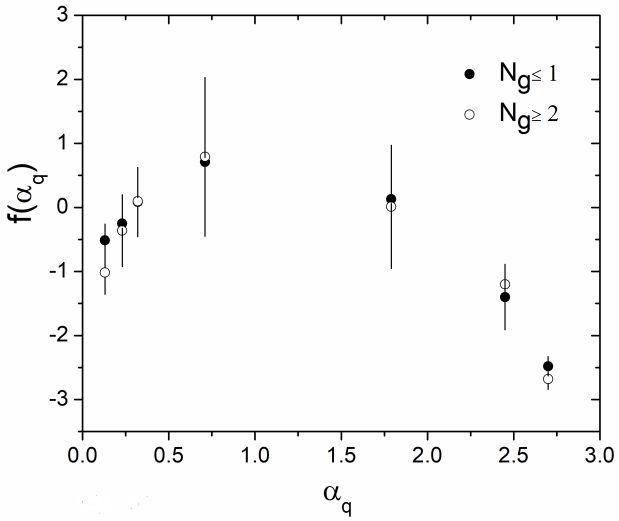

Figure 6.30: The dependence of multifractal spectral function, $f(\alpha_q)$, on α_q in ^{28}Si-nucleus collisions for two groups of events, $N_g \leq 1$ and $N_g \geq 2$.

In conclusion, a power-law behaviour is observed in the variation of lnG_q with ln_M. A concave downward trend is found to exist for spectral function, $f(\alpha_q)$. These observations, which are for experimental and FRITIOF events, indicate the presence of multifractality in the mechanism of multiparticle production. The deviation of $T_q{}^{dyn}$ from $(q-1)$ indicates the presence of dynamical contribution to the fluctuations. The decreasing trend in the value of D_q with increasing q confirms the presence of multifractality. The variation of the parameters T_q, D_q on q and $f(\alpha_q)$ on α_q is observed to be almost similar for the two groups of events, $N_g \leq 1$ and $N_g \geq 2$.

6.3 Summary

Using the Scaled Factorial Moment (SFM) approach, detailed results on intermittency in Au+Au collisions in the FAIR energy range of 2-12 A GeV in pseudorapidity $\chi(\eta)$, azimuthal $\chi(\phi)$, and pseudorapidity-azimuthal $\chi(\eta-\phi)$ spaces are discussed. A hybrid version of the Ultra-relativistic Quantum Molecular Dynamics (UrQMD) event generator is used for the simulations. Three different equations of state (EoS) are used to explore the intermittency within the

hydrodynamic scenario: pure Hadron Gas (HG), Chiral + HG, and the Bag Model EoS. Chiral+HG EoS exhibits a weak intermittent type of emission in both one-dimensional and two-dimensional space and at all beam energies. For Bag Model EoS, however, a significant intermittent kind of emission is observed. The dependence of intermittency on incident beam energy has also been studied. The strength of the intermittency is observed to reduce as beam energy increases.

In addition, Multifractal approaches are also used to explore separately the intermittency of ^{16}O-AgBr interactions at 60 A and 200 A GeV and ^{28}Si-nucleus interactions at 14.5 A GeV/c. The multifractal moments, G_q, is estimated as a function of pseudorapidity bin size for the various orders of moments, q in both data sets. In the examined data sets, the power-law distribution is observed. The changes in multifractal dimension, D_q, and multifractal spectral function, f(α_q), with the order of the moments, q, are thoroughly explored. D_q is observed to decrease as the order of the moments, q, increased, demonstrating a self-similar behaviour in the multiparticle production in the considered collisions.

Chapter 7

Summary and Outlook

The purpose of the relativistic heavy-ion collision experiments is to produce and study the properties of the quark-gluon plasma (QGP), the thermalized de-confined state of strongly interacting matter in the laboratory. The Compressed Baryonic Matter Experiment (CBM) is a heavy-ion experiment planned to be operated at the future Facility for Antiproton and Ion Research (FAIR) in Darmstadt, Germany. The physics goal of CBM is to explore the QCD phase diagram at low temperature and moderate to high baryon density regime. The foreseen energy domain of FAIR (SIS100) will allow the one-of-a-kind opportunity to study nuclear matter at extremely high densities similar to the core of neutron stars. The CBM experiment is designed to replicate the signals from the early and dense stage of relativistic heavy-ion collisions in the laboratory. It offers a unique opportunity to investigate the signatures of partonic degrees of freedom and locate the conjectured onset of the first-order de-confinement phase transition and QCD critical point. Among various observables, dileptons are believed to be a very promising observable carrying undistorted information about the dense matter of the collision. These signals are rarely produced, either due to low cross-section or low branching ratio into lepton pairs produced from the decay Low Mass Vector Meson (LMVM) or charmonia. The anticipated high interaction rate of about 10 MHz for nuclear collision at CBM will offer a unique facility to investigate these rare probes more extensively. In the energy range of 2 - 40 A GeV, the experimental data on dileptons coming from the decays of LMVM or charmonia is not yet available. During the first few years of operation, the CBM experiment at FAIR intends to conduct a detailed study of the production of dileptons in heavy-ion nuclear collisions at beam energies, E_{lab} = 2-12 A GeV. The Muon Chamber (MuCh) sub-system at CBM will be dedicated to tracking and identifying muon pairs originating from the decay of LMVM and charmonia. The first two MuCh stations will incorporate Gas Electron Multiplier (GEM) detectors to cope with the expected high particle fluxes (0.5 MHz/cm^2). Further, due to the relatively lower particle fluxes (30

kHz/cm^2), a Resistive plate Chamber (RPC) is considered as one of the feasible options for the remaining two stations.

As mentioned before, the thesis is broadly divided into two parts. The first part deals with the optimization of the muon detector system for the CBM experiment at SIS100 energies. This is carried out through Monte Carlo (MC) simulations by studying the feasibility of di-muon detection decaying from LMVMs produced at SIS100 energies.

The second part of this thesis work describes a comprehensive study on intermittency using Scaled Factorial Moment (SFM) technique in Au+Au collisions in the FAIR energy range of 2-12 A GeV in pseudorapidity $\chi(\eta)$, azimuthal $\chi(\phi)$, and pseudorapidity-azimuthal $\chi(\eta - \phi)$ spaces

A general overview of the physics of quark-gluon plasma formed in relativistic heavy ion collisions is covered in chapter 1.

An overview of the CBM experiment at FAIR is discussed in Chapter 2. It begins with the layout of the FAIR accelerator facility, followed by a discussion of the different physics goals of the CBM experiment and the corresponding potential observables required to investigate the high-density matter anticipated at FAIR. A brief description of the configuration of the CBM experimental setup and each subsystem ends the chapter.

Chapter 3 describes the muon chamber detector set-up used for muon identification. One of the important aspects of the CBM experiment is to measure muons created by the decays of LMVM (ω, η, ϕ, etc.) or charmonia (J/ψ). Thus, MuCh is needed for their detection. The simulation procedure for optimization of the MuCh parameters is also described in this chapter.

The CBM simulation framework and the optimization of MuCh geometry are covered in chapter 4. The following topics are covered in this chapter.

Implementation of MuCh geometries in CBMRoot software

Initially, the geometry parameters of MuCh were provided at the time of transport in ASCII format, and the CbmMuchGeoScheme class handled the construction. We had to modify CBM geometries in ROOT format and implement them as nodes to make the system transparent, usable, and user-friendly interfaces. Additionally, each detector geometry can be visualized stand-alone using the GL viewer of ROOT TBrowser, and a geometry database can handle the geometry files. The task of "rootification" includes the development of a macro to create the MuCh geometry and the development of GeoHandler classes to include the rootified geometry in transport simulations.

First absorber optimization

The MuCh detector subsystem comprises multiple hadron absorbers and a triplet

of tracking detectors positioned between the absorbers. In previous simulations with the MuCh setup, the first absorber was composed of high-density (ρ=2.26 g/cm^3) pure carbon having a thickness of 60 cm. Subsequent R&D for the mechanical design of the absorber blocks and a detailed market survey reveals the unavailability of high-density pure carbon in bulk, required to build the first absorber of surface area 260×250 cm^2. Therefore to keep the absorption profile and the physical thickness of the 1^{st} absorber block similar as it was with the carbon of density 2.26 g/cm^3, the possibility of having a composite absorber block made of two different materials instead of only carbon being explored. Concrete is chosen as an alternate option compared to other materials because it has the advantage from the mechanical and activation point of view. After investigating the influence of different absorber configurations on the reconstruction performance of ω meson ($\rightarrow \mu^+\mu^-$) in 8 A GeV central Au+Au collisions, a composite absorber of carbon with ρ = 1.78 g/cm^3 (28 cm) and concrete with ρ = 2.3 g/cm^3 (30 cm) has been adopted as the feasible configuration for MuCh first absorber. This configuration would provide an additional 2 cm gap between the absorber and first detector station, which would useful for service work of the first station.

Investigation & implementation of realistic GEM chamber design
It has been decided from the detector R&D that triple GEM chambers to be used as the tracking detectors in the first two stations of MuCh will be operated with Ar/CO_2 gas mixture in a 70:30 volume ratio. The drift gap of the chambers will be 3 mm, and the transfer and induction gaps will be 2 mm each. In the previous geometry, pure Argon of thickness 3 mm was only included as the active medium, in the transport simulations. The transfer and induction gaps were not taken into consideration. To make the simulation more realistic in the present work, passive volumes (of 6 mm thickness) are implemented, and the gas mixture is changed from Ar to Ar/CO_2 in a 70:30 volume ratio. There is no significant change in the ω reconstruction efficiency and signal-to-background ratio observed after implementing the realistic MuCh chamber geometry.

The reconstruction of the LMVM (η, ϕ and ω) through the dimuon channel for central Au+Au collisions at 8 A GeV/c is reported in chapter 5. Firstly, the various track selection cuts for choosing dimuon candidates, based on the separation powers of these cuts to distinguish between signal and background, are optimised. The final results of the feasibility study on LMVMs (ω, ϕ, and η) detection through the dimuon channel in Au+Au collisions at 8 A GeV/c are presented. The Super Event (SE) technique calculates the dimuon combinatorial background. Due to the absorption of low-energy muons, the phase-space

acceptance for LMVM (ω, ϕ, and η) is found to be shifted toward forward rapidities. The efficiency and the signal-to-background ratio (S/B) are calculated within a $\pm 2\sigma$ mass range around the signal peak. The S/B value is found to be less than 1 for each LMVM, which makes it extremely critical to precisely estimate the dimuon combinatorial background. The efficiency and acceptance correction matrices are constructed to compare the reconstructed spectra with results from other generators, simulations, models or detectors. This completes the first part of the thesis.

Investigations related to the second part of the thesis are depicted in chapter 6. This includes the study of intermittency in Au+Au collisions at energies relevant to FAIR SIS100. For this purpose, we have employed the scaled factorial moment (SFM) technique in pseudorapidity $\chi(\eta)$, azimuthal $\chi(\phi)$, and pseudorapidity-azimuthal $\chi(\eta - \phi)$ spaces. The simulations were performed with a hybrid version of the Ultra-relativistic Quantum Molecular Dynamics (UrQMD) event generator. Three alternative equations of state (EoS) are employed to investigate the intermittency within the hydrodynamic scenario, namely pure Hadron Gas(HG), Chiral + HG, and Bag Model EoS. In both one and two-dimensional spaces and at all beam energies, a weak intermittent type of emission had been observed for Chiral+HG EoS. In contrast, a strong intermittent kind of emission is observed for Bag Model EoS. The incident beam energy dependency of intermittency has also been investigated. The strength of the intermittency has been seen to diminish with increasing beam energy.

In addition, a multifractal analysis to study the multiparticle dynamics in 60 A and 200 A GeV, ^{16}O-AgBr collisions and 14.5 A GeV/c, ^{28} Si-nucleus interaction were performed in the pseudorapidity phase space. Multifractal moments, G_q, as the function of pseudorapidity bin size for the different orders of the moments, q, is calculated. The power-law behaviour is observed in the considered data sets. The variations of multifractal dimension, D_q, and the multifractal spectral function, $f(\alpha_q)$, with the order of the moments, q, are studied thoroughly. D_q is found to decrease with increasing order of the moments, q, indicating thereby a self-similar behaviour in the multiparticle production in the considered collisions.

References

[1] G. Ecker, "Quantum chromodynamics", in 2005 European School of High-Energy Physics (Apr. 2006).

[2] Y. Nambu, "Axial vector current conservation in weak interactions", Phys. Rev. Lett. **4**, edited by T. Eguchi, 380–382 (1960).

[3] O. W. Greenberg, "Spin and Unitary Spin Independence in a Paraquark Model of Baryons and Mesons", Phys. Rev. Lett. **13**, 598–602 (1964).

[4] D. J. Gross and F. Wilczek, "Ultraviolet Behavior of Nonabelian Gauge Theories", Phys. Rev. Lett. **30**, edited by J. C. Taylor, 1343–1346 (1973).

[5] A. Bazavov and P. Petreczky, "Chiral and deconfinement transitions in lattice QCD with improved staggered action", in Meeting of the APS Division of Particles and Fields (Oct. 2011).

[6] S. Borsanyi, Z. Fodor, C. Hoelbling, S. D. Katz, S. Krieg, C. Ratti, and K. K. Szabo, "Is there still any T_c mystery in lattice QCD? Results with physical masses in the continuum limit III", JHEP **09**, 073 (2010).

[7] A. Bazavov et al., "Chiral crossover in QCD at zero and non-zero chemical potentials", Phys. Lett. B **795**, 15–21 (2019).

[8] W.-j. Fu, J. M. Pawlowski, and F. Rennecke, "QCD phase structure at finite temperature and density", Phys. Rev. D **101**, 054032 (2020).

[9] A. Andronic et al., "Hadron Production in Ultra-relativistic Nuclear Collisions: Quarkyonic Matter and a Triple Point in the Phase Diagram of QCD", Nucl. Phys. A **837**, 65–86 (2010).

[10] K. Fukushima and T. Hatsuda, "The phase diagram of dense qcd", Reports on Progress in Physics **74**, 014001 (2010).

[11] L. Adamczyk et al., "Bulk Properties of the Medium Produced in Relativistic Heavy-Ion Collisions from the Beam Energy Scan Program", Phys. Rev. C **96**, 044904 (2017).

[12] M. S. Abdallah et al., "Measurements of Proton High Order Cumulants in $\sqrt{s_{\mathrm{NN}}} = 3$ GeV Au+Au Collisions and Implications for the QCD Critical Point", Phys. Rev. Lett. **128**, 202303 (2022).

[13]A. Laszlo, "The NA61/SHINE Experiment at the CERN SPS", Nucl. Phys. A **830**, edited by P. Stankus, D. Silvermyr, S. Sorensen, and V. Greene, 559C–562C (2009).

[14]M. Gazdzicki, "Ion Program of Na61/Shine at the CERN SPS", J. Phys. G **36**, edited by F. Liu, Z. Xiao, and P. Zhuang, 064039 (2009).

[15]D. Blaschke and al., "Topical issue on Exploring Strongly Interacting Matter at High Densities NICA White Paper", Eur. Phys. J. A **52**, 267 (2016).

[16]S. A. Bass et al., "Microscopic models for ultrarelativistic heavy ion collisions", Prog. Part. Nucl. Phys. **41**, 255–369 (1998).

[17]M. Bleicher et al., "Relativistic hadron hadron collisions in the ultrarelativistic quantum molecular dynamics model", J. Phys. G **25**, 1859–1896 (1999).

[18]T. Galatyuk, "Future facilities for high μ_B physics", Nucl. Phys. A **982**, edited by F. Antinori, A. Dainese, P. Giubellino, V. Greco, M. P. Lombardo, and E. Scomparin, 163–169 (2019).

[19]M. L. Miller, K. Reygers, S. J. Sanders, and P. Steinberg, "Glauber modeling in high energy nuclear collisions", Ann. Rev. Nucl. Part. Sci. **57**, 205–243 (2007).

[20]S. Pal, "Characterizations of Cathode pad chamber as tracking detector for MUON Spectrometer of ALICE", PhD thesis (Saha Inst., Nov. 2008).

[21]J. W. Harris and B. Muller, "The Search for the quark - gluon plasma", Ann. Rev. Nucl. Part. Sci. **46**, 71–107 (1996).

[22]S. A. Bass, M. Gyulassy, H. Stoecker, and W. Greiner, "Signatures of quark gluon plasma formation in high-energy heavy ion collisions: A Critical review", J. Phys. G **25**, R1–R57 (1999).

[23]C. Y. Wong, *Introduction to high-energy heavy ion collisions* (1995).

[24]R. Vogt, *Ultrarelativistic heavy-ion collisions* (Elsevier, Amsterdam, 2007).

[25]J. Stachel and P. Braun-Munzinger, "Stopping in High-energy Nucleus Nucleus Collisions: Analysis in the Landau Hydrodynamic Model", Phys. Lett. B **216**, 1–6 (1989).

[26]J. D. Bjorken, "Highly Relativistic Nucleus-Nucleus Collisions: The Central Rapidity Region", Phys. Rev. D **27**, 140–151 (1983).

[27]L. D. McLerran, M. Kataja, P. V. Ruuskanen, and H. von Gersdorff, "Studies of the Hydrodynamical Evolution of Matter Produced in Fluctuations in p anti-p Collisions and in Ultrarelativistic Nuclear Collisions. 2. Transverse Momentum Distributions", Phys. Rev. D **34**, 2755 (1986).

[28]S. Acharya et al., "Measurements of inclusive jet spectra in pp and central Pb-Pb collisions at $\sqrt{s_{\mathrm{NN}}}$ = 5.02 TeV", Phys. Rev. C **101**, 034911 (2020).

[29]J. Adam et al., "Measurement of jet suppression in central Pb-Pb collisions at $\sqrt{s_{\mathrm{NN}}}$ = 2.76 TeV", Phys. Lett. B **746**, 1–14 (2015).

[30]B. Abelev et al., "Measurement of charged jet suppression in Pb-Pb collisions at $\sqrt{s_{NN}}$ = 2.76 TeV", JHEP **03**, 013 (2014).

[31]J. Adam et al., "Measurement of jet quenching with semi-inclusive hadron-jet distributions in central Pb-Pb collisions at $\sqrt{s_{\mathrm{NN}}}$ = 2.76 TeV", JHEP **09**, 170 (2015).

[32]L. Adamczyk et al., "Measurements of jet quenching with semi-inclusive hadron+jet distributions in Au+Au collisions at $\sqrt{s_{NN}}$ = 200 GeV", Phys. Rev. C **96**, 024905 (2017).

[33]G. Aad et al., "Measurement of the jet radius and transverse momentum dependence of inclusive jet suppression in lead-lead collisions at $\sqrt{s_{NN}}$= 2.76 TeV with the ATLAS detector", Phys. Lett. B **719**, 220–241 (2013).

[34]M. Aaboud et al., "Measurement of the nuclear modification factor for inclusive jets in Pb+Pb collisions at $\sqrt{s_{\mathrm{NN}}}$ = 5.02 TeV with the ATLAS detector", Phys. Lett. B **790**, 108–128 (2019).

[35]V. Khachatryan et al., "Measurement of inclusive jet cross sections in pp and PbPb collisions at $\sqrt{s_{NN}}$ = 2.76 TeV", Phys. Rev. C **96**, 015202 (2017).

[36]M. L. Mangano, "Two lectures on heavy quark production in hadronic collisions", Proc. Int. Sch. Phys. Fermi **137**, edited by I. I. Y. Bigi and L. Moroni, 95–137 (1998).

[37]M. Strickland, "Thermal Bottomonium Suppression", AIP Conf. Proc. **1520**, edited by V. P. Gonçalves, M. L. L. da Silva, J. T. de Santana Amaral, and M. V. T. Machado, 179–184 (2013).

[38]T. Matsui and H. Satz, "J/ψ Suppression by Quark-Gluon Plasma Formation", Phys. Lett. B **178**, 416–422 (1986).

[39]B. Abelev et al., "J/ψ suppression at forward rapidity in Pb-Pb collisions at $\sqrt{s_{NN}}$ = 2.76 TeV", Phys. Rev. Lett. **109**, 072301 (2012).

[40]J. Adam et al., "J/ψ suppression at forward rapidity in Pb-Pb collisions at $\sqrt{\mathbf{s}_{\mathrm{NN}}}$ = **5.02** TeV", Phys. Lett. B **766**, 212–224 (2017).

[41]A. M. Sirunyan et al., "Measurement of nuclear modification factors of Y(1S), Y(2S), and Y(3S) mesons in PbPb collisions at $\sqrt{s_{\mathrm{NN}}}$ = 5.02 TeV", Phys. Lett. B **790**, 270–293 (2019).

[42]A. Adare et al., "J/ψ Production vs Centrality, Transverse Momentum, and Rapidity in Au+Au Collisions at $\sqrt{s_{NN}} = 200$ GeV", Phys. Rev. Lett. **98**, 232301 (2007).

[43]A. Adare et al., "J/ψ suppression at forward rapidity in Au+Au collisions at $\sqrt{s_{NN}} = 200$ GeV", Phys. Rev. C **84**, 054912 (2011).

[44]S. S. Adler et al., "Systematic studies of the centrality and s(NN)**(1/2) dependence of the d E(T) / d eta and d (N(ch) / d eta in heavy ion collisions at mid-rapidity", Phys. Rev. C **71**, [Erratum: Phys.Rev.C 71, 049901 (2005)], 034908 (2005).

[45]P. Stankus, "Direct photon production in relativistic heavy-ion collisions", Ann. Rev. Nucl. Part. Sci. **55**, 517–554 (2005).

[46]L. D. McLerran and T. Toimela, "Photon and Dilepton Emission from the Quark - Gluon Plasma: Some General Considerations", Phys. Rev. D **31**, 545 (1985).

[47]Y. Akiba, "Quest for the quark–gluon plasma—hard and electromagnetic probes", PTEP **2015**, 03A105 (2015).

[48]O. Linnyk, E. L. Bratkovskaya, and W. Cassing, "Effective QCD and transport description of dilepton and photon production in heavy-ion collisions and elementary processes", Prog. Part. Nucl. Phys. **87**, 50–115 (2016).

[49]M. M. Aggarwal et al., "Observation of direct photons in central 158-A-GeV Pb-208 + Pb-208 collisions", Phys. Rev. Lett. **85**, 3595–3599 (2000).

[50]A. Adare et al., "Direct-Photon Production in $p+p$ Collisions at $\sqrt{s} = 200$ GeV at Midrapidity", Phys. Rev. D **86**, 072008 (2012).

[51]I. Tserruya, "Photons and low-mass dileptons: results from PHENIX", Nucl. Phys. A **904-905**, edited by T. Ullrich, B. Wyslouch, and J. W. Harris, 225c–232c (2013).

[52]S. Acharya et al., "Direct photon production at low transverse momentum in proton-proton collisions at $\sqrt{\mathbf{s}} = \mathbf{2.76}$ and 8 TeV", Phys. Rev. C **99**, 024912 (2019).

[53]J. Adam et al., "Direct photon production in Pb-Pb collisions at $\sqrt{s_{NN}} = 2.76$ TeV", Phys. Lett. B **754**, 235–248 (2016).

[54]S. Chatrchyan et al., "Measurement of isolated photon production in pp and PbPb collisions at $\sqrt{s_{NN}} = 2.76$ TeV", Phys. Lett. B **710**, 256–277 (2012).

[55]G. Aad et al., "Centrality, rapidity and transverse momentum dependence of isolated prompt photon production in lead-lead collisions at $\sqrt{s_{\rm NN}} = 2.76$ TeV measured with the ATLAS detector", Phys. Rev. C **93**, 034914 (2016).

[56]R. Rapp and H. van Hees, "Thermal Dileptons as Fireball Thermometer and Chronometer", Phys. Lett. B **753**, 586–590 (2016).

[57]F. Karsch and M. Lutgemeier, "Deconfinement and chiral symmetry restoration in an SU(3) gauge theory with adjoint fermions", Nucl. Phys. B **550**, 449–464 (1999).

[58]P. Roy, S. Sarkar, J. Alam, B. Dutta-Roy, and B. Sinha, "omega meson as a chronometer and thermometer in hot and dense hadronic matter", Phys. Rev. C **59**, 2778–2781 (1999).

[59]J. K. Nayak, J. Alam, S. Sarkar, and B. Sinha, "Thermal photon to dilepton ratio in high-energy nuclear collisions", Phys. Rev. C **78**, 034903 (2008).

[60]T. Matsui and H. Satz, "J/ψ Suppression by Quark-Gluon Plasma Formation", Phys. Lett. B **178**, 416–422 (1986).

[61]H. Heiselberg, "Event-by-event physics in relativistic heavy ion collisions", Phys. Rept. **351**, 161–194 (2001).

[62]M. A. Stephanov, K. Rajagopal, and E. V. Shuryak, "Signatures of the tricritical point in QCD", Phys. Rev. Lett. **81**, 4816–4819 (1998).

[63]M. M. Aggarwal et al., "Event-by-event fluctuations in particle multiplicities and transverse energy produced in 158-A-GeV Pb + Pb collisions", Phys. Rev. C **65**, 054912 (2002).

[64]S. Jeon and V. Koch, "Charged particle ratio fluctuation as a signal for QGP", Phys. Rev. Lett. **85**, 2076–2079 (2000).

[65]E. V. Shuryak and M. A. Stephanov, "When can long range charge fluctuations serve as a QGP signal?", Phys. Rev. C **63**, 064903 (2001).

[66]J. Adams et al., "Multiplicity fluctuations in Au+Au collisions at s(NN)**(1/2) = 130-GeV", Phys. Rev. C **68**, 044905 (2003).

[67]B. I. Abelev et al., "Beam-Energy and System-Size Dependence of Dynamical Net Charge Fluctuations", Phys. Rev. C **79**, 024906 (2009).

[68]B. Abelev et al., "Net-Charge Fluctuations in Pb-Pb collisions at $\sqrt{s_{NN}} = 2.76$ TeV", Phys. Rev. Lett. **110**, 152301 (2013).

[69]J. Rafelski and B. Muller, "Strangeness Production in the Quark - Gluon Plasma", Phys. Rev. Lett. **48**, [Erratum: Phys.Rev.Lett. 56, 2334 (1986)], 1066 (1982).

[70]J. Rafelski, "Strangeness Production in the Quark Gluon Plasma", Nucl. Phys. A **418**, edited by T. W. Ludlam and H. E. Wegner, 215C–235C (1984).

[71]J. Rafelski and B. Müller, "Strangeness production in the quark-gluon plasma", Phys. Rev. Lett. **56**, 2334–2334 (1986).

[72]P. Koch, B. Muller, and J. Rafelski, "Strangeness in Relativistic Heavy Ion Collisions", Phys. Rept. **142**, 167–262 (1986).

[73]J. Rafelski, "Strange anti-baryons from quark - gluon plasma", Phys. Lett. B **262**, 333–340 (1991).

[74]P. Koch, B. Muller, and J. Rafelski, "Strangeness in Relativistic Heavy Ion Collisions", Phys. Rept. **142**, 167–262 (1986).

[75]F. Antinori et al., "Enhancement of hyperon production at central rapidity in 158-A-GeV/c Pb-Pb collisions", J. Phys. G **32**, 427–442 (2006).

[76]F. Antinori et al., "Strangeness enhancements at central rapidity in 40 A GeV/c Pb-Pb collisions", J. Phys. G **37**, edited by E. Fraga, T. Kodama, S. Padula, and J. Takahashi, 045105 (2010).

[77]B. I. Abelev et al., "Enhanced strange baryon production in Au + Au collisions compared to p + p at s(NN)**(1/2) = 200-GeV", Phys. Rev. C **77**, 044908 (2008).

[78]J. Adams et al., "Scaling Properties of Hyperon Production in Au+Au Collisions at s**(1/2) = 200-GeV", Phys. Rev. Lett. **98**, 062301 (2007).

[79]J. Adams et al., "Multistrange baryon production in Au-Au collisions at S(NN)**1/2 = 130 GeV", Phys. Rev. Lett. **92**, 182301 (2004).

[80]B. B. Abelev et al., "Multi-strange baryon production at mid-rapidity in Pb-Pb collisions at $\sqrt{s_{NN}}$ = 2.76 TeV", Phys. Lett. B **728**, [Erratum: Phys.Lett.B 734, 409–410 (2014)], 216–227 (2014).

[81]A. Taranenko, "PHENIX studies of the scaling properties of elliptic flow at RHIC", J. Phys. G **34**, edited by Y.-G. Ma, Z.-Y. Zhu, E.-K. Wang, X. Cai, H.-Z. Huang, and X.-N. Wang, S1069–1072 (2007).

[82]E. L. Simili, "Elliptic flow measurement at ALICE", PhD thesis (Utrecht U., 2009).

[83]T. Ludlam and L. McLerran, "What have we learned from the Relativistic Heavy Ion Collider?", Phys. Today **56N10**, 48–54 (2003).

[84]S. Voloshin and Y. Zhang, "Flow study in relativistic nuclear collisions by Fourier expansion of Azimuthal particle distributions", Z. Phys. C **70**, 665–672 (1996).

[85]M. Elnimr, "Dihadron Fragmentation Functions In Proton-Proton Collisions At The Relativistic Heavy Ion Collider (rhic)", PhD thesis (Wayne State U., Detroit, 2010).

[86]K. Aamodt et al., "Elliptic flow of charged particles in Pb-Pb collisions at 2.76 TeV", Phys. Rev. Lett. **105**, 252302 (2010).

[87]G. Aad et al., "Measurement of the distributions of event-by-event flow harmonics in lead-lead collisions at = 2.76 TeV with the ATLAS detector at the LHC", JHEP **11**, 183 (2013).

[88]A. Bilandzic, R. Snellings, and S. Voloshin, "Flow analysis with cumulants: Direct calculations", Phys. Rev. C **83**, 044913 (2011).

[89]A. M. Poskanzer and S. A. Voloshin, "Methods for analyzing anisotropic flow in relativistic nuclear collisions", Phys. Rev. C **58**, 1671–1678 (1998).

[90]J. Barrette et al., "Energy and charged particle flow in a 10.8-A/GeV/c Au + Au collisions", Phys. Rev. C **55**, [Erratum: Phys.Rev.C 56, 2336–2336 (1997)], 1420–1430 (1997).

[91]K. H. Ackermann et al., "Elliptic flow in Au + Au collisions at (S(NN))**(1/2) = 130 GeV", Phys. Rev. Lett. **86**, 402–407 (2001).

[92]C. Adler et al., "Elliptic flow from two and four particle correlations in Au+Au collisions at s(NN)**(1/2) = 130-GeV", Phys. Rev. C **66**, 034904 (2002).

[93]K. Adcox et al., "Flow measurements via two particle azimuthal correlations in Au+Au collisions at s(NN)**(1/2) = 130-GeV", Phys. Rev. Lett. **89**, 212301 (2002).

[94]B. B. Back et al., "Pseudorapidity and centrality dependence of the collective flow of charged particles in Au+Au collisions at s(NN)**(1/2) = 130-GeV", Phys. Rev. Lett. **89**, 222301 (2002).

[95]J. Adam et al., "Anisotropic flow of charged particles in Pb-Pb collisions at $\sqrt{s_{\mathrm{NN}}} = 5.02$ TeV", Phys. Rev. Lett. **116**, 132302 (2016).

[96]J. M. Heuser, "The compressed baryonic matter experiment at FAIR", Nucl. Phys. A **904-905**, edited by T. Ullrich, B. Wyslouch, and J. W. Harris, 941c–944c (2013).

[97]A. Schmah, "Highlights of the Beam Energy Scan from STAR", Central Eur. J. Phys. **10**, 1238–1241 (2012).

[98]A. Aduszkiewicz, "NA61/SHINE at the CERN SPS: Plans, status and first results", Acta Phys. Polon. B **43**, edited by H. Bialkowska and W. Florkowski, 635 (2012).

[99] D., D. Blaschke, V. Kharzeev, A. Matveev, H. Sorin, O. Socker, I. Teryaev, N. Tserruya, and Xu, eds., *Searching for a qcd mixed phase at the nuclotron-based ion collider facility (nica white paper)* (NICA White Paper, 2011), Draft v 5.01.

[100] https://fair-center.eu/, FAIR — Facility for Antiproton and Ion Research.

[101] A. Malakhov and A. Shabunov, eds., *Technical design report for the CBM superconducting dipole magnet* (GSI, Darmstadt, 2013), 80 S.

[102] *CBM progress report 2018*, tech. rep. CBM Progress Report 2018 (Darmstadt, 2019), 220 p.

[103] K. Kasinski, A. Rodriguez-Rodriguez, J. Lehnert, W. Zubrzycka, R. Szczygiel, P. Otfinowski, R. Kleczek, and C. J. Schmidt, "Characterization of the STS/MUCH-XYTER2, a 128-channel time and amplitude measurement IC for gas and silicon microstrip sensors", Nucl. Instrum. Meth. A **908**, 225–235 (2018).

[104] P. Senger and V. Friese, *CBM progress report 2020*, tech. rep. 2021-00421 (Darmstadt, 2021), 235 p.

[105] *CBM progress report 2019*, tech. rep. CBM-PR-2019 (Darmstadt, 2020), 216 p.

[106] *CBM progress report 2017*, tech. rep. CBM Progress Report 2017, ccby 4.0 CBM Progress Report 2017 - GSI-2018-00526 Barcode Bibliothek Sammlung Ort Beschreibung Ausleihfrist Status Abgabe-Datum Option(en)00040006 GSI/FAIR Library Monography S CBM 2017 - 4 weeks available - 00039994 GSI/FAIR Library Monography S CBM 2017 - 4 weeks available - (Darmstadt, 2018), V, 214 Seiten : Illustrationen, grafische Darstellungen.

[107] I. Selyuzhenkov and A. Toia, eds., *CBM progress report 2016*, Literaturangaben (GSI, Darmstadt, 2017), 223 Seiten : Illustrationen, grafische Darstellungen.

[108] J. Heuser, W. Müller, V. Pugatch, P. Senger, C. J. Schmidt, C. Sturm, and U. Frankenfeld, eds., *[GSI report 2013-4] technical design report for the CBM silicon tracking system (STS)* (GSI, Darmstadt, 2013), 167 p.

[109] *Technical design report for the CBM ring imaging cherenkov detector*, tech. rep. (2013), 215 p.

[110] *The transition radiation detector of the CBM experiment at FAIR : technical design report for the CBM transition radiation detector (TRD)*, tech. rep. FAIR Technical Design Report, ccby4 "This work was supported in part by the GSI Helmholtzzentrum für Schwerionenforschung, Darmstadt,its $F\&E-cooperation$ contracts with Frankfurt and Münster, the Facility for Antiproton andIon Research (FAIR), the German BMBF-Verbundforschung (05P15RFFC1 and 05P16PMFC1),the

EU FP6 and FP7 projects HadronPhysics2 (WP18 “FutureGas”) and HadronPhysics3 (WP19 “FuturePID”), the Romanian ANCSI/CAPACITATI Modul III Contract F02, the NUCLEU Project Contract PN 09370103, the Hessian LOEWE initiative HICforFAIR and the ExtreMe Matter Institute EMMI at GSI." (Darmstadt, 2018), 165 p.

[111]M. Petriş et al., “Performance of a two-dimensional position sensitive MRPC prototype with adjustable transmission line impedance”, Nucl. Instrum. Meth. A **920**, 100–105 (2019).

[112]A. Senger, “Simultaneous muon and reference hadron measurements in the Compressed Baryonic Matter experiment at FAIR”, Int. J. Mod. Phys. E **29**, 2030003 (2020).

[113]F. Guber and I. Selyuzhenkov, eds., *Technical design report for the CBM projectile spectator detector (PSD)* (GSI, Darmstadt, 2015), 75 S.

[114]P. M. Hohler and R. Rapp, “Evaluating chiral symmetry restoration through the use of sum rules”, EPJ Web Conf. **36**, edited by A. Badala, M. Bleicher, L. Fabbietti, C. Markert, R. F. Rapp, and J. Stroth, 00012 (2012).

[115]H. J. Specht, J. M. Nieves, E. Oset, and M. J. V.-V. and, “Thermal dileptons from hot and dense strongly interacting matter”, in AIP conference proceedings (2010).

[116]R. Arnaldi, “J/psi production in p-A and A-A collisions at fixed target experiments”, Nucl. Phys. A **830**, edited by P. Stankus, D. Silvermyr, S. Sorensen, and V. Greene, 345C–352C (2009).

[117]H. Santos, “J/psi and psi production in pb-pb collisions at 158 gev/nucleon”, Ph.D. thesis (Universidade Técnica de Lisboa-IST, Lisbon, 2004).

[118]S. Chattopadhyay, Y. P. Viyogi, P. Senger, W. F. J. Müller, and C. J. Schmidt, eds., *Technical design report for the CBM : muon chambers (much)* (GSI, Darmstadt, 2015), 190 S.

[119]S. Ahmad et al., “Design and performance simulation of a segmented-absorber based muon detection system for high energy heavy ion collision experiments”, Nucl. Instrum. Meth. A **775**, 139–147 (2015).

[120]`https://cbm-wiki.gsi.de/foswiki/bin/view/MuonSystem/MuchSimulation`, Muon simulations with CBMROOT.

[121]G. Battistoni, J. Bauer, T. T. Boehlen, F. Cerutti, M. P. W. Chin, R. Dos Santos Augusto, A. Ferrari, P. G. Ortega, W. Kozłowska, G. Magro, A. Mairani, K. Parodi, P. R. Sala, P. Schoofs, T. Tessonnier, and V. Vlachoudis, "The fluka code: an accurate simulation tool for particle therapy", Frontiers in Oncology **6** (2016) 10.3389/fonc.2016.00116.

[122]G. Battistoni et al., "Overview of the FLUKA code", Annals Nucl. Energy **82**, 10–18 (2015).

[123]A. Senger and P. Senger, "Probing Dense QCD Matter: Muon Measurements with the CBM Experiment at FAIR", Particles **4**, 205–213 (2021).

[124]I. Hrivnacova, D. Adamova, V. Berejnoi, R. Brun, F. Carminati, A. Fasso, E. Futo, A. Gheata, I. G. Caballero, and A. Morsch, "The virtual monte carlo", (2003) 10.48550/ARXIV.CS/0306005.

[125]*Root user's guide*, https://root.cern.ch/root/html534/guides/users-guide/ROOTUsersGuideA4.pdf.

[126]https://cds.cern.ch/record/1073159/files/cer-002728534.pdf, GEANT - Detector Description and Simulation Tool.

[127]I. Frohlich, T. Galatyuk, R. Holzmann, J. Markert, B. Ramstein, P. Salabura, and J. Stroth, "Design of the Pluto Event Generator", J. Phys. Conf. Ser. **219**, edited by J. Gruntorad and M. Lokajicek, 032039 (2010).

[128]I. B. Smirnov, "Modeling of ionization produced by fast charged particles in gases", Nucl. Instrum. Meth. A **554**, 474–493 (2005).

[129]I. B. Smirnov, *Cern comput. newslett. 226, 13*, http://cds.cern.ch/record/1024512/files/n-226.pdf, 1996.

[130]*Cbm-much digitization scheme for both event by event and time based mode*, https://git.cbm.gsi.de/computing/cbmroot/-/blob/master/sim/detectors/much/CbmMuchDigitizeGem.cxx.

[131]D. E. Groom, N. V. Mokhov, and S. I. Striganov, "Muon stopping power and range tables 10-MeV to 100-TeV", Atom. Data Nucl. Data Tabl. **78**, 183–356 (2001).

[132]U. Fano, "Penetration of protons, alpha particles, and mesons", Ann. Rev. Nucl. Part. Sci. **13**, 1–66 (1963).

[133]*Passage of particles through matter*, https://pdg.lbl.gov/2004/reviews/passagerpp.pdf.

[134]I. Kisel, "Event reconstruction in the CBM experiment", Nucl. Instrum. Meth. A **566**, edited by R. Bernhard, J. Gassner, F. Lehner, M. Needham, O. Steinkamp, U. Straumann, and A. Vollhardt, 85–88 (2006).

[135]I. Abt, I. Kisel, S. Masciocchi, and D. Emelyanov, "CATS: A cellular automaton for tracking in silicon for the HERA-B vertex detector", Nucl. Instrum. Meth. A **489**, 389–405 (2002).

[136]K. Große, ed., *GSI scientific report 2004 [GSI report 2005-1]*, Vol. 2005-1, GSI Report, Wissenschaftlicher Ergebnisbericht der GSI, GSI Annual Report (GSI, Darmstadt, 2005), 496 p.

[137]Q. Li, R. Li, K. Ji, and W. Dai, "Kalman filter and its application", in 2015 8th international conference on intelligent networks and intelligent systems (icinis) (2015), pp. 74–77.

[138]*Kalman filter*, https://www.kalmanfilter.net/default.aspx.

[139]C. K. Chui and G. Chen, *Kalman filtering* (Springer Cham).

[140]C. Amsler et al., "Review of Particle Physics", Phys. Lett. B **667**, 1–1340 (2008).

[141]W. Press, S. Teukolsky, W. Vetterling, and B. Flannery, *Numerical recipes: the art of scientific computing*, 3rd ed. (Cambridge University Press, 2007).

[142]R. Frühwirth and R. K. Bock, *Data analysis techniques for high-energy physics experiments*, edited by H. Grote, D. Notz, and M. Regler, Vol. 11 (Cambridge University Press, 2000).

[143]N. Bhatia and Vandana, "Survey of nearest neighbor techniques", CoRR **abs/1007.0085** (2010).

[144]E. Akishina, E. Alexandrov, I. Alexandrov, I. Filozova, V. Friese, and V. Ivanov, "Experience of the Development of the Geometry Database for the CBM Experiment", EPJ Web Conf. **214**, edited by A. Forti, L. Betev, M. Litmaath, O. Smirnova, and P. Hristov, 02030 (2019).

[145]https://redmine.cbm.gsi.de/projects/cbmroot/wiki/Guide, CbmRooT.

[146]https://root.cern.ch/doc/master/classTGeoManager.html, ROOT Reference Guide.

[147]https://git.cbm.gsi.de/CbmSoft/cbmroot_geometry/-/tree/master/macro/much, MuCh geometry on Cbm git repository.

[148]https://git.cbm.gsi.de/CbmSoft/cbmroot_geometry/-/blob/master/media.geo, Media used for CBM geometries.

[149]https://redmine.cbm.gsi.de/versions/14, CbmRoot release APR20.

[150]A. Senger and P. Senger, "Probing dense qcd matter: muon measurements with the cbm experiment at fair", Particles **4**, 205–213 (2021).

[151]S. Bachmann, A. Bressan, L. Ropelewski, F. Sauli, A. Sharma, and D. Mormann, "Charge amplification and transfer processes in the gas electron multiplier", Nucl. Instrum. Meth. A **438**, 376–408 (1999).

[152]M. Alfonsi et al., "Status of triple GEM muon chambers for the LHCb experiment", Nucl. Instrum. Meth. A **581**, edited by J. Hrubec, M. Jeitler, M. Krammer, M. Regler, and G. Badurek, 283–286 (2007).

[153]https://indico.cern.ch/event/45813/attachments/948117/1345155/LargeGEM.pdf, A large area gem detector.

[154]M. Ziegler, P. Sievers, and U. Straumann, "A triple GEM detector with two-dimensional readout", Nuclear Instruments and Methods in Physics Research Section A: Accelerators, Spectrometers, Detectors and Associated Equipment **471**, 260–263 (2001).

[155]P. P. Bhaduri and S. Chattopadhyay, "Response simulation of the GEM detector for the CBM experiment", DAE Symp. Nucl. Phys. **57**, edited by S. R. Jain, P. Shukla, A. Chatterjee, and V. M. Datar, 848–849 (2012).

[156]http://web-docs.gsi.de/~uhlig/doxygen/html/classCbmGeant3Settings.html, CbmGeant3Settings Class Reference.

[157]R. Brun, F. Bruyant, F. Carminati, S. Giani, M. Maire, A. McPherson, G. Patrick, and L. Urban, "GEANT Detector Description and Simulation Tool", (1994) 10.17181/CERN.MUHF.DMJ1.

[158]H. J. Specht, "Thermal Dileptons from Hot and Dense Strongly Interacting Matter", AIP Conf. Proc. **1322**, edited by J. M. Nieves, E. Oset, and M. J. Vicente Vacas, 1–10 (2010).

[159]J. Adamczewski-Musch et al., "Probing dense baryon-rich matter with virtual photons", Nature Phys. **15**, 1040–1045 (2019).

[160]R.-A. Tripolt, "Electromagnetic and weak probes: theory", Nucl. Phys. A **1005**, edited by F. Liu, E. Wang, X.-N. Wang, N. Xu, and B.-W. Zhang, 121755 (2021).

[161]T. Galatyuk, P. M. Hohler, R. Rapp, F. Seck, and J. Stroth, "Thermal Dileptons from Coarse-Grained Transport as Fireball Probes at SIS Energies", Eur. Phys. J. A **52**, 131 (2016).

[162]J. Cleymans, H. Oeschler, K. Redlich, and S. Wheaton, "Comparison of chemical freeze-out criteria in heavy-ion collisions", Phys. Rev. C **73**, 034905 (2006).

[163]H. T. Ding et al., "Chiral Phase Transition Temperature in (2+1)-Flavor QCD", Phys. Rev. Lett. **123**, 062002 (2019).

[164]W. Cassing, E. L. Bratkovskaya, and A. Sibirtsev, "Open charm production in relativistic nucleus-nucleus collisions", Nucl. Phys. A **691**, 753–778 (2001).

[165]A. Andronic, P. Braun-Munzinger, and J. Stachel, "Hadron production in central nucleus-nucleus collisions at chemical freeze-out", Nucl. Phys. A **772**, 167–199 (2006).

[166]L. Van Hove, "Two Problems Concerning Hot Hadronic Matter and High-Energy Collisions (Equilibrium Formation, Plasma Deflagration)", Z. Phys. C **21**, edited by A. Giovannini, 93–98 (1983).

[167]M. Gyulassy, K. Kajantie, H. Kurki-Suonio, and L. D. McLerran, "Deflagrations and Detonations as a Mechanism of Hadron Bubble Growth in Supercooled Quark Gluon Plasma", Nucl. Phys. B **237**, 477–501 (1984).

[168]A. Bialas and R. B. Peschanski, "Moments of Rapidity Distributions as a Measure of Short Range Fluctuations in High-Energy Collisions", Nucl. Phys. B **273**, 703–718 (1986).

[169]W. Ochs and J. Wosiek, "Intermittency and Jets", Phys. Lett. B **214**, 617–620 (1988).

[170]A. Bialas and R. B. Peschanski, "Intermittency in Multiparticle Production at High-Energy", Nucl. Phys. B **308**, 857–867 (1988).

[171]Y.-L. Xie, G. Chen, J.-L. Wang, Z.-H. Liu, and M.-J. Wang, "Scaling properties of multiplicity fluctuations in heavy ion collisions simulated by AMPT model", Nucl. Phys. A **920**, 33–44 (2013).

[172]A. Bialas and M. Gazdzicki, "A New variable to study intermittency", Phys. Lett. B **252**, 483–486 (1990).

[173]W. Ochs, "The importance of phase space dimension in the intermittency analysis of multi - hadron production", Phys. Lett. B **247**, 101–106 (1990).

[174]P. Lipa and B. Buschbeck, "From strong to weak intermittency", Phys. Lett. B **223**, 465–469 (1989).

[175]R. C. Hwa, "Fractal Measures in Multiparticle Production", Phys. Rev. D **41**, 1456 (1990).

[176]A. Bialas and R. C. Hwa, "Intermittency parameters as a possible signal for quark - gluon plasma formation", Phys. Lett. B **253**, 436–438 (1991).

[177]J. Wosiek, "Intermittency in the ising systems", Acta Physica Polonica, Series B **19**, 863–866 (1988).

[178]H. Satz, "Intermittency and Critical Behavior", Nucl. Phys. B **326**, 613–618 (1989).

[179]N. G. Antoniou, E. N. Argyres, C. G. Papadopoulos, A. P. Contogouris, and S. D. P. Vlassopulos, "Intermittency, Kadanoff Scaling and Hadronization", Phys. Lett. B **245**, 619–623 (1990).

[180]J. L. Klay et al., "Charged pion production in 2 to 8 agev central au+au collisions", Phys. Rev. C **68**, 054905 (2003).

[181]J. L. Klay et al., "Longitudinal flow from 2-A-GeV to 8-A-GeV Au+Au collisions at the Brookhaven AGS", Phys. Rev. Lett. **88**, 102301 (2002).

[182]D. Zschiesche, S. Schramm, J. Schaffner-Bielich, H. Stoecker, and W. Greiner, "Particle ratios at RHIC: Effective hadron masses and chemical freezeout", Phys. Lett. B **547**, 7–14 (2002).

[183]J. Steinheimer, S. Schramm, and H. Stocker, "The hadronic SU(3) Parity Doublet Model for Dense Matter, its extension to quarks and the strange equation of state", Phys. Rev. C **84**, 045208 (2011).

[184]D. H. Rischke, Y. Pursun, and J. A. Maruhn, "Relativistic hydrodynamics for heavy ion collisions. 2. Compression of nuclear matter and the phase transition to the quark - gluon plasma", Nucl. Phys. A **595**, [Erratum: Nucl.Phys.A 596, 717–717 (1996)], 383–408 (1995).

[185]V. Klochkov and I. Selyuzhenkov, "Centrality determination in heavy-ion collisions with the CBM experiment", J. Phys. Conf. Ser. **798**, edited by A. Galper, A. Petrukhin, A. Taranenko, I. Selyushenkov, M. Skorokhvatov, S. Rubin, V. Dmitrnko, and Y. Gurov, 012059 (2017).

[186]M. J. Kirkby, "The fractal geometry of nature. benoit b. mandelbrot. w. h. freeman and co., san francisco, 1982. no. of pages: 460. price: £22.75 (hardback)", Earth Surface Processes and Landforms **8**, 406–406 (1983).

[187]G. Paladin and A. Vulpiani, "Anomalous scaling laws in multifractal objects", Physics Reports **156**, 147–225 (1987).

[188]H. Hentschel and I. Procaccia, "The infinite number of generalized dimensions of fractals and strange attractors", Physica D: Nonlinear Phenomena **8**, 435–444 (1983).

[189]P. Grassberger and I. Procaccia, "Dimensions and entropies of strange attractors from a fluctuating dynamics approach", Physica D: Nonlinear Phenomena **13**, 34–54 (1984).

[190]T. C. Halsey, M. H. Jensen, L. P. Kadanoff, I. Procaccia, and B. I. Shraiman, "Fractal measures and their singularities: the characterization of strange sets", Phys. Rev. A **33**, 1141–1151 (1986).

[191]M. H. Jensen, L. P. Kadanoff, A. Libchaber, I. Procaccia, and J. Stavans, "Global universality at the onset of chaos: results of a forced rayleigh-bénard experiment", Phys. Rev. Lett. **55**, 2798–2801 (1985).

[192]I. Ajinenko, Y. Belokopytov, H. Böttcher, F. Botterweck, P. Chliapnikov, F. Crijns, A. De Roeck, E. De Wolf, K. Dziunikowska, P. Ermolov, Z. Garutchava, N. Grigoryan, P. Van Hal, T. Haupt, W. Kittel, B. Levchenko, J. Mäkelä, E. Markhorst, F. Meijers, A. Michałowska, V. Nikolaenko, L. Oliveira, K. Olkiewicz, V. Ronjin, A. Rybin, H. Rollof, H. Saarikko, L. Scholten, V. Shakbazyan, J. Stepaniak, O. Tchikilev, A. Tomoradze, V. Uvarov, F. Verbeure, R. Wischnewski, W. Zielinski, and S. Zotkin, "Intermittency patterns in +p and k+p collisions at 250 gev/c", Physics Letters B **222**, 306–310 (1989).

[193]C. B. Chiu and R. C. Hwa, "Multifractal Structure of Multiparticle Production in the Branching Models", Phys. Rev. D **43**, 100–103 (1991).

[194]J. Feder, *Fractals* (Springer New York, NY).

[195]M. I. Adamovich et al., "Scaled factorial moment analysis of 200-A/GeV sulfur + gold interactions", Phys. Rev. Lett. **65**, 412–415 (1990).

[196]M. I. Adamovich et al., "Produced particle multiplicity dependence on centrality in nucleus-nucleus collisions", J. Phys. G **22**, 1469–1481 (1996).

[197]M. Adamovich, M. Aggarwal, N. Andreeva, Z. Anson, Z. Ameeva, R. Arora, Y. Alexandrov, S. Azimov, E. Basova, K. Bhalla, A. Bhasin, V. Bhatia, V. Bubnov, R. Bondarenko, T. Burnett, X. Cai, I. Chasnicov, L. Chernova, M. Chernyavsky, B. Dressel, L. Eremenko, G. Eligbaeva, E. Friedlander, S. Gadzhieva, A. Gaitinov, E. Ganssauge, S. Garpman, S. Gerassimov, A. Gill, J. Grote, K. Gulamov, U. Gulyamov, S. Hackel, H. Heckman, B. Judek, S. Kachroo, F. Kadyrov, H. Kallies, G. Kalyachkina, E. Kanygina, G. Kaul, M. Kaur, S. Kharlamov, T. Koss, V. Kumar, P. Lal, V. Larionova, P. Lindstrom, L. Liu, S. Lokanathan, J. Lord, N. Lukicheva, L. Mangotra, N. Maslennikova, I. Mittra, S. Mookerjee, C. Mueller, S. Nasyrov, V. Navotny, G. Orlova, I. Otterlund, N. Peresadko, S. Persson, N. Petrov, W. Qian, R. Raniwala, S. Raniwala, N. Rao, J. Rhee, N. Saidkhanov, N. Salmanova, T. Shakhova, W. Schultz, V. Shukla, D. Skelding, K. Soderstrom, E. Stenlund, R. Storey, S. Strausz, J. Sun, L. Svechnikova, M. Tretyakova, T. Trofimova, H. Wang, Z. Weng, R. Wilkes, G. Xu, D. Zhang, P. Zheng, D. Zhou, and J. Zhou, "Rapidity densities and their fluctuations in

central 200 a gev 32s interactions with au and ag, br nuclei emu01 collaboration", Physics Letters B **227**, 285–290 (1989).

[198]M. Adamovich, Y. Alexandrov, S. Asimov, S. Badyal, E. Basova, K. Bhalla, A. Bhasin, R. Bondarenkov, T. Burnett, X. Cai, L. Chernova, M. Chernyavsky, B. Dressel, E. Friedlander, S. Gadzhieva, E. Ganssauge, S. Garpman, S. Gerassimov, A. Gill, J. Grote, K. Gulamov, V. Gulyamov, V. Gupta, S. Hackel, H. Heckman, B. Jakobsson, B. Judek, F. Kadyrov, H. Kallies, Y. Karant, S. Kharlamov, S. Kitroo, J. Kohli, G. Koul, V. Kumar, P. Lal, V. Larinova, P. Lindstrom, L. Liu, S. Lokanathan, J. Lord, N. Lukicheva, L. Mangotra, N. Maslennikova, E. Monnand, S. Mookerjee, C. Mueller, S. Nasyrov, W. Nawotny, G. Orlova, I. Otterlund, N. Peresadko, S. Persson, N. Petrov, R. Raniwala, S. Raniwala, N. Rao, J. Rhee, N. Salmanova, W. Schulz, F. Schussler, V. Shukla, D. Skelding, K. Soderstrom, E. Stenlund, R. Storey, J. Sun, M. Tretyakova, T. Trofimova, Z. Weng, R. Wilkes, G. Xu, and P. Zheng, "Multiplicities and rapidity densities in 200 a gev 16o interactions with emulsion nuclei", Physics Letters B **201**, 397–402 (1988).

[199]M. I. Adamovich, M. M. Aggarwal, Y. A. Alexandrov, Z. V. Ameeva, N. P. Andreeva, Z. V. Anzon, R. Arora, S. K. Badyal, K. B. Bhalla, A. Bhasin, V. S. Bhatia, V. I. Bubnov, T. H. Burnett, X. Cai, I. Y. Chasnikov, L. P. Chernova, M. M. Chernyavski, B. Dressel, G. Z. Eligbaeva, L. E. Eremenko, E. M. Friedlander, S. I. Gadzhieva, A. S. Gaitinov, E. R. Ganssauge, S. Garpman, S. G. Gerassimov, A. Gill, J. G. Grote, K. G. Gulamov, U. G. Gulyamov, V. K. Gupta, S. Hackel, H. H. Heckman, H. Haung, B. Judek, S. Kachroo, F. G. Kadyrov, G. S. Kalyachkina, E. K. Kanygina, G. L. Kaul, M. Kaur, S. P. Kharlamov, T. Koss, V. Kumar, P. Lal, V. G. Larionova, P. J. Lindstrom, L. S. Liu, S. Lokanathan, J. J. Lord, N. S. Lukicheva, S. B. Luo, N. V. Maslennikova, L. K. Mangotra, I. S. Mittra, S. Mookerjee, C. Mueller, S. H. Nasyrov, V. S. Navotny, G. I. Orlova, I. Otterlund, N. G. Peresadko, S. Persson, N. V. Petrov, W. Y. Qian, R. Raniwala, S. Raniwala, N. K. Rao, J. T. Rhee, N. A. Salmanova, W. Schultz, C. I. Shakhova, V. S. Shukla, B. Singh, D. Skelding, K. Soderstrom, E. Stenlund, S. C. Strausz, J. F. Sun, L. N. Svechnikova, M. I. Tretyakova, H. Q. Wang, Z. Q. Weng, R. J. Wilkes, G. F. Xu, D. H. Zhang, P. Y. Zheng, D. C. Zhou, and J. C. Zhou, "Scaled-factorial-moment analysis of 200a-gev sulfur+gold interactions", Phys. Rev. Lett. **65**, 412–415 (1990).

[200]S. Ahmad, A. Ahmad, A. Chandra, M. Zafar, and M. Irfan, "Forward–backward multiplicity fluctuations in 200a gev/c 16o–agbr and 32s–agbr collisions", Physica Scripta **87**, 045201 (2013).

[201]S. Ahmad, M. M. Khan, S. Khan, A. Khatun, and M. Irfan, "A study of event-by-event fluctuations in relativistic heavy-ion collisions", Int. J. Mod. Phys. E **23**, 1450065 (2014).

[202]R. Hasan, M. Zafar, M. S. Ahmad, and A. Tufail, "Evidence for intermittency in hadron nucleus and nucleus nucleus collisions at relativistic energies", Int. J. Mod. Phys. A **14**, 3451–3465 (1999).

[203]D. Zhang, H. Zhao, F. Liu, C. He, H. Jia, X. Li, Z. Li, and J. Li, "Multifractal analysis of multiplicity fluctuations in 16o–emulsion interactions at 3.7agev", Radiation Measurements **43**, Proceedings of the 23rd International Conference on Nuclear Tracks in Solids, S229–S233 (2008).

[204]P. L. Jain, G. Singh, and A. Mukhopadhyay, "Multifractals at relativistic energies", Phys. Rev. C **46**, 721–726 (1992).

[205]N. Ahmad, A. Kamal, M. M. Khan, Hushnud, and A. Tufail, "On Multifractal Spectra and Renyi Dimensions in 14.5A GeV/c ^{28}Si-nucleus Collisions", J. Mod. Phys. **5**, 1288–1293 (2014).

[206]B. Nilsson-Almqvist and E. Stenlund, "Interactions Between Hadrons and Nuclei: The Lund Monte Carlo, Fritiof Version 1.6", Comput. Phys. Commun. **43**, 387 (1987).

[207]R. K. Shivpuri and N. Parashar, "Target and energy dependence of intermittency and multifractality in interactions at cosmic ray energies", Phys. Rev. D **49**, 219–229 (1994).

[208]D. Ghosh, P. Ghosh, A. Deb, A. Ghosh, and J. Roy, "Study on fractality in nucleus-nucleus interaction at a few GeV/c", Phys. Lett. B **272**, 5–10 (1991).

[209]P. Mali, A. Mukhopadhyay, S. K. Manna, P. K. Haldar, and G. Singh, "Multifractal analysis of charged particle distributions using horizontal visibility graph and sandbox algorithm", Mod. Phys. Lett. A **32**, 1750024 (2017).

[210]C. B. Chiu and R. C. Hwa, "Multifractal Structure of Multiparticle Production in the Branching Models", Phys. Rev. D **43**, 100–103 (1991).

[211]R. K. Shivpuri and V. K. Verma, "Target dependence of intermittency and multifractality of multiplicity fluctuations in 800-GeV proton emulsion nuclei interactions", Phys. Rev. D **47**, [Erratum: Phys.Rev.D 48, 436 (1993)], 123–132 (1993).

[212]G. Paladin and A. Vulpiani, "Anomalous scaling laws in multifractal objects", Physics Reports **156**, 147–225 (1987).

[213]R. B. Peschanski, "On the Existence of a Nonthermal Phase Transition in Multiparticle Production", Nucl. Phys. B **327**, 144–156 (1989).

List of publications

Journals

- **Intermittency analysis in relativistic hydrodynamic simulations of heavy-ion collision at FAIR energies.**
  O. Singh, Anjali Sharma and N. Ahmad
  communicated with Eur. Phys. J. A

- **A multifractal study of charged secondaries produced in relativistic nucleus–nucleus collisions**
  Nazeer Ahmad , Tufail Ahmad, **Omveer Singh**
  Eur. Phys. J. Plus (2022) 137:653

- **Commissioning and testing of pre-series triple GEM prototypes for CBM-MuCh in the mCBM experiment at the SIS18 facility of GSI**
  A. Kumar, A. Agarwal, S. Chatterjee, S. Chattopadhyay, A.K. Dubey, C. Ghosh, E. Nandy, V. Negi, S.K. Prasad, J. Saini, V. Singhal, **O. Singh**, G. Sikder, J. de Cuveland, I. Deppner, D. Emschermann, V. Friese, J. Frühauf, M. Gumiński, N. Herrmann, D. Hutter, M. Kis, J. Lehnert, P.-A. Loizeau, C.J. Schmidt, C. Sturm, F. Uhlig and W. Zabołotny
  ***Journal of Instrumentation*, 16, 2021, P09002**

- **A study of multifractal analysis in ^{16}O-AgBr collisions at 60 A and 200 A GeV.**
  N. Ahmad , A. Tufail and **Omveer Singh**
  ***Journal of Modern Physics*, 2018, Vol. 9 No.5, 1029-1036**

National conference proceedings & Internal notes

- **Realistic Muon Chamber (MuCh) geometry simulation for the CBM experiment at FAIR**
  Omveer Singh, Partha Pratim Bhaduri, Subhasis Chattopadhyay, Nazeer Ahmad
  ***DAE Symp.Nucl.Phys.* 63 (2018) 1002-1003**

- **On Scaling Properties of Multiplicity Fluctuations in 60 A and 200 A GeV/c ^{16}O-AgBr Collisions**
  N Ahmad, M. Mohshin Khan, **Omveer Singh**, Tufail Ahmad
  ***DAE Symp.Nucl.Phys.* 63 (2018) 1008-1009**

- **On Multifractality in 60 A and 200 A GeV/c ^{16}O-AgBr Collisions**
  Nazeer Ahmad, **Omvir Singh**, Shakeel Ahmad
  ***DAE Symp.Nucl.Phys.* 62 (2017) 860-861**

- **Multifractality in pp Collisions at LHC Energies**
  N. Ahmad and **Omveer Singh**
  ***DAE Symp.Nucl.Phys.* 61 (2016) 834-835**

- **Implementation of Muon Chamber (MuCh) geometries in the CbmRoot software**
  Omveer Singh, Ekata Nandy, Partha Pratim Bhaduri, David Emschermann, Vikas Singhal and Subhasis Chattopadhyay
  ***CBM-CN-19002*, 13 July 2019**

- **Non-monolithic design of the 5 th MuCh absorber parameters and tolerances**
  Sayak Chatterjee, Partha Pratim Bhaduri, **Omveer Singh**, Volodia Nikulin and Subhasis Chattopadhyay
  ***CBM-TN-20006*, September 30, 2020**

- **Implementation and performance simulation of realistic design of the GEM chambers for the first two stations of MuCh**
  O. Singh, S. Chatterjee, P. P. Bhaduri, and S. Chattopadhyay
  ***CBM Progress Report 2020*, p. 79-80, ISBN 978-3-9815227-9-2, DOI:10.15120/GSI-2021-00421**

- **Reconstruction of J/ψ mesons at SIS100 energies with realistic MuCh set up**
  S. Chatterjee, **O. Singh**, A. Senger, P. P. Bhaduri, and S. Chattopadhyay
  ***CBM Progress Report 2019*, p. 181-182, ISBN 978-3-9815227-8-5,**
  DOI: 10.15120/GSI-2020-009041

- **Reconstruction of ω mesons at SIS100 with realistic MuCh set up**
  O. Singh, S.Chatterjee, P. P. Bhaduri, S. Chattopadhyay, A. Senger, and T. Galatyuk
  ***CBM Progress Report 2019* p. 179-180, ISBN 978-3-9815227-8-5,**
  DOI: 10.15120/GSI-2020-00904

- **Effect of gaps on the fifth absorber of Muon Chamber (MuCh) for the CBM experiment at FAIR**
  S. Chatterjee, **O. Singh**, P. P. Bhaduri, S. Chattopadhyay, and V. Nikulin
  ***CBM Progress Report 2019* p. 99-100, ISBN 978-3-9815227-8-5,**
  DOI: 10.15120/GSI-2020-00904

- **Effect of absorbers surface tolerance on the Muon Chamber (MuCh) performance for the CBM experiment at FAIR**
  S. Chatterjee, **O. Singh**, P. P. Bhaduri, S. Chattopadhyay, A. Senger, and V. Nikulin
  ***CBM Progress Report 2019* p. 97-98, ISBN 978-3-9815227-8-5,**
  DOI: 10.15120/GSI-2020-00904

- **Evolution of First Absorber in Muon Chamber**
  O. Singh, P. P. Bhaduri, E. Nandy, S. Chatterjee, S. Chattopadhyay, A. Senger, V. Nikulin, and N. Ahmad
  ***CBM Progress Report 2019* p. 95-96, ISBN 978-3-9815227-8-5,**
  DOI: 10.15120/GSI-2020-00904

- **Optimization of RPC detector segmentation and charge threshold in 3^{rd} and 4^{th} MUCH Station**
  Ekata Nandy, **Omveer Singh**, Vikas Singhal, Zubayer Ahammed, Partha Pratim Bhaduri, and Subhasis Chattopadhyay
  ***CBM Progress Report 2019* p. 76-77, ISBN 978-3-9815227-8-5,**
  DOI: 10.15120/GSI-2020-00904

- **Implementation of RPC geometry and digitization in the 3^{rd} and 4^{th} MUCH station**

E. Nandy, **O. Singh**, V. Singhal, Z. Ahammed, P. P. Bhaduri, and S. Chattopadhyay
CBM Progress Report 2018 **p. 163-164, ISBN 978-3-9815227-6-1, DOI:10.15120/GSI-2019-01018**

- **Realistic Muon Chamber (MuCh) geometry simulation for the CBM experiment at FAIR**
  O. Singh, P. Bhaduri, E. Nandy, S. Chattopadhyay, and N. Ahmad
  CBM Progress Report 2018 **p. 161-162, ISBN 978-3-9815227-6-1, DOI:10.15120/GSI-2019-01018**

- **Development of muon detection system (MUCH) for the CBM experiment at FAIR**
  S. Chattopadhyay, A.K. Dubey, Z. Ahammed, J. Saini, P. Bhaduri, E. Nandy, V. Negi, M. Mandal, A. Kumar, C.Ghosh, S. Prasad, S. Biswas, S. Das, D. Emschermann, C. Schmidt, P. A. Loizeau, A. Senger, **O. Singh**
  The CBM collaboration, and the FAIR@GSI division, GSI-FAIR SCIENTIFIC REPORT 2017 **p. 21, RESEARCH-NQM-CBM-11, DOI:10.15120/GR-2018-1**

- **First results of mMUCH simulation for the mCBM full system setup at SIS18**
  O. Singh, P. Bhaduri, E. Nandy, S. Chattopadhyay, and N. Ahmad
  CBM Progress Report 2017 **p. 178, ISBN 978-3-9815227-5-4, DOI: 10.15120/GSI-2018-00485**

- **Description of the CBM-MUCH geometry in CbmRoot**
  O. Singh, P. Bhaduri, D. Emschermann, V. Singhal, S. Chattopadhyay, and N. Ahmad
  CBM Progress Report 2017 **p. 140, ISBN 978-3-9815227-5-4, DOI: 10.15120/GSI-2018-00485**

- **Implementation of RPC geometry for the 3^{rd} and 4^{th} station of CBM-MUCH**
  E. Nandy, Z. Ahmed, **O. Singh**, and S. Chattopadhyay
  CBM Progress Report 2017 **p. 68, ISBN 978-3-9815227-5-4, DOI: 10.15120/GSI-2018-00485**

Journal pre-prints

Eur. Phys. J. Plus (2022) 137:653
https://doi.org/10.1140/epjp/s13360-022-02787-4

THE EUROPEAN PHYSICAL JOURNAL PLUS

Regular Article

A multifractal study of charged secondaries produced in relativistic nucleus–nucleus collisions

Nazeer Ahmad, Tufail Ahmad[a], Omveer Singh

Department of Physics, Aligarh Muslim University, Aligarh 202002, India

Received: 31 January 2021 / Accepted: 2 May 2022

Abstract An analysis of the data obtained in 14.5A GeV/c ^{28}Si–nucleus interactions has been carried out to study the multiplicity fluctuations by using the method of multifractality. A power-law behaviour is found to exist in this study. Experimental results have been compared with those of FRITIOF-generated events. The dependence of various parameters characterizing multifractality for two groups of events chosen on the basis of grey particle multiplicity is also looked into.

1 Introduction

The multiparticle production process, in hadron–nucleus (hA) and nucleus–nucleus (AA) collisions, has been studied extensively in the past [1–27]. The major goal to study AA collisions is to investigate the properties of quark–gluon plasma (QGP) [28, 29] that is the de-confined state of matter. There are many signatures [30–33] of QGP; one of the techniques to study this is the fluctuations in the particle densities. Fluctuations in individual events/interactions may give rise to peaks or spikes in the phase space domains [34–36]. These may be studied using the method of scaled factorial moments of the multiplicity distributions by dividing them into different pseudo-rapidity, η, bin sizes [37]. Pseudo-rapidity is defined as:

$$\eta = -\ln \tan\frac{\theta}{2} \tag{1}$$

where θ is the space angle of a charged particle track made with the mean primary direction.

To study the self-similarity of multiplicity fluctuations in particle production, Bialas and Peschanski [38] proposed that if we study the variations of factorial moments with decreasing bin sizes, it shows a power-law behaviour, which is referred to as intermittency. The search for a link between intermittency and phase transition leads to the thermodynamic formulation of fractal dimensions of which intermittency is a special case. This has been discussed by various workers [39–42].

A fractal or a self-similar object has the characteristics of satisfying a power-law behaviour which reflects the underlying dynamics [43]. In the present work, the method of multifractal moments,G_q [43], has been used to investigate the scaling properties of relativistic AA collisions. The investigation of heavy-ion collisions at relativistic energies may reveal some information about the nature of the interaction mechanism. To understand multiparticle production, the nuclear emulsion technique [44, 45] has been used. The nuclear emulsion is a material that detects charged particles only. It is one of the oldest particle detection techniques. It is compact and has a 4π detection capability. The nuclear emulsion consists of various elements like hydrogen (H), carbon (C), nitrogen (N), oxygen (O), silver (Ag) and bromine (Br). When a high energy particle or ion interacts with the nuclei of emulsion, a large number of particles are produced.

2 Mathematical formalism

To study multifractality on event-by-event basis, a given pseudo-rapidity range, $\Delta\eta$ $(= \eta_{\max} - \eta_{\min})$, is divided into M bins (1–15) of width $\delta\eta = \Delta\eta/M$. The qth-order multifractal moments, G_q, are defined [41, 43] as:

$$G_q = \sum_{j=1}^{M} p_j^q \tag{2}$$

[a] e-mail: tufailahmadphys@gmail.com (corresponding author)

Published online: 03 June 2022

where summation has been performed over the non-empty bins only, which constitute a fractal set. Here $p_j = n_j/n_t$; n_j denote the number of particles in the considered bin and n_t is the total number of particles in the considered η range in an event which is (0–6) that is η_{max} is 6 and η_{min} is zero. When it is averaged over the entire data sample consisting of N events, it may be expressed as:

$$\langle G_q \rangle = \left(\frac{1}{N}\right) \sum_{1}^{N} G_q \tag{3}$$

For the observation of multifractality in the rapidity distribution, mean values of multifractal moments, $\langle G_q \rangle$, should give rise to a power-law behaviour over a small η range in the following way:

$$\langle G_q \rangle \propto (\delta\eta)^{T_q} \tag{4}$$

where T_q are the mass exponents and may be determined from the observed linear dependence of $\ln \langle G_q \rangle$ on $\ln M$ using Eq. 4.

The generalized dimensions D_q and multifractal spectral function, $f(\alpha_q)$, may be obtained [43] by applying Legendre transform that is the standard procedure of multifractals [38] from the following equations:

$$D_q = \frac{T_q}{(q-1)} \tag{5}$$

$$\text{and} \quad f(\alpha_q) = q\alpha_q - \mathrm{T}_q \tag{6}$$

where α_q is referred to as the Lipchitz–Holder exponents [46] and is defined as:

$$\alpha_q = \frac{\mathrm{d}T_q}{\mathrm{d}q}. \tag{7}$$

Regarding the investigation of multifractality, a spectral function is considered as one of the main parameters. For the observance of a multifractal structure, the spectral function is smooth concave downwards with its maximum at $\alpha_q = 0$. The left ($q > 0$) and right ($q < 0$) wings of the plots of the multifractal function, $f(\alpha_q)$, indicate the fluctuation in the particle density in the dense and sparse regions of single-particle pseudo-rapidity distribution [47]. The in-homogeneity in the pseudo-rapidity distribution is determined by the width of the distribution. There is non-existence of a sharp peak in the plot of $f(\alpha_q)$, versus α_q at α_q corresponding to $q = 0$, which reveals the non-smooth nature of the pseudo-rapidity distribution. One of the basic properties of the fractals that describe the scaling behaviour is the generalized dimensions, D_q. It is found that D_q decreases with increasing order of the moments; this decreasing pattern is known as multifractal, and on the other hand, if D_q is constant with q, the pattern is referred to as mono-fractal [48, 49].

3 Details of the data

The emulsion stack used in the present study was exposed to a 14.5A GeV/c silicon beam at Alternating Gradient Synchrotron (AGS), Brookhaven National Laboratory (BNL). The method of line scanning was adopted to search the interactions by using M4000 Cooke's series microscopes with 15 × eyepieces and 20 × objectives. The events/interactions were picked up after leaving 3 mm from the leading edges of the pellicles to avoid any distortion effects. The interactions that were produced 35 μm from the top or bottom surface of the pellicles were excluded from the data.

To avoid any contamination of primary events with secondary interactions, the primaries of all the events were followed back up to the edge of the pellicles. Only those events whose primary remained parallel to the main direction of the beam and which did not show any significant change in their ionization were finally picked up as genuine primary events. The different types of particles appear in the form of tracks and usual emulsion terminology [44, 45] was applied to categorise such tracks. The tracks were classified on the basis of their specific ionization g^* ($= g/g_0$), where g is the ionization of the track and g_0 is the ionization of the primary. The tracks with $g^* < 1.4$, $1.4 \leq g^* \leq 10$, and $g^* > 10$ were named as shower, grey, and black tracks/particles, respectively. The number of the shower, grey, and black tracks in an event has been denoted by N_s, N_g, and N_b, respectively.

The angular measurements were taken by using an oil immersion objective of 100 × magnification. For the calculation of space angle, the projected angle is to be measured first. The tracks of relativistic charged particles in the most forward cone overlap with each other so it becomes difficult to measure the projected angle of such tracks directly, for this purpose coordinate method [49] was applied. In this X, Y, and Z coordinates were measured. The star vertex, the point from where different tracks originate, is moved along the X-axis of the stage of the microscope, and when the track looked separated, their X, Y, and Z coordinates were measured and the projected angle was calculated. Thus, after applying the above-discussed criterion, a sample of 555 clean events was selected for the present study.

4 Results and discussion

To compare the experimental results with the Lund model, FRITIOF [50, 51], on multiparticle production and Monte Carlo random number generator (MC-RAND), 5000 events for each were generated with similar characteristics as that of experimental events observed in 14.5A GeV/c ^{28}Si-nucleus interactions. FRITIOF events were generated based on the average value of relativistic charged particles and dispersion of its experimental multiplicity distribution so that we get the average value in the case of simulated data as almost the same as that of the experimental events. However, in the generation of the MC-RAND events, we tried to make sure that the multiplicity distribution of the produced particles should be similar to that of experimental events and there should not be any correlation amongst the produced particles. The pseudo-rapidity distribution for experimental as well as generated events is shown in Fig. 1. The shape of the distribution is of Gaussian type for both the data. One more criterion which we applied is that the mean value and dispersion of the produced particles are comparable to the experimental values. The basic difference between FRITIOF and MC-RAND is that the MC-RAND events are correlation-free, whereas FRITIOF events have the same correlation as that of the experimental events [50, 51].

Before we proceed further for results and discussions, we calculated mean number of relativistic charged particles ($\langle N_s \rangle$) for experimental as well as FRITIOF events. The mean number of relativistic charged particles is calculated by dividing the total number of charged particles in the data sample by the total number of events. Mean pseudo-rapidity is calculated as the sum of pseudo-rapidities of all the relativistic charged particles divided by the total number of relativistic charged particles in the entire data sample. The dispersion of the pseudo-rapidity distribution, $D(\eta)$, is calculated as $D(\eta) = \sqrt{\left(\langle \eta^2 \rangle - \langle \eta \rangle^2\right)}$. We found the mean number of relativistic charged particles, average pseudo-rapidity, and dispersion of the pseudo-rapidity distribution as 19.76 ± 1.91, 2.45 ± 0.08, and 0.95 ± 0.08, respectively, for experimental events. The mean multiplicity of the relativistic charged particles, average pseudo-rapidity, and dispersion of the pseudo-rapidity distribution for FRITIOF simulated events come out to be 21.32 ± 0.95, 2.83 ± 0.16, and 1.28 ± 0.03, respectively, which are very close to that of the experimental events. As the average values and the dispersion in the two cases, i.e., experimental and FRITIOF, are found to be almost the same, we can say that the experimental data matches with the data of the FRITIOF model.

The values of $\ln\langle G_q \rangle$ have been plotted as a function of $\ln M$ for experimental and FRITIOF in Fig. 2 for $q = -6, -4, -2$, 0, 2, 4 and 6. A linear increase in the variation of fractal moments with increasing bin size, M, is observed for both the data sets. Furthermore, the moments with positive values of q and for negative q values give a linear relationship over a wide range of $\ln M$; thus, the moment shows self-similarity in the mechanism of particle production for the nuclear interactions considered. The plots for the simulated events are in good agreement with that of the experimental events. Similar results have been reported for hA [52] and AA [53] collisions.

The variation of $\ln\langle G_q \rangle$ with $\ln M$ at 14.5A GeV/c ^{28}Si–nucleus interactions for two groups of events, i.e. $N_g \leq 1$ and $N_g \geq 2$, is exhibited in Fig. 3. The multifractal moments are observed to increase linearly with decreasing bin width, $\delta\eta$ for the two groups of interactions considered in the study. Furthermore, it is observed that G_q moments have slightly higher values for the interactions having $N_g \geq 2$ than those of having $N_g \leq 1$.

The mass exponents, T_q, are obtained by studying the dependence of $\ln\langle G_q \rangle$ on $\ln M$. For carrying out approximations, only the portions of the curves that show linearity are taken into account to avoid the saturation effect. The values of T_q, in ^{28}Si–nucleus collisions obtained for experimental and FRITIOF data are displayed in Fig. 4. The mass exponents, T_q, are observed to increase with increasing order of the moments, q, for both the data sets.

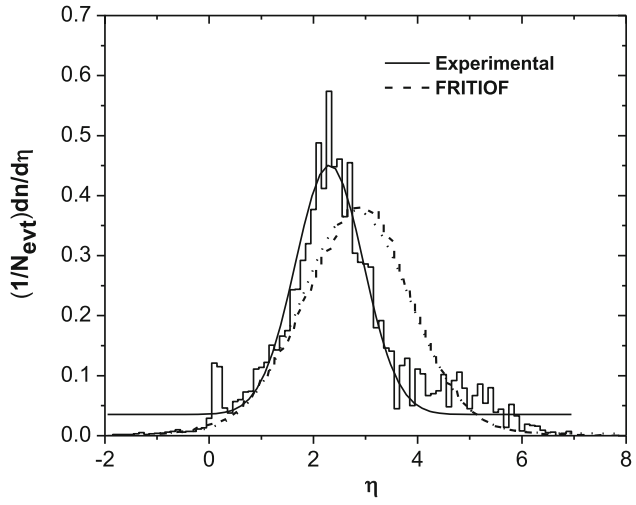

Fig. 1 Normalized pseudo-rapidity distributions of relativistic charged particles in ^{28}Si–nucleus interactions. Solid (Experimental) and dotted (FRITIOF) curves are the best fits to the data

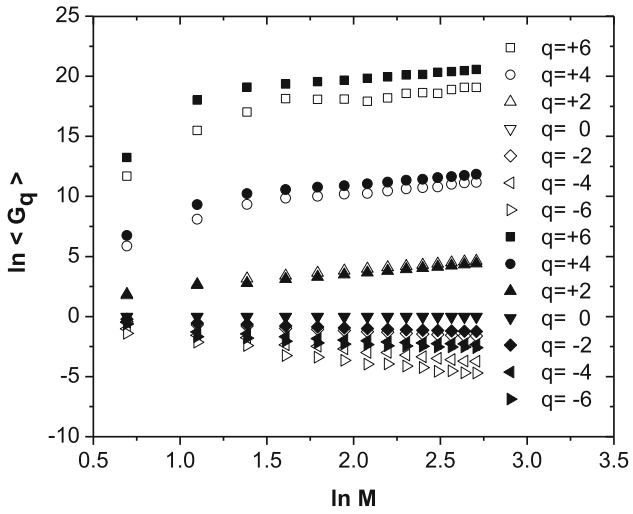

Fig. 2 The variations of ln $\langle G_q \rangle$ with ln M in ^{28}Si–nucleus interactions. Open symbols (experimental) and solid symbols (FRITIOF)

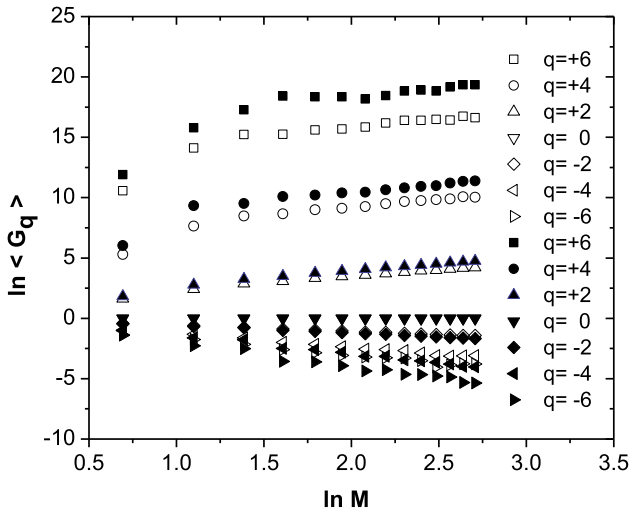

Fig. 3 The plot of ln $\langle G_q \rangle$ versus ln M for two groups of events in ^{28}Si–nucleus collisions. Open symbols ($N_g \leq 1$) and solid symbols ($N_g \geq 2$)

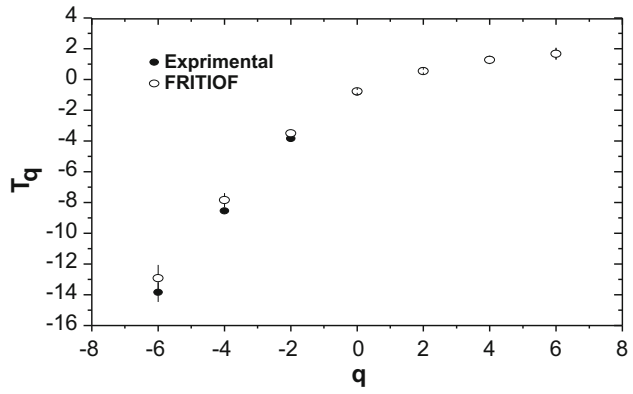

Fig. 4 The variations of T_q with q in ^{28}Si–nucleus interactions. This is for entire sample in which all N_g are included

The dependence of the mass exponents, T_q, on q for two groups of events, i.e. $N_g \leq 1$ and $N_g \geq 2$, is given in Fig. 5. From the figure, it may be seen that T_q increases with the increase in the order of the moments, q. However, it seems to saturate at higher values of q. We find that the dependence of T_q on q is almost similar for the two groups of events.

To study the contribution of the dynamical component of the multifractal moments, experimental results were compared with those of the MC-RAND events. For this purpose, the values of G_q as well as T_q moments for the MC-RAND data which is written

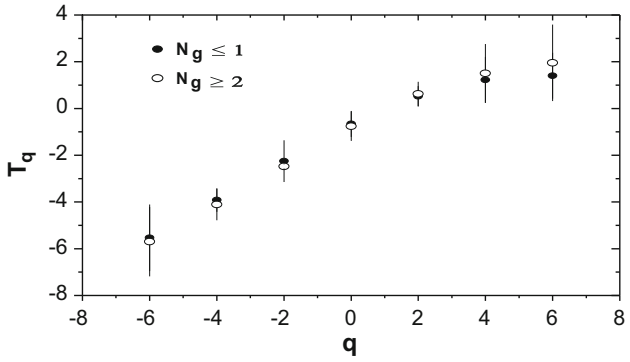

Fig. 5 T_q versus q plots for ^{28}Si–nucleus interactions having $N_g \leq 1$ and $N_g \geq 2$ groups of experimental events

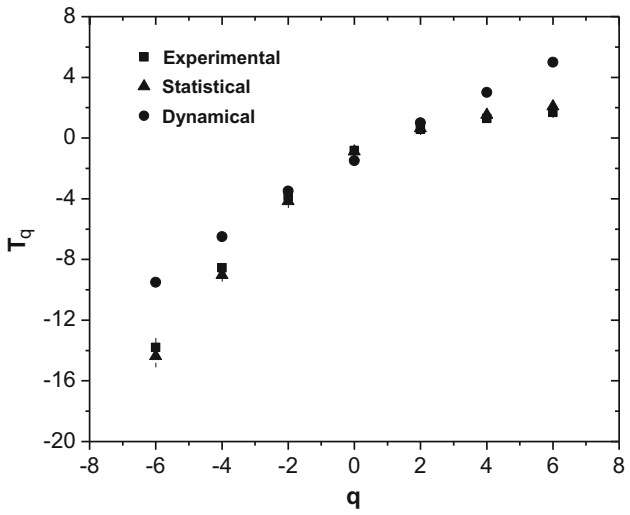

Fig. 6 The variation of T_q, T_q^{dyn} and T_q^{stat} with q in ^{28}Si–nucleus collisions

as G_q^{stat} and T_q^{stat} respectively, have also been calculated in the same way as that for the experimental data. Further, the statistical component (T_q^{stat}) and dynamical component (T_q^{dyn}) of the mass exponents are related [9] as:

$$T_q^{dyn} = T_q - T_q^{stat} + (q-1) \tag{8}$$

The variations of T_q, T_q^{stat} and T_q^{dyn} with the moment order, q, are shown in Fig. 6. It may be seen from the figure that T_q increases with increasing q; however, the rate of increase in the regions which correspond to positive and negative values of q are quite different. In the regions corresponding to the negative q values, the increase in T_q is relatively more rapid in comparison with that for the region in which q have positive values. This observation is consistent with the predictions of the gluon model [47]. Furthermore, the deviation in the values of T_q from T_q^{dyn} may, therefore, lead to the deviation in the T_q^{dyn} from $(q-1)$. It should be mentioned that any deviation of T_q^{dyn} from $(q-1)$ will indicate the presence of dynamical contribution to the fluctuations. Therefore, T_q may be considered as a more sensitive measure of dynamical fluctuation than G_q itself. One more observation that may be made is that T_q^{dyn} coincides with T_q^{stat} in the mid-region of q values, whereas for the q values in the region $(-2 \geq q \geq 2)$, a significant departure is observed.

The variations of the generalized dimensions, D_q, with q, in ^{28}Si–nucleus collisions for experimental and FRITIOF data are exhibited in Fig. 7. The generalized dimensions are found to be positive for all orders of the moments, q and demonstrate a decreasing trend with increasing q. This behaviour is in excellent agreement with the predictions of the multifractal cascade model [54]. It may also be observed from the figure that the values of D_q are greater than unity for $q \leq -2$, and this result is in agreement with those reported [37] earlier for different projectiles over a wide energy range.

To examine the variation of the generalized dimensions with a certain order of the moment, we have plotted D_q as a function of q in Fig. 8 again for the same two groups of events, i. e. $N_g \leq 1$ and $N_g \geq 2$. From the figure, we note that the generalized dimensions, D_q, are almost the same in the case of negative as well as positive values of q for both the groups of events. However, it is also observed that these values are slightly higher for $N_g \geq 2$ group of events for positive q values. One of the reasons for the higher value of D_q in the case of $N_g \geq 2$ may be due to an expected increase in the average multiplicity [55].

Figure 9 shows the dependence of $f(\alpha_q)$ on α_q for the experimental and FRITIOF events. The width of the multifractal spectra for experimental events and for the simulated events is almost the same. This means that the nature of the spectra is same as concave

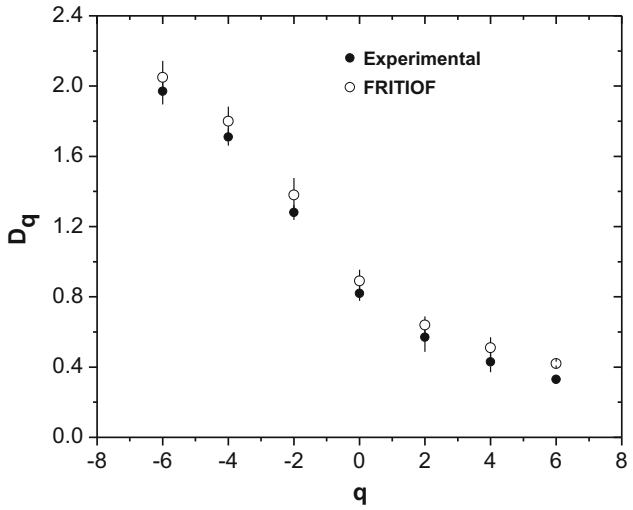

Fig. 7 Variation of generalized dimension, D_q, with q for experimental and FRITIOF data in ^{28}Si–nucleus collisions

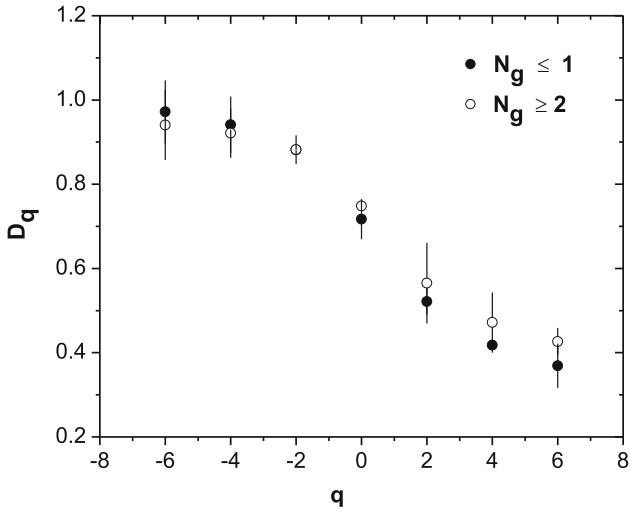

Fig. 8 The variations of generalized dimension, D_q, with q in ^{28}Si–nucleus interactions

downwards centred around α_q corresponding to $q = 0$ and have a common tangent at an angle of 45°. This observation agrees fairly well with the predictions of the gluon model [47]. However, $f(\alpha_q)$ has no peak in any of the cases studied, which is an indication of the non-smooth nature of the multiplicity distribution of the particles produced in the interactions considered for the present study. To see the dependence of $f(\alpha_q)$ spectra on α_q for two groups of events, $N_g \leq 1$ and $N_g \geq 2$ are plotted in Fig. 10. The shape of the spectra is found to be same for both groups of events.

5 Concluding remarks

The conclusions that may be drawn from the present investigation are as follows:

1. A power-law behaviour is observed in the variation of $\ln \langle G_q \rangle$ with $\ln M$. A concave downward trend is found to exist for spectral function, $f(\alpha_q)$. These observations, which are for experimental and FRITIOF events, indicate the presence of multifractality in the mechanism of multiparticle production.
2. The deviation of T_q^{dyn} from $(q-1)$ indicates the presence of dynamical contribution to the fluctuations.
3. The decreasing trend in the value of D_q with increasing q confirms the presence of multifractality.
4. The variation of the parameters T_q, D_q on q and $f(\alpha_q)$ on α_q is observed to be almost similar for the two groups of events, $N_g \leq 1$ and $N_g \geq 2$.

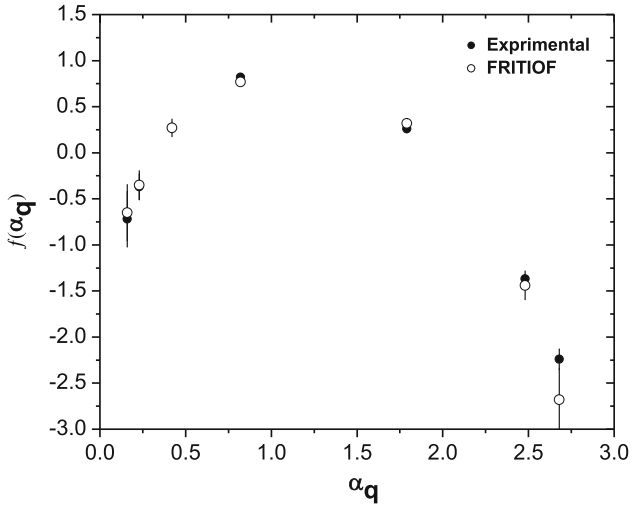

Fig. 9 The dependence of multifractal spectral function, $f(\alpha_q)$, on α_q in ^{28}Si–nucleus collisions

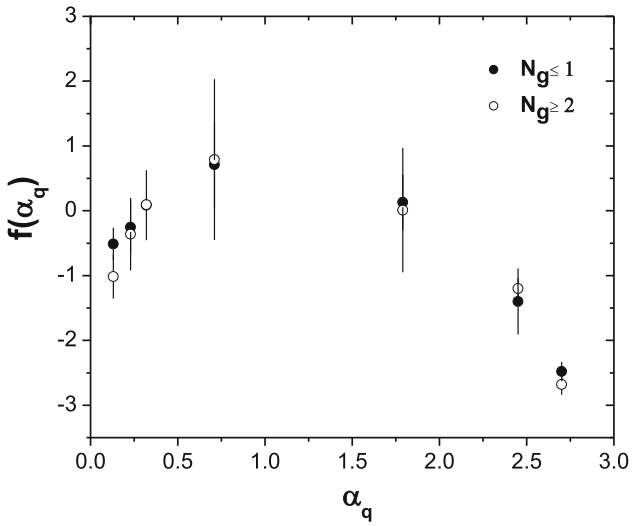

Fig. 10 The dependence of multifractal spectral function, $f(\alpha_q)$, on α_q in ^{28}Si–nucleus collisions for two groups of events, $N_g \leq 1$ and $N_g \geq 2$

Data Availability Statement This manuscript has associated data in a data repository. [Authors' comment: This is our results.]

References

1. Z.V. Anzon et al., Nucl. Phys. B **129**, 205 (1977). https://doi.org/10.1016/0550-3213(77)90192-4
2. R.K. Shivpuri et al., Phys. Rev. D **35**, 3508 (1987). https://doi.org/10.1103/PhysRevD.35.3508
3. A. Abduzhamilov et al., Phys. Rev. D **39**, 86 (1989). https://doi.org/10.1103/PhysRevD.39.86
4. T. Ahmad, ISRN High Energy Phys. **2014**, 1 (2014). https://doi.org/10.1155/2014/604730
5. A. Tufail et al., Phys. Rev. D **42**, 2187 (1990). https://doi.org/10.1103/PhysRevD.42.2187
6. A. Tufail et al., Int. J. Mod. Phys. A **6**, 929 (1991). https://doi.org/10.1142/S0217751X91000502
7. M.H. Rasool et al., J. Korean Phys. Soc. **67**, 448 (2015). https://doi.org/10.3938/jkps.67.448
8. P.L. Jain et al., Phys. Rev. C **46**, 721 (1992). https://doi.org/10.1103/PhysRevC.46.721
9. P. Mali et al., Mod. Phys. Lett. A **32**, 1750024 (2017). https://doi.org/10.1142/S0217732317500249
10. C.B. Chiu, R.C. Hwa, Phys. Rev. D **45**, 2276 (1992). https://doi.org/10.1103/PhysRevD.45.2276
11. N. Parashar, Il Nuovo Cimento A **108**, 789 (1995). https://doi.org/10.1007/BF02813380
12. R.K. Shivpuri et al., Phys. Rev. C **51**, 1367 (1995). https://doi.org/10.1103/PhysRevC.51.1367
13. D. Ghosh et al., Phys. Rev. C **70**, 054903–055001 (2004). https://doi.org/10.1103/PhysRevC.70.054903
14. R. Hasan et al., Int. J. Mod. Phys. E **13**, 479 (2004). https://doi.org/10.1142/S0218301304002284
15. K. Kajantie, L. McLerran, Phys. Lett. B **119**, 203 (1982). https://doi.org/10.1016/0370-2693(82)90277-5
16. M.K. Singh et al., Eur. Phys. J. Plus **136**, 419 (2021). https://doi.org/10.1140/epjp/s13360-021-01429-5
17. E.V. Shuryak, Phys. Rep. **115**, 151 (1984). https://doi.org/10.1016/0370-1573(84)90037-1
18. J. Cleymans et al., Phys. Rep. **130**, 217 (1986). https://doi.org/10.1016/0370-1573(86)90169-9
19. S. Bhattacharyya et al., Adv. High Energy Phys. **2018**, 6384357 (2018). https://doi.org/10.1155/2018/6384357
20. M.K. Singh, V. Singh, Eur. Phys. J. Plus **135**, 740 (2020). https://doi.org/10.1140/epjp/s13360-020-00748-3
21. N. Marimuthu et al., Int. J. Mod. Phys. E **28**, 1950058 (2019). https://doi.org/10.1142/S0218301319500587

22. R. Gupta et al., Adv. High Energy Phys. **2020**, 7319894 (2020). https://doi.org/10.1155/2020/7319894
23. R. Sharma et al., Adv. High Energy Phys. **2018**, 6283801 (2018). https://doi.org/10.1155/2018/6283801
24. T. Ahmad, N. Ahmad, J. Korean Phys. Soc. **77**, 107 (2020). https://doi.org/10.3938/jkps.77.107
25. U. Singh et al., J. Korean Phys. Soc. **76**, 297 (2020). https://doi.org/10.3938/jkps.76.297
26. J. Wu et al. https://arxiv.org/abs/2104.11524
27. B. Abelev et al., Phys. Rev. Lett. **110**, 152301 (2013). https://doi.org/10.1103/PhysRevLett.110.152301
28. J. Weil et al., Euro Phys. J. A **48**, 111 (2012). https://doi.org/10.1140/epja/i2012-12111-9
29. R. Rapp et al., Nucl. Phys. A **431**, 696 (2014). https://doi.org/10.1016/j.nuclphysa.2014.08.008
30. C.P. Singh, Phys. Rep. **236**, 147 (1993). https://doi.org/10.1016/0370-1573(93)90172-A
31. T. Niida, Y. Miake, AAPPS Bull. **31**, 12 (2021). https://doi.org/10.1007/s43673-021-00014-3
32. E.L. Bratkovskaya et al. https://arxiv.org/abs/1007.2812v1
33. B. Abelev et al., Phys. Rev. Lett. **110**, 152301 (2013). https://doi.org/10.1103/PhysRevLett.110.152301
34. T.H. Burnett et al., Phys. Rev. Lett. **50**, 2062 (1983). https://doi.org/10.1103/PhysRevLett.50.2062
35. B. Buschbeck, P. Lipa, Mod. Phys. Lett. A **4**, 1871 (1989). https://doi.org/10.1142/S0217732389002112
36. T.H. Burnett et al., Phys. Rev. Lett. **57**, 3249 (1986). https://doi.org/10.1103/PhysRevLett.57.3249
37. G. Paladin, A. Vulpiani, Phys. Rep. **156**, 147 (1987). https://doi.org/10.1016/0370-1573(87)90110-4
38. A. Bialas, R. Peschanski, Nucl. Phys. B **273**, 703 (1986). https://doi.org/10.1016/0550-3213(86)90386-X
39. T. Bohr, M.H. Jensen, Phys. Rev. A **36**, 4904 (1987). https://doi.org/10.1103/PhysRevA.36.4904
40. P. Szepfalusy et al., Phys. Rev. A **36**, 3525 (1987). https://doi.org/10.1103/PhysRevA.36.3525
41. R.C. Hwa, Phys. Rev. D **45**, 1476 (1992). https://doi.org/10.1103/PhysRevD.45.1476
42. C.B. Chiu et al., Mod. Phys. Lett. A **5**, 2651 (1990). https://doi.org/10.1142/S0217732390003085
43. R.C. Hwa, Phys. Rev. D **41**, 1456 (1990). https://doi.org/10.1103/PhysRevD.41.1456
44. W.H. Barkas, *Nuclear Research Emulsion* (Academic Press, London, 1963)
45. C.F. Powel, P.H. Fowler, D.H. Perkins, *The study of Elementary Particles by Photographic Method*, 2nd edn. (Pergamon, Oxford, 1959)
46. E.A. De Wolf et al., Phys. Rep. **270**, 1 (1996). https://doi.org/10.1016/0370-1573(95)00069-0
47. C.B. Chiu, R.C. Hwa, Phys. Rev. D **43**, 100 (1991). https://doi.org/10.1103/PhysRevD.43.100
48. H.G.E. Hentschel, I. Procaccia, Phys. D Nonlinear Phenom. **8**, 435 (1983). https://doi.org/10.1016/0167-2789(83)90235-X
49. N. Ahmad, Ph. D. Thesis, Aligarh Muslim University, Aligarh, U.P. India (2002)
50. B. Nilsson-Almqvist, E. Stenlund, Comput. Phys. Commun **43**, 387 (1987). https://doi.org/10.1016/0010-4655(87)90056-7
51. C.A. Sanchez et al., J. Arkansas Acad. Sci. **49**, 34 (1995). https://scholarworks.uark.edu/jaas/vol49/iss1/34
52. R.K. Shivpuri, N. Parashar, Phys. Rev. D **49**, 219 (1994). https://doi.org/10.1103/PhysRevD.49.219
53. D. Ghosh et al., Phys. Lett. B **272**, 5 (1991). https://doi.org/10.1016/0370-2693(91)91003-E
54. R.K. Shivpuri, V.K. Verma, Phys. Rev. D **47**, 123 (1993). https://doi.org/10.1103/PhysRevD.47.123
55. R. Peschanski, Nucl. Phys. B **327**, 144 (1989). https://doi.org/10.1016/0550-3213(89)90289-7

Appendix

Transition to a modern CMake-based build system for CbmRoot

0.1 Introduction

A well-designed software architecture and development environment reduces management overhead, allowing even small teams to maintain and improve complicated projects https://cmake.org/. CMake is a tested tool that helps programmers design a robust build environment. Modern CMake can be used, among other things, for handling multiple build targets, automating pre- and post-build tasks, and coordinating cross-platform toolchains. CMake can generate a native build environment that incorporates executables, compiles source code, and generates libraries and wrappers. CMake can generate a build environment across platforms and users by generating a variety of build contexts, from the more traditional Makefiles to the more recent Ninja build system. Also, the generation of the specific config files for various IDEs is possible as the output of a CMake execution. Because of these facts, CMake has been widely adopted in multiple projects to allow smooth cross-platform integration.

CMake acts as an integrator for various tasks during the configuration and builds a process of the actual artefact; it neither interacts directly with the toolchains nor replaces them. There are several aspects of CMake that are significant:

- It continues to focus on supporting modern compilers and toolchains, for ex. arm64.
- CMake supports building for Linux and macOS, allowing it to be truly cross-platform.
- It produces project files for well-known IDEs, including Eclipse CDT, Xcode, and Microsoft Visual Studio.
- CMake allows one to organize files into reusable targets and projects because it operates at the proper level of abstraction.

- CMake is used to build many projects, and most of them provide a simple way to include them in the project, for example, FairRoot and other external dependencies in the case of the CbmRoot project. If one requires a preinstalled library, there is a strong chance that it has a find CMake script or config CMake script.
- Testing, packaging, and installation are considered integral parts of the build process by CMake.
- There is an available knowledge base that helps to use the synergies with the SDE group and other FairRoot users from our community, like Panda.

Beginning with CMake 3.0, new features were introduced in CMake, which allows to define the dependencies on a different level. This change was called by some CMake users “modern CMake”. one may spend most of the time coding rather than adding lines to an unreadable, unmaintainable Make file since it is clear, strong, and elegant. Additionally, modern CMake is claimed to be significantly faster! There are some advantages of modern CMake over old CMake, which will be discussed below.

One of the main differences between “old” and “modern” CMake are the introduction and refinement of targets. With modern CMake, targets are no longer limited to the level where they are defined but as global objects. Old CMake defines targets on the directory level such that they are not known in other directories or even one level up in hierarchies. One even can reuse targets defined by other projects in their installations.

In old CMake, the user had to know sometimes the hidden dependencies of the used direct dependencies. In modern CMake, the target knows about its dependencies such that when using a target, the full information about needed “include directories" and used libraries are available for the consument of the target.

Modern CMake reduces errors by automatically propagating dependencies to users, while in old CMake, all requirements are specified via a variable.

0.2 The concept of a target

If one has ever used GNU Make, one has probably come across the concept of a target. It is a recipe used by a build system to compile a list of files into another file. It can be a .cpp implementation file compiled into an .o object file, a collection of .o files packaged into an .a static library, or any combination of

these. It can build an executable from source files directly. CMake knows how to generate object files from source files or how to link libraries for all supported platforms and compilers. One does not need to specify how this is done in detail. One needs only to define on a higher level the input and the output. Therefore, compiling any object files doesn't require writing a specific recipe. In CMake, It can build a target with one of three commands:

1. `add_executable()`
2. `add_library()`
3. `add_custom_target()`

The CMake command `target_link_libraries()` is used to build a dependency between targets.

```
target_link_libraries(<target>
<PRIVATE|PUBLIC|INTERFACE> <item>...
[<PRIVATE|PUBLIC|INTERFACE> <item>...]...)
```

Propagation keywords work like this:

PRIVATE Appends the source value to the private property of the destination. For example When target 'A' links to target 'B' as PRIVATE, it means that target 'A' uses target 'B' in its implementation, but target 'B' is not used in any part of the public API of target 'A'.

INTERFACE Appends the source value to the interface property of the destination. For example When target 'A' links to target 'B' as INTERFACE, it means that target 'A' doesn't use target 'B' in its implementation, but target 'B' is used in the public API of target 'A'.

PUBLIC Appends to both properties of the destination. For example When target 'A' links to target 'B' as "PUBLIC", it's a combination of "PRIVATE" and "INTERFACE." It says that the implementation of target 'A' uses target 'B', and the public API of target 'A' also uses target 'B'.

The CMake command `target_include_directories()` adds an include directory to a target. For an executable, **PUBLIC** means nothing, but for a library, it tells CMake that any targets that link to this target must also have that include directory.

```
target_include_directories(<target> [SYSTEM] [AFTER|BEFORE]
<INTERFACE|PUBLIC|PRIVATE> [item1...]
[<INTERFACE|PUBLIC|PRIVATE> [item2...] ...])
```

The SYSTEM keyword instructs the compiler that the provided directories are supposed to be standard system directories.

If imagine targets as objects like c++, CMake has a constructor, member variable and member functions;
Analogy to constructors:

- **add_executable()**
  Add as an executable to be built from the source files listed in the command input.
- **add_library()**
  Add as a library target to be built from the source files listed in the command input.

Analogy to member variables:

- target properties()

Analogy to member function:

- **target_compile_definitions()**
  To set the compile definitions with their visibility (PRIVATE, PUBLIC, INTERFACE) to the target.
- **target_compile_features()**
  To set the compile features with their visibility (PRIVATE, PUBLIC, INTERFACE) to the target.
- **target_compile_options()**
  To set the compile options with their visibility (PRIVATE, PUBLIC, INTERFACE) to the target.
- **target_include_directories()**
  To set the include directories with their visibility (PRIVATE, PUBLIC, INTERFACE) to the target. It's better to use this command instead of include_dircetories() because it doesn't associate with any target. It has a directory scope, which means it is set for all targets defined in the CMakeLists.txt file, even at the subdirectory level.

- **target_link_libraries()**
  With this, usage requirements are propagated from the dependent-target to the depending-target. Additionally, the command supports transitive dependencies.

- **target_sources()**
  It provides sources for building a target and/or its dependents.

- **get_target_property()**
  To get the target properties.

- **set_target_property()**
  To set the target properties.

0.3 Finding installed packages

Every system has its method of installing and managing packages. Finding the path where a package exists can be difficult and time-consuming, especially if one needs to support the majority of today's OS systems. Fortunately, The CMake command `find_package()` can often handle this issue for the user if the package in question has a config-file that allows CMake to determine the variables necessary to support the package. Many projects today cope with this requirement and offer CMake config-file during installation. If any library or package doesn't provide it, There are chances that CMake authors have bundled the file with CMake itself (these are called find-modules to differentiate from config-files). If a package also doesn't provide a find-module, then the user can provide such a CMake module himself. The `find_package()` command's arguments are somewhat lengthy, so the basic signatures are concentrated here. Here's how it looks:

```
find_package(<Name> [version] [EXACT] [QUIET] [CONFIG] [REQUIRED])
```

version It allows the option of requesting a particular version.

EXACT keyword indicates that an exact version; a range is not permitted in this context.

QUIET When a package is found or not found, this keyword mutes all notifications.

CONFIG keyword implies that only Config mode can be used to find the package.

REQUIRED this keyword will stop execution and print a diagnostic message if a package cannot be identified (even if QUIET is enabled).

Here is a simple example which uses the ROOT package via the config file.

```
cmake_minimum_required(VERSION 3.1...3.23)
project(RootExample LANGUAGES CXX)

# Finding the ROOT package
find_package(ROOT 6.16 CONFIG REQUIRED)

# Adding an executable program and linking to needed ROOT libraries

add_executable(RootExample main.cxx)
target_link_libraries(RootExample PUBLIC ROOT::Physics)
```

So, In modern CMake, we don't need to know the internal properties of the ROOT package. It propagates automatically in the form of the usage-requirements. Additionally, one can use IMPORTED targets (ROOT::Physics) which are provided by ROOT itself. The `target_link_libraries()` command will also create a target which can be later used. This target now defines all information needed by a consumer of that target. The consumer doesn't need to know that the target depends on ROOT.

0.4 Dictionary generation

Dictionary generation is ROOT's approach to missing a reflection feature in C++. It permits ROOT to understand the details of the class to save it, provide methods in the Cling interpreter, and so on. The following command is used to generate the root dictionary.

```
root_generate_dictionary(G__Example Example.h LINKDEF ExampleLinkDef.h)
```

This command creates three files:

1. G__Example.cxx: This file should be included in the sources when one makes the library.
2. libExample.rootmap: The rootmap file in plain text.
3. libExample_rdict.pcm: A ROOT pre-compiled module file

0.5 CMake Functions and Macros

In order to provide a named abstraction for some repetitive tasks, CMake supports both functions and macros. A function or macro is always used to create a new command.

0.5.1 Function

The function can be defined as;

```
function(<name> [<arg1> ...])
 # <commands>
endfunction()
```

where "name" is the function's name, and arg1, arg2, etc., are its arguments. In this scenario, the function name is case-insensitive. Although one can call, in any case, it is always advised to use the name that was declared in the function definition. The CMake function can be used by two types of arguments.

Named or keyword arguments: If named arguments are not provided, an error will come. A comma is not required between argument names.

Optional arguments: Some predefined variables can be used to access optional arguments.

- ARGC : Total number of arguments(named arguments + optional arguments)
- ARGV: list of variables containing both named and optional arguments
- ARGN: list of variables containing only optional arguments

In addition to those three variables, CMake offers the following ones: ARGV0, ARGV1, ARGV2,... These variables will contain the actual values of the arguments provided.

CMake functions introduce new scopes, and variables modified inside them are not accessible outside them. CMake's functions don't return any value, which is another problem. The function will be challenging to utilise as a consequence. Thus, setting a variable in the parent scope is possible with the help of the CMake keyword PARENT SCOPE.

0.5.2 Macro

Macro can be defined in CMake as;

```
macro(<name> [<arg1> ...])
#  <commands>
endmacro()
```

Macro names are also case-insensitive, much like functions. Although using is always allowed, using the name provided in the macro definition is usually advised. When a function is called, it always creates a new scope. In the case of a macro, the macro call is replaced by the macro body, and arguments are replaced by string substitution. There is no new scope introduced. As a result, in some cases, functions and macros behave differently.

0.6 CMake in CbmRoot framework

The CBM software framework (CbmRoot) is based on the FairRoot simulation and analysis framework built with the CMake build generator. Up to now, in CbmRoot, it was built with old commands of CMake. Indeed, there was no shortage of problems when building. For example, one had to define the internal properties of the dependency explicitly. Because of this, there were lots of scope variables defined in the CMakeList.txt file. Modern CMake, which start after v3.0, has a perfect solution to solve these problems. It's all about targets and properties(i.e., compile definitions, compile options, compile features, include directories and library dependencies). The properties of the target can be set on the target directly in modern CMake. These properties propagate themselves to another target which depends on it. That is the most important advantage of modern CMake. The developer does not need to understand the whole system to reason about a single target. The build system handles transitivity. Similarly, one can add compile features and flags on target. Additionally, In modern CMake, the ALIAS targets can be created to keep usage consistent. Modern CMake also allows using modern find modules that declare exported targets. Keeping these advantages in mind, the transition to modern CMake to generate the build system of CbmRoot has been implemented. The modified CMakeLists.txt file can be found in a git repository.

There are lots of packages which are required to build CbmRoot, like FairRoot, Root, Boost etc. By using `find_package()` command, one can import these packages into our project (see the example of section 0.3). Most of the packages

has own config file provided by the package's author. But some of the packages don't provide the config file like FairRoot.

At the sub-directory level, all CMakeLists.txt files are modified and committed to the git repository. To create a library target, a macro is introduced in the CbmMacros.cmake module inside the CMake modules directory. Here is a short example of the `CbmBase` library target. "Default" and "Modern CMake" are the CMakeLists.txt using old and modern CMake, respectively. In the old CMake file, include_directories() and link_directories() commands are used that operate on the directory level. It means these settings are not set on a particular target, and the propagation of usage-requirements from the depending target is not automatic. For example, the CbmBase library target depends on the Boost library, so the internal properties of the boost have to define in old CMake. But in Modern CMake, It doesn't need to define explicitly. It comes automatically by the Boost dependency inform of usage-requirement. Additionally, in modern CMake, ALIAS targets have been used that creates another reference to a target under a different name. Alias targets can not install or export because they are not displayed in the generated build system, and the properties of alias targets are read-only. They are helpful in situations when some portion of a project requires a target with a specified name. Still, the actual implementation may be available under different names depending on the circumstances.

Default

```
Set(SYSTEM_INCLUDE_DIRECTORIES
  ${BASE_INCLUDE_DIRECTORIES}
  ${Boost_INCLUDE_DIR}
  )

Include_Directories(SYSTEM
  ${SYSTEM_INCLUDE_DIRECTORIES}
  )

Set(INCLUDE_DIRECTORIES
  ${CMAKE_CURRENT_SOURCE_DIR}
  ${CMAKE_CURRENT_SOURCE_DIR}/report
  ${CMAKE_CURRENT_SOURCE_DIR}/draw
  ${CMAKE_CURRENT_SOURCE_DIR}/utils

  ${CBMDATA_DIR}
  ${CBMDATA_DIR}/base
  ${CBMDATA_DIR}/sts
  ${CBMDATA_DIR}/tof
  ${CBMDATA_DIR}/rich
  ${CBMDATA_DIR}/much
  ${CBMDATA_DIR}/mvd
  ${CBMDATA_DIR}/trd
  ${CBMDATA_DIR}/psd
)
Include_Directories(
  ${INCLUDE_DIRECTORIES}
  )

Set(LINK_DIRECTORIES
  ${ROOT_LIBRARY_DIR}
  ${FAIRROOT_LIBRARY_DIR}
  ${Boost_LIBRARY_DIRS}
)
 link_directories(
   ${LINK_DIRECTORIES}
   )

set(SRCS
  CbmDigiManager.cxx
  CbmDigitizeBase.cxx
  .
  draw/CbmDrawHist.cxx
  report/CbmReport.cxx
  .
  utils/CbmUtils.cxx
  .
  )

If(${FairRoot_VERSION} VERSION_LESS 18.4.0)
  set_source_files_properties(
    utils/CbmGeometryUtils.cxx
    PROPERTIES COMPILE_DEFINITIONS
    OLD_MODULE_VERSION
    )
EndIf()

Set(LINKDEF CbmBaseLinkDef.h)
Set(LIBRARY_NAME CbmBase)
Set(DEPENDENCIES
    CbmData Base boost_regex boost_filesystem
)

GENERATE_LIBRARY()

Install(FILES
  CbmDigitize.h
  report/CbmReportElement.h
  DESTINATION include
  )
```

CMakeLists.txt for CbmBase library target.

Modern CMake

```
set(INCLUDE_DIRECTORIES
  ${CMAKE_CURRENT_SOURCE_DIR}
  ${CMAKE_CURRENT_SOURCE_DIR}/report
  ${CMAKE_CURRENT_SOURCE_DIR}/draw
  ${CMAKE_CURRENT_SOURCE_DIR}/utils
  )
set(SRCS
  CbmDigiManager.cxx
  CbmDigitizeBase.cxx
  .
  draw/CbmDrawHist.cxx
  report/CbmReport.cxx
  .
  utils/CbmUtils.cxx
  .
  )
set(LIBRARY_NAME CbmBase)
set(LINKDEF ${LIBRARY_NAME}LinkDef.h)
set(PUBLIC_DEPENDENCIES
  CbmData
  FairRoot::Base
  ROOT::Core
  ROOT::Gpad
  ROOT::Hist
  )
set(PRIVATE_DEPENDENCIES
  FairLogger::FairLogger
  FairRoot::GeoBase
  Boost::filesystem
  ROOT::Geom
  ROOT::Graf
  ROOT::MathCore
  ROOT::RIO
  ROOT::Tree
  )
generate_library()
Install(FILES
   CbmDigitize.h
   CbmTrackingDetectorInterfaceBase.h
   report/CbmReportElement.h
   DESTINATION include
       )
```

```
    macro(generate_cbm_library)
#macro for generating Cbm libraries

  ############## Changing the file extension .cxx to .h ################
  foreach (SRCS ${SRCS})
    string(REGEX REPLACE "[.]cxx$" ".h" HEADER "${SRCS}")
      if(EXISTS "${CMAKE_CURRENT_SOURCE_DIR}/${HEADER}")
        set(HEADERS ${HEADERS} ${HEADER})
      endif()
  endforeach()

  foreach (HEADER ${HEADERS})
    # strip relative path from headers to pass them to rootcling
    get_filename_component(_rootheader ${HEADER} NAME)
    list(APPEND ROOT_HEADERS ${_rootheader})
  endforeach()

  ######################### build the library ############################
  add_library(${LIBRARY_NAME} SHARED ${HEADERS} ${SRCS} ${NO_DICT_SRCS} ${LINKDEF})

  target_link_libraries(${LIBRARY_NAME}
    PUBLIC ${DEPENDENCIES} ${PUBLIC_DEPENDENCIES}
    PRIVATE ${PRIVATE_DEPENDENCIES}
    INTERFACE ${INTERFACE_DEPENDENCIES})

  target_include_directories(${LIBRARY_NAME}
    PUBLIC ${INCLUDE_DIRECTORIES})

  if(LINKDEF)
    root_generate_dictionary(G__${LIBRARY_NAME}
      ${ROOT_HEADERS}
      MODULE ${LIBRARY_NAME}
      LINKDEF ${LINKDEF})
    if (CMAKE_CXX_COMPILER_ID MATCHES Clang)
      set_target_properties(G__${LIBRARY_NAME}
      PROPERTIES COMPILE_FLAGS
      "-Wno-overloaded-virtual
      -Wno-shadow
      -Wno-deprecated-declarations
      -Wno-unused-parameter")
    else()
      set_target_properties(G__${LIBRARY_NAME}
      PROPERTIES COMPILE_FLAGS
      "-Wno-ctor-dtor-privacy
      -Wno-overloaded-virtual
      -Wno-null-pointer-subtraction
      -Wno-shadow
      -Wno-deprecated-declarations
      -Wno-unused-parameter")
    endif()
  endif(LINKDEF)

  ############# Install target and corresponding header files ############
  install(TARGETS ${LIBRARY_NAME} DESTINATION lib)
  install(FILES ${HEADERS} DESTINATION include)


  if(LINKDEF)
    set(rootmap_file ${CMAKE_CURRENT_BINARY_DIR}/${CMAKE_SHARED_LIBRARY_PREFIX}${LIBRARY_NAME}.rootmap)
    set(pcm_file ${CMAKE_CURRENT_BINARY_DIR}/${CMAKE_SHARED_LIBRARY_PREFIX}${LIBRARY_NAME}_rdict.pcm)

    add_custom_command(TARGET ${LIBRARY_NAME} POST_BUILD
                       COMMAND ${CMAKE_COMMAND} -E copy_if_different ${rootmap_file} ${LIBRARY_OUTPUT_PATH}
                       COMMAND ${CMAKE_COMMAND} -E copy_if_different ${pcm_file} ${LIBRARY_OUTPUT_PATH}
                       DEPENDS ${LIBRARY_NAME}
                      )

    install(FILES ${rootmap_file} ${pcm_file} DESTINATION lib)
  endif(LINKDEF)

  set(LIBRARY_NAME)
  set(LINKDEF)
  set(SRCS)
  set(HEADERS)
  set(NO_DICT_SRCS)
  set(DEPENDENCIES)
  set(PUBLIC_DEPENDENCIES)
```

```
  set(PRIVATE_DEPENDENCIES)
  set(INTERFACE_DEPENDENCIES)
  set(ROOT_HEADERS)

endmacro(generate_cbm_library)
```

Here is the Macro to generate the library target. First, the extension of the source files is changed to make the header file and store it in the new variable. Then the relative path from the header is stripped to pass them to rootcling. After that, a library target has been created using `add_library()` command. The include directories and dependencies have been linked using `target_include_directories()` and `target_link_libraries()` with their visibility (PRIVATE, PUBLIC and INTERFACE) to the library target. As already discussed, these command propagates usage requirements from the dependent target to the depending target. Then the dictionary is generated using `root_generate_dictionary()` that helps ROOT to understand the specifics of the class so that it may store it, show methods in the Cling interpreter, etc. In the end, targets and files have been installed.

Within CbmRoot, around 100 CMakeList.txt files have been modified to modern CMake. All modified files are committed to the git repository and tested with CI. The most important thing is that nobody has felt the change. After modification, almost 25 % area is cleaned in each CMakeLists.txt file. As a user, anyone doesn't have to modify the build system to move to modern CMake. These modifications will be included in the next CbmRoot release.